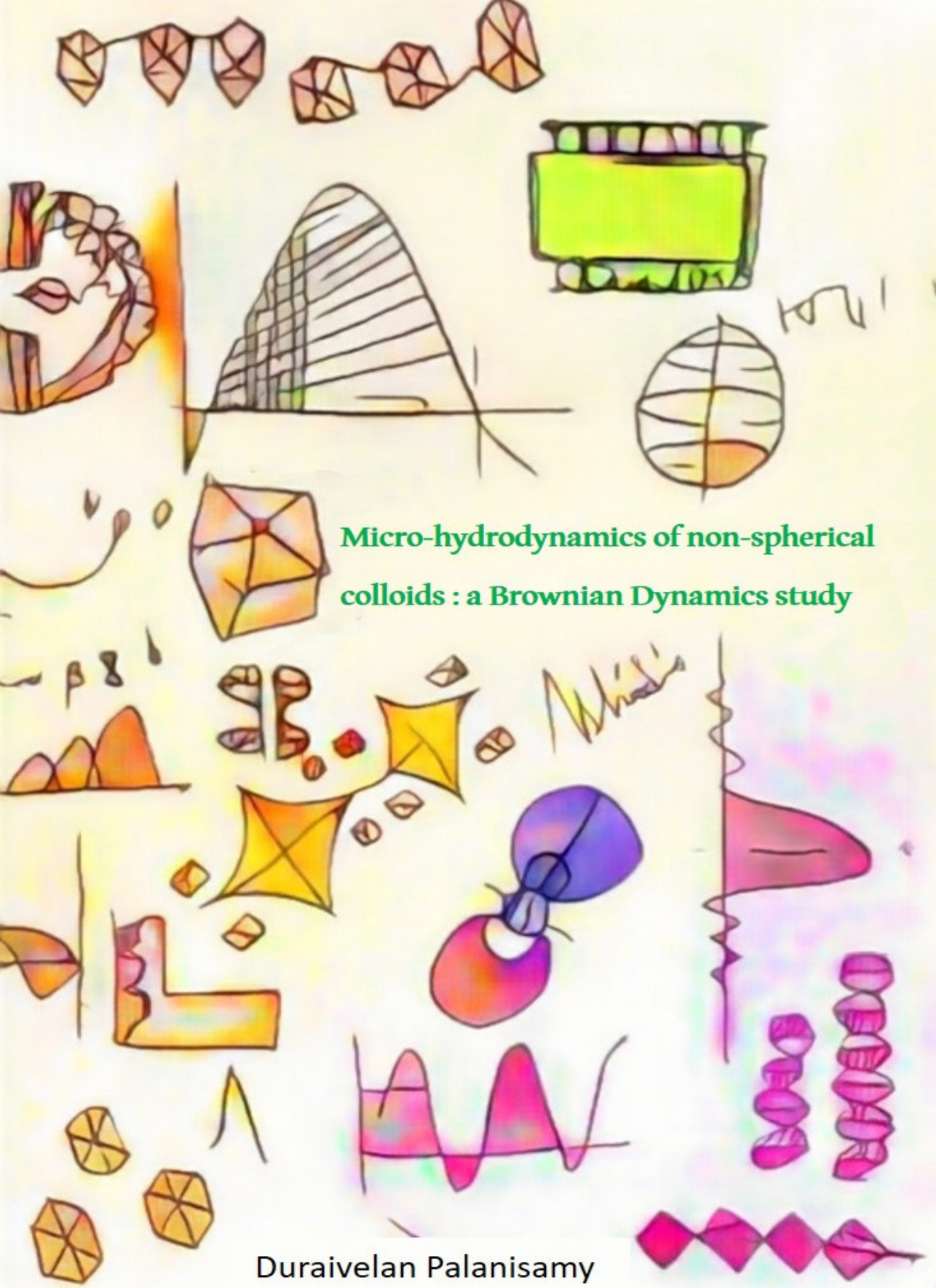

Micro-hydrodynamics of non-spherical colloids : a Brownian Dynamics study

Duraivelan Palanisamy

MICRO-HYDRODYNAMICS OF NON-SPHERICAL COLLOIDS: A BROWNIAN DYNAMICS STUDY

Duraivelan Palanisamy

MICRO-HYDRODYNAMICS OF NON-SPHERICAL COLLOIDS: A BROWNIAN DYNAMICS STUDY

DISSERTATION

to obtain
the degree of doctor at the University of Twente,
on the authority of the rector magnificus,
Prof.dr. T.T.M. Palstra,
on account of the decision of the Doctorate Board,
to be publicly defended
on Thursday the 16th of May 2019 at 12:45 hrs

by

Duraivelan Palanisamy
born on the 27th of August 1990
in Neyveli, India.

This dissertation has been approved by:

Supervisor: Prof.dr.rer.-nat. S. Luding
Co-supervisor: Dr.ir. W.K. den Otter

MESA+
INSTITUTE FOR NANOTECHNOLOGY

UNIVERSITY OF TWENTE.

NWO | Netherlands Organisation for Scientific Research

The work in this thesis was carried out at the Multi Scale Mechanics (MSM) group, MESA+ Institute of Nanotechnology, Faculty of Engineering Technology (ET), University of Twente, Enschede, The Netherlands.

This work is part of the research programme of the Foundation for Fundamental Research on Matter (FOM), which is part of the Netherlands Organisation for Scientific Research (NWO). Project Nr. 13CSER060, 'Simulating semi-solid rechargeable flow batteries', Computational sciences for energy research (CSER). This research programme is co-financed by Shell Global Solutions International B.V..

Cover design: Y. Thangavel, D. Palanisamy
Printed by: Ipskamp Printing, Enschede, The Netherlands
ISBN: 978-90-365-4769-7
DOI: 10.3990/1.9789036547697

Graduation committee:

Chairman:	Prof.dr. G.P.M.R. Dewulf	University of Twente, ET
Secretary:	Prof.dr. G.P.M.R. Dewulf	University of Twente, ET
Supervisor:	Prof.dr.rer.-nat. S. Luding	University of Twente, ET
Co-supervisor:	Dr.ir. W.K. den Otter	University of Twente, ET
Members:	Prof.dr. W.J. Briels	University of Twente, TNW
	Prof.dr.ir. C.H. Venner	University of Twente , ET
	Prof.dr. J.D.R. Harting	Helmholtz Institute Erlangen-Nürnberg
	Prof.dr. J.J.C. Geerlings	Delft University of Technology
	Dr. D. J. Kraft	Leiden University

To my family and friends

Contents

1

Introduction

In this chapter we will give a brief overview on how the current trend towards renewable energy laid the foundation to our project on "Semi-solid flow batteries". We outline the workings of a redox flow battery with particular focus on slurry rheology. Optimization challenges in slurry flow motivated our research topic on Brownian simulation of non-spherical colloids. We set out to improve the existing hydrodynamic models and propose newer algorithms geared towards Brownian simulation of colloidal aggregates in flow-fields.

1.1. Energy storage needs

There is a growing worldwide consensus that the global warming currently taking place is at least to a large extent caused by human activity. Slowly but steadily more and more resources are being devoted towards reducing CO_2 emissions across the globe, on both a national and an international level. An example of these efforts are the Europe 2020 targets set by the European Commission, which includes among others the goal to reduce greenhouse gas emissions by 20% compared to 1990 levels, and to generate at least 20% of the total energy consumption from renewables by the year 2020 [1]. Another example is the 2015 United Nations Conference on Climate Change held in Paris, where it was agreed upon by all 195 world nations present to keep global warming below 2 °C between now and the year 2100 [2]. The main requirement for achieving these goals is to reduce and eventually stop completely the burning of fossil fuels for energy generation, e.g. for transportation and electricity. On the other hand, the worldwide electricity demand is projected to increase by 70% by the year 2040 [3]. Thus, if the overall CO_2 emissions are to decrease despite the projected increase in energy demand, rigorous actions are required. Renewable energy sources such as solar, wind and biomass will therefore play an increasingly important role in the generation of energy in the coming decades. For example, the total installed solar power capacity has steadily increased in the past 15 years reaching a total of 178 GW worldwide, a trend that

is expected to accelerate in the future [4]. Similar trends are observed for wind energy as well, whose market has been steadily growing for more than a decade and has seen a 44% growth in 2014 [5].
However the energy generation by renewables such as solar and wind is unpredictable and may strongly fluctuate during the day, as it is strongly dependent on daily weather conditions. The power consumption on the other hand also fluctuates significantly at all time-scales since it is dependent on the collective consumption of millions of households. Thus the power production does not necessarily match the power consumption, and any excess energy during peak production must be stored so that it can be used during peak consumption. The timescale over which energy must be stored varies from seconds and minutes (solar energy for instance, due to the passing of clouds) to weeks and even months (due to seasonal variations), while fast discharging may be required due to sudden drops in energy generation. Having access to storage technologies that can full-fill these requirements is of equal importance as the development and deployment of solar cells and wind turbines they support. In addition to these requirements, the safety aspects, the cyclability (i.e. the number of charge and discharge cycles the technology can undergo before displaying deteriorated performance), the flexibility in terms of storage capacity and power output and the building and operating costs of the storage technology are also of great importance.

1.1.1. Storage methods

A wide variety of electrical storage methods are in existence such as capacitors, pumped hydroelectric energy storage, compressed air energy storage and electrochemical storage [6].

Capacitors are in essence the most simple way to store electrical energy, involving no energy conversion but directly storing the electrical energy by polarizing a dielectric material. Electricity is then recovered by relaxation of the polarization, bringing about the movement of electrons. Since capacitors involve no energy conversion and no moving parts other than the separation of charges in the dielectric material, they are inherently very efficient and have a long life time due to negligible wear and tear. However, the high device costs, fast self-discharge and low total energy capacity make capacitors unsuitable for e.g. solar or wind energy storage.

Pumped hydroelectric energy storage (PHES) involves pumping water to higher elevations, thus converting electrical energy to potential energy. The energy is recovered by flowing the water through a turbine and the overall process has a maximum efficiency of about 85%. Furthermore PHES has a high energy capacity and high power output, but the main disadvantages are the very high investment costs and the need for elevated terrain, meaning that it is not applicable everywhere, like for example in Netherlands.

Electrochemical storage encompasses a broad array of battery set-ups like standard lead-acid batteries, flow batteries (aqueous, non-aqueous), solid state batteries, all

of which store the electrical energy by chemical conversion of atoms or molecules and the energy is recovered by reversing the reaction. Such methods are in general very promising due to the flexibility and scalability at reasonable to high efficiencies, making them the most suitable candidate for applications like transportation, electrical grid systems, etc.

1.1.2. The redox flow battery

Redox flow battery (RFB) is one of the most promising candidates for worldwide application as a stationary energy storage technology due to good cyclability, flexibility and scalability. The RFB consists of an anode chamber and a cathode chamber containing a porous electrode, while the chambers are separated by an ion-exchange membrane, either anionic or cationic. During operation, anodic and cathodic electrolyte solutions containing redox active species (termed the anolyte and catholyte, respectively) flow through the electrode in their respective chambers and redox reactions take place. The anolyte and catholyte are stored externally in separate tanks, and the flow of these solutions through the chambers is achieved by means of a pump, sometimes aided by gravity. The electrons generated at the anode during discharge flow through an external circuit, delivering electrical energy. To maintain charge neutrality in both chambers, ions pass the membrane from the cathode to the anode (anions) or the other way around (cations). The redox reactions occurring during discharge are reversible, and the battery is recharged simply by supplying electrical energy, reversing the above process.

An important advantage of the generic RFB design described above is that the size of the tanks containing the anolyte and the catholyte is independent of the power conversion section, making RFBs a highly flexible storage technology. Thus the total energy capacity, which depends on the storage tank size and the redox active species concentration, and the power output, which depends on the number of batteries in the stack and the total electrode area, can be chosen separately. As such, RFBs are suitable for any stationary application, from small scale storage of solar energy for single households to large scale storage of energy from wind farms.

1.2. Semi solid flow batteries

The charge carriers in RFBs are ions in the electrolyte. Usually simple acids like HCl, H_3PO_4 are used as electrolytes. Since all the constituents are in liquid state, the ion concentrations are low in the range of (1M - 2M). Compared to the solid state lithium batteries which has active material concentration in the range of 20 - 90 M [8]. To improve the charge density of the flow battery Duduta *et al.* [9] incorporated the intercalation materials with a liquid solvent to create a suspension type electrolyte. This semi-solid flow battery (SSFB) combines the high energy density feature of the solid state battery and the scalability and flexibility of the flow battery (see Figure 1.1). They hypothesized a solid content of 50% which is a 5-20 times increase in active material concentration. However a major drawback of the RFB design is the fact that the anolyte and the catholyte have to be pumped around. Not only does

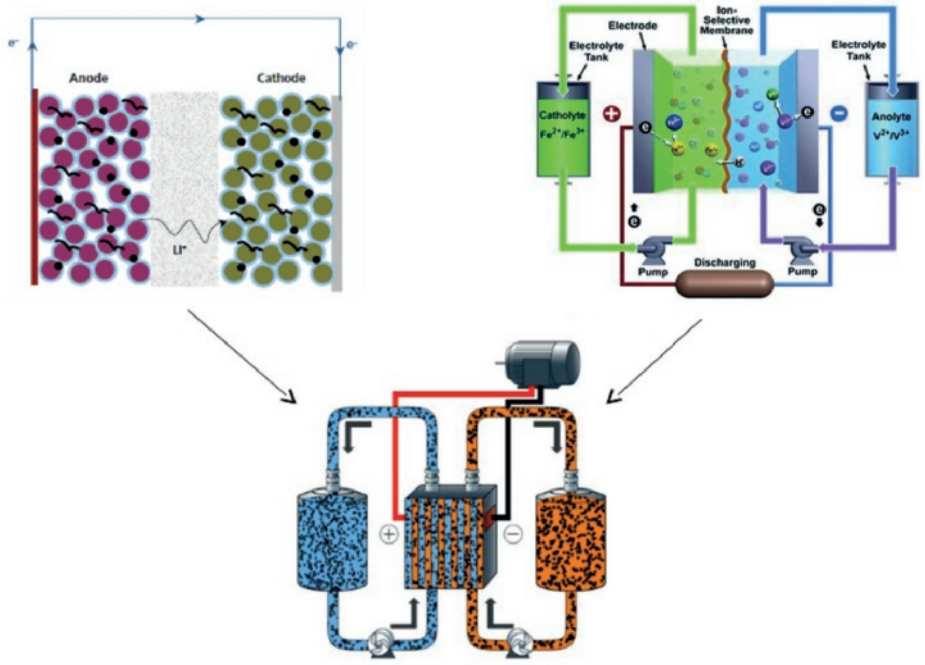

Figure 1.1: Semi-solid flow battery: A hybrid between the solid state Li cell and liquid state redox cell battery (copied with permission from [7]).

this lead to energy losses, but it also places extra restrictions on the anolyte and the catholyte. Most notably, the maximum concentration of the redox active species is limited in order to allow the fluid to be pumped around, leading to a lower energy density of the battery.

1.2.1. Electrolyte material

One of the innovation of semi-solid flow battery was the increase in the density of the active material concentration. However since the active materials were dispersed as micron-sized particles in the solvent the transfer of charge between the colloidal active particle and the outer circuit was limited. This problem was overcome by utilizing carbon black (CB) material to establish percolating structures within the electrolyte [10]. CB has an interesting aggregate structure. The primary particle is an agglomerate of fine graphite nano-plates sticking to each other. They minimize their surface energy to form spherical particles in the size range of few nano-meters. These primary particles aggregate to form larger structures of several hundred nano-meters. When the aggregates are suspended in a highly ionic environment like the solvent of the battery electrolyte, the surface charges of

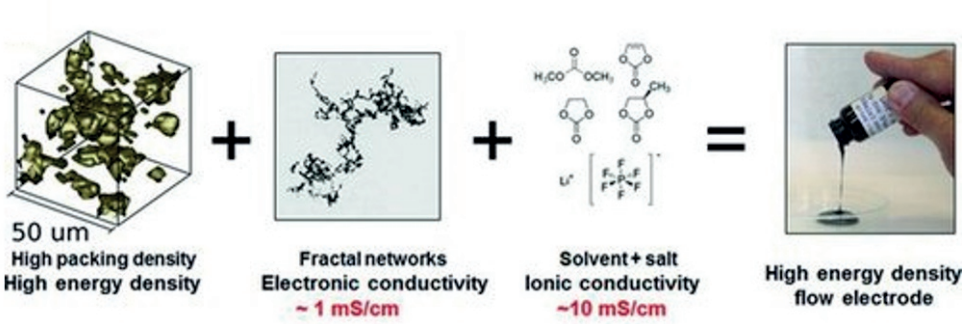

Figure 1.2: Semi-solid flow battery consists of a) the high energy density Li complexes , b) carbon black networks and c) solvent (copied with permission from [9]).

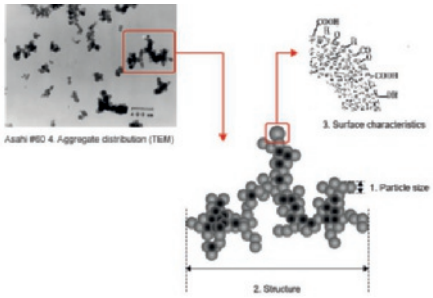

Figure 1.3: the hierarchical structure of carbon black aggregates (copied with permission from Asahi-carbon Co. Ltd. [11]).

CB particles are screened and the smaller aggregates can stick to each other due to Van-der-Waals attraction forming percolating porous network. The network is fractal in nature and the grow mechanism has been identified as diffusion limited cluster aggregation (DLCA).

This type of structure when combined with the active Li material leads to highly effective pathway for the semi-solid flow battery to transfer the charge from the inner volume of electrolyte bath to the current collectors.

1.2.2. Slurry optimization

The carbon black forms weak gel like structures at very low volume fractions in the range of 7×10^{-4}. As the concentration of CB is increased it forms strong electrically-percolating clusters. However these percolating networks can deform and restructure under normal flow conditions. Youssry *et al.*[10] studied the shear rate dependent conductivity of the SSFB electrolyte suspension. They identified significant shear-dependent trends in the suspension properties. As shown in Fig.1.4, the conductivity of suspension is high under no-shear condition ($10^{-2} mS.cm^{-1}$). Since the percolating structure of CB is intact and provides good electronic wiring

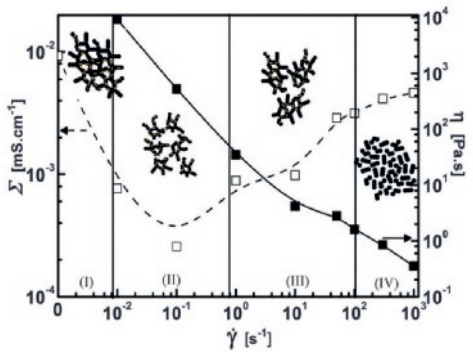

Figure 1.4: Variation of the conductivity and viscosity with the shear rate and schematic drawing of the several states within the CB suspension, ϕ_{CB} = 0.021 (copied with permission from Youssry *et al.* [10]).

in the electrolyte bath, but the viscosity of the suspension is also high (3×10^2 Pa.s). But as the suspension was flown in the cell, the CB network started to break-up leading into agglomerates which deteriorated the conductivity of the suspension and lowered the suspension viscosity. When the flow rate was increased further the smaller hydroclusters were formed. Hence an optimization of the suspension is needed since at low shear rates the viscosity is high requiring more energy to pump the fluid while at the higher shear rates the efficiency is low due to break-up of CB clusters.

Several alternative approaches has been proposed to improve the electrolyte. For e.g. Endo *et al.* [12], Madec *et al.* [13] suggested inclusion of carbon nanofibers could improve the network connectivity and achieve better shear-dependent conductivity. Later experiments confirmed that inclusion of the carbon nanofibers led to increase in conductivity between the Li-ions [14]. Fongy *et al.* [15] suggested this might be due to the nanochannels formed by the fibers in the electrolyte.

1.2.3. Market commercialization and future research directions of RFBs

Since the SSFBs were a recent innovation, it's still yet to reach market maturity. However the founders of this battery technology (Duduta and Yet-Ming Chiang) have established a start-up called 24M Technologies. It was spun out of A123 systems, a company which produced Li-ion batteries but filed for bankruptcy in 2012. Some of the interesting possibilities of the SSFBs listed by the inventors include the use of these batteries in automobiles. The semi-solid electrolyte can serve as a fuel which could be re-fueled in gas stations hence utilizing the already established infrastructure of gasoline. Further stacking of the fuel cells is possible leading to customized usage of the battery for different applications [16]. The cost of the active Lithium complex materials are estimated around \$10-15 kg^{-1} and \$14 kg^{-1} for non-aqueous electrolyte. There are two types of battery model being considered. i) small scale setup for transportation purposes costing \$250 kWh^{-1}

Figure 1.5: A working prototype of SSFB from 24M CO., LTD. (copied from www.24-m.com)

and ii) large scale grid level storage systems costing \$100 kWh^{-1}. 24M has raised \$50 million in investments so far. Further the start-up has received funding from the United States Department of Energy's ARPA-E program to explore the potential use of the semi-solid electrolyte [17, 18]. 24M claimed they could achieve \$100 per kilowatt-hour by 2017. However as of 2019 they are yet to enter production [19]. The RFB is one of the most promising stationary storage technologies due to the decoupled power output and energy capacity and the high cyclability, making them applicable for virtually any stationary application. A significant amount of ongoing research is currently focused on developing an electrolyte system with a price range comparable to solid-state Li batteries. Further large advances can be made by improving the electrode and membrane materials. Should such improvements be made, RFB will become a truly attractive storage technology worldwide.

1.3. Modelling of flow batteries

Modelling forms an important part of the research process by providing fundamental insights of a phenomena. To better understand the rheology properties of the flow battery in particular the formation and aggregation kinetics of CB clusters and their flow dependent behaviour we resort to computer simulations. Since the size of carbon black particles ($\approx 100\ nm$) are orders of magnitude larger compared to the surrounding solvent molecules ($\approx 1\ nm$) conventional techniques like molecular dynamics (MD) can't be used. Hence we employ a mesoscale simulation technique called Brownian dynamics (BD) to model the colloidal particles. Further the typical time-scales in BD range from few milli-seconds to several hours/days which are roughly time-scales of interest in rheological studies. Hence BD serves as an excellent candidate for simulating colloidal rheology. In the following section we give an brief overview of the BD simulation method.

1

1.3.1. Brownian Dynamics

Consider a colloidal particle of mass m and position r in bath a bath of solvent molecules. The force acting on a colloid particle i can be written as

$$m_i \ddot{\mathbf{r}}_i = \mathbf{F}_i^{cc} + \mathbf{F}_i^{cs} \tag{1.1}$$

where $\mathbf{F}_i^{cc}$ is the colloid-colloid interaction force, $\mathbf{F}_i^{cs}$ is the colloid-solvent interaction force and $\ddot{\mathbf{r}}_i$ colloidal particle acceleration. This represents the explicit solvent models like MD, Lattice Boltzmann where the solvent interactions are fully resolved. However the typical time-steps for such models are limited to few femtoseconds ($\approx$ solvent molecule velocities). Whereas implicit solvent models in the solvent interactions are represented by coarse grained fields enabling large time-steps.

$$m_i \ddot{\mathbf{r}}_i = \mathbf{F}_i^{cc} - \gamma_i \dot{\mathbf{r}}_i + \delta\mathbf{F} \tag{1.2}$$

In above equation the solvent interaction is replaced by a viscous term $-\gamma_i \dot{\mathbf{r}}_i$ and a stochastic term $\delta\mathbf{F}$ which obeys the fluctuation-dissipation theorem. γ is the damping constant and $\dot{\mathbf{r}}_i$ is the colloidal particle velocity. This equation is referred to as Langevin dynamics with typical timescales in range of nanoseconds ($\approx$ colloidal particle velocities). If the size of colloidal particle is considerably bigger than solvent molecule, Langevin dynamics can be further coarse-grained by neglecting inertia terms.

$$\dot{\mathbf{r}}_i = \mathbf{F}_i^{cc}/\gamma_i + \delta\dot{\mathbf{r}}_i = \mu_i \mathbf{F}_i^{cc} + \delta\dot{\mathbf{r}}_i \tag{1.3}$$

where μ_i it the colloidal particle mobility and $\delta\dot{\mathbf{r}}_i$ is the stochastic velocity obeying fluctuation-dissipation theorem. This is the BD equation of motion for a spherical colloidal particle. The equation can be extended for non-spherical particles as well by considering a tensor mobility matrix rather than scalar one. Typical time-steps for BD simulation are in milliseconds which enables calculation of experimentally relevant colloidal properties like diffusion, aggregation rates, shear rheology, etc . It should be noted that even though we can access longer timescales by the process of coarse-graining we lose information of hydrodynamic interactions. Hydrodynamic interactions are a given in explicit solvent techniques while for implicit solvent models additional effort has to be made. Hence a major theme of thesis will revolve around incorporating such hydrodynamic properties to the BD system while still retaining its efficiency. This will enable a more accurate and faster simulations of colloidal suspensions and their rheological properties.

1.4. Thesis Outline

The ultimate aim of our work is to understand the shear rheology of colloidal suspension with particular focus on carbon black aggregates for flow batteries. Before modeling the highly complex fractal aggregates we analyze the existing hydrodynamic models for simpler colloidal shapes like ellipsoids. This will help us in understanding the shortcomings of the prevailing models and thereby improving them. We derive an extended mobility matrix with shear-coupling terms enabling shear simulations of arbitrary shaped colloids. We also present a new efficient Brownian

dynamics scheme compatible with the afore mentioned extended mobility matrix in Chapter 2. We perform simulations on a set of standard non-spherical particles like ellipsoids, hemi-spherical caps to validate our algorithm against known results. Our extended mobility calculation enables access to the stresses acting on the body and thereby the intrinsic viscosity of a dilute suspension of these objects. In Chapter 3 we leverage on our new BD algorithm by performing simulation under various flow rates. We obtain shear rheology for an array range of non-spherical particles like ellipsoids, hemi-spherical caps, helices. Viscosities for suspensions of ellipsoidal particles, for a wide range of aspect ratios and Peclet numbers ranging from the Brownian-dominated regime to the shear-dominated regime are calculated. We compare them against theoretical predictions on the shear-thinning behaviour of these suspensions. In Chapter 4 we show that current theoretical and numerical approaches with the hydrodynamic (self-)interactions accounted for by the Brownian equation of motion and the stress expression, yield inconsistent values for the viscosity. This situation is remedied by revising the inclusion of fluctuating hydrodynamic stresses on the colloids. Further the fluctuating instantaneous stresses enable calculation of viscosity via stress auto-correlation and Green-Kubo relations. We present numerical results on a variety of isolated non-spherical particles, illustrating the necessity of these corrections to obtaining consistent values of the Einstein viscosities of dilute solutions of these particles. In Chapter 5 we give the complete derivation of the above mentioned corrections to colloidal Brownian stresses. Stress contributions from rotational derivatives of the mobility matrix and the extended fluctuation-dissipation theorem are shown. Further dynamic viscoelastic analysis of the colloidal suspensions are performed by Fourier transformation of stress auto-correlations. In Chapter 6 we perform aggregation simulation of the colloidal particles using a simple hit-and-stick model to study their kinetics. Inclusion of rotational Brownian motion and intra-cluster hydrodynamics results in faster aggregation and more stringy clusters than previous simulations employing scaling-based rotational dynamics. Later we extend the model to rod shaped particles mimicking carbon nanofibers as conducting colloids. For rod shaped particles the stringy clustering effect become more pronounced with increasing aspect ratios, suggesting better electrical connectivity for carbon nanofiber based suspensions as seen in experiments. Further the cluster-size distributions collapse onto a master curve in the diffusion-limited regime, the deviations observed for more concentrated systems are in agreement with experiments. The theories and algorithms presented in these chapters will serve as essential ingredients in studying colloidal aggregation under shear flow.

References

[1] E. Commission, *Europe 2020 targets,* (2015).

[2] U. Nations, *United nations conference on climate change,* (2015).

[3] I. E. Agency, *World energy outlook 2015,* (2015).

[4] S. P. Europe, *Global market outlook 2015-2019,* (2015).

[5] G. W. E. Council, *Global wind power statistics,* (2015).

[6] H. Ibrahim, A. Ilinca, and J. Perron, *Energy storage systems-characteristics and comparisons,* Renewable Sustainable Energy Rev. **12**, 1221 (2008).

[7] W. Wang, Q. Luo, B. Li, X. Wei, L. Li, and Z. Yang, *Recent progress in redox flow battery research and development,* Adv. Funct. Mater. **23**, 970 (2013).

[8] M. Winter and J. O. Besenhard, *Electrochemical lithiation of tin and tin-based intermetallics and composites,* Electrochim. Acta **45**, 31 (1999).

[9] M. Duduta, B. Ho, V. C. Wood, P. Limthongkul, V. E. Brunini, W. C. Carter, and Y.-M. Chiang, *Semi-solid lithium rechargeable flow battery,* Adv. Energy Mater. **1**, 511 (2011).

[10] M. Youssry, L. Madec, P. Soudan, M. Cerbelaud, D. Guyomard, and B. Lestriez, *Non-aqueous carbon black suspensions for lithium-based redox flow batteries: rheology and simultaneous rheo-electrical behavior,* Phys. Chem. Chem. Phys. **15**, 14476 (2013).

[11] A. carbon Co. LTD., *Carbon black properties,* (2010).

[12] M. Endo, Y. Kim, T. Hayashi, K. Nishimura, T. Matusita, K. Miyashita, and M. Dresselhaus, *Vapor-grown carbon fibers (vgcfs): basic properties and their battery applications,* Carbon **39**, 1287 (2001).

[13] L. Madec, M. Youssry, M. Cerbelaud, P. Soudan, D. Guyomard, and B. Lestriez, *Electronic vs ionic limitations to electrochemical performance in Li4Ti5O12-based organic suspensions for lithium-redox flow batteries,* J. Electrochem. Soc. **161**, A693 (2014).

[14] M. Youssry, D. Guyomard, and B. Lestriez, *Suspensions of carbon nanofibers in organic medium: rheo-electrical properties,* Phys. Chem. Chem. Phys. **17**, 32316 (2015).

[15] C. Fongy, S. Jouanneau, D. Guyomard, and B. Lestriez, *Carbon nanofibers improve both the electronic and ionic contributions of the electrochemical performance of composite electrodes,* J. Power Sources **196**, 8494 (2011).

[16] ARPA-E, *Semi-solid flowable battery electrodes,* (2010).

[17] J. S. John, *24m unveils the reinvented lithium-ion battery,* (2015).

[18] Nanalyze, *Black goo flow batteries by 24m technologies,* (2014).

[19] J. Spector, *24m raises more money to fund advanced lithium-ion manufacturing,* (2018).

2

Efficient Brownian Dynamics of rigid colloids in linear flow fields

We present an efficient general method to simulate in the Stokesian limit the coupled translational and rotational dynamics of arbitrarily shaped colloids subject to external potential forces and torques, linear flow fields and Brownian motion. The colloid's surface is represented by a collection of spherical primary particles. The hydrodynamic interactions between these particles, here approximated at the Rotne-Prager-Yamakawa level, are evaluated only once to generate the body's (11×11) *grand mobility matrix. The constancy of this matrix in the body frame, combined with the convenient properties of quaternions in rotational Brownian Dynamics, enable an efficient simulation of the body's motion. Simulations in quiescent fluids yield correct translational and rotational diffusion behaviour, and sample Boltzmann's equilibrium distribution. Simulations of ellipsoids and spherical caps under shear, in the absence of thermal fluctuations, yield periodic orbits in excellent agreement with the theories by Jeffery and Dorrepaal. The time-varying stress tensors provide the Einstein coefficient and viscosity of dilute suspensions of these bodies.*

2.1. Introduction

Colloidal suspensions are ubiquitous in nature and in man-made materials. The dynamics of colloidal particles is therefore of interest to both academia and industry. Several important analytical results have been derived in the Stokes limit of colloids

Parts of this chapter have been published in Journal of Chemical Physics **148**, 194112 (2018) [1].

moving at low Reynolds numbers, including Stokes's drag on a spherical colloid, Einstein's viscosity of a dilute suspension of spherical colloids and Jeffery's tumbling motion of an ellipsoidal colloid in a linear shear flow [2–7]. Solving the mobility matrix and resulting motions of complex-shaped rigid particles, however, typically requires a numerical approach. One way is to explicitly solve the flow around the body using direct numerical simulations, *e.g.* lattice Boltzmann simulations, but this is comuptationally demanding and becomes difficult at low Reynolds numbers. [8, 9]

Building on the work by Oseen [10] and Burgers [11] for the flow field generated by a point force, Riseman and Kirkwood [12] derive translational and rotational diffusion tensors for rigid clusters of particles in the Stokesian limit. Bloomfield and co-workers [13–15] and Goldstein [16], among others, extended this framework by incorporating the improved hydrodynamic interactions between two spheres derived by Rotne and Prager [17] and Yamakawa [18]. The result is a (6×6) mobility matrix relating the translational and rotational velocities of a colloidal body to the total force and torque acting on that body, taking into account the hydrodynamic interactions between the various parts of the body and implicitly solving the constraint forces and torques that rigidify the body. Several authors reported on codes to calculate this matrix [19, 20], while García de la Torre *et al.* [21, 22] made their `Hydro++` code publicly available. The latter also combined a rotationally averaged weighted translational mobility matrix with a volume correction to predict intrinsic viscosities at zero shear rate. [23, 24] Brady and collaborators developed Stokesian Dynamics (SD) to simulate suspensions of (non-connected) spherical particles [25, 26]. In this scheme, the generalized velocities and forces are supplemented with stress and strain matrices to improve the accuracy of the hydrodynamic calculations, to simulate suspensions in linear flow fields, and to calculate viscosities of quiescent and flowing suspensions.Several authors hinted at and/or have worked out a generalized mobility matrix for arbitrarily shaped colloids including stress and strain [20, 27–29], but a detailed description and thorough test of a generic method appears to be missing in the literature. The aim of the current paper is to describe the derivation of a generalized (11×11) grand mobility matrix, implemented in the publicly available `Oseen11` code, and to compare simulation results obtained with this matrix against a number of analytic results for validation.

The generalized mobility matrix, obtained by the method outlined above or by the boundary element method [30, 31], can be used to efficiently simulate the dynamics of the body. For a rigid object the mobility matrix in the body-based frame remains constant, hence it needs to be evaluated only once and its time-varying counterpart in the laboratory-based frame is readily obtained through rotation. The literature contains a number of simulations of this type, [19, 32, 33] using quaternions to describe the orientation of the body relative the its hydrodynamic center. We show that this is a fortuitous choice. It is well known that the use of four quaternion coordinates removes the degeneracy encountered with three rotational coordinates, like the Euler angles or the components of a rotation vector [34]. In the simulation of Brownian motion, however, the use of non-Cartesian coordinates gives rise to an additional metric-related term in the equations of motion. Fur-

thermore, in the usual Itô representation of stochastic differential equations, the orientation-dependence of the space-based mobility matrix also gives rise to an additional term in the equations of motion [35–37]. Naess, Elgsaeter and co-workers [38–42] derived expressions for these additional terms for simulations employing Euler angles and a rotation vector, respectively, assuming a block-diagonal mobility matrix. Ilie *et al.*[43] showed that the additional terms vanish identically when using quaternions, in combination with an exactly solved constraint to preserve the unit length of the quaternion vector,again assuming a block-diagonal mobility matrix. Their derivation is extended here to general mobility matrices, arriving at the convenient result that the additional terms cancel out when using quaternions to represent rotations around the mobility center. Alternatively, Makino and Doi [30] employed a Fokker-Planck equation to derive an equation of motion using the nine elements of the rotation matrix as coordinates to describe the orientation of the object; their time evolution obeys the six orthonormality conditions to a rotation matrix only in the limit of vanishing time step, and consequently the calculated motion is subject to a gradual drift.

The outline of this paper is as follows: The derivations of the grand mobility matrix and the equations of motion are presented in Section 2.2, with details referred to the appendices, culminating in the central expression of Eq. (2.19). Simulation results validating the algorithm are presented in Section 2.3, where it is shown that translational and rotational Brownian Dynamics, as well as the equilibrium Boltzmann distribution, are faithfully sampled for colloids in a quiescent fluid, while colloids in sheared fluids, in the absence of Brownian motion and external forces, correctly trace the analytical Jeffery orbits of ellipsoidal particles [4] and spherical caps [44]. We end with a brief summary of the main results.

2.2. Theory

The constant body-based generalized mobility matrix of a rigid colloid fully describes the response of the colloid to external influences. In the following two subsection, we derive this matrix for a body consisting of primary spherical particles, and construct the corresponding Brownian Dynamics equation of motion.

2.2.1. Mobility matrix

Consider a collection of N unconnected spherical particles suspended in an incompressible Newtonian viscous fluid. At low Reynolds numbers, the equations of motion of each particle are solved by balancing the potential-based force and torque on the particle with the hydrodynamic drag force and torque experienced by the particle, which in turn depend on the motions of all particles in the system. [7] In the mobility representation, the translational velocity $\bar{\mathbf{v}}_i$ and rotational velocity $\bar{\boldsymbol{\omega}}_i$ of the i^{th} particle with position $\bar{\mathbf{x}}_i$ are related to the potential-based forces $\bar{\mathbf{f}}_j$ and

torques $\bar{\boldsymbol{\tau}}_j$ on all particles j, via the grand mobility matrix,

$$\begin{pmatrix} \bar{\mathbf{v}}_i - \bar{\mathbf{v}}_i^\infty \\ \bar{\boldsymbol{\omega}}_i - \bar{\boldsymbol{\omega}}^\infty \\ -\bar{\bar{\mathbf{E}}}^\infty \end{pmatrix} = \sum_{j=1}^{N} \begin{pmatrix} \bar{\bar{\bar{\boldsymbol{\mu}}}}_{f,j}^{v,i} & \bar{\bar{\bar{\boldsymbol{\mu}}}}_{\tau,j}^{v,i} & \bar{\bar{\bar{\boldsymbol{\mu}}}}_{S,j}^{v,i} \\ \bar{\bar{\bar{\boldsymbol{\mu}}}}_{f,j}^{\omega,i} & \bar{\bar{\bar{\boldsymbol{\mu}}}}_{\tau,j}^{\omega,i} & \bar{\bar{\bar{\boldsymbol{\mu}}}}_{S,j}^{\omega,i} \\ \bar{\bar{\bar{\boldsymbol{\mu}}}}_{f,j}^{E,i} & \bar{\bar{\bar{\boldsymbol{\mu}}}}_{\tau,j}^{E,i} & \bar{\bar{\bar{\boldsymbol{\mu}}}}_{S,j}^{E,i} \end{pmatrix} \begin{pmatrix} \bar{\mathbf{f}}_j \\ \bar{\boldsymbol{\tau}}_j \\ \bar{\bar{\mathbf{S}}}_j \end{pmatrix}. \tag{2.1}$$

Here the balance is solved in the presence of a linear background flow field, $\bar{\mathbf{v}}_i^\infty = \bar{\mathbf{v}}^\infty(\bar{\mathbf{x}}_i)$ with

$$\bar{\mathbf{v}}^\infty(\bar{\mathbf{x}}) = \bar{\mathbf{v}}_0^\infty + \bar{\bar{\mathbf{E}}}^\infty \bar{\mathbf{x}} + \bar{\boldsymbol{\omega}}^\infty \times \bar{\mathbf{x}}, \tag{2.2}$$

where the strain rate $\bar{\bar{\mathbf{E}}}^\infty$ and angular velocity $\bar{\boldsymbol{\omega}}^\infty$ are uniform throughout the system and $\bar{\mathbf{v}}_0^\infty$ denotes the flow velocity at the origin of the laboratory coordinate system. The vector on the r.h.s. of Eq. (2.1) collects the force, torque and stress, $\bar{\bar{\mathbf{S}}}_j$, transmitted by particle j onto the fluid. The deformations of the particles are obtained by balancing the hydrodynamic stresses on the particle (*i.e.* $-\bar{\bar{\mathbf{S}}}_j$) and the potential-based stresses on the particle with the deformation stresses within the particle; for rigid particles the latter reduce to Lagrange multipliers that balance any imposed stress at vanishing deformation of the particle. Approximate analytic expressions for the grand mobility matrix of two interacting spherical particles are available in the literature [6, 25] and summarized in Appendix 2.A.1. Our objective in this subsection will be to derive, starting from Eq. (2.1) or from the equivalent (inverse) resistance problem in Eq. (2.6), a mobility matrix relating the translation, rotation and stress of a rigid cluster of N spherical particles to the total potential force, torque and flow field. Two brief comments on the notation: the number of bars highlights the rank of a tensor, with each spatial index running over the usual three dimensions; for tensors with both a subscript and a superscript, the former denotes the intended multiplication partner and the latter the resulting outcome.

The combination of various ranks in the grand mobility tensor disallows the use of standard numerical routines for square matrices. We therefore rewrite the strain rate of the flow field as a linear combination of nine (3×3) 'basis matrices' $\bar{\bar{\mathbf{e}}}_\kappa^E$ and their 'dual basis matrices' $\bar{\bar{\mathbf{e}}}_E^\kappa$,

$$\bar{\bar{\mathbf{E}}}^\infty = \sum_\kappa \bar{\bar{\mathbf{e}}}_\kappa^E \mathcal{E}_\kappa^\infty, \tag{2.3a}$$

$$\mathcal{E}_\kappa^\infty = \bar{\bar{\mathbf{e}}}_E^\kappa : \bar{\bar{\mathbf{E}}}^\infty, \tag{2.3b}$$

where the set of coefficients $\mathcal{E}_\kappa^\infty$ constitute a column vector $\bar{\boldsymbol{\mathcal{E}}}^\infty$ and the colon denotes a double contraction. Since in the context of hydrodynamics it proves convenient to use a non-orthogonal set of basis matrices, the basis matrices in the reverse transformation differ from those in the forward transformation [6]; we refer to Appendix 2.A.2 for more details. Because the strain rate is defined as the symmetric part of the flow field gradient, for any divergence-free flow only five coefficients are required. If one is not interested in the hydrostatic pressure, the stresses on the

particles – symmetric by definition – likewise reduce to a five-vector, $\bar{\boldsymbol{s}}_j$. We then arrive at

$$\begin{pmatrix} \bar{\mathbf{v}}_i - \bar{\mathbf{v}}_i^\infty \\ \bar{\boldsymbol{\omega}}_i - \bar{\boldsymbol{\omega}}^\infty \\ -\bar{\boldsymbol{\mathcal{E}}}^\infty \end{pmatrix} = \sum_{j=1}^{N} \begin{pmatrix} \bar{\bar{\boldsymbol{\mu}}}_{f,j}^{v,i} & \bar{\bar{\boldsymbol{\mu}}}_{\tau,j}^{v,i} & \bar{\bar{\boldsymbol{\mu}}}_{S,j}^{v,i} \\ \bar{\bar{\boldsymbol{\mu}}}_{f,j}^{\omega,i} & \bar{\bar{\boldsymbol{\mu}}}_{\tau,j}^{\omega,i} & \bar{\bar{\boldsymbol{\mu}}}_{S,j}^{\omega,i} \\ \bar{\bar{\boldsymbol{\mu}}}_{f,j}^{\mathcal{E},i} & \bar{\bar{\boldsymbol{\mu}}}_{\tau,j}^{\mathcal{E},i} & \bar{\bar{\boldsymbol{\mu}}}_{S,j}^{\mathcal{E},i} \end{pmatrix} \begin{pmatrix} \bar{\mathbf{f}}_j \\ \bar{\boldsymbol{\tau}}_j \\ \bar{\boldsymbol{S}}_j \end{pmatrix}, \tag{2.4}$$

where

$$\bar{\bar{\boldsymbol{\mu}}}_{f,j}^{\mathcal{E},i} = \bar{\bar{\bar{\mathbf{e}}}}_E^{\mathcal{E}} : \bar{\bar{\bar{\boldsymbol{\mu}}}}_{f,j}^{E,i}, \tag{2.5a}$$

$$\bar{\bar{\boldsymbol{\mu}}}_{S,j}^{v,i} = \quad \bar{\bar{\bar{\boldsymbol{\mu}}}}_{S,j}^{v,i} \bar{\bar{\bar{\mathbf{e}}}}_S^{S}, \tag{2.5b}$$

$$\bar{\bar{\boldsymbol{\mu}}}_{S,j}^{\mathcal{E},i} = \bar{\bar{\bar{\mathbf{e}}}}_E^{\mathcal{E}} : \bar{\bar{\bar{\boldsymbol{\mu}}}}_{S,j}^{E,i} \bar{\bar{\bar{\mathbf{e}}}}_S^{S}, \tag{2.5c}$$

etcetera, where $\bar{\bar{\bar{\mathbf{e}}}}_E^{\mathcal{E}}$ and $\bar{\bar{\bar{\mathbf{e}}}}_S^{S}$ denote the third-rank tensor combining the five basis matrices $\{\bar{\bar{\mathbf{e}}}_E^{\kappa}\}$ and $\{\bar{\bar{\mathbf{e}}}_\kappa^{S}\}$ respectively. Since we have recovered conventional vector-matrix products in Eq. (2.4), henceforth the bars will be omitted for notational convenience. Note that particles i and j are now coupled by an (11×11) matrix. Inversion of the $(11N \times 11N)$ grand mobility matrix yields the $(11N \times 11N)$ grand resistance matrix in the resistance representation of a collection of unconnected particles,

$$\begin{pmatrix} \mathbf{f}_i \\ \boldsymbol{\tau}_i \\ \boldsymbol{S}_i \end{pmatrix} = \sum_{j=1}^{N} \begin{pmatrix} \boldsymbol{\xi}_{v,j}^{f,i} & \boldsymbol{\xi}_{\omega,j}^{f,i} & \boldsymbol{\xi}_{\mathcal{E},j}^{f,i} \\ \boldsymbol{\xi}_{v,j}^{\tau,i} & \boldsymbol{\xi}_{\omega,j}^{\tau,i} & \boldsymbol{\xi}_{\mathcal{E},j}^{\tau,i} \\ \boldsymbol{\xi}_{v,j}^{S,i} & \boldsymbol{\xi}_{\omega,j}^{S,i} & \boldsymbol{\xi}_{\mathcal{E},j}^{S,i} \end{pmatrix} \begin{pmatrix} \mathbf{v}_j - \mathbf{v}_j^\infty \\ \boldsymbol{\omega}_j - \boldsymbol{\omega}^\infty \\ -\boldsymbol{\mathcal{E}}^\infty \end{pmatrix}. \tag{2.6}$$

The summation results on the r.h.s. can be interpreted as minus the hydrodynamic force, torque and stress on particle i at given linear and angular velocities of all particles j in a given flow field. The hydrodynamic interactions remain unchanged when the particles are connected to form a rigid cluster. The particle velocities in a rigid cluster are related by

$$\mathbf{v}_j = \mathbf{v} + \boldsymbol{\omega} \times \mathbf{r}_j, \tag{2.7a}$$

$$\boldsymbol{\omega}_j = \boldsymbol{\omega}, \tag{2.7b}$$

where $\mathbf{r}_j = \mathbf{x}_j - \mathbf{x}$ denotes the vector connecting particle j to a reference point on the cluster with spatial position $\mathbf{x}$, henceforth referred to as the position of the cluster, $\mathbf{v} = \dot{\mathbf{x}}$ represents the translational velocity of the cluster and $\boldsymbol{\omega}$ its rotational velocity. The background flow velocity experienced by particle j, see Eq. (2.2), is then readily expressed as the background flow velocity experienced by the cluster, $\mathbf{v}^\infty(\mathbf{x})$, plus a linear transformation of $\mathbf{r}_j$.

Given the forces, torques and stresses on the individual particles in a rigid cluster,

the total force, torque and stress on the cluster follow by the addition rules

$$\mathbf{f} = \sum_{i=1}^{N} \mathbf{f}_i, \tag{2.8a}$$

$$\boldsymbol{\tau} = \sum_{i=1}^{N} \left(\boldsymbol{\tau}_i + \mathbf{r}_i \times \mathbf{f}_i\right), \tag{2.8b}$$

$$\mathbf{S} = \sum_{i=1}^{N} \left(\mathbf{S}_i + \mathbf{r}_i \otimes \mathbf{f}_i\right). \tag{2.8c}$$

The first two of these equations are readily applied to the potential-based forces and torques on the particles, whereas in the third equation the stresses on the particles are still unknown. Applying these addition rules, in combination with Eq. (2.7), to the r.h.s. of Eq. (2.6) yields the (11×11) grand resistance matrix of the cluster,

$$\begin{pmatrix} \mathbf{f} \\ \boldsymbol{\tau} \\ \boldsymbol{\mathcal{S}} \end{pmatrix} = \begin{pmatrix} \boldsymbol{\xi}_v^f & \boldsymbol{\xi}_\omega^f & \boldsymbol{\xi}_\mathcal{E}^f \\ \boldsymbol{\xi}_v^\tau & \boldsymbol{\xi}_\omega^\tau & \boldsymbol{\xi}_\mathcal{E}^\tau \\ \boldsymbol{\xi}_v^\mathcal{S} & \boldsymbol{\xi}_\omega^\mathcal{S} & \boldsymbol{\xi}_\mathcal{E}^\mathcal{S} \end{pmatrix} \begin{pmatrix} \mathbf{v} - \mathbf{v}^\infty(\mathbf{x}) \\ \boldsymbol{\omega} - \boldsymbol{\omega}^\infty \\ -\boldsymbol{\mathcal{E}}^\infty \end{pmatrix}, \tag{2.9}$$

where the r.h.s. represents minus the generalized hydrodynamic forces on the cluster. Explicit expressions for the nine sub-matrices are provided in Appendix 2.A.3. The generalized constraint forces acting between the particles in a rigid cluster are all internal to the cluster and therefore do not contribute to the dynamics of the cluster. Simulating the dynamics of the cluster requires evaluation of the velocities for given potential-based generalized forces and a given background flow field. This is achieved by a partial inversion of the above equation, see Appendix 2.A.4, to arrive at the grand mobility matrix of the cluster,

$$\begin{pmatrix} \mathbf{v} - \mathbf{v}^\infty(\mathbf{x}) \\ \boldsymbol{\omega} - \boldsymbol{\omega}^\infty \\ \boldsymbol{\mathcal{S}} \end{pmatrix} = \begin{pmatrix} \boldsymbol{\mu}_f^v & \boldsymbol{\mu}_\tau^v & \boldsymbol{\mu}_\mathcal{E}^v \\ \boldsymbol{\mu}_f^\omega & \boldsymbol{\mu}_\tau^\omega & \boldsymbol{\mu}_\mathcal{E}^\omega \\ \boldsymbol{\mu}_f^\mathcal{S} & \boldsymbol{\mu}_\tau^\mathcal{S} & \boldsymbol{\mu}_\mathcal{E}^\mathcal{S} \end{pmatrix} \begin{pmatrix} \mathbf{f} \\ \boldsymbol{\tau} \\ -\boldsymbol{\mathcal{E}}^\infty \end{pmatrix}. \tag{2.10}$$

While the laboratory-based grand mobility matrix will vary with the orientation of the rigid cluster, the body-based matrix remains constant. Hence, in principle the dynamics of the cluster can be simulated based on a single evaluation of the mobility matrix.

2.2.2. Brownian Dynamics

The laboratory positions of all particles in a rigid cluster can be expressed as

$$\mathbf{x}_i = \mathbf{x} + \mathbf{A}_{(\mathrm{b})}^{(\mathrm{s})} \mathbf{r}_i \tag{2.11}$$

where $\mathbf{x}$ denotes the space-based position of the reference point on the cluster that defines the origin of the body-based coordinate system, $\mathbf{r}_i$ represents the body-based coordinates of particle i, and $\mathbf{A}_{(\mathrm{b})}^{(\mathrm{s})}$ is the rotation matrix from the body frame

(b) to the space frame (s). For numerical convenience, see Section 2.1, the rotation will be described in terms of the four-vector quaternions $\mathbf{q}$, with a constraint of unit length, $|\mathbf{q}| = 1$. Details on the rotation matrix, and the corresponding transformation matrices for angular velocities, can be found in Appendix 2.A.5. The generalized mobility matrix to be used henceforth is the matrix evaluated in the body frame. The objective now is to obtain equations of motion for the position $\mathbf{x}$ and orientation $\mathbf{q}$ of the cluster.

For a particle in a quiescent fluid, experiencing a conservative potential Φ, the Brownian equation of motion in generalized coordinates $\mathbf{Q}$ reads as [35–37]

$$\begin{aligned}\Delta\mathbf{Q}(t) &= \mathbf{Q}(t+\Delta t) - \mathbf{Q}(t) \\ &= -\boldsymbol{\mu}_Q \boldsymbol{\nabla}_Q \mathcal{A}_Q \Delta t + k_B T \boldsymbol{\nabla}_Q \cdot \boldsymbol{\mu}_Q \Delta t + \delta\mathbf{Q},\end{aligned} \tag{2.12}$$

with $\Delta\mathbf{Q}(t)$ the displacement at time t over a time step Δt, mobility matrix $\boldsymbol{\mu}_Q$, free energy $\mathcal{A}_Q$, Boltzmann's constant k_B, temperature T and random Brownian displacements $\delta\mathbf{Q}$. The free energy is defined as

$$\begin{aligned}\mathcal{A}_Q(\mathbf{Q}) &= -k_B T \ln P_Q(\mathbf{Q}) \\ &= \Phi(\mathbf{Q}) - \frac{1}{2} k_B T \ln g_Q(\mathbf{Q}),\end{aligned} \tag{2.13}$$

with the Boltzmann equilibrium probability distribution for a particle experiencing a potential Φ given by

$$P_Q(\mathbf{Q}) d\mathbf{Q} \propto g_Q^{1/2}(\mathbf{Q}) \exp\left[-\frac{\Phi(\mathbf{Q})}{k_B T}\right] d\mathbf{Q} \tag{2.14}$$

and where the metric g_Q measures (the square of) the volume in coordinate space of $d\mathbf{Q}$. The first term on the last line of Eq. (2.12) is akin to Eq. (2.10), with minus the gradient of the free energy providing the driving force and a multiplication by Δt to turn velocities into displacements. In the third term on the last line of Eq. (2.12), the components of the Brownian displacements vector $\delta\mathbf{Q}$ have zero average, no memory of the preceding time steps (*i.e.* Markovian), and their correlations are related to the mobility matrix by the fluctuation-dissipation theorem,[35–37]

$$\langle \delta\mathbf{Q} \otimes \delta\mathbf{Q} \rangle = 2 k_B T \boldsymbol{\mu}_Q \Delta t, \tag{2.15}$$

where the pointed brackets denote a canonical average. In the Itô representation, *i.e.* all terms on the last line of Eq. (2.12) are evaluated at time t, the equation of motion contains a divergence term (here, the second term on the r.h.s.) accounting for spatial variations of the mobility. Inclusion of this term, which appears natural when deriving the first order equation of motion from the second order Langevin equation [37], ensures that the proper equilibrium distribution is sampled by Brownian systems with coordinate-dependent mobilities, like the non-spherical colloids in this study. All aforementioned contributions are imperative in simulations using Euler angles or a rotation vector to represent the orientation of the cluster, along with Taylor expansions to solve weak singularities at specific orientations [38–42].

Ilie *et al.* [43] have recently shown that the equations of motion simplify considerably when using quaternions, which will be the approach followed and extended here.

For a (6×6) mobility matrix, and assuming translation and rotation to be decoupled, Ilie *et al.* [43] derived the Brownian equations of motion for translation and rotation as

$$\Delta\mathbf{x} = \mathbf{A}^{(\mathrm{s})}_{(\mathrm{b})}\left[\boldsymbol{\mu}^{v(\mathrm{b})}_{f(\mathrm{b})}\mathbf{A}^{(\mathrm{b})}_{(\mathrm{s})}\mathbf{f}^{(\mathrm{s})}\Delta t + \delta\mathbf{x}^{(\mathrm{b})}\right], \tag{2.16a}$$

$$\Delta\mathbf{q} = \mathbf{B}^{\dot{q}}_{(\mathrm{b})}\left[\boldsymbol{\mu}^{\omega(\mathrm{b})}_{\tau(\mathrm{b})}\mathbf{A}^{(\mathrm{b})}_{(\mathrm{s})}\boldsymbol{\tau}^{(\mathrm{s})}\Delta t + \delta\boldsymbol{\psi}^{(\mathrm{b})}\right] + \lambda\mathbf{q}, \tag{2.16b}$$

respectively. Both equations have the same structure: the force (torque) in the space frame is rotated to the body frame by the inverse rotation matrix, $\mathbf{A}^{(\mathrm{b})}_{(\mathrm{s})} = (\mathbf{A}^{(\mathrm{s})}_{(\mathrm{b})})^{-1}$, the balance with the hydrodynamic friction force (torque) is solved in the body frame, and the resulting (angular) velocity is rotated back to the space frame to update the coordinates. The (4×3) matrix $\mathbf{B}^{\dot{q}}_{(\mathrm{b})}$ combines the rotation of a body-based angular velocity to the space frame with the conversion to time derivatives of quaternions, see Appendix 2.A.5. The stochastic translations $\delta\mathbf{x}^{(\mathrm{b})}$ and rotations $\delta\boldsymbol{\psi}^{(\mathrm{b})}$ are sampled in the body frame, each with zero mean and each separately obeying a fluctuation-dissipation theorem akin to Eq. (2.15). These random displacements are easily generated using two independent three-vectors $\boldsymbol{\Theta}_x$ and $\boldsymbol{\Theta}_\psi$ of uncorrelated memory-free random numbers with zero mean and unit variance, in combination with the symmetric square roots of the (3×3) mobility matrices,

$$\delta\mathbf{x}^{(\mathrm{b})} = \sqrt{2k_BT\Delta t}\left(\boldsymbol{\mu}^{v(\mathrm{b})}_{f(\mathrm{b})}\right)^{1/2}\boldsymbol{\Theta}_x, \tag{2.17a}$$

$$\delta\boldsymbol{\psi}^{(\mathrm{b})} = \sqrt{2k_BT\Delta t}\left(\boldsymbol{\mu}^{\omega(\mathrm{b})}_{\tau(\mathrm{b})}\right)^{1/2}\boldsymbol{\Theta}_\psi. \tag{2.17b}$$

The metric and divergence terms in the generalized equation of motion vanish identically when simulating the translational motion in Cartesian coordinates. Neither term vanishes in the description of the rotational motion, but both turn out to be parallel to $\mathbf{q}$ and therefore they cancel against the constraint force along $\nabla_q|\mathbf{q}| = \mathbf{q}$ that preserves the unit length of the quaternion vector [43]. The strength of the constraint force, *i.e.* the Lagrange multiplier λ, is solved from the condition of unit length,

$$\left|\mathbf{q}(t+\Delta t)\right| = \left|\mathbf{q}^{\mathrm{u}}(t+\Delta t) + \lambda\mathbf{q}(t)\right| = 1, \tag{2.18}$$

where $\mathbf{q}^{\mathrm{u}}(t+\Delta t)$ denotes the quaternions following the unconstrained time step. One readily shows that this condition constitutes a quadratic equation in λ.

The above equations of motion can be generalized to (6×6) mobility matrices with coupled translational-rotational motion, *i.e.* matrices for which the cross-terms $\boldsymbol{\mu}^v_\tau$ and $\boldsymbol{\mu}^\omega_f = (\boldsymbol{\mu}^v_\tau)^{\mathrm{T}}$ are non-zero. We present the main results here, and refer the reader interested in the mathematical details of the derivation to Appendix 2.A.6. The equations of motion including Brownian noise take their simplest form when $\boldsymbol{\mu}^\omega_f = \boldsymbol{\mu}^v_\tau$, which occurs when the origin of the body-based coordinate system coincides with the hydrodynamic center of the cluster. We will henceforth adhere to

this convenient choice and identify $\mathbf{x}$ with the space-based position of the hydrodynamic center – note that the equations of motion in the absence of Brownian noise will be of the same form for any chosen reference point. Equations to locate this center, and to subsequently 'shift' the cluster mobility matrix to this center without repeating the calculation of the previous section, are included in Appendix 2.A.7. Upon adding the displacements due to the linear flow field, the equations of motion read as

$$\begin{pmatrix} \Delta\mathbf{x} \\ \Delta\mathbf{q} \end{pmatrix} = \begin{pmatrix} \mathbf{A}^{(\mathrm{s})}_{(\mathrm{b})} & 0 \\ 0 & \mathbf{B}^{\dot{q}}_{(\mathrm{b})} \end{pmatrix} \left[\begin{pmatrix} \boldsymbol{\mu}_f^v & \boldsymbol{\mu}_\tau^v & \boldsymbol{\mu}_\mathcal{E}^v \\ \boldsymbol{\mu}_f^\omega & \boldsymbol{\mu}_\tau^\omega & \boldsymbol{\mu}_\mathcal{E}^\omega \end{pmatrix}^{(\mathrm{b})}_{(\mathrm{b})} \begin{pmatrix} \mathbf{A}^{(\mathrm{b})}_{(\mathrm{s})}\mathbf{f}^{(\mathrm{s})} \\ \mathbf{A}^{(\mathrm{b})}_{(\mathrm{s})}\boldsymbol{\tau}^{(\mathrm{s})} \\ -\boldsymbol{\mathcal{E}}^{\infty(\mathrm{b})} \end{pmatrix} \Delta t + \begin{pmatrix} \delta\mathbf{x}^{(\mathrm{b})} \\ \delta\boldsymbol{\psi}^{(\mathrm{b})} \end{pmatrix} \right] + \begin{pmatrix} \mathbf{v}^{\infty(\mathrm{s})} \\ \mathbf{B}^{\dot{q}}_{(\mathrm{s})}\boldsymbol{\omega}^{\infty(\mathrm{s})} \end{pmatrix} \Delta t + \begin{pmatrix} 0 \\ \lambda\mathbf{q} \end{pmatrix}. \tag{2.19}$$

In the first term between square brackets, the forces and torques in the space frame are converted to the body frame by a single rotation, while the corresponding conversion of the strain rate involves two rotations followed by a reduction to five-vector,

$$\mathcal{E}_\kappa^{\infty(\mathrm{b})} = \mathbf{e}_E^\kappa : \left[\mathbf{A}^{(\mathrm{b})}_{(\mathrm{s})}\mathbf{E}^{\infty(\mathrm{s})}\mathbf{A}^{(\mathrm{s})}_{(\mathrm{b})}\right]. \tag{2.20}$$

The generalized velocities are solved from a force balance in the body frame, converted back to the space frame and multiplied by the time step to obtain a displacement. In the second term between square brackets, the stochastic displacements are calculated using the symmetric square root matrix of the symmetric (6×6) top-left sub-matrix of the grand mobility matrix, in combination with a random six-vector $\boldsymbol{\Theta}_{x\psi}$ whose elements have zero mean, unit variance and are devoid of correlations,

$$\begin{pmatrix} \delta\mathbf{x}^{(\mathrm{b})} \\ \delta\boldsymbol{\psi}^{(\mathrm{b})} \end{pmatrix} = \sqrt{2k_BT\Delta t}\left[\begin{pmatrix} \boldsymbol{\mu}_f^v & \boldsymbol{\mu}_\tau^v \\ \boldsymbol{\mu}_f^\omega & \boldsymbol{\mu}_\tau^\omega \end{pmatrix}^{(\mathrm{b})}_{(\mathrm{b})}\right]^{1/2} \boldsymbol{\Theta}_{x\psi}. \tag{2.21}$$

The penultimate term to Eq. (2.19) describes the particle being carried along and rotated by the flow field. The final term represents the constraint introduced to preserve the unit length of the quaternion vector, which is solved using Eq. (2.18).

In the absence of Brownian motion, *i.e.* for $T = 0$, the mobility matrix gives the stresses exerted by the body on the fluid, expressed in the body frame, as

$$\boldsymbol{\mathcal{S}}^{(\mathrm{b})}(0) = \begin{pmatrix} \boldsymbol{\mu}_f^\mathcal{S} & \boldsymbol{\mu}_\tau^\mathcal{S} & \boldsymbol{\mu}_\mathcal{E}^\mathcal{S} \end{pmatrix}^{(\mathrm{b})}_{(\mathrm{b})} \begin{pmatrix} \mathbf{A}^{(\mathrm{b})}_{(\mathrm{s})}\mathbf{f}^{(\mathrm{s})} \\ \mathbf{A}^{(\mathrm{b})}_{(\mathrm{s})}\boldsymbol{\tau}^{(\mathrm{s})} \\ -\boldsymbol{\mathcal{E}}^{\infty(\mathrm{b})} \end{pmatrix}. \tag{2.22}$$

Conversion to a stress tensor in the space frame is achieved by a vector to tensor transformation, followed by two rotations,

$$\mathbf{S}^{(\mathrm{s})} = \mathbf{A}^{(\mathrm{s})}_{(\mathrm{b})}\left[\sum_\kappa \mathbf{e}_\kappa^\mathcal{S}\mathcal{S}_\kappa^{(\mathrm{b})}\right]\mathbf{A}^{(\mathrm{b})}_{(\mathrm{s})}. \tag{2.23}$$

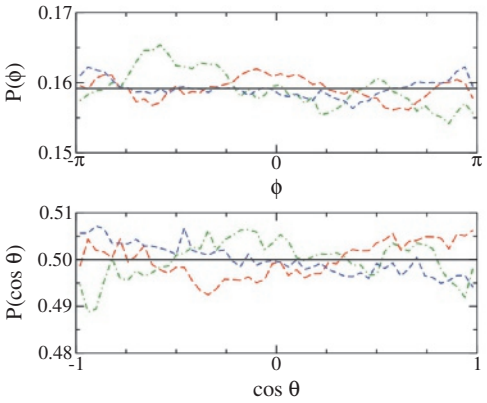

Figure 2.1: Probability distributions of the azimuthal angles ϕ and (the cosines of) the polar angles θ, relative to the space frame, of the three body-fixed eigenvectors of the mobility matrix of an anisotropic particle performing Brownian rotational diffusion. The solid lines represent the theoretical predictions.

We note that for a non-Brownian cluster the stresses are linearly related to the velocities of the body and hence to the displacements over a time step Δt. Extending this relation to the Brownian case, *i.e.* assuming that Brownian forces and external forces that generate identical displacements will also induce identical stresses, one arrives at

$$\boldsymbol{\mathcal{S}}^{(\mathrm{b})}(T) = \boldsymbol{\mathcal{S}}^{(\mathrm{b})}(0) + \sqrt{\frac{2k_BT}{\Delta t}} \begin{pmatrix} \boldsymbol{\mu}_f^{\mathcal{S}} & \boldsymbol{\mu}_\tau^{\mathcal{S}} \end{pmatrix}^{(\mathrm{b})}_{(\mathrm{b})} \left[\begin{pmatrix} \boldsymbol{\mu}_f^{v} & \boldsymbol{\mu}_\tau^{v} \\ \boldsymbol{\mu}_f^{\omega} & \boldsymbol{\mu}_\tau^{\omega} \end{pmatrix}^{(\mathrm{b})}_{(\mathrm{b})} \right]^{-1/2} \boldsymbol{\Theta}_{x\psi}. \tag{2.24}$$

The prefactor $\Delta t^{-1/2}$ in the last term appears because the stress represents the time-averaged stress over the time step Δt, while the standard deviation of the Brownian force, *i.e.* a series of uncorrelated kicks by the solvent molecules, increases as $\Delta t^{1/2}$. Since for any given configuration the last term in the above expression averages to zero, we conclude that in the stationary state Brownian motion affects the stress only indirectly, *i.e.* by its impact on the distribution being sampled.

2.3. Simulation results

To validate the proposed algorithm, the various contributions to the equations of motion were tested, on an individual basis and/or in combinations, by comparison against known analytic solutions. The units used in the simulation are ϵ for energy, σ for distance and τ for time.

2.3.1. Brownian motion

To test the Brownian contributions to the equations of motion, we consider an anisotropic particle with the body-based diagonal translational and rotational mo-

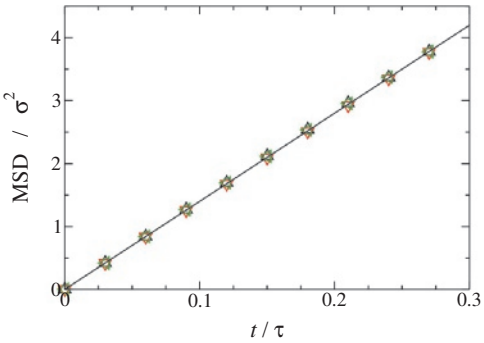

Figure 2.2: Mean square displacements along the three space-fixed axes (markers) of a Brownian diffusing anisotropic particle, along with the theoretical prediction (line).

bility matrices having the diagonal values $(5, 7, 9)\,\sigma^2(\tau\epsilon)^{-1}$ and $(0.5, 4, 10)\,(\tau\epsilon)^{-1}$, respectively. The temperature is set at $k_BT = 1\epsilon$, the timestep at $\Delta t = 1 \cdot 10^{-4}\tau$.

The orientational probability distribution of the particle, in an isotropic environment, is analysed by sampling the orientations of the three body-fixed eigenvectors $\hat{\mathbf{u}}_i^{(\mathrm{b})}$ of the mobility matrix, as seen from the space-fixed frame, $\hat{\mathbf{u}}_i^{(\mathrm{s})}(t) = \mathbf{A}_{(\mathrm{b})}^{(\mathrm{s})}(t)\hat{\mathbf{u}}_i^{(\mathrm{b})}$. The probability distributions of the polar angles θ_i and azimuthal angles ϕ_i for the three body-based basis vectors, see Fig. 2.1, agree well with the expected isotropic distributions.

The dynamic properties are analysed by measuring the diffusional behaviour of the particle. In an isotropic medium, with all particle orientations equally likely, the average translational diffusion coefficient along any space-fixed direction is given by $D^{(\mathrm{s})} = \frac{1}{3}k_BT\mathrm{Tr}(\boldsymbol{\mu}_{f(\mathrm{b})}^{\nu(\mathrm{b})})$, where Tr denotes the trace. The simulated time-dependent mean square displacements along the three space-fixed Cartesian axes overlay the theoretically expected curves, see Fig. 2.2.

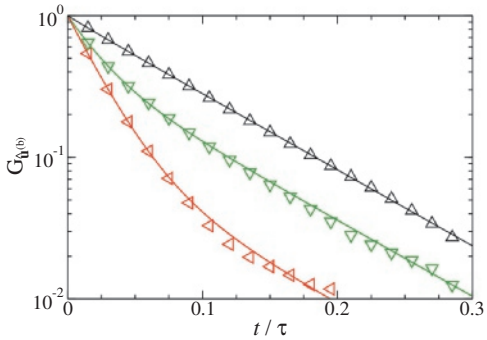

Figure 2.3: Time-correlation functions of the three body-fixed eigenvectors of the rotational mobility matrix, as seen in the lab frame, compared with theoretical prediction (lines).

The rotational diffusion is characterized by calculating the time correlation of a

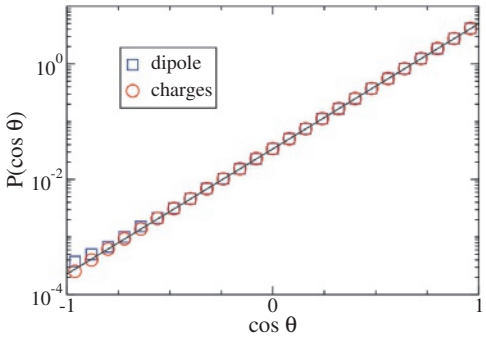

Figure 2.4: Probability distribution of the angle θ between the dipole moment of a particle and an external uniform electric field, for $\beta pE = 5$, and the corresponding theoretical result (line).

body-fixed vector $\hat{\mathbf{u}}^{(\mathrm{b})}$ as seen from the space-fixed frame,

$$G_{\hat{\mathbf{u}}^{(\mathrm{b})}}(t) = \frac{3}{2}\left\langle \left(\hat{\mathbf{u}}^{(\mathrm{s})}(t)\cdot\hat{\mathbf{u}}^{(\mathrm{s})}(0)\right)^2\right\rangle - \frac{1}{2}, \tag{2.25}$$

with $\hat{\mathbf{u}}^{(\mathrm{s})}(t) = \mathbf{A}^{(\mathrm{s})}_{(\mathrm{b})}(t)\hat{\mathbf{u}}^{(\mathrm{b})}$. The time-correlation function has been solved theoretically as a sum of five exponentials [30, 45],

$$G_{\hat{\mathbf{u}}^{(\mathrm{b})}}(t) = \sum_{i=1}^{5} a_i e^{-t/\tau_i}, \tag{2.26}$$

where the five amplitudes a_i and relaxation times τ_i are functions of the three rotational diffusion coefficients of the body and the three body-fixed components of the vector $\hat{\mathbf{u}}^{(\mathrm{b})}$. Figure 2.3 shows good agreement between the time-correlation functions from the simulations and the theoretical curves.

The aforementioned tests were repeated with an asymmetric body, a helix of 81 nearly-touching particles forming a single 360° turn with a radius of 12.5σ and a height of 25σ. The simulation results (data not shown) are again in good agreement with theory.Taken together, these tests validate the inclusion of the stochastic terms in the equations of motion.

2.3.2. Potentials

Consider a particle with two point charges $q_i = \pm q$ placed at distances $\pm\frac{1}{2}d$ from the center of the particle along a direction $\hat{\mathbf{u}}^{(\mathrm{b})}$, creating a constant dipole moment $\mathbf{p}^{(\mathrm{b})} = qd\hat{\mathbf{u}}^{(\mathrm{b})}$ in the body frame and a variable dipole moment $\mathbf{p}^{(\mathrm{s})}(t) = \mathbf{A}^{(\mathrm{s})}_{(\mathrm{b})}(t)\mathbf{p}^{(\mathrm{b})}$ in the space frame. In the presence of an external electric field $\mathbf{E}^{(\mathrm{s})}$, the charges experience forces $\mathbf{f}_i^{(\mathrm{s})} = q_i\mathbf{E}^{(\mathrm{s})}$. The net force acting on the particle is zero, while the two forces induce a torque $\boldsymbol{\tau}^{(\mathrm{s})} = \mathbf{p}^{(\mathrm{s})} \times \mathbf{E}^{(\mathrm{s})}$ that tends to align the dipole with the field. In the presence of thermal noise, the angle θ between the electric field and the dipole moment should obey the Boltzmann distribution $P(\cos\theta) =$

Table 2.1: Einstein coefficients B_{xy} for a hollow sphere of 2082 primary particles in an xy shear flow, calculated using Eq. (2.27), assuming the three definitions of the sphere's volume discussed in the main text. The last line shows the effective radius corresponding to the theoretical value $B_{xy} = 2.5$. The standard deviations result from the rotating spherical shell not being perfectly spherical.

Surface	R	B_{xy}
centers	32	$2.6488 \pm 1 \cdot 10^{-4}$
centers & bumps	32–33	$2.5672 \pm 1 \cdot 10^{-4}$
circumscribed	33	$2.4152 \pm 1 \cdot 10^{-4}$
effective sphere	$32.6226 \pm 1 \cdot 10^{-4}$	2.5

$Z^{-1} \exp(\beta p E \cos\theta)$, where Z is the normalizing configuration integral, irrespective of the mobility matrix. A particle with the aforementioned mobilities was simulated both using a single torque acting on a body-fixed dipole vector and using two forces acting on two body-fixed charges, obtaining good agreement with theory in both cases, see Fig. 2.4. These tests validate the implementation of the conservative and stochastic terms in the equation of motion.

2.3.3. Flow Fields

The flow-induced particle dynamics was tested in the absence of conservative and stochastic terms, to allow comparison with analytical expressions in the literature. Simulations of spheres, ellipsoids and hemispherical caps were performed at a shear rate of $\dot{\gamma} = 0.01\tau^{-1}$ in a solvent of viscosity $\eta_s = (6\pi)^{-1}\epsilon\tau/\sigma^3$, using a time step $\Delta t = 0.01\tau$.

2.3.3.1. Spheres

The simplest body is a rigid sphere. Due to its symmetries the mobility matrix is block diagonal and the sphere merely translates and rotates along with the background fluid, $\mathbf{v} = \mathbf{v}^\infty(\mathbf{x})$ and $\boldsymbol{\omega} = \boldsymbol{\omega}^\infty$. The presence of a rigid body induces stress in the fluid, which is evaluated by Eq. (2.22) and Eq. (2.23). For ease of comparison, we convert all calculated stresses into Einstein coefficients,

$$B_{\alpha\beta} = \frac{1}{\eta_s V_c} \frac{S^{(s)}_{\alpha\beta}}{E^{\infty(s)}_{\alpha\beta}}, \tag{2.27}$$

with V_c the volume of the colloid. For a rigid sphere all elements of $\mathbf{B}$ should be equal to 5/2 [3, 7]. When simulating the sphere as a single primary particle in a shear flow with shear rate $\dot{\gamma}$, hence $\mathbf{v}^\infty(\mathbf{x}) = \dot{\gamma} y \hat{\mathbf{e}}^{(s)}_x$, the two non-zero elements of the stress and strain matrices, xy and yx, both yield Einstein coefficients that approach the theoretical value to within numerical accuracy. Besides shear flow, the algorithm also permits planar, uniaxial and biaxial extensional flows. In all cases, the non-zero elements in the stress and strain tensor yield an Einstein coefficient of 5/2, in agreement with theory.

The simulation of more complex bodies requires the construction of a rigid shell of primary spheres, such that the collective outer envelope of the primary particles

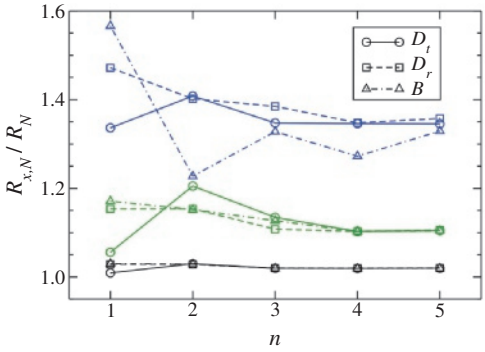

Figure 2.5: Impact of truncating the hydrodynamic pair interactions at order n in the reciproke inter-particle distance, r_{ij}^{-1}. For ease of comparison, the calculated translation diffusion coefficient D_t rotation diffusion coefficient D_r and Einstein coefficient B for spherical shells of $N = 8$ (blue), 102 (green) and 2082 (black) primary particles, have been converted to effective sphere radii $R_{x,N}$ using their well-known theoretical expressions and divided by the radius R_N of the sphere through the centers of the primary particles.

closely approaches the outer surface of the desired body. To assess the validity of this approach, a sphere was modeled as a collection of $N = 2082$ beads of radius $a = 1\sigma$ forming a hollow shell. The beads were placed on the vertices of a geodesic spherical dome, created with the `DistMesh` routine [46] in `matlab`[47], and subsequently shifted along the radial direction to place all bead centers at equal distance $R = 32\sigma$ from the sphere's center. Table 2.1 collects the Einstein coefficients obtained from the simulations, with standard deviations resulting from the time-varying orientation of the near-spherical body relative to the shear flow (the sphere rotates with an angular velocity $\omega = \omega^{\infty(\mathrm{s})} = \dot{\gamma}/2$ around the vorticity direction). Since the body's surface is not uniquely defined, the volume entering Eq. (2.27) was calculated based on i) a sphere with radius R matching the distance between bead centers and sphere center, ii) the former volume augmented with the collective volume $\frac{2}{3}N\pi a^3$ of the hemispherical bumps decorating the former surface, and iii) the volume of the circumscribed sphere of radius $R + a$. The second option yields a B_{xy} nearest the theoretical Einstein coefficient of 2.5. Assuming the latter value as given, one may also invert the calculation to determine the effective radius of the body, as in the last line of Table 2.1. Comparing the calculated translation and rotation diffusion coefficients with their well-known theoretical counterparts, $D_t = k_B T/(6\pi\eta_s R)$ and $D_r = k_B T/(8\pi\eta_s R^3)$, yields relative errors for translation diffusion of -2.1%, 1.2% and -0.03%, and for rotation diffusion of -5.8%, 3.3% and -0.02%, when using sphere radii based on the centers of the primary particles, the circumscribed sphere, and the effective sphere, respectively.

When modelling a body as a shell of nearly touching identical primary particles, the numerical results depend on the number of particles N as well as on the highest order r_{ij}^{-n} included in the expansion of the hydrodynamic interactions between pairs of particles, *i.e.* the series in Eq. (2.35). Figure 2.5 collects results for the translation

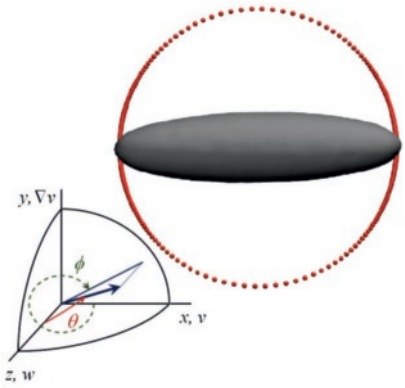

Figure 2.6: Snapshot of a prolate ellipsoid with aspect ratio $p = 5$, periodically tumbling clockwise around the z axis in a linear shear flow $\mathbf{v}^{\infty}(\mathbf{x}) = \dot{\gamma} y \hat{\mathbf{e}}_x^{(\mathrm{s})}$. The red dots, marking the position of one tip at equal time intervals, illustrate the non-linear angular velocity $\dot{\phi}$ of the particle's Jeffery orbit, with $\theta = \pi/2$ throughout.

diffusion coefficient, the rotation diffusion coefficient and the Einstein coefficient of a spherical body for three values of N and five values of n. To enable comparison, all coefficients are converted into effective radii using the aforementioned expressions, and divided by the radius of the sphere containing the centers of the particles. For the $N = 8$ cubic representation frequently used in the literature, [24, 48] the rescaled radii show significant differences that decrease in a non-monotonic way with increasing order n. With increasing number of particles, the three effective radii tend to be in better agreement while the radius of the body increases. Consequently, at $N = 102$ the standard deviation of the six effective radii for $n = 4$ and 5 has reduced to $\sim 1‰$ of the average, while for $N = 2082$ the nine effective radii for $n \geq 3$ agree to within $\sim 0.3‰$ of the average. Hence, employing more primary particles appears as the more appealing method to attaining an accurate description of a complex body, rather than extending the hydrodynamic pair interaction to higher orders in the distance.

2.3.3.2. Ellipsoids

The second body shape considered is a prolate ellipsoid of revolution, a.k.a. a prolate spheroid, which has been studied extensively in the past [4, 11, 49]. Because of the reduced symmetry relative to the sphere, the block diagonal grand mobility matrix of the sphere becomes augmented by off-diagonal blocks coupling flow and rotation, *i.e.* $\boldsymbol{\mu}_{\mathcal{E}}^{\omega}$ and $\boldsymbol{\mu}_{\tau}^{\mathcal{S}}$. A characteristic feature of an ellipsoid in shear flow is its non-uniform tumbling motion, see Fig. 2.6, commonly referred to as Jeffery orbits, while the center of the ellipsoid translates uniformly with the flow. Jeffery [4] derived that ellipsoidal bodies trace periodic orbits with the in-plane rotation angle of

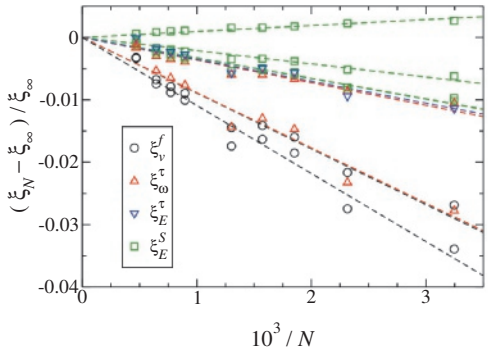

Figure 2.7: Deviations of the nine unique non-zero components of the resistance matrix of a prolate ellipsoid, relative to their theoretical values (indicated by a subscript ∞), plotted against the reciprocal number of primary particles in the representation of the ellipsoid. The markers denote the corresponding blocks of the resistance matrix, the straight lines are fitted by imposing a vanishing intercept.

the long axis evolving as

$$\tan\phi(t) = p\tan\frac{\dot{\gamma}pt}{p^2+1}, \tag{2.28}$$

where $p = L/D$ denotes the aspect ratio of the ellipsoid, with L and D the lengths of the long and short axes, respectively. Due to the asymmetric shape, the stress induced on the fluid varies with the orientation of the ellipsoid. Jeffery also evaluated the excess work when shearing a fluid containing an ellipsoid of volume V_c, which for an ellipsoid tumbling at $\theta = \pi/2$ translates into an orientation dependent Einstein coefficient

$$B_{xy}(\phi) = \frac{4}{3V_p}\left\{F\sin^2 2\phi + G\right\}, \tag{2.29}$$

where F and G are functions of the aspect ratio.

In the simulations, ellipsoids with an aspect ratio $p = 5$ are modelled as hollow shells composed of spherical beads. The positions of the primary particles $\mathbf{x}_j$ are generated by triangulation of the ellipsoids surface, again using `DistMesh`. Each particle is then displaced along the vector $\mathbf{r}_j = \mathbf{x}_j - \mathbf{x}$, with $\mathbf{x}$ the center of the ellipsoid, to ensure that the outer surfaces of all particles touch the circumscribed ellipsoid of desired aspect ratio. The body's grand resistance and mobility matrices are calculated using the method outlined in the previous section, taking the primary particle's radius a as (slightly less than) half the minimum distance between two adjacent vertices. Analysis of the nine unique non-zero matrix elements of the resistance matrix shows that their relative differences from their theoretical values [6] scale approximately linearly with N^{-1}, see Fig. 2.7. The deviations from the fitted lines are correlated, especially those of the translational and rotational resistances, suggesting that the accuracy in describing an ellipsoidal body depends not only directly on the number of beads but also indirectly via the N-dependent triangulation of the surface.

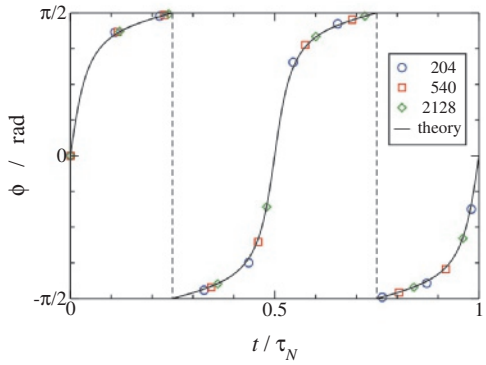

Figure 2.8: Periodic tumbling of an ellipsoid in a shear flow, with ϕ the angle between the long axis and the velocity gradient direction (mapped to the range $[-\pi/2, \pi/2]$), with a long axis permanently perpendicular to the vorticity direction, $\theta = \pi/2$. The markers, denoting the numbers of primary particles N, are equally spaced in time and ought ideally have coalesced for the three representations of the same ellipsoidal body. Agreement with Jeffery's theory (solid line) is obtained by rescaling the orbits with their respective periods τ_N, see also Fig. 2.9.

Simulations of the ellipsoidal bodies in simple shear flows yield periodic orbits, with the long axis rotating in a non-uniform fashion around the vorticity direction while simultaneously the short axes rotate around the long axis. The magnitudes of these two motions vary with the angle θ, culminating in a pure tumbling motion for $\theta = \pi/2$ and a pure rolling motion for $\theta = 0$; these are also the only two values at which θ remains constant, while all other orientations result in a coupling between θ and ϕ in excellent agreement with Jeffery's theory [4]. As an example, Fig. 2.8 shows the pure tumbling motions of an ellipsoidal body when simulated using three differing numbers of primary particles, as well as the theoretical prediction, with all four orbits re-scaled by their respective periods τ_N for ease of comparison. The angular velocity $\dot{\phi}$ periodically varies between near-zero, when the long axis is flow-aligned, and $\omega = \dot{\gamma} = 2\omega^{\infty(\mathrm{s})}$, when the particle is oriented along the gradient direction. In contrast, the center of the body translates at a uniform velocity. The periods of a dozen realizations of the same ellipsoidal body converge with increasing N to the theoretical limit, τ_∞, see Fig. 2.9. Over the explored range of $90 \leq N \leq 2128$, the periods are well described by a power law, $(\tau_N - \tau_\infty)/\tau_\infty \approx 6.6N^{-0.73}$.

The tumbling motion of the body causes the Einstein coefficient B_{xy} to vary periodically too. Simulation results, for three representations of a $p = 5$ ellipsoidal body, yield the same characteristic curve as the theoretical prediction,[4, 50] see Fig. 2.10. The coefficient shows broad minima for nearly flow-aligned orientations, with B_{xy} slightly undershooting the value of 2.5 for a sphere, alternating with maxima when the particle is at increased angles to the flow velocity; the narrow dip in this maximum coincides with the particle briefly reaching an angular velocity matching the shear rate of the imposed flow. The largest difference between numerical and theoretical values, both in relative and in absolute terms, is found at the minima of the curves. With increasing number of primary particles, the simulation results

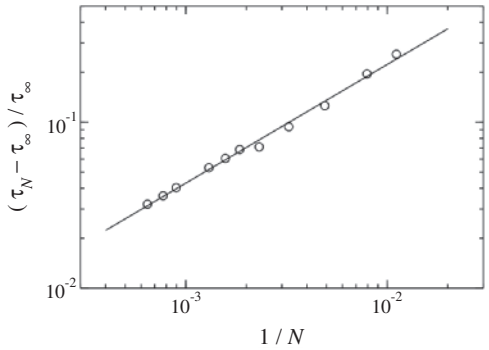

Figure 2.9: Relative deviation in the tumbling periods τ_N of $p = 5$ ellipsoidal bodies, modelled as rigid shells of N spherical primary particles, in a shear flow. The limiting value, τ_∞, is the period derived by Jeffery. The line is a power-law fit.

increase to their theoretical values over the entire time range. The effect of the volume evaluation on the Einstein coefficient is explored in Fig. 2.11. Like for the spherical body, the volume is calculated based on i) the ellipsoidal body formed by the centers of the primary particles, ii) the increment hereof by including the collective volume of the half-spheres protruding from this body, and iii) the ellipsoidal body that circumscribes the primary particles. The analytical result is bracketed by the latter two volumes over the entire time range, suggesting that the effective volume of the simulated body lies between these two limits. When using a number of primary particles in the low hundreds, however, the Einstein coefficients calculated using these two limiting volumes no longer bracket the theoretical curved over the entire range (data not shown), indicating that the compound body ceases to accurately describe the desired ellipsoidal shape for low N.

2.3.3.3. Hemi-spherical caps

A spherical cap, *i.e.* a fragment of a spherical shell with radius R and top angle Θ, also performs periodic orbits in a linear shear flow, see Fig. 2.12. We again focus on orbits with the rotational symmetry axis of the body at a constant angle of $\theta = \pi/2$ to the vorticity direction. As shown by Dorrepaal [44], the rotational motion of the spherical cap is similar to that of an ellipsoid,

$$\tan \phi(t) = \rho \tan \frac{2\pi t}{\tau}, \tag{2.30}$$

where the scaled period $\dot{\gamma}\tau$ and the equivalent axis ratio ρ are functions of the relative dimensions of the cap. In the simulations, a hemi-spherical cap, $\Theta = \pi/2$, is modelled by primary particles distributed over the surface by the `DistMesh` routine. The minimum distance between any two particles is again used to define their diameter. Whereas an infinitely thin shell was assumed by Dorrepaal, the simulated shell will only converge to this limit when the cap's radius far exceeds the particle's diameter, *i.e.* for $N \to \infty$. The procedure of the previous section is used to determine the mobility matrix that enters in the actual simulation of the

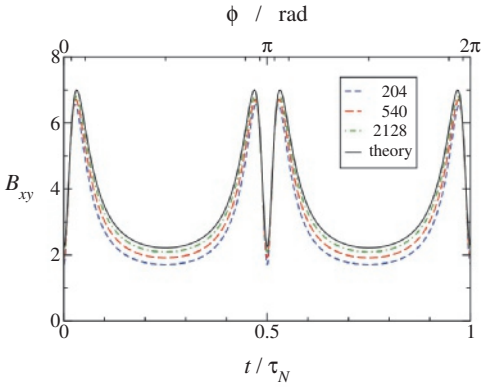

Figure 2.10: Time evolution of the Einstein coefficient B_{xy} for an ellipsoidal body in a shear flow, as simulated using differing numbers of primary particles and as derived from Jeffery's theory. The volume entering Eq. (2.27) is that of the ellipsoid enveloping the primary particles [see also Fig. 2.11]. On the top axis, the interval between successive ticks corresponds to a rotation $\Delta\phi = \pi/6$.

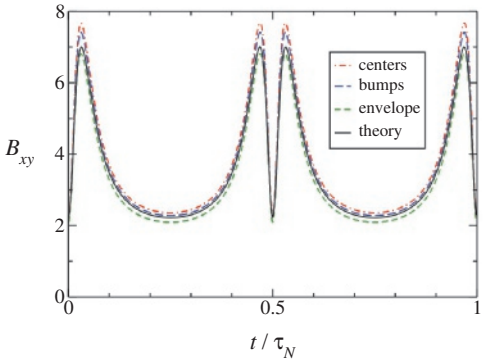

Figure 2.11: Influence of the volume calculation on the Einstein coefficient of an ellipsoidal body approximated by a shell of 2128 primary particles, see Eq. (2.27).

motion, supplemented by a shift of the reference point to the hydrodynamic center of the cap by the procedure of Appendix 2.A.7. The simulated periods of bodies of 526 and 2051 primary particles closely approximate the analytical periods, being shorter by 0.4% and 0.03%, respectively.

Due to the lack of fore-aft symmetry, resulting in a non-zero $\boldsymbol{\mu}_{\mathcal{E}}^{v}$, the hydrodynamic center moves periodically [51]. The paths traced by three points on the symmetry axis of a simulated hemi-spherical cap are shown in Fig. 2.12. Unlike for points on the ellipsoidal body at $\theta = \pi/2$, see Fig. 2.6, the paths are non-circular and there is no stationary point on the body. For a quantitative comparison with theory, Dorrepaal's point Q on the symmetry axis (the red bead in Fig. 2.12) is selected. The simulated motions of this point, for two caps with differing numbers of primary particles, agree well with theory, as shown in Fig. 2.13, indicating once

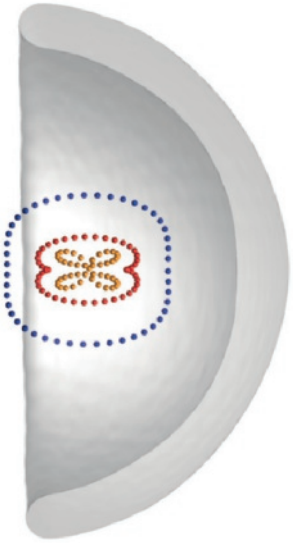

Figure 2.12: Cross-section of a hemi-spherical cap through its symmetry axis. The coloured dots denote the positions, equally spaced in time, of three points on the cap's symmetry axis (arrow starting at the center of the cap) during the combined rotational and translational motion of this body in a linear shear flow. The axes system and flow orientation are identical to those in Fig. 2.6; the orientation shown corresponds with $\phi = 3\pi/2$.

more that the rotational and translational motions are simulated correctly. In the absence of Brownian motion, Eq. (2.19) can be applied using any point in the body frame as the reference point. Tests with randomly chosen reference points indeed recovered the orbits depicted in Figs 2.12 and 2.13 (data not shown).

Evaluation of the Einstein coefficient, based on the volume $V_c = \frac{2}{3}\pi R^3$ enclosed by the cap, yields a periodically undulating B_{xy} akin to that for the ellipsoid (data not shown). The main differences are a considerable reduction and widening of the symmetric double peaks flanking the minima at $\phi = \pm\pi/2$. These minima are again approximately equally low as the minima attained in the flow-aligned state, $\phi = 0$ and $\phi = \pi$, and all minima undershoot the constant value of 2.5 attained for a sphere.

2.4. Summary and conclusions

The Brownian motion of a rigid arbitrary shaped colloidal body is conveniently simulated using Cartesian coordinates for the position of the hydrodynamic center and unit quaternions for the orientation of the body. As shown by Ilie *et al.*[43], the use of quaternions – in combination with a unit-length constraint – simplifies the Brownian equation of motion in the Itô representation by eliminating several terms. Whereas Ilie *et al.* assumed a (6×6) mobility matrix consisting of two (3×3)

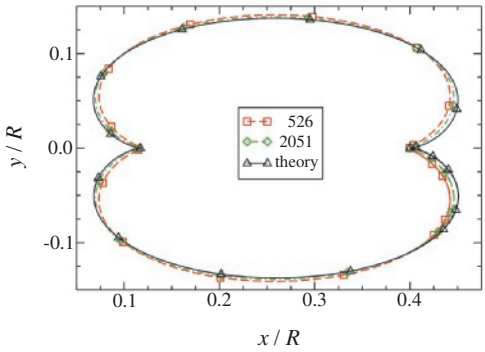

Figure 2.13: Orbit of the center of free rotation of a hemi-spherical cap in a shear flow, showing simulations with two differing numbers of primary particles and Dorrepaal's theory. The markers are equidistant in time and ideally should have coalesced. The center of the cap (the starting point of the arrow in Fig. 2.12) coincides with the origin of the coordinate system for $\phi = 0$.

blocks for the translational and rotation motion, respectively, the formalism is expanded here to an equation of motion based on a (11×11) grand mobility matrix, see Eq. (2.19). The advantages of this expansion are the proper inclusion of translation-rotation coupling beyond the rotation-dependence of the translational mobility, the ability to simulate bodies in linear flow fields and access to the body-induced stress in the fluid. The grand mobility matrix is constructed by representing (the surface of) the body by a collection of spherical primary particles, followed by a weighted summation of the hydrodynamic interactions over all combinations of two primary particles. A code to calculate the grand mobility matrix is available at `www2.msm.ctw.utwente.nl/Oseen11`. Simulation results employing this approach to differing particles of various complexities yield excellent agreement with theory, recovering the Boltzmann distribution and Favro's rotational relaxation [45] for colloids in quiescent fluids and the periodic orbits derived by Jeffery [4] and Dorrepaal [44] for ellipsoids and spherical caps, respectively, immersed in shear flows in the absence of thermal noise. The proposed framework enables computational studies on the complex dynamics of bodies under the combined effects of potential forces, flow and Brownian motion, for which only approximate theoretical descriptions exist to date, like the Einstein viscosity of dilute suspensions of non-spherical colloids [11, 50, 52].

Acknowledgments

We thank Prof. Stefan Luding for stimulating discussions. This work is part of the 'Computational sciences for energy research' of the Netherlands Organisation for Scientific Research (NWO) under Project Nr. 13CSER060. This research programme is co-financed by Shell Global Solutions International B.V..

References

[1] D. Palanisamy and W. K. den Otter, *Efficient brownian dynamics of rigid colloids in linear flow fields based on the grand mobility matrix,* J. Chem. Phys. **148**, 194112 (2018).

[2] G. G. Stokes, *On the effect of the internal friction of fluids on the motion of pendulums,* Trans. Cambridge Philos. Soc. **9**, 8 (1851).

[3] A. Einstein, *Eine neue bestimmung der moleküldimensionen,* Ann. Phys. **19**, 289 (1906).

[4] G. B. Jeffery, *The motion of ellipsoidal particles immersed in a viscous fluid,* Proc. Royal. Soc. London A **102**, 161 (1922).

[5] G. K. Batchelor, *An Introduction to Fluid Dynamics*, Cambridge Mathematical Library (Cambridge University Press, Cambridge, U.K., 2000).

[6] S. Kim and S. J. Karrila, *Microhydrodynamics: Principles and Selected Applications*, Butterworth-Heinemann Series in Chemical Engineering (Butterworth-Heinemann, Stoneham, MA, U.S.A., 1991).

[7] E. Guazzelli and J. F. Morris, *A Physical Introduction to Suspension Dynamics*, Cambridge Texts in Applied Mathematics (Cambridge University Press, Cambridge, U.K., 2012).

[8] H. Huang, X. Yang, M. Krafczyk, and X.-Y. Lu, *Rotation of spheroidal particles in couette flows,* J. Fluid Mech. **692**, 369 (2012).

[9] J. Einarsson, F. Candelier, F. Lundell, J. Angilella, and B. Mehlig, *Rotation of a spheroid in a simple shear at small reynolds number,* Phys. Fluids **27**, 063301 (2015).

[10] C. W. Oseen, *Neuere Methoden und Ergebnisse in der Hydrodynamik* (Akad. Verl.-Ges., Leipzig, Germany, 1927).

[11] J. M. Burgers, *On the motion of small particles of elongated form suspended in a viscous liquid,* in *Second Report on Viscosity and Plasticity* (Noord-Hollandsche Uitgeversmaatschappij, Amsterdam, The Netherlands, 1938) Chap. III, reprinted in [nieuwstadt2012selected].

[12] J. Riseman and J. G. Kirkwood, *The intrinsic viscosity, translational and rotatory diffusion constants of rod-like macromolecules in solution,* J. Chem. Phys. **18**, 512 (1950).

[13] V. Bloomfield, W. Dalton, and K. van Holde, *Frictional coefficients of multisubunit structures. i. theory,* Biopolymers **5**, 135 (1967).

[14] J. García de la Torre and V. Bloomfield, *Hydrodynamic properties of macromolecular complexes. i. translation,* Biopolymers **16**, 1747 (1977).

[15] J. García de la Torre and V. Bloomfield, *Hydrodynamic properties of macromolecular complexes. ii. rotation,* Biopolymers **16**, 1765 (1977).

[16] R. F. Goldstein, *Macromolecular diffusion constants: a calculational strategy,* J. Chem. Phys. **83**, 2390 (1985).

[17] J. Rotne and S. Prager, *Variational treatment of hydrodynamic interaction in polymers,* J. Chem. Phys. **50**, 4831 (1969).

[18] H. Yamakawa, *Transport properties of polymer chains in dilute solution: hydrodynamic interaction,* J. Chem. Phys. **53**, 436 (1970).

[19] R. Kutteh, *Rigid body dynamics approach to stokesian dynamics simulations of nonspherical particles,* J. Chem. Phys. **132**, 174107 (2010).

[20] J. Wang, E. J. Tozzi, M. D. Graham, and D. J. Klingenberg, *Flipping, scooping, and spinning: Drift of rigid curved nonchiral fibers in simple shear flow,* Phys. Fluids **24**, 123304 (2012).

[21] B. Carrasco and J. García de la Torre, *Improved hydrodynamic interactions in macromolecular bead models,* J. Chem. Phys. **111**, 4817 (1999).

[22] J. García de la Torre, G. del Rio Echenique, and A. Ortega, *Improved calculation of rotational diffusion and intrinsic viscosity of bead models for macromolecules and nanoparticles,* J. Phys. Chem. B **111**, 955 (2007).

[23] J. García de la Torre and B. Carrasco, *Intrinsic viscosity and rotational diffusion of bead models for rigid macromolecules and bioparticles,* Euro. Biophys. J. **27**, 549 (1998).

[24] J. García de la Torre, D. Amorós, and A. Ortega, *Intrinsic viscosity of bead models for macromolecules and nanoparticles,* Euro. Biophys. J. **39**, 381 (2010).

[25] L. Durlofsky, J. F. Brady, and G. Bossis, *Dynamic simulations of hydrodynamically interacting particles,* J. Fluid Mech. **180**, 21 (1987).

[26] J. F. Brady and G. Bossis, *Stokesian dynamics,* Ann. Rev. Fluid Mech. **20**, 111 (1988).

[27] W. A. Wegener, *Viscoelasticity of rigid macromolecules with irregular shapes in the limit of overwhelming brownian motion,* Biopolymers **23**, 2243 (1984).

[28] J. W. Swan, J. F. Brady, R. S. Moore, and ChE 174, *Modeling hydrodynamic self-propulsion with stokesian dynamics. or teaching stokesian dynamics to swim,* Phys. Fluids **23**, 071901 (2011).

[29] Y. M. Harshe, L. Ehrl, and M. Lattuada, *Hydrodynamic properties of rigid fractal aggregates of arbitrary morphology,* J. Colloid Interface Sci. **352**, 87 (2010).

[30] M. Makino and M. Doi, *Brownian motion of a particle of general shape in Newtonian fluids,* J. Phys. Soc. Japan **73**, 2739 (2004).

[31] S. Aragon, *Recent advances in macromolecular hydrodynamic modeling,* Methods **54**, 101 (2011).

[32] E. Dickinson, *Brownian dynamic with hydrodynamic interactions: the application to protein diffusional problems,* Chem. Soc. Rev. **14**, 421 (1985).

[33] Y. M. Harshe and M. Lattuada, *Viscosity contribution of an arbitrary shape rigid aggregate to a dilute suspension,* J. Colloid Interface Sci. **367**, 83 (2012).

[34] H. Goldstein, *Classical mechanics*, 2nd ed. (Addison-Wesley, Reading, MA, U.S.A., 1980).

[35] N. G. van Kampen, *Stochastic Processes in Physics and Chemistry* (revised and enlarged edition, Elsevier, Amsterdam, The Netherlands, 1992).

[36] H. C. Öttinger, *Stochastic Processes in Polymeric Fluids* (Springer-Verlag, Berlin, Germany, 1996).

[37] C. Gardiner, *Stochastic Methods. A handbook for the Natural and Social Sciences*, 4th ed., Springer Series in Synergetics (Springer-Verlag, Berlin, Germany, 2009).

[38] S. N. Naess and A. Elgsaeter, *Use of cartesian rotation vectors in brownian dynamics algorithms: Theory and simulation results,* Macromol. Theory Simul. **13**, 419 (2004).

[39] T. R. Evensen, A. Elgsaeter, and S. N. Naess, *Transient molecular electro-optics: Cartesian rotation vector versus eulerian angles,* Colloids Surf., B **56**, 80 (2007).

[40] T. R. Evensen, S. N. Naess, and A. Elgsaeter, *Free rotational diffusion of rigid particles with arbitrary surface topology: a Brownian Dynamics study using Eulerian angles,* Macromol. Theory Simul. **17**, 121 (2008).

[41] T. R. Evensen, S. N. Naess, and A. Elgsaeter, *Brownian Dynamics simulations of rotational diffusion using the cartesian components of the rotation vector as generalized coordinates,* Macromol. Theory Simul. **17**, 403 (2008).

[42] T. R. Evensen, S. N. Naess, and A. Elgsaeter, *Use of the rotation vector in Brownian Dynamics simulation of transient electro-optical properties,* Macromol. Theory Simul. **18**, 50 (2009).

[43] I. M. Ilie, W. J. Briels, and W. K. den Otter, *An elementary singularity-free rotational brownian dynamics algorithm for anisotropic particles,* J. Chem. Phys. **142**, 114103 (2015).

[44] J. M. Dorrepaal, *The stokes resistance of a spherical cap to translational and rotational motions in a linear shear flow,* J. Fluid Mech. **84**, 265 (1978).

[45] L. D. Favro, *Theory of the rotational brownian motion of a free rigid body,* Phys. Rev. **119**, 53 (1960).

[46] P.-O. Persson and G. Strang, *A simple mesh generator in matlab,* SIAM Rev. **46**, 329 (2004).

[47] MATLAB R2014a, The MathWorks Inc., Natick, MA, U.S.A. (2014).

[48] R. W. Wilson and V. A. Bloomfield, *Hydrodynamic properties of macromolecular complexes. V. Improved calculation of rotational diffusion coefficient and intrinsic viscosity,* Biopolymers **53**, 1205 (1979).

[49] L. G. Leal and E. J. Hinch, *The effect of weak brownian rotations on particles in shear flow,* J. Fluid Mech. **46**, 685 (1971).

[50] S. Mueller, E. W. Llewellin, and H. M. Mader, *The rheology of suspensions of solid particles,* Proc. Royal. Soc. A **466**, 1201 (2010).

[51] A. Nir and A. Acrivos, *On the creeping motion of two arbitrary-sized touching spheres in a linear shear field,* J. Fluid Mech. **59**, 209 (1973).

[52] E. J. Hinch and L. G. Leal, *The effect of brownian motion on the rheological properties of a suspension of non-spherical particles,* J. Fluid Mech. **52**, 683 (1972).

2.A. Appendices:

2.A.1. Pair mobilities

The generalized mobility and resistance tensors appearing in the various equations of the main text are of mixed units. With a the radius of the particle, τ the unit of time and η_s the solvent viscosity, the pair mobility problem can be re-expressed as

$$\begin{pmatrix} (\mathbf{v}_i - \mathbf{v}_i^{\infty})\tau/a \\ (\boldsymbol{\omega}_i - \boldsymbol{\omega}^{\infty})\tau \\ -\mathbf{E}^{\infty}\tau \end{pmatrix} = \frac{1}{6\pi}\sum_{j=1}^{N} \boldsymbol{\mu}_j^i \begin{pmatrix} \mathbf{f}_j\tau/\left(\eta_s a^2\right) \\ \boldsymbol{\tau}_j\tau/\left(\eta_s a^3\right) \\ \mathbf{S}_j\tau/\left(\eta_s a^3\right) \end{pmatrix}. \tag{2.31}$$

All elements of the generalized vectors (between large brackets) on the l.h.s. and r.h.s. of this expression are dimensionless, and hence all elements of the tensors $\boldsymbol{\mu}_j^i$ are also dimensionless. Following the steps outlined in the main text, the dimensionless mobility problem of the cluster becomes

$$\begin{pmatrix} \left(\mathbf{v} - \mathbf{v}^{\infty(s)}\right)\tau/a \\ (\boldsymbol{\omega} - \boldsymbol{\omega}^{\infty})\tau \\ \boldsymbol{\mathcal{S}}_j\tau/\left(\eta_s a^3\right) \end{pmatrix} = \frac{1}{6\pi}\boldsymbol{\mu} \begin{pmatrix} \mathbf{f}_j\tau/\left(\eta_s a^2\right) \\ \boldsymbol{\tau}_j\tau/\left(\eta_s a^3\right) \\ -\boldsymbol{\mathcal{E}}^{\infty}\tau \end{pmatrix}. \tag{2.32}$$

The corresponding dimensionless equation of motion is readily obtained.

The tensorial character of the pair mobility matrix $\boldsymbol{\mu}_j^i$ imposes the structure of the hydrodynamic interactions between particles i and j, with difference vector $\mathbf{r}^{ij} = \mathbf{x}_j - \mathbf{x}_i$, parallel unit vector $\hat{\mathbf{r}}^{ij} = \mathbf{r}^{ij}/r_{ij}$, traceless dyadic $\mathbf{d}^{ij} = \hat{\mathbf{r}}^{ij} \otimes \hat{\mathbf{r}}^{ij} - \frac{1}{3}1$ and perpendicular projection $\mathbf{p}^{ij} = 1 - \hat{\mathbf{r}}^{ij} \otimes \hat{\mathbf{r}}^{ij}$, where for compactness of notation the particle-pair label is denoted as superscript to the vectors and matrices. Using auxiliary functions x, y and z in the dimensionless distance $\tilde{r}_{ij} = r_{ij}/a$, the elements of the mobility matrix read as [1–4]

$$\mu_{f,j,\beta}^{v,i,\alpha} = x_{f,j}^{v,i}\hat{r}_{\alpha}^{ij}\hat{r}_{\beta}^{ij} + y_{f,j}^{v,i}p_{\alpha\beta}^{ij} \tag{2.33a}$$

$$\mu_{f,j,\beta}^{\omega,i,\alpha} = y_{f,j}^{\omega,i}\epsilon_{\alpha\beta\gamma}\hat{r}_{\gamma}^{ij}, \tag{2.33b}$$

$$\mu_{\tau,j,\beta}^{\omega,i,\alpha} = x_{\tau,j}^{\omega,i}\hat{r}_{\alpha}^{ij}\hat{r}_{\beta}^{ij} + y_{\tau,j}^{\omega,i}p_{\alpha\beta}^{ij}, \tag{2.33c}$$

$$\mu_{f,j,\gamma}^{E,i,\alpha\beta} = x_{f,j}^{E,i}d_{\alpha\beta}^{ij}\hat{r}_{\gamma}^{ij} + y_{f,j}^{E,i}\left(\hat{r}_{\alpha}^{ij}p_{\beta\gamma}^{ij} + \hat{r}_{\beta}^{ij}p_{\alpha\gamma}^{ij}\right), \tag{2.33d}$$

$$\mu_{\tau,j,\gamma}^{E,i,\alpha\beta} = y_{\tau,j}^{E,i}\left(\hat{r}_{\alpha}^{ij}\epsilon_{\beta\gamma\delta} + \hat{r}_{\beta}^{ij}\epsilon_{\alpha\gamma\delta}\right)\hat{r}_{\delta}^{ij}, \tag{2.33e}$$

$$\begin{aligned} \mu_{S,j,\gamma\delta}^{E,i,\alpha\beta} = {} & x_{S,j}^{E,i}d_{\alpha\beta}^{ij}d_{\gamma\delta}^{ij} \\ & + y_{S,j}^{E,i}\Big[\hat{r}_{\alpha}^{ij}p_{\beta\gamma}^{ij}\hat{r}_{\delta}^{ij} + \hat{r}_{\alpha}^{ij}p_{\beta\delta}^{ij}\hat{r}_{\gamma}^{ij} \\ & \quad + \hat{r}_{\beta}^{ij}p_{\beta\gamma}^{ij}\hat{r}_{\delta}^{ij} + \hat{r}_{\beta}^{ij}p_{\beta\delta}^{ij}\hat{r}_{\gamma}^{ij}\Big] \\ & + z_{S,j}^{E,i}\Big[p_{\alpha\gamma}^{ij}p_{\beta\delta}^{ij} + p_{\beta\gamma}^{ij}p_{\alpha\delta}^{ij} - p_{\alpha\beta}^{ij}p_{\gamma\delta}^{ij}\Big], \end{aligned} \tag{2.33f}$$

with the remaining elements following from the symmetry relations

$$\mu^{v,j,\beta}_{\tau,i,\alpha} = \mu^{\omega,i,\alpha}_{f,j,\beta}, \tag{2.34a}$$
$$\mu^{v,j,\gamma}_{S,i,\alpha\beta} = \mu^{E,i,\alpha\beta}_{f,j,\gamma}, \tag{2.34b}$$
$$\mu^{\omega,j,\gamma}_{S,i,\alpha\beta} = \mu^{E,i,\alpha\beta}_{\tau,j,\gamma}. \tag{2.34c}$$

In the Rotne-Prager-Yamakawa approximation, the auxiliary functions are given by

$$x^{v,i}_{f,j} = \delta_{ij} + (1-\delta_{ij})\left(\tfrac{3}{2}\tilde{r}_{ij}^{-1} - \tilde{r}_{ij}^{-3}\right), \tag{2.35a}$$
$$y^{v,i}_{f,j} = \delta_{ij} + (1-\delta_{ij})\left(\tfrac{3}{4}\tilde{r}_{ij}^{-1} + \tfrac{1}{2}\tilde{r}_{ij}^{-3}\right), \tag{2.35b}$$
$$y^{\omega,i}_{f,j} = -(1-\delta_{ij})\ \tfrac{3}{4}\tilde{r}_{ij}^{-2} \tag{2.35c}$$
$$x^{\omega,i}_{\tau,j} = \tfrac{3}{4}\delta_{ij} + (1-\delta_{ij})\ \tfrac{3}{4}\tilde{r}_{ij}^{-3}, \tag{2.35d}$$
$$y^{\omega,i}_{\tau,j} = \tfrac{3}{4}\delta_{ij} - (1-\delta_{ij})\ \tfrac{3}{8}\tilde{r}_{ij}^{-3}, \tag{2.35e}$$
$$x^{E,i}_{f,j} = (1-\delta_{ij})\left(\tfrac{9}{4}\tilde{r}_{ij}^{-2} - \tfrac{18}{5}\tilde{r}_{ij}^{-4}\right), \tag{2.35f}$$
$$y^{E,i}_{f,j} = (1-\delta_{ij})\ \tfrac{6}{5}\tilde{r}_{ij}^{-4}, \tag{2.35g}$$
$$y^{E,i}_{\tau,j} = -(1-\delta_{ij})\ \tfrac{9}{8}\tilde{r}_{ij}^{-3}, \tag{2.35h}$$
$$x^{E,i}_{S,j} = \tfrac{27}{20}\delta_{ij} - (1-\delta_{ij})\left(\tfrac{27}{4}\tilde{r}_{ij}^{-3} - \tfrac{81}{5}\tilde{r}_{ij}^{-5}\right), \tag{2.35i}$$
$$y^{E,i}_{S,j} = \tfrac{9}{20}\delta_{ij} + (1-\delta_{ij})\left(\tfrac{9}{8}\tilde{r}_{ij}^{-3} - \tfrac{18}{5}\tilde{r}_{ij}^{-5}\right), \tag{2.35j}$$
$$z^{E,i}_{S,j} = \tfrac{9}{20}\delta_{ij} + (1-\delta_{ij})\ \tfrac{9}{10}\tilde{r}_{ij}^{-5}. \tag{2.35k}$$

One may readily substitute these functions with higher-order approximations [3].

2.A.2. The basis matrices

Like the strain rate in Eq. (2.3), the stress is converted between matrix and vector representations by

$$\mathbf{S} = \mathbf{e}^{\mathcal{S}}_{\kappa}\mathcal{S}_{\kappa}, \qquad \mathcal{S}_{\alpha\beta} = (\mathbf{e}^{\mathcal{S}}_{\kappa})_{\alpha\beta}\mathcal{S}_{\kappa}, \tag{2.36a}$$
$$\mathcal{S}_{\kappa} = \mathbf{e}^{\kappa}_{\mathcal{S}} : \mathbf{S}, \qquad \mathcal{S}_{\kappa} = (\mathbf{e}^{\kappa}_{\mathcal{S}})_{\alpha\beta}S_{\alpha\beta}, \tag{2.36b}$$

where the Einstein summation convention is used, with Greek indices from the start of the alphabet ($\alpha, \beta, \ldots$) running over the three Cartesian directions and Greek indices from the middle of the alphabet (κ, λ) running over 1 through 5. For the five components defining the symmetric traceless stress tensor, it proves convenient to select the three shear-stresses, $\mathcal{S}_1 = S_{xy}$, $\mathcal{S}_2 = S_{xz}$ and $\mathcal{S}_3 = S_{yz}$, in combination with the first and second normal stress differences, $\mathcal{S}_4 = S_{xx} - S_{yy}$ and $\mathcal{S}_5 = S_{yy} - S_{zz}$, respectively. The corresponding five basis matrices (akin to basis vectors)

to convert the stress from vector $\boldsymbol{\mathcal{S}}$ to matrix $\mathbf{S}$ then read as

$$\begin{aligned}
\mathbf{e}_1^S &= \begin{pmatrix} 0 & 1 & 0 \\ 1 & 0 & 0 \\ 0 & 0 & 0 \end{pmatrix}, \quad \mathbf{e}_2^S = \begin{pmatrix} 0 & 0 & 1 \\ 0 & 0 & 0 \\ 1 & 0 & 0 \end{pmatrix}, \\
\mathbf{e}_3^S &= \begin{pmatrix} 0 & 0 & 0 \\ 0 & 0 & 1 \\ 0 & 1 & 0 \end{pmatrix}, \quad \mathbf{e}_4^S = \tfrac{1}{3}\begin{pmatrix} 2 & 0 & 0 \\ 0 & -1 & 0 \\ 0 & 0 & -1 \end{pmatrix}, \\
\mathbf{e}_5^S &= \tfrac{1}{3}\begin{pmatrix} 1 & 0 & 0 \\ 0 & 1 & 0 \\ 0 & 0 & -2 \end{pmatrix}.
\end{aligned} \tag{2.37}$$

Since these basis matrices are not orthogonal, in the sense that $\mathbf{e}_\kappa^S : \mathbf{e}_S^\lambda \neq \delta_{\kappa\lambda}$ with δ the Kronecker delta, conversion of the stress from matrix $\mathbf{S}$ to vector $\boldsymbol{\mathcal{S}}$ requires the reciprocal basis

$$\begin{aligned}
&\mathbf{e}_S^1 = \tfrac{1}{2}\mathbf{e}_1^S, \quad \mathbf{e}_S^2 = \tfrac{1}{2}\mathbf{e}_2^S, \quad \mathbf{e}_S^3 = \tfrac{1}{2}\mathbf{e}_3^S, \\
&\mathbf{e}_S^4 = \begin{pmatrix} 1 & 0 & 0 \\ 0 & -1 & 0 \\ 0 & 0 & 0 \end{pmatrix}, \ \mathbf{e}_S^5 = \begin{pmatrix} 0 & 0 & 0 \\ 0 & 1 & 0 \\ 0 & 0 & -1 \end{pmatrix},
\end{aligned} \tag{2.38}$$

as is readily verified using Eq. (2.36).

The particle-particle grand mobility matrices in Eq. (2.1) satisfy a number of symmetry rules, derivable from the Lorentz reciprocal theorem [3]. Consequently, when choosing the (dual) basis matrices for the strain rate as

$$\mathbf{e}_\kappa^E = \mathbf{e}_S^\kappa, \tag{2.39a}$$

$$\mathbf{e}_E^\kappa = \mathbf{e}_\kappa^S, \tag{2.39b}$$

the particle-particle grand mobility matrices in Eq. (2.4) will inherit these symmetries, and the cluster's grand mobility matrix in Eq. (2.10) will be symmetric. The five elements of the strain rate vector then represent the three shear rates, $\mathcal{E}_1^\infty = 2E_{xy}^\infty = \partial v_x^\infty/\partial y + \partial v_y^\infty/\partial x$, $\mathcal{E}_2^\infty = 2E_{xz}^\infty$ and $\mathcal{E}_3^\infty = 2E_{yz}^\infty$, as well as the two extensional rates $\mathcal{E}_4^\infty = E_{xx}^\infty = \partial v_x^\infty/\partial x$ and $\mathcal{E}_5^\infty = -E_{zz}^\infty$, respectively. The imposition of symmetry is convenient, but not compulsory, to the approach taken in this paper.

2.A.3. Grand resistance matrix

In the vectorial representation of the strain rate, the background flow field experienced by particle j can be expressed as a sum of matrix-vector products through

$$\mathbf{v}^\infty(\mathbf{x}_j) = \mathbf{v}^\infty(\mathbf{x}) + \boldsymbol{\varphi}_j \boldsymbol{\mathcal{E}}^\infty - \boldsymbol{\varepsilon}_j \boldsymbol{\omega}^\infty, \tag{2.40}$$

where use is made of the (3×5) matrices

$$\varphi_{j,\alpha\kappa} = \varphi_{\alpha\kappa}(\mathbf{r}_j) = \sum_\beta (\mathbf{e}_\kappa^E)_{\alpha\beta} r_{j,\beta} \tag{2.41}$$

and the (3×3) matrices

$$\varepsilon_{j,\alpha\beta} = \varepsilon_{\alpha\beta}(\mathbf{r}_j) = \epsilon_{\alpha\gamma\beta} r_{j,\gamma}, \tag{2.42}$$

with $\boldsymbol{\epsilon}$ the Levi-Civita tensor. Inserting these velocities in Eq. (2.6) yields minus the hydrodynamic forces on the particles, which are readily summed, see Eq. (2.8a), to obtain minus the total hydrodynamic force on the cluster. The force-related submatrices in the grand mobility of the cluster are then extracted as

$$\boldsymbol{\xi}^f_v = \sum_{i,j=1}^{N} \boldsymbol{\xi}^{f,i}_{v,j}, \tag{2.43a}$$

$$\boldsymbol{\xi}^f_\omega = \sum_{i,j=1}^{N} \left[\boldsymbol{\xi}^{f,i}_{\omega,j} - \boldsymbol{\xi}^{f,i}_{v,j} \boldsymbol{\varepsilon}_j \right], \tag{2.43b}$$

$$\boldsymbol{\xi}^f_\mathcal{E} = \sum_{i,j=1}^{N} \left[\boldsymbol{\xi}^{f,i}_{\mathcal{E},j} + \boldsymbol{\xi}^{f,i}_{v,j} \boldsymbol{\varphi}_j \right]. \tag{2.43c}$$

Similarly, insertion of the hydrodynamic forces into the summation expression for the torques, see Eq. (2.8b), yields

$$\boldsymbol{\xi}^\tau_v = \sum_{i,j=1}^{N} \left[\boldsymbol{\xi}^{\tau,i}_{v,j} + \boldsymbol{\varepsilon}_i \boldsymbol{\xi}^{f,i}_{v,j} \right], \tag{2.44a}$$

$$\boldsymbol{\xi}^\tau_\omega = \sum_{i,j=1}^{N} \left[\boldsymbol{\xi}^{\tau,i}_{\omega,j} - \boldsymbol{\xi}^{\tau,i}_{v,j} \boldsymbol{\varepsilon}_j - \boldsymbol{\varepsilon}_i \boldsymbol{\xi}^{f,i}_{v,j} \boldsymbol{\varepsilon}_j + \boldsymbol{\varepsilon}_i \boldsymbol{\xi}^{f,i}_{\omega,j} \right], \tag{2.44b}$$

$$\boldsymbol{\xi}^\tau_\mathcal{E} = \sum_{i,j=1}^{N} \left[\boldsymbol{\xi}^{\tau,i}_{\mathcal{E},j} + \boldsymbol{\xi}^{\tau,i}_{v,j} \boldsymbol{\varphi}_j + \boldsymbol{\varepsilon}_i \boldsymbol{\xi}^{f,i}_{v,j} \boldsymbol{\varphi}_j + \boldsymbol{\varepsilon}_i \boldsymbol{\xi}^{f,i}_{\mathcal{E},j} \right]. \tag{2.44c}$$

In the vectorial representation of the stress, the addition rule of Eq. (2.8c) can be expressed as a sum of matrix-vector products through

$$\boldsymbol{\mathcal{S}} = \sum_{i=1}^{N} \left[\boldsymbol{\mathcal{S}}_i + \boldsymbol{\psi}_i \mathbf{f}_i \right], \tag{2.45}$$

with (5×3) matrices

$$\psi_{i,\kappa\alpha} = \psi_{\kappa\alpha}(\mathbf{r}_i) = \sum_{\beta} r_{i,\beta} (\mathbf{e}^\kappa_S)_{\beta\alpha}. \tag{2.46}$$

Then

$$\boldsymbol{\xi}_v^{\mathcal{S}} = \sum_{i,j=1}^{N} \left[\boldsymbol{\xi}_{v,j}^{\mathcal{S},i} + \boldsymbol{\psi}_i \boldsymbol{\xi}_{v,j}^{f,i} \right], \tag{2.47a}$$

$$\boldsymbol{\xi}_\omega^{\mathcal{S}} = \sum_{i,j=1}^{N} \left[\boldsymbol{\xi}_{\omega,j}^{\mathcal{S},i} - \boldsymbol{\xi}_{v,j}^{\mathcal{S},i} \boldsymbol{\varphi}_j - \boldsymbol{\psi}_i \boldsymbol{\xi}_{v,j}^{f,i} + \boldsymbol{\psi}_i \boldsymbol{\xi}_{\omega,j}^{f,i} \right], \tag{2.47b}$$

$$\boldsymbol{\xi}_\mathcal{E}^{\mathcal{S}} = \sum_{i,j=1}^{N} \left[\boldsymbol{\xi}_{\mathcal{E},j}^{\mathcal{S},i} + \boldsymbol{\xi}_{v,j}^{\mathcal{S},i} \boldsymbol{\varphi}_j + \boldsymbol{\psi}_i \boldsymbol{\xi}_{v,j}^{f,i} \boldsymbol{\varphi}_j + \boldsymbol{\psi}_i \boldsymbol{\xi}_{\mathcal{E},j}^{f,i} \right]. \tag{2.47c}$$

From the symmetry of the (6×6) top-left sub-matrix of the particle-based grand resistance matrices, it readily follows that the (6×6) top-left sub-matrix of the cluster's grand resistance matrix is also symmetric. Retainment of the symmetries of the particle-based sub-matrices related to the stress and strain, however, is subject to the chosen basis matrices, see Appendix 2.A.2.

2.A.4. Partial inversion

To solve $\mathbf{B}$ and $\mathbf{C}$ in the relation

$$\begin{pmatrix} \mathbf{A} \\ \mathbf{B} \end{pmatrix} = \begin{pmatrix} \mathbf{Q} & \mathbf{R} \\ \mathbf{S} & \mathbf{T} \end{pmatrix} \begin{pmatrix} \mathbf{C} \\ \mathbf{D} \end{pmatrix}, \tag{2.48}$$

one first solves $\mathbf{C}$ from the top line, followed by substitution of this result in the bottom line, yielding

$$\begin{pmatrix} \mathbf{C} \\ \mathbf{B} \end{pmatrix} = \begin{pmatrix} \mathbf{Q}^{-1} & -\mathbf{Q}^{-1}\mathbf{R} \\ \mathbf{S}\mathbf{Q}^{-1} & \mathbf{T} - \mathbf{S}\mathbf{Q}^{-1}\mathbf{R} \end{pmatrix} \begin{pmatrix} \mathbf{A} \\ \mathbf{D} \end{pmatrix}. \tag{2.49}$$

In the context of Eq. (2.9), $\mathbf{B}$ and $\mathbf{C}$ refer to the five hydrodynamic stresses and the six generalized velocities of the cluster, respectively, while $\mathbf{A}$ and $\mathbf{D}$ represent the six generalized conservative forces on the cluster and minus the strain rate of the fluid, respectively.

2.A.5. Quaternions

A rotation matrix in three dimensional space can be expressed in terms of the unit quaternion four-vector, $\mathbf{q} = (q_0, q_1, q_2, q_3)$ with $|\mathbf{q}| = 1$, where for the conversion from the body frame (b) to the space frame (s) we use

$$\mathbf{A}_{(\mathrm{b})}^{(\mathrm{s})} = \begin{pmatrix} q_0^2 + q_1^2 - q_2^2 - q_3^2 & 2q_1q_2 - 2q_0q_3 & 2q_1q_3 + 2q_0q_2 \\ 2q_1q_2 + 2q_0q_3 & q_0^2 - q_1^2 + q_2^2 - q_3^2 & 2q_2q_3 - 2q_0q_1 \\ 2q_1q_3 - 2q_0q_2 & 2q_2q_3 + 2q_0q_1 & q_0^2 - q_1^2 - q_2^2 + q_3^2 \end{pmatrix}. \tag{2.50}$$

The conversion from the space frame to the body frame is realised by $\mathbf{A}_{(\mathrm{s})}^{(\mathrm{b})}$, which is simply the transposed (as well as the inverse) of the above matrix. In the simulation

algorithm, the conversion of angular velocities in the space frame to quaternion velocities is realized by

$$\mathbf{B}^{\dot{q}}_{(\mathrm{s})} = \frac{\partial \dot{\mathbf{q}}}{\partial \boldsymbol{\omega}^{(\mathrm{s})}} = \frac{1}{2q^4}\begin{pmatrix} -q_1 & -q_2 & -q_3 \\ q_0 & q_3 & -q_2 \\ -q_3 & q_0 & q_1 \\ q_2 & -q_1 & q_0 \end{pmatrix}, \tag{2.51}$$

with $q = |\mathbf{q}|$, and the conversion of angular velocities in the body frame to quaternion velocities is realized by

$$\mathbf{B}^{\dot{q}}_{(\mathrm{b})} = \frac{\partial \dot{\mathbf{q}}}{\partial \boldsymbol{\omega}^{(\mathrm{b})}} = \frac{1}{2q^4}\begin{pmatrix} -q_1 & -q_2 & -q_3 \\ q_0 & -q_3 & q_2 \\ q_3 & q_0 & -q_1 \\ -q_2 & q_1 & q_0 \end{pmatrix}. \tag{2.52}$$

One readily shows that the latter two matrices are related by $\mathbf{B}^{\dot{q}}_{(\mathrm{b})} = \mathbf{B}^{\dot{q}}_{(\mathrm{s})}\mathbf{A}^{(\mathrm{s})}_{(\mathrm{b})}$.

2.A.6. Brownian equation of motion

In deriving the rigid-body equation of motion from the generic Brownian equation of motion, see Eqs. (2.12) and (2.19), we start by noting that the intended set of coordinates, $\mathbf{Q} = (\mathbf{x}^{\mathrm{T}}, \mathbf{q}^{\mathrm{T}})^{\mathrm{T}}$, includes one surplus coordinate relative to the six coordinates needed to describe rigid body translation and rotation. One readily sees from Eq. (2.50) that the four quaternions describe rotation as well as enlargement, $\mathbf{A}^{(\mathrm{s})}_{(\mathrm{b})}(\mathbf{q}) = q^2\mathbf{A}^{(\mathrm{s})}_{(\mathrm{b})}(\mathbf{q}/q)$. For pure rotations, the quaternion vector must be constrained to unit length, $q = 1$, throughout the simulation. Furthermore, as noted by Ilie *et al.* [5], a Brownian equation of motion using quaternions requires a mobility matrix that decouples enlargement from translation and rotation. Assuming a quiescent solvent for convenience, we construct the mobility matrix entering the generic expression as

$$\boldsymbol{\mu}_Q = \begin{pmatrix} \mathbf{A}^{(\mathrm{s})}_{(\mathrm{b})} & 0 \\ 0 & \mathbf{B}^{\dot{q}}_{(\mathrm{b})} \end{pmatrix}\begin{pmatrix} \boldsymbol{\mu}^{v}_{f} & \boldsymbol{\mu}^{v}_{\tau} \\ \boldsymbol{\mu}^{\omega}_{f} & \boldsymbol{\mu}^{\omega}_{\tau} \end{pmatrix}^{(\mathrm{b})}_{(\mathrm{b})}\begin{pmatrix} \mathbf{A}^{(\mathrm{s})}_{(\mathrm{b})} & 0 \\ 0 & \mathbf{B}^{\dot{q}}_{(\mathrm{b})} \end{pmatrix}^{\mathrm{T}}, \tag{2.53}$$

where the central matrix on the r.h.s. is the cartesian body-based mobility matrix, the matrix to its left converts body-based velocities to space-based and quaternion velocities, and the transposed matrix to its right is dictated by the symmetry of $\boldsymbol{\mu}_Q$. Since the columns of $\mathbf{B}^{\dot{q}}_{(\mathrm{b})}$ are orthogonal to $\mathbf{q}$, see Eq. (2.52), the left-most matrix in the triple product ensures that this mobility matrix conserves the length of the quaternion vector (in the limit of $\Delta t \to 0$). The restrictions on the use of quaternions are therefore met.

Upon insertion of the above mobility matrix in Eq. (2.12), it readily follows from $\left(\mathbf{A}^{(\mathrm{s})}_{(\mathrm{b})}\right)^{\mathrm{T}} = \mathbf{A}^{(\mathrm{b})}_{(\mathrm{s})}$ that conservative forces in the space frame, $f^{(\mathrm{s})}_{\alpha} = -\partial\Phi/\partial Q_{\alpha} = -\partial\Phi/\partial x_{\alpha}$ with $\alpha \in \{1, 2, 3\}$, are converted to forces in the body frame before left-multiplication with the body-based mobility matrix. The generalized forces with

respect to the four rotational coordinates, $f^q_{\rho+4} = -\partial\Phi/\partial Q_{\rho+4} = -\partial\Phi/\partial q_\rho$ with $\rho \in \{0,1,2,3\}$, are converted by $\left(\mathbf{B}^{\dot{q}}_{(\mathrm{b})}\right)^{\mathrm{T}}$ before left-multiplication with the body-based mobility matrix. Using the matrices introduced in Appendix 2.A.5, it follows that

$$\begin{aligned}\left(\mathbf{B}^{\dot{q}}_{(\mathrm{b})}\right)^{\mathrm{T}}\frac{\partial\Phi}{\partial\mathbf{q}} &= \left(\mathbf{A}^{(\mathrm{s})}_{(\mathrm{b})}\right)^{\mathrm{T}}\left(\mathbf{B}^{\dot{q}}_{(\mathrm{s})}\right)^{\mathrm{T}}\frac{\partial\Phi}{\partial\mathbf{q}} \\ &= \mathbf{A}^{(\mathrm{b})}_{(\mathrm{s})}\frac{\partial\Phi}{\partial\mathbf{q}}\frac{\partial\dot{\mathbf{q}}}{\partial\boldsymbol{\omega}^{(\mathrm{s})}} = \mathbf{A}^{(\mathrm{b})}_{(\mathrm{s})}\frac{\partial\Phi}{\partial\boldsymbol{\psi}^{(\mathrm{s})}},\end{aligned} \tag{2.54}$$

where the rotation vector $\boldsymbol{\psi}^{(\mathrm{s})}$ collects the rotation angles around the three space-based coordinate axes, with rates of change $\dot{\boldsymbol{\psi}}^{(\mathrm{s})} = \boldsymbol{\omega}^{(\mathrm{s})}$. The final derivative of the potential energy with respect to $\boldsymbol{\psi}^{(\mathrm{s})}$ yields minus the usual torque vector in the space frame, $\boldsymbol{\tau}^{(\mathrm{s})}$. Hence, the above derivation shows that the conservative potential enters Eqs. (2.12) and (2.19) in the same way, with the latter form being easier to calculate. Note that the rows of $\left(\mathbf{B}^{\dot{q}}_{(\mathrm{b})}\right)^{\mathrm{T}}$ are perpendicular to $\mathbf{q}$, hence conservative forces that strive to enlarge the body, *i.e.* force components $\partial\Phi/\partial\mathbf{q}$ parallel to $\mathbf{q}$, are eliminated by the third matrix on the r.h.s. to Eq. (2.53).

Using the above mobility matrix $\boldsymbol{\mu}_Q$, we next derive the divergence term in Eq. (2.12). The derivative of $\boldsymbol{\mu}_Q$ with respect to the position $\mathbf{x}$ is clearly zero, hence neither $\boldsymbol{\mu}^v_f$ nor $\boldsymbol{\mu}^\omega_f$ contributes to the divergence. A straightforward but laborious derivation, using the matrices of Appendix 2.A.5 and the symmetry of $\boldsymbol{\mu}^{\omega(\mathrm{b})}_{\tau(\mathrm{b})}$, yields the vector

$$\frac{\partial\left(\boldsymbol{\mu}_Q\right)_{\sigma\phi}}{\partial Q_\phi} = \begin{pmatrix} -\left(\mathbf{A}^{(\mathrm{s})}_{(\mathrm{b})}\right)_{\sigma\alpha}\epsilon_{\alpha\beta\gamma}\left(\boldsymbol{\mu}^{v(\mathrm{b})}_{\tau(\mathrm{b})}\right)_{\beta\gamma}/q^4 \\ q_{\sigma-4}\,\mathrm{Tr}\left(\boldsymbol{\mu}^{\omega(\mathrm{b})}_{\tau(\mathrm{b})}\right)/\left(4q^8\right) \end{pmatrix}, \tag{2.55}$$

where the top line applies to translational coordinates, *i.e.* $\sigma \in \{1,2,3\}$, while the bottom line applies to rotational coordinates, *i.e.* $\sigma \in \{4,5,6,7\}$. Furthermore, $\{\alpha,\beta,\gamma\} \in \{1,2,3\}$, $\phi \in \{1,\ldots,7\}$ and Tr denotes the trace. The first three elements of this vector vanish identically when the matrix $\boldsymbol{\mu}^{v(\mathrm{b})}_{\tau(\mathrm{b})}$ is symmetric, as is the case when the mobility matrix is evaluated relative to the hydrodynamic center of the cluster, see Appendix 2.A.7. This selection of the body-based origin is assumed in Eq. (2.19). The last four elements of the vector contribute a displacement parallel to $\mathbf{q}$ to the rotational coordinates. Since this displacement is parallel to the constraint term $\lambda\mathbf{q}$ maintaining the unit length of $\mathbf{q}$, it will be eliminated by the constraint – thereby removing the need to determine the contribution of the divergence term to the rotational motion.

The metric g_Q or Jacobian $J_Q = g_Q^{1/2}$ is used to measure the (squared) volume of elements $d\mathbf{Q}$ in a general coordinate space. To determine the metric when using Cartesian coordinates $\mathbf{x}$ and quaternions $\mathbf{q}$ to describe a rigid body, we switch to the proportional mass-metric $M_Q = |\mathbf{M}_Q|$. The latter tensor relates the kinetic energy K to the generalized velocities, which for a rigid cluster with body-based density

distribution $\rho^{(\mathrm{b})}(\mathbf{r})$ reads as

$$K = \frac{1}{2}\dot{\mathbf{Q}}^{\mathrm{T}}\mathbf{M}_Q\dot{\mathbf{Q}} = \frac{1}{2}\int\left[\dot{\mathbf{x}} + \frac{\partial \mathbf{A}^{(\mathrm{s})}_{(\mathrm{b})}}{\partial \mathbf{q}}\dot{\mathbf{q}}\mathbf{r}\right]^2 \rho^{(\mathrm{b})}(\mathbf{r})d\mathbf{r}. \tag{2.56}$$

In the creeping flow limit, the mass distribution is irrelevant for the motion of the cluster. We therefore select a density such that the center of mass coincides with the origin of the body frame, the three eigenvectors of the inertia tensor are parallel to the axes of the body frame, and the three corresponding eigenvalues are identical. This renders the mass-metric block diagonal, combining a constant translational block with an orientation-dependent rotational block,

$$\left(\mathbf{M}_Q\right)_{\rho\sigma} \propto \frac{\partial\left(\mathbf{A}^{(\mathrm{s})}_{(\mathrm{b})}\right)_{\alpha\beta}}{\partial q_{\rho-4}}\frac{\partial\left(\mathbf{A}^{(\mathrm{s})}_{(\mathrm{b})}\right)_{\alpha\beta}}{\partial q_{\sigma-4}}, \tag{2.57}$$

with $\{\rho,\sigma\} \in \{4,5,6,7\}$. After some work follows

$$g_Q \propto M_Q \propto |\mathbf{q}|^8. \tag{2.58}$$

The resulting derivative of the metric entering the equation of motion, see Eqs. (2.12) and (2.13), is parallel to $\mathbf{q}$ and therefore is eliminated by the $\left(\mathbf{B}^{\dot{q}}_{(\mathrm{b})}\right)^{\mathrm{T}}$ in the mobility matrix, see Eq. (2.53).

The seven coordinates $\mathbf{Q}$ require, following Eq. (2.12), seven random displacements $\delta\mathbf{Q}$ for every time step. But the constraint of a unit length rotation vector $\mathbf{q}$ introduces a dependence that reduces the number of independent random displacements to six. These six are conveniently sampled in the body frame following Eq. (2.21), with the rotation and conversion in Eq. (2.19) resulting in seven coupled random displacements $\delta\mathbf{Q}$. One readily shows that these $\delta\mathbf{Q}$ obey the fluctuation dissipation theorem of Eq. (2.15), with the mobility matrix of Eq. (2.53).

The non-cancelling terms that are retained in Eq. (2.19), as well as the flow-induced alignment term in the penultimate term to that equation, result in rotational displacements perpendicular to $\mathbf{q}$. The quaternion vector therefore retains its length under infinitesimal time steps, but this length will gradually drift from the unit value under finite time steps. A constraint on the length is therefore included as the last term in Eq. (2.19), with the Lagrange multiplier solved by Eq. (2.18).

2.A.7. Hydrodynamic center

The values of the elements of the generalized mobility matrix will depend on the reference position $\mathbf{x}$ and the reference orientation used in the derivations of Section 2.2.1. For the Brownian Dynamics simulations it proves advantageous to identify the reference point with the hydrodynamic center of the cluster, *i.e.* the point that renders $\boldsymbol{\mu}^{v}_{\tau}$ and $\boldsymbol{\mu}^{\omega}_{f} = (\boldsymbol{\mu}^{v}_{\tau})^{\mathrm{T}}$ symmetric. A shift of the reference point from $\mathbf{x}$ to $\mathbf{x}' = \mathbf{x} + \Delta\mathbf{x}$ can be achieved without elaborate recalculation of the grand mobility matrix: by combining Eq. (2.10) with Eqs. (2.2), (2.7) and (2.8), it can be shown that the blocks of the shifted mobility matrix (on the l.h.s.) are related to their

non-shifted counterparts (on the r.h.s.) by

$$\boldsymbol{\mu}_f^v(\mathbf{x}') = \boldsymbol{\mu}_f^v + \boldsymbol{\mu}_\tau^v \boldsymbol{\varepsilon}_\Delta - \boldsymbol{\varepsilon}_\Delta \boldsymbol{\mu}_f^\omega - \boldsymbol{\varepsilon}_\Delta \boldsymbol{\mu}_\tau^\omega \boldsymbol{\varepsilon}_\Delta, \tag{2.59a}$$

$$\boldsymbol{\mu}_\tau^v(\mathbf{x}') = \boldsymbol{\mu}_\tau^v - \boldsymbol{\varepsilon}_\Delta \boldsymbol{\mu}_\tau^\omega, \tag{2.59b}$$

$$\boldsymbol{\mu}_\mathcal{E}^v(\mathbf{x}') = \boldsymbol{\mu}_\mathcal{E}^v - \boldsymbol{\varepsilon}_\Delta \boldsymbol{\mu}_\mathcal{E}^\omega + \boldsymbol{\varphi}(\Delta\mathbf{x}), \tag{2.59c}$$

$$\boldsymbol{\mu}_f^\omega(\mathbf{x}') = \boldsymbol{\mu}_f^\omega + \boldsymbol{\mu}_\tau^\omega \boldsymbol{\varepsilon}_\Delta, \tag{2.59d}$$

$$\boldsymbol{\mu}_f^\mathcal{S}(\mathbf{x}') = \boldsymbol{\mu}_f^\mathcal{S} + \boldsymbol{\mu}_\tau^\mathcal{S} \boldsymbol{\varepsilon}_\Delta - \boldsymbol{\psi}(\Delta\mathbf{x}), \tag{2.59e}$$

with $\boldsymbol{\varepsilon}_\Delta = \boldsymbol{\varepsilon}(\Delta\mathbf{x})$, while the remaining four blocks are unchanged. The shift to reach the hydrodynamic center is solved from

$$\Delta\mathbf{x} = \left[\boldsymbol{\mu}_\tau^\omega - \mathrm{Tr}\left(\boldsymbol{\mu}_\tau^\omega\right)1\right]^{-1} (\boldsymbol{\epsilon} : \boldsymbol{\mu}_\tau^v), \tag{2.60}$$

with Tr denoting the trace. This equation also locates the hydrodynamic center of the (6×6) mobility matrix [6]. Note, however, that the (6×6) and (11×11) mobility matrices obtained via the sequence of steps in the main text in the absence and presence of stress and strain terms, respectively, in general result in two distinct hydrodynamic centers for the same body.

References

[1] D. J. Jeffrey and Y. Onishi, *Calculation of the resistance and mobility functions for two unequal rigid spheres in low-reynolds-number flow,* J. Fluid Mech. **139**, 261 (1984).

[2] S. Kim and R. T. Mifflin, *The resistance and mobility functions of two equal spheres in low-reynolds-number flow,* Phys. Fluids **28**, 2033 (1985).

[3] S. Kim and S. J. Karrila, *Microhydrodynamics: Principles and Selected Applications*, Butterworth-Heinemann Series in Chemical Engineering (Butterworth-Heinemann, Stoneham, MA, U.S.A., 1991).

[4] L. Durlofsky, J. F. Brady, and G. Bossis, *Dynamic simulations of hydrodynamically interacting particles,* J. Fluid Mech. **180**, 21 (1987).

[5] I. M. Ilie, W. J. Briels, and W. K. den Otter, *An elementary singularity-free rotational brownian dynamics algorithm for anisotropic particles,* J. Chem. Phys. **142**, 114103 (2015).

[6] B. Carrasco and J. García de la Torre, *Hydrodynamic properties of rigid particles: comparison of different modeling and computational procedures,* Biophys. J. **76**, 3044 (1999).

3

Einstein viscosities of non-spherical colloids

A numerical study is presented on the intrinisic viscosity of sheared dilute suspensions of non-spherical Brownian colloidal particles. Simulations of oblate and prolate spheroids – with the dual aims of validating recently introduced schemes to simulate the motions and stresses of randomly-shaped colloids against theoretical predictions and vice versa of comparing theoretical predictions of the intrinsic viscosities at weak and strong Brownian noise against numerical results based on the same premises – yield good agreement over a wide range of aspect ratio. Numerical data are provided for intrinsic viscosities in the intermediate shear-thinning regime. Having established the correctness of the simulation approach, we also present numerical results on less symmetric particles, in particular spherical shells and helices. Also discussed is the drift of the latter body along the vorticity, due to its skewedness, with left- and right-handed helices moving in opposite directions.

3.1. Introduction

In his thesis, submitted in the *annus mirabilis* 1905, Einstein showed that the viscosity of a dilute suspension of spherical colloids increases proportional with the colloidal volume fraction at low Reynolds number [1, 2]. The extension of this result to non-spherical particles has attracted many researchers ever since. Jeffery analytically solved the periodic tumbling motion of spheroids – ellipsoidal particles with a rotational symmetry axis – in a simple shear flow, in the absence of Brownian motion [3]. This tumbling motion is common to particles of almost all shapes [4, 5]. Jeffery also determined the variation of the shear stress with the orientation of the particle, which led him to speculate that the stationary orientation distribution of the spheroid corresponds with the minimum rate of energy dissipa-

tion [3]. Because the Jeffery orbits are closed, the viscosity of a dilute solution of non-interacting particles is determined by the initial orientation of these particles. This peculiar dependence is broken, and memory of the initial distribution is lost, by deviations from these orbits induced by inertial effects and/or Brownian motion [6]. The combination of shear flow with Brownian motion involves constructing and solving a Fokker-Planck equation for the orientation distribution function, followed by an evaluation of the orientation-averaged stress. Two routes are taken in the literature, depending on the rotary Péclet number Pe, *i.e.* the ratio of the shear rate to the rotational diffusion coefficient. For low Pe, Burgers treated shear as a perturbation to the orientation Brownian motion, with the latter giving rise to a uniform distribution on the unit sphere [7]. Closely related expressions for the intrinsic viscosities of prolate and/or oblate spheroids were derived by Onsager [8], Simha [9], Kuhn and Kuhn [10], Giesekus [11] and Hinch and Leal [12]. For high Pe, Leal and Hinch treated Brownian motion as a perturbation to the Jeffrey orbit [12, 13] giving rise to a slow diffusion of the orbital coordinate, *i.e.* the constant of motion in Jeffery's solution that determines the shape of the orbit. To the best of our knowledge, there are no analytic solutions for the intermediate regime, for Pe of the order of unity, where shear-induced motion and Brownian motion are of comparable strength.

Experimental measurements on the intrinsic viscosity of suspension of Brownian particles show a surprising variation between different researchers, with values for supposedly identical systems varying by as much as an order of magnitude [14–18]. This indicates that the experiments are very sensitive to the prevailing conditions, including the Péclet and Reynolds numbers, polydispersity of the colloids, interactions between the colloids and interactions between the colloids and the suspending fluid. For rods and ellipsoidal colloids the quadratic scaling behaviour of the intrinsic viscosity B with the aspect ratio p is clearly borne out by the experimental data, $B \propto p^2$, while it is difficult to confirm the theoretical pre-factor $4/(15 \ln p)$.

Computer simulations provide an ideal testing ground for exploring theoretical models. The motion of spheroidal and ellipsoidal colloids in shear flows is attracting attention lately, with authors studying the impact of particle inertia [19, 20], of fluid inertia [21], or both inertias [22–25], of weak Brownian noise [26], to all of the above. The hydrodynamic contribution to the motions are either condensed in a resistance or mobility matrix rotating with the body, or in explicit solutions of time-varying flow and stress fields. Similar approaches have been applied to more complex rigid bodies, including two-bladed paddles [27], fractals of sticky particles [28], curved non-chiral fibers [29] and irregular particles with edges and holes [30]. The emphasis in most of these studies is on the dynamics of the particles, while some studies also explored the resulting intrinsic viscosities of dilute suspensions of these particles [26, 31–33].

We have recently shown that Brownian Dynamics simulations of isolated rigid bodies benefit greatly from describing the rotational motions in terms of unit-quaternions [34], *i.e.* a four-vector of unit length that enables expressing all elements of a rotation matrix in quadratic forms [35]. Several authors have exploited quaternions in BD simulations of colloids to avoid the divergencies occurring when using three ro-

tational coordinates, like the Euler angles or the components of the rotation vector [26]. Less appreciated is that quaternions have the additional advantages of eliminating both a metric tensor term associated with BD simulations in non-Cartesian coordinates and a mobility term associated with the orientation dependence of the mobility matrix [34, 36]. The latter cancellation occurs only if the orientation of the colloids are determined relative to the hydrodynamic center in the mobility picture [34]. This Brownian Dynamics scheme is briefly described in Section 3.2, along with the procedure to extract shear stresses from the simulations. Both are used in Section 3.3 to calculate the intrinsic viscosities of dilute suspensions of spheroids. The algorithm is validated against the aforementioned theoretical predictions at low and high Péclet numbers, and numerical data are provided covering the entire intermediate shear-thinning region for aspect ratios ranging from 1/100 to 100. Simulations are also presented of two less symmetric bodies, namely a spherical cap and a helix, with the former periodically bobbing up and down while tumbling in a shear flow and the latter converting the flow-induced rotational motion into a translational drift. The main conclusions are summarized in Section 3.4.

3.2. Theory

3.2.1. Brownian Dynamics

Consider a colloidal particle experiencing a force $\bar{\mathbf{f}}$ and a torque $\bar{\boldsymbol{\tau}}$ derived from a potential Φ while suspended in a newtonian fluid with a linear flow field,

$$\bar{\mathbf{v}}^{\infty}(\bar{\mathbf{r}}) = \bar{\mathbf{v}}_0^{\infty} + \bar{\bar{\mathbf{E}}}_{\infty}\bar{\mathbf{r}} + \bar{\boldsymbol{\omega}}_{\infty} \times \bar{\mathbf{r}}, \tag{3.1}$$

where $\bar{\mathbf{r}}$ denotes position, $\bar{\mathbf{v}}_0^{\infty}$ the flow velocity at the origin of the laboratory coordinate system, and where the strain rate $\bar{\bar{\mathbf{E}}}_{\infty}$ and the angular velocity $\bar{\boldsymbol{\omega}}_{\infty}$ are constant throughout the flow. In the Stokes approximation, the velocity $\bar{\mathbf{v}}$ and angular velocity $\bar{\boldsymbol{\omega}}$ of a colloid at position $\mathbf{x}$ are solved from

$$\begin{pmatrix} \bar{\mathbf{v}} - \bar{\mathbf{v}}^{\infty}(\bar{\mathbf{x}}) \\ \bar{\boldsymbol{\omega}} - \bar{\boldsymbol{\omega}}_{\infty} \\ \bar{\bar{\mathbf{S}}} \end{pmatrix} = \begin{pmatrix} \bar{\bar{\boldsymbol{\mu}}}_f^v & \bar{\bar{\boldsymbol{\mu}}}_\tau^v & \bar{\bar{\boldsymbol{\mu}}}_E^v \\ \bar{\bar{\boldsymbol{\mu}}}_f^\omega & \bar{\bar{\boldsymbol{\mu}}}_\tau^\omega & \bar{\bar{\boldsymbol{\mu}}}_E^\omega \\ \bar{\bar{\boldsymbol{\mu}}}_f^S & \bar{\bar{\boldsymbol{\mu}}}_\tau^S & \bar{\bar{\boldsymbol{\mu}}}_E^S \end{pmatrix} \begin{pmatrix} \bar{\mathbf{f}} \\ \bar{\boldsymbol{\tau}} \\ -\bar{\bar{\mathbf{E}}}_{\infty} \end{pmatrix}, \tag{3.2}$$

where $\bar{\bar{\mathbf{S}}}$ is minus the stress induced on the cluster by the fluid. The velocities result from a balance between the potential and flow driving the motion and friction – represented by the generalized mobility matrix $\boldsymbol{\mu}$ – opposing the motion. The stress is not the result of a balance, though it can be used in a balance for the deformation of non-rigid colloids. The generalized mobility matrices $\boldsymbol{\mu}$ of spherical and ellipsoidal bodies are tabulated in the literature [37], while those of more generally shaped rigid bodies can be constructed by either by the boundary element method [27, 38, 39] or by assuming the body composed of primary spherical particles [29, 34, 40, 41]. The latter approach is followed here; Appendix 3.A.1 provides a brief summary of the method, freely available on line as `Oseen11`[42]. A brief comment on notation: the bars in the above expression highlight that the generalized mobility

matrix combines matrices of various ranks; the bars will be omitted for convenience henceforth.

For a rigid body composed of multiple beads, the positions of the i^{th} bead in the space frame (s) are related to those in the body frame (b) by

$$\mathbf{x}_i^{(\mathrm{s})} = \mathbf{x} + \mathbf{A}_{(\mathrm{b})}^{(\mathrm{s})} \mathbf{r}_i^{(\mathrm{b})}, \tag{3.3}$$

where $\mathbf{A}_{(\mathrm{b})}^{(\mathrm{s})}$ is a rotation matrix and the origin of the body-based coordinate system maps onto the reference position of the cluster, $\mathbf{x}$. The generalized mobility matrix of the cluster is constant in the body-based frame and rotates with the body, *e.g.*

$$\mu_{f(\mathrm{s})\gamma}^{v(\mathrm{s})\alpha} = A_{(\mathrm{b})\kappa}^{(\mathrm{s})\alpha} \mu_{f(\mathrm{b})\mu}^{v(\mathrm{b})\kappa} A_{(\mathrm{s})\gamma}^{(\mathrm{b})\mu}, \tag{3.4a}$$

$$\mu_{\tau(\mathrm{s})\gamma}^{S(\mathrm{s})\alpha\beta} = A_{(\mathrm{b})\kappa}^{(\mathrm{s})\alpha} A_{(\mathrm{b})\lambda}^{(\mathrm{s})\beta} \mu_{\tau(\mathrm{b})\mu}^{S(\mathrm{b})\kappa\lambda} A_{(\mathrm{s})\gamma}^{(\mathrm{b})\mu}, \tag{3.4b}$$

$$\mu_{E(\mathrm{s})\gamma\delta}^{S(\mathrm{s})\alpha\beta} = A_{(\mathrm{b})\kappa}^{(\mathrm{s})\alpha} A_{(\mathrm{b})\lambda}^{(\mathrm{s})\beta} \mu_{E(\mathrm{b})\mu\nu}^{S(\mathrm{b})\kappa\lambda} A_{(\mathrm{s})\gamma}^{(\mathrm{b})\mu} A_{(\mathrm{s})\delta}^{(\mathrm{b})\nu}, \tag{3.4c}$$

where the Einstein convention of summing over repeated indices is implied. Hence, it suffices to perform one computationally intensive evaluation of the hydrodynamic interactions between all beads to arrive at the generalized mobility matrix in the body frame, which is then combined with cheap rotations to obtain the mobility of the body at arbitrary rotation in the space frame.

A colloidal particle suspended in a quiescent fluid will perform a Brownian motion. In terms of generalized coordinates $\mathbf{Q}$, the discretized equation of motion of a particle in a potential Φ reads as [43–45]

$$\Delta\mathbf{Q}(t) = \mathbf{Q}(t + \Delta t) - \mathbf{Q}(t) \tag{3.5a}$$

$$= -\boldsymbol{\mu}_Q \boldsymbol{\nabla}_Q \left(\Phi - \frac{1}{2} k_B T \ln g_Q \right) \Delta t \tag{3.5b}$$

$$+ k_B T \boldsymbol{\nabla}_Q \cdot \boldsymbol{\mu}_Q \Delta t + \delta\mathbf{Q},$$

where t denotes time, Δt the integration time step, k_B Boltzmann's constant, T the temperature, g_Q the metric of the coordinate space and $\delta\mathbf{Q}$ the Brownian displacements. The metric is explicitly included as it is required in simulations of the body's orientation in terms of Euler angles or a rotation vector [46–50]. In the last term, the Brownian displacements have zero mean and no memory of preceding steps (Markovian) while they are correlated by the fluctuation-dissipation theorem,

$$\langle \delta\mathbf{Q} \otimes \delta\mathbf{Q} \rangle = 2 k_B T \boldsymbol{\mu}_Q \Delta t. \tag{3.6}$$

Here it is tacitly assumed that the mobility matrix remains constant over the time step – for a coordinate-dependent mobility an additional displacement emerges, which is accounted for by the divergence term in Eq. (3.5b). A dependence of the mobility matrix on the rotation is evident for non-spherical bodies. Note that the mobility matrix $\boldsymbol{\mu}_Q$ is related to the space- (or body-) based mobility matrix by a transformation matrix that is derived by expressing the angular velocities in the

space (body) frame in terms of the generalized velocities $\dot{\mathbf{Q}}$ – this matrix diverges for certain combinations of Euler angles and requires L'Hôpital's rule for small rotation vectors. These complications are avoided when describing rotations in terms of quaternions, *i.e.* a four-vector $\mathbf{q}$, at the relatively minor effort of a length constraint, $|\mathbf{q}| = 1$. With this choice the transformation matrix is linear, see Appendix 3.A.2, while the gradient of the metric lies parallel to $\mathbf{q}$ and therefore cancels against the constraint [36]. Furthermore, if the origin of the body-based coordinate system coincides with the hydrodynamic mobility center, *i.e.* the point at which $\boldsymbol{\mu}_{\tau(\mathrm{b})}^{v(\mathrm{b})} = \boldsymbol{\mu}_{f(\mathrm{b})}^{\omega(\mathrm{b})}$, the divergence term vanishes identically from the equation of motion [34].

By combining the above expressions, one arrives at the equation of motion of a rigid Brownian colloid suspended in a flow and subject to a potential, [34]

$$\begin{pmatrix} \Delta\mathbf{x} \\ \Delta\mathbf{q} \end{pmatrix} = \begin{pmatrix} \mathbf{A}_{(\mathrm{b})}^{(\mathrm{s})} & \mathbf{0} \\ \mathbf{0} & \mathbf{B}_{(\mathrm{b})}^{\dot{q}} \end{pmatrix} \left[\begin{pmatrix} \boldsymbol{\mu}_f^v & \boldsymbol{\mu}_\tau^v & \boldsymbol{\mu}_E^v \\ \boldsymbol{\mu}_f^\omega & \boldsymbol{\mu}_\tau^\omega & \boldsymbol{\mu}_E^\omega \end{pmatrix}_{(\mathrm{b})}^{(\mathrm{b})} \begin{pmatrix} \mathbf{A}_{(\mathrm{s})}^{(\mathrm{b})}\mathbf{f}^{(\mathrm{s})} \\ \mathbf{A}_{(\mathrm{s})}^{(\mathrm{b})}\boldsymbol{\tau}^{(\mathrm{s})} \\ -\mathbf{A}_{(\mathrm{s})}^{(\mathrm{b})}\mathbf{E}_\infty^{(\mathrm{s})}\mathbf{A}_{(\mathrm{b})}^{(\mathrm{s})} \end{pmatrix} \Delta t + \begin{pmatrix} \delta\mathbf{x}^{(\mathrm{b})} \\ \delta\boldsymbol{\psi}^{(\mathrm{b})} \end{pmatrix} \right] + \begin{pmatrix} \mathbf{v}_\infty^{(\mathrm{s})} \\ \mathbf{B}_{(\mathrm{s})}^{\dot{q}}\boldsymbol{\omega}_\infty^{(\mathrm{s})} \end{pmatrix} \Delta t + \begin{pmatrix} \mathbf{0} \\ \lambda\mathbf{q} \end{pmatrix}, \tag{3.7}$$

with $\Delta\mathbf{x}$ and $\Delta\mathbf{q}$ the increments of the position and orientation, repectively, over a time step Δt at time t. Expressions for the rotation matrix in terms of quaternions, as well as for the corresponding matrices $\mathbf{B}_{(\mathrm{b})}^{\dot{q}}$ and $\mathbf{B}_{(\mathrm{s})}^{\dot{q}}$ to convert angular velocities to quaternion velocities, are provided in Appendix 3.A.2. The random displacements obeying the fluctuation-dissipation theorem are sampled using

$$\begin{pmatrix} \delta\mathbf{x}^{(\mathrm{b})} \\ \delta\boldsymbol{\psi}^{(\mathrm{b})} \end{pmatrix} = \sqrt{2k_B T\Delta t} \left[\begin{pmatrix} \boldsymbol{\mu}_f^v & \boldsymbol{\mu}_\tau^v \\ \boldsymbol{\mu}_f^\omega & \boldsymbol{\mu}_\tau^\omega \end{pmatrix}_{(\mathrm{b})}^{(\mathrm{b})} \right]^{1/2} \boldsymbol{\Theta}_{x\psi}, \tag{3.8}$$

where the square root of a symmetric matrix is again a symmetric matrix, and $\boldsymbol{\Theta}_{x\psi}$ represents a vector of six uncorrelated random numbers without memory. Because the columns of $\mathbf{B}_{(\mathrm{b})}^{\dot{q}}$ and $\mathbf{B}_{(\mathrm{s})}^{\dot{q}}$ are all perpendicular to $\mathbf{q}$, the length of the quaternion vector is conserved in the limit of infinitely small time steps. To conserve the length for a finite time step, a Lagrange multiplier λ is included as last term to the equation of motion. Denoting the quaternion vector after the unconstrained step by $\mathbf{q}^u$, the constraint condition

$$\left|\mathbf{q}(t+\Delta t)\right| = \left|\mathbf{q}^u(t+\Delta t) + \lambda\mathbf{q}(t)\right| = 1 \tag{3.9}$$

yields a readily solved quadratic expression in λ.

3.2.2. Stress

The stress in the fluid is derived from Eq. (3.2), whose bottom line provides an expression for minus the instantaneous hydrodynamic stress on a non-Brownian

cluster subjected to a potential and flow. To include the Brownian contribution, the Brownian displacements in the equation of motion are converted to Brownian forces and torques, yielding averages over the time step, to be added to the potential forces and torques in the stress expression. The time-average stress over the time step then reads as

$$\mathbf{S}^{(\mathrm{s})} = \boldsymbol{\mu}_{F(\mathrm{s})}^{S(\mathrm{s})} \left[\mathbf{F}^{(\mathrm{s})} + \frac{1}{\Delta t} \left(\boldsymbol{\mu}_{F(\mathrm{s})}^{\dot{Q}(\mathrm{s})} \right)^{-1} \delta \mathbf{Q}^{(\mathrm{s})} \right] - \boldsymbol{\mu}_{E(\mathrm{s})}^{S(\mathrm{s})} \mathbf{E}_{\infty}^{(\mathrm{s})} + k_B T \boldsymbol{\nabla}_Q \cdot \boldsymbol{\mu}_{F(\mathrm{s})}^{S(\mathrm{s})}, \tag{3.10}$$

3

where $\mathbf{Q}^{(\mathrm{s})} = (\mathbf{x}^{(\mathrm{s})}, \boldsymbol{\psi}^{(\mathrm{s})})$ represents the six coordinates in the space frame, with corresponding velocities $\dot{\mathbf{Q}}^{(\mathrm{s})}$, Brownian displacements $\delta\mathbf{Q}^{(\mathrm{s})}$ and forces $\mathbf{F}^{(\mathrm{s})}$. While the contribution of the Brownian displacements to the stress clearly averages out, the Brownian motion also gives rise to the non-vanishing last term in the expression. This subtle term results from correlations, within the timestep Δt, between the random displacements and the change of the mobility matric due to these displacements, as shown by Bossis and Brady [51]; their result in the resistance picture is re-expressed here in the mobility picture using Eq. (3.31). Since the mobilities are translationally invariant, the divergence reduces to the rotational contribution,

$$\boldsymbol{\nabla}_Q \cdot \boldsymbol{\mu}_{F(\mathrm{s})}^{S(\mathrm{s})} = \mathcal{R} \cdot \boldsymbol{\mu}_{\tau(\mathrm{s})}^{S(\mathrm{s})} = \mathbf{G}^{(\mathrm{s})}, \tag{3.11}$$

where $\mathcal{R}$ is the rotational operator [52, 53]. With $\boldsymbol{\mu}_{\tau(\mathrm{s})}^{S(\mathrm{s})}$ expressed in $\boldsymbol{\mu}_{\tau(\mathrm{b})}^{S(\mathrm{b})}$ and $\mathbf{A}_{(\mathrm{b})}^{(\mathrm{s})}$ by Eq. (3.4b), the divergence is evaluated as

$$\mathbf{G}^{(\mathrm{s})} = \mathbf{A}_{(\mathrm{b})}^{(\mathrm{s})} \mathbf{G}^{(\mathrm{b})} \mathbf{A}_{(\mathrm{s})}^{(\mathrm{b})}, \tag{3.12a}$$

$$G^{(\mathrm{b})\alpha\beta} = \epsilon_{\lambda}^{\alpha\kappa} \mu_{\tau(\mathrm{b})\kappa}^{S(\mathrm{b})\lambda\beta} + \epsilon_{\lambda}^{\beta\kappa} \mu_{\tau(\mathrm{b})\kappa}^{S(\mathrm{b})\alpha\lambda}, \tag{3.12b}$$

where $\mathbf{G}^{(\mathrm{b})}$ is constant in the body frame; the Levi-Civita symbol $\epsilon_{\gamma}^{\alpha\beta}$ equals $+1$ (-1) when α, β, γ is a cyclic (anti-cyclic) permutation of $1, 2, 3$ and equals zero otherwise. This result agrees with the Brownian stress traditionally derived from the 'effective thermodynamic force' $-\boldsymbol{\nabla}_Q k_B T \ln P$, with P the probability distribution along $\mathbf{Q}$. Combining the above steps, the stress is now evaluated in the body frame as

$$\begin{aligned} \mathbf{S}^{(\mathrm{b})} = &\begin{pmatrix} \boldsymbol{\mu}_f^S & \boldsymbol{\mu}_\tau^S & \boldsymbol{\mu}_E^S \end{pmatrix}_{(\mathrm{b})}^{(\mathrm{b})} \begin{pmatrix} \mathbf{A}_{(\mathrm{s})}^{(\mathrm{b})} \mathbf{f}^{(\mathrm{s})} \\ \mathbf{A}_{(\mathrm{s})}^{(\mathrm{b})} \boldsymbol{\tau}^{(\mathrm{s})} \\ -\mathbf{A}_{(\mathrm{s})}^{(\mathrm{b})} \mathbf{E}_{\infty}^{(\mathrm{s})} \mathbf{A}_{(\mathrm{b})}^{(\mathrm{s})} \end{pmatrix} + k_B T \mathbf{G}^{(\mathrm{b})} \\ &+ \frac{1}{\Delta t} \begin{pmatrix} \boldsymbol{\mu}_f^S & \boldsymbol{\mu}_\tau^S \end{pmatrix}_{(\mathrm{b})}^{(\mathrm{b})} \left[\begin{pmatrix} \boldsymbol{\mu}_f^v & \boldsymbol{\mu}_\tau^v \\ \boldsymbol{\mu}_f^\omega & \boldsymbol{\mu}_\tau^\omega \end{pmatrix}_{(\mathrm{b})}^{(\mathrm{b})} \right]^{-1} \begin{pmatrix} \delta\mathbf{x}^{(\mathrm{b})} \\ \delta\boldsymbol{\psi}^{(\mathrm{b})} \end{pmatrix}, \end{aligned} \tag{3.13}$$

where the displacements are identical to those in Eq. (3.7), followed by the transformation

$$\mathbf{S}^{(\mathrm{s})} = \mathbf{A}_{(\mathrm{b})}^{(\mathrm{s})} \mathbf{S}^{(\mathrm{b})} \mathbf{A}_{(\mathrm{s})}^{(\mathrm{b})} \tag{3.14}$$

to the space frame.

The presence of particles in the fluid affects the stress field in the fluid and thereby raises the viscosity of the pure fluid, η_0, to the effective viscosity of the suspension, η_s. A convenience way to express this impact is the Einstein coefficient or intrinsic viscosity B, defined by

$$\eta_s = \eta_0 (1 + B\phi), \tag{3.15}$$

where $\phi \ll 1$ denotes the volume fraction of particles. For a dilute suspension of rigid spherical colloids, Einstein derived the seminal result $B = 5/2$ [1, 2, 54]. By using that the viscosity is related to the average shear stress, one readily shows that

$$B = \frac{1}{\eta_0 v_c} \frac{\langle S_{xy}^{(s)} \rangle}{2E_{xy}^{\infty(s)}}, \tag{3.16}$$

where v_c denotes the volume of the colloid and $2E_{xy}^{\infty(s)} = \dot{\gamma}$ for simple shear.

3.2.3. Spheroids

For a non-Brownian spheroid of aspect ratio $p = L/D$, where L is the length and D the diameter, see Fig. 3.1, Jeffery analytically solved the orbit traced out by the symmetry axes as a function of time [3],

$$\tan\theta = C\left(\cos^2\chi + p^2\sin^2\chi\right)^{1/2}, \tag{3.17a}$$

$$\tan\phi = p\tan\chi, \tag{3.17b}$$

$$\chi = \kappa t = \frac{\dot{\gamma}}{p + (1/p)} t, \tag{3.17c}$$

where θ denotes the angle of the symmetry axes relative to the vorticity direction and ϕ the rotation angle around the vorticity axes, see Fig. 3.2, C is a constant of the motion determining the orbit, and where the revolution period, $\mathcal{T} = 2\pi/\kappa$, is equal for all orbits. A spheroid at $C = \infty$ is forever tumbling in the $\theta = \pi/2$ plane, its symmetry axis permanently perpendicular to the vorticity, with a variable angular velocity $\dot{\phi}$ that reaches minima (maxima) when the symmetry axis is parallel (perpendicular) to the flow direction. A spheroid at $C = 0$ performs a rotation around its symmetry axis, which is forever oriented along the vorticity direction. Intermediate values of C correspond to a 'kayaking' motion of the symmetry axis, see Fig. 3.2, with the spheroid simultaneously rotating around its symmetry axis (not shown). Jeffery also derived expressions for the instantaneous orientation-dependent Einstein coefficient of a spheroid, based on the excess work required in shearing the particle-laden fluid [3]. For a particle tumbling at constant $\theta = \pi/2$,

$$B(\phi) = \frac{4}{3v_c}\left(F\sin^2 2\phi + G\right), \tag{3.18}$$

where F and G are functions of the aspect ratio.

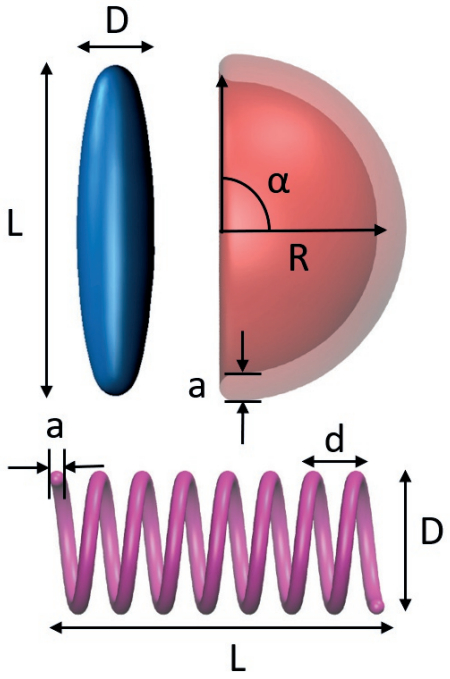

Figure 3.1: Pictorial representations of a prolate spheroid (blue) of length L and diameter $\varnothing$, a hemispherical cap (red) of radius R, thickness a and top angle α, and a helix (pink) of length L, diameter $\varnothing$ pitch d and thickness a.

In the presence of Brownian motion, the orbit parameter C is no longer conserved. For weak Brownian noise, $\mathrm{Pe} \to \infty$, Leal and Hinch [12, 13] assumed that the motion can be described by augmenting Jeffery's solution with a slow (compared to the tumbling period) diffusion of the orbit parameter C. The stationary orientation probability distribution then takes the form of a product,

$$P(C, \tilde{\chi}) = P_C(C) P_\chi(\tilde{\chi}|C), \tag{3.19}$$

where $P_\chi(\tilde{\chi}|C)$ denotes the conditional distribution of χ, mapped to its modulo $\tilde{\chi}$ in the $[0, \pi)$ interval, as obtained from an unperturbed Jeffery orbit at the given C. The stationary distribution across these orbits, $P_C(C)$, is solved from a Fokker-Planck equation by demanding that the average flux crossing any closed Jeffery orbit equals zero. In combination with Jeffery's expression for the excess work, the intrinsic viscosity is obtained as [13]

$$B = \begin{cases} 3.183 - 1.792p & \text{for} \quad p \to 0 \\ 2 + \dfrac{0.315p}{\ln(2p) - 1.5} & \text{for} \quad p \to \infty, \end{cases} \tag{3.20}$$

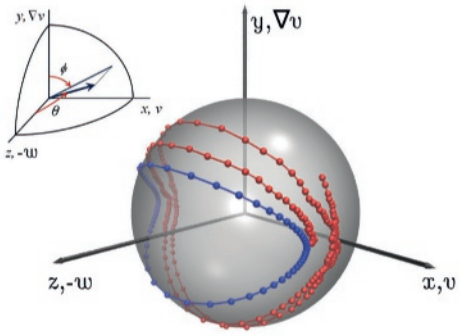

Figure 3.2: Orientation of the flow field relative to the coordinate system, with the flow velocity $\mathbf{v}_\infty$, the velocity gradient $\nabla\mathbf{v}_\infty$ and the vorticity $\mathbf{w}$ parallel to the x-axis, the y-axis and the (negative) z-axis, respectively. Also shown are the paths traced on the unit sphere (grey) by the symmetry axis of a non-Brownian (blue, $\mathrm{Pe} = \infty$) and a moderately Brownian (red, $\mathrm{Pe} = 3 \cdot 10^3$) prolate $p = 5$ spheroid suspended in this shear flow, with the dots denoting orientations at regular intervals in time. The symmetry axes moves slowest, and hence the impact of the Brownian motion is largest, when the axes is nearly flow-aligned.

with the limiting behaviour [12],

$$B = \begin{cases} 3.183 & \text{for} \quad p \to 0 \\ 0.315 \dfrac{p}{\ln p} & \text{for} \quad p \to \infty. \end{cases} \tag{3.21}$$

Since the numerical values in the published equations do not match, we took the liberty of selecting those values that agree best with the simulation results presented below.

In the opposite limit of strong Brownian noise, $\mathrm{Pe} \ll 1$, the orientation distribution in the angles θ and ϕ was assumed by Burgers [7] to be nearly isotropic, with the flow giving rise to a weak perturbation. Onsager [8], Simha [9], Kuhn and Kuhn [10], Giesekus [11] and Hinch and Leal [12] derived identical limiting expressions for the intrinsic viscosity,

$$B = \begin{cases} \dfrac{32}{15\pi} \dfrac{1}{p} & \text{for} \quad p \to 0 \\ \dfrac{4}{15} \dfrac{p^2}{\ln p} & \text{for} \quad p \to \infty. \end{cases} \tag{3.22}$$

To the best of our knowledge, there are no analytic solutions for intermediate Brownian noise, *i.e.* $\mathrm{Pe} \sim 1$.

3.3. Results

The equations of motion reviewed in the previous section now be applied to spheroids in Section 3.2.3 and to two more complex bodies – a hemi-spherical cap and he-

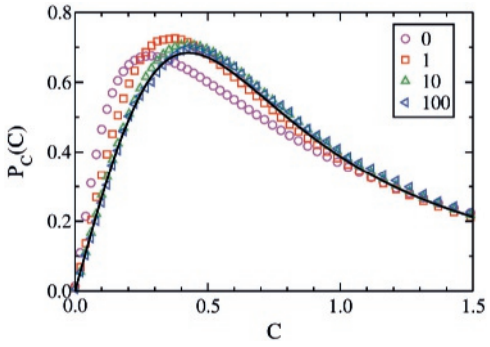

Figure 3.3: Probability distributions of the Jeffery orbit parameter C for prolate ellipsoids, $p = 5$, in simple shear flows at various Péclet numbers, see legend, and in a quiescent fluid ($\mathrm{Pe} = 0$). The solid line shows the theoretical prediction by Leal and Hinch.

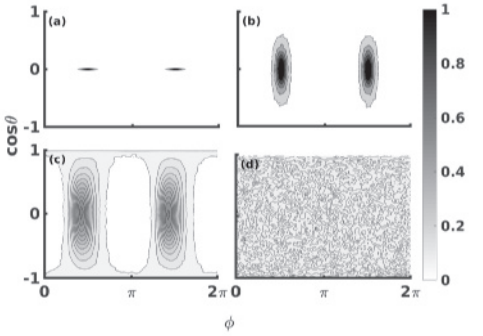

Figure 3.4: Distribution of the polar angles of spheroids in (a) a quiescent fluid, $\mathrm{Pe} = 0$, in sheared fluids at (b) $\mathrm{Pe} = 30$ and (c) $\mathrm{Pe} = 3000$, and (d) a spheroid in a Jeffery orbit at constant $\theta = \pi/2$ in a sheared fluid without thermal noise, $\mathrm{Pe} = \infty$. The selected projection turns an isotropic distribution into a uniform $P(\cos\theta, \phi) = 1/(4\pi)$.

lices, see Fig. 3.1 – in Section 3.3.2. The units used in these simulation are ϵ for the energy, σ for distance and τ for time. The imposed simple shear gives rise to a flow field $\mathbf{v}_\infty = \dot{\gamma} y \hat{\mathbf{e}}_x$, see Fig. 3.2, with a constant shear rate $\dot{\gamma} = 0.01\tau^{-1}$. The solvent viscosity is fixed at $\eta_0 = (6\pi)^{-1}\epsilon\tau/\sigma^3$. The Péclet number Pe is varied by changing the thermal energy, $k_B T$, and hence the strength of the Brownian noise.

3.3.1. Spheroids

3.3.1.1. Distributions

A typical path traced by an prolate spheroid at low Pe is shown in Fig. 3.2, where the kayaking motion of the particle is still recognizable while the superimposed diffusion of the orbit parameter results in a non-closed path. Distributions of the orbit parameter over long simulations are presented in Fig. 3.3 for a wide range of Pe, defined as $\mathrm{Pe} = \dot{\gamma}/D_r$ where the rotational diffusion coefficient D_r is obtained as

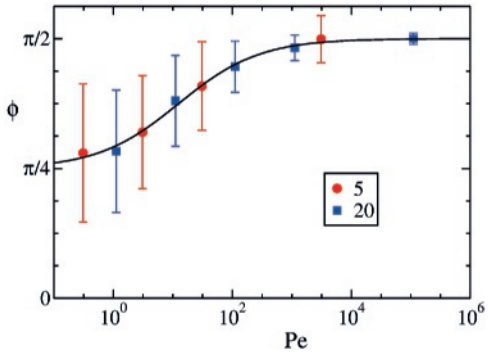

Figure 3.5: The location of the peaks in the orientation distribution, as determined by fitting with Eq. (3.23), plotted against the Péclet number, for aspect ratios of 5 and 20. The line is a guide to the eye.

$k_B T$ times the degenerate eigenvalue of $\boldsymbol{\mu}_\tau^\omega$. For large Pe the sampled distribution closely approximates the theoretical expression for $P_C(C)$ derived by Leal and Hinch [13]. Note, however, that the distribution at high Pe is very similar to that at $\mathrm{Pe} = 0$, as obtained for a spheroid in a quiescent fluid. The distribution of the polar angles reveals a much more pronounced impact of flow on orientation, see Fig. 3.4. In a quiescent fluid the spheroid samples an isotropic distribution, as expected for a Brownian particle, while a clear preference for the two flow-aligned orientations, $\theta = \pi/2$ and $\phi = \{\pi/2, 3\pi/2\}$, emerges with increasing Pe. The peaks shift and sharpen with Pe, as confirmed by fitting the sampled distributions with bivariate normal distributions,

$$P(\cos\theta, \phi) = a + b_1 e^{-c_1 \cos^2\theta - d_1(\phi-\phi_1)^2} + b_2 e^{-c_2 \cos^2\theta - d_2(\phi-\phi_2)^2}. \tag{3.23}$$

The locations of the peaks are plotted in Fig. 3.5 as a function of the Péclet number, for spheroids with aspect ratios of 5 and 20. At low Péclet the particles are seen to align along the direction of the elongation component of the flow field, while at high Péclet the particles align along the flow field itself, in accordance with the predictions by Burgers [7]. The widths of the peaks, as represented by the standard deviations $\sigma_\phi = (2d_i)^{-1/2}$, are indicated in the figure by error bars. One clearly sees a narrowing of the distribution with Péclet. The obtained agreement between the corresponding parameters of the two peaks (not shown) indicates that the distributions are well-sampled.

The simulations also permit an assessment of the impact of the Brownian motion on the tumbling period. Over a range of Péclet numbers, the increments and decrements of the angle ϕ were added up to count the numbers of revolutions during the simulations. For ease of interpretation, the angle θ was constrained to the value of $\pi/2$. In Fig. 3.6 the average tumbling periods are compared against the periods calculated by Jeffery's theory, *i.e.* in the absence of thermal noise. For $\mathrm{Pe} \gtrsim 1$

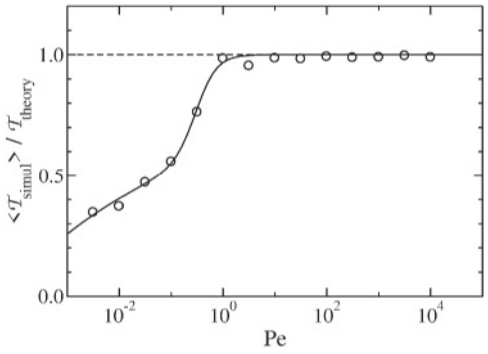

Figure 3.6: The ratio of the average tumbling period in the simulation to the theoretical tumbling period in the absence of noise, plotted against the Péclet number, for a spheriod with aspect ratio $p = 5$.

an excellent agreement is observed, indicating that the systematic tumbling motion dominates over the erratic Brownian motion. Lower Péclet numbers see a marked deviation from the theoretical period, with a drop in the average period. Notably, the Brownian motion consistently makes the particles perform a larger number of rotations than expected, in stead of merely inducing fluctuations around the expected number of rotations. This suggests that the flow field biases the Brownian motion, by acting as a ratchet that promotes rotation in the forward direction and hinders rotation in the reverse direction.

3.3.1.2. Viscosity

The instantaneous Einstein coefficients in non-Brownian simulations are shown in Fig. 3.7 to be in good agreement with Jeffery's expression, Eq. (3.18). The shear stress is at its lowest when the particle is slowly rotating through the flow aligned state, resulting in the broad minima in the figure, and when the particle is directed along the gradient direction and the rotational speed briefly matches the flow velocity, $\omega = \dot{\gamma}$, at the narrow minima. In these orientations, the value of B drops below the constant value of 5/2 for a sphere. The short-lived intermediate orientations are accompanied by a significant rise in the flow resistance, as here the orientation and velocity of the particle hamper the flow of the fluid around the particle.

Simulation results for the intrinsic viscosities of spheroidal colloids, over a wide range of aspect ratios and Péclet numbers, are collected in Figs 3.8. Both prolate and oblate colloids show pronounced shear-thinning, which increases with the deviation from the spherical shape, $p = 1$. The decrease of intrinsic viscosity with increasing Pe reflects the flow-induced alignment of the particles, see Fig. 3.4, which results in a reduction of the hindrance to the flow by the colloids, see Fig. 3.7. With increasing Péclet number, shear thinning starts at $\mathrm{Pe} \sim 1$, irrespective of the aspect ratio, and finishes at $\mathrm{Pe} \sim p^3$ (prolate) or $\mathrm{Pe} \sim p^{-3}$ (oblate). The plateau values at low Péclet, B_0, are plotted in Fig. 3.9 (left) as function of the aspect ratio. A clear minimum is reached for spherical colloids, with B_0 showing power law

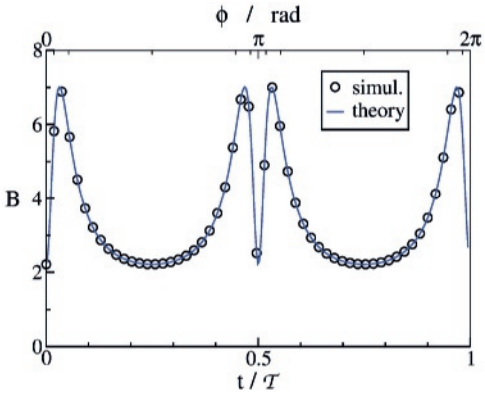

Figure 3.7: The instantaneous Einstein coefficient of a non-Brownian prolate spheroid ($p = 5$) tumbling in a simple shear flow at constant $\theta = \pi/2$, as functions of time (bottom axis) and rotation angle (top axis, with ticks at intervals of $\Delta\phi = \pi/6$). The simulation results (markers) are in good agreement with Jeffery's theory, Eqs. (3.17) and (3.18).

behaviour for both smaller and larger aspect ratios. The solid lines represent the theoretical predictions of Eq. (3.22), which are in excellent agreement with the simulations for $p \leq 10^{-1}$ and $p \geq 10^{1}$. The plateau values of the intrinsic viscosities at high Péclet, B_∞, are plotted in Fig. 3.9 (right) as function of the aspect ratio. For oblate spheroids a plateau value of about 2.5 is obtained from the fits to the shear-thinning curves (see below), while the simulations at the highest Pe indicate a slightly higher plateau value still below 3 – it should be noted that sampling configuration space, by diffusion of the orbit parameter C, becomes prohibitively slow for extreme aspect ratios at high Péclet numbers. After a shallow minimum for spheres, a power law growth of B_∞ with p sets in. The solid lines in the figure represent the theoretical predictions by Leal and Hinch [13], see Eq. (3.20), which are in good agreement with the simulations for $p \leq 10^{-1}$ and $p \geq 10^{1}$. The dashed lines denote their asymptotic predictions, Eq. (3.21), which are a good approximation for oblate spheroids at the smallest aspect ratios but for the prolate spheroid require aspect ratios much larger than those considered here.

The intrinsic viscosities in Fig. 3.8 are fitted very well with a variation on the Carreau model,

$$B(\mathrm{Pe}) = \frac{B_0 - B_\infty}{\left[1 + (\alpha \mathrm{Pe})^\beta\right]^\gamma} + B_\infty, \tag{3.24}$$

drawn as solid lines in that figure. The two fit parameters for the plateau heights, B_0 and B_∞, were discussed before. The obtained values for the scaling factor α and the powers β and γ are presented in Fig. 3.10. For the former a V-shaped profile is observed, with $\alpha \approx -0.13 \log p$ for $p < 1$ and $\alpha \approx 0.2 \log p$ for $p > 1$, where the tip of $\alpha = 0$ coincides with the absence of shear-thinning for a sphere. While the three coefficients clearly vary with p, their variations are fairly minor. The biggest fluctuations are seen for $1/10 \lesssim p \lesssim 10$, where the transition between the

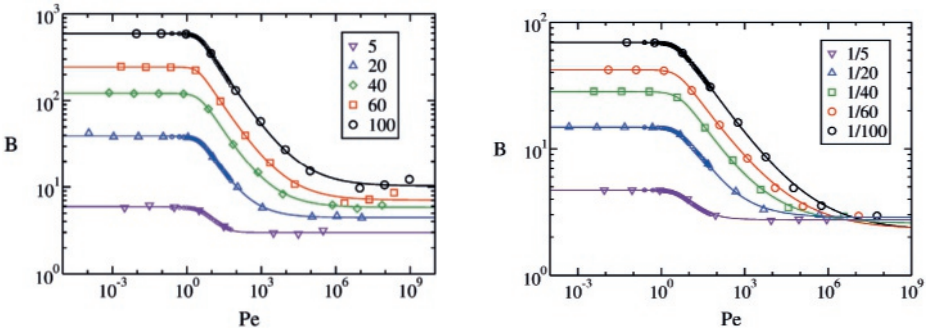

Figure 3.8: The intrinsic viscosity of dilute suspensions of prolate (left) and oblate (right) spheroids of various aspect ratios p, see legend, as functions of the Péclet number. The smooth lines are fits with Eq. (3.24), yielding the fit parameters plotted in Figs 3.9 and 3.10. Tiny markers for $0.25 \leq \mathrm{Pe} \leq 60$ represent numerical results by Scheraga [55].

two plateau values occurs within a relatively narrow range of Péclet numbers. The insensitivity to p suggests that the phenomenological formula of Eqs. (3.24), upon inserting B_0 and B_∞ read off from Fig. 3.9, α evaluated by the above expression, along with $\beta = 1.5$ and $\gamma = 0.3$, provides a reasonable approximation of the intrinsic viscosity for $100^{-1} \leq p \leq 100$. The resulting curves agree with the simulation results to within an order of magnitude in Pe. Of the four parameter variations on Eq. (3.24), the Carreau model ($\beta = 2$) and hemi-Carreau model ($\beta = 1$) both performing considerably better than the Cross model ($\gamma = 1$), especially in the sharp corner at the onset of shear-thinning, with the Carreau and hemi-Carreau models working best for prolate and oblate spheroids, respectively.

It is suggested in the literature that the intrinsic viscosity in the shear-thinning region follows a power law, $B \propto \mathrm{Pe}^{-\delta}$, with $\delta = 1/3$ [5, 12, 52, 56, 57]. Plots of the local powers extrated from the simulations reveal that, following the onset of shear-thinning, δ rises within one to two orders in Pe to a maximum that increases with p, barely reaching 0.3 for $p = 1/100$ and just passing 0.4 for $p = 100$, followed by a more gradual steady decay back to zero over many orders in Pe (data not shown). These peak closely match the products $\beta\gamma$ of the fitted powers in Eq. (3.24) at these two extremes, see Fig. 3.10. Since this product has approximately leveled off for $p = 1/100$ while it is slowly decaying for $p = 100$, the proposed $\delta = 1/3$ power law might still appear at far more extreme aspect ratios.

Figure 3.8 also shows the early electronic calculation by Scheraga [55], based on the theory by Saitô [58] combining a very slowly converging series of spherical harmonics for the orientation distribution function for near-spheres, due to Peterlin [59], with Jeffery's solution of the hydrodynamics around a spheroid. The numerical results, only available up to $\mathrm{Pe} = 60$, are in excellent agreement with the intrinsic viscosities from our simulations – for the dozen (Pe, p) combinations where both values are available – and with the fitted functions to the later.

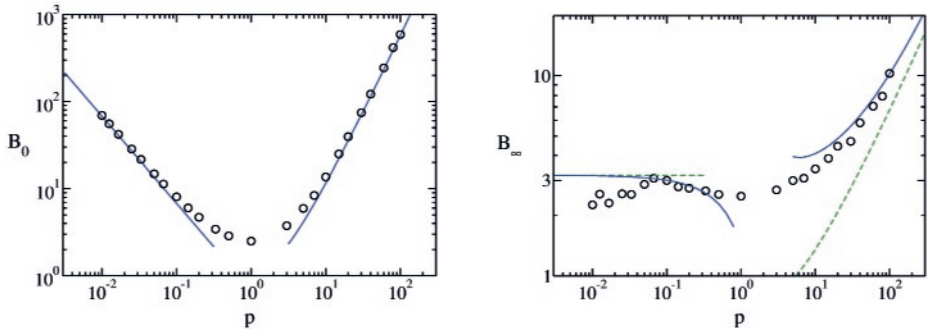

Figure 3.9: The plateau value of the intrinsic viscosity B in the low (left) and high (right) Péclet limit, see Figs 3.8 as a function of the aspect ratio p. The lines represent theoretical predictions, with Eqs. (3.22) and (3.21) as solid lines in the left and right plots, respectively, and Eq. (3.20) as dashed lines in the right plot.

3.3.2. Complex particle shapes

The methodology applied above to spheroids can also be used to colloids of more complex shapes. Where the generalized mobility matrix $\boldsymbol{\mu}$ of a sphere is block diagonal, a spheroid adds rotation-strain coupling, $\boldsymbol{\mu}_E^{\omega}$ and $\boldsymbol{\mu}_\tau^S$, a hemi-spherical cap adds translation-strain coupling, $\boldsymbol{\mu}_E^{v}$ and $\boldsymbol{\mu}_f^S$, and a helix adds rotation-translation coupling, $\boldsymbol{\mu}_\tau^{v}$ and $\boldsymbol{\mu}_f^{\omega}$, thus step by step filling in all nine blocks of the matrix. Analytic expressions for the generalized mobility matrices of spheres and spheroids can be found in textbooks; those for the hemi-spherical cap and the helix were determined numerically by considering the bodies as rigid collections of nearly-touching unit-radius spherical primary particles, with hydrodynamic interactions at the Rotne-Prager-Yamakawa level [60, 61], using the publicly available `Oseen11` code [42] as detailed in [34] and outlined in Appendix 3.A.1. We verified that application of this technique to hollow spheroidal-shaped aggregates yields good agreement with the intrinsic viscosities discussed above.

3.3.2.1. Hemi-spherical cap

The hemi-spherical cap, see Fig. 3.1, was selected as the first body beyond the spheroid because Dorrepaal [62] derived analytic expressions for its mobility in a simple shear flow. He showed that, on top of the spheroid-like tumbling orbits, a cap also exhibits translational orbits due to a lack of fore-aft symmetry. As shown in our previous work [34], the employed simulation method accurately capture this motion (in the absence of Brownian noise). The cap-like aggregate, with a top angle $\alpha = \pi/2$, was constructed by positioning 2051 primary particles on the cornerpoints of a triangulated mesh generated with the `DistMesh` routine [63] in `matlab` [64], resulting in a cap with radius $R \approx 47.8\sigma$. Simulation results are presented in Fig. 3.11. The Péclet number is again defined as $\mathrm{Pe} = \dot{\gamma}/D_r$ where the rotational diffusion coefficient D_r is obtained as k_BT times the degenerate eigenvalue of $\boldsymbol{\mu}_\tau^{\omega}$, while the colloidal volume is taken as $v_c = \frac{2}{3}\pi R^3$. The hemi-spherical

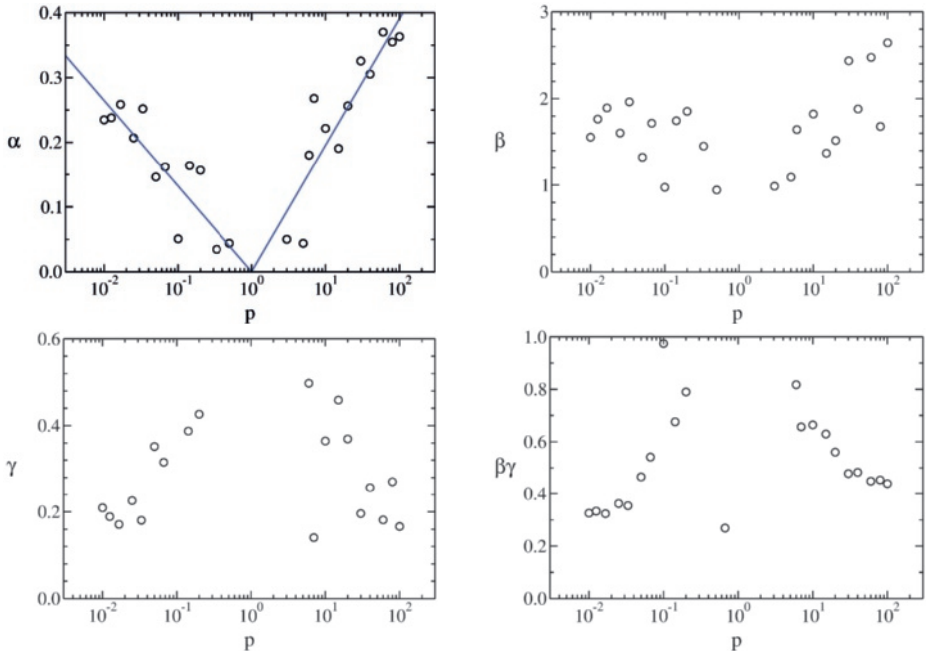

Figure 3.10: The scaling factor α (top-left) and the powers β (top-right) and γ (bottom-left) in Eq. (3.24), as obtained by fitting the intrinsic viscosities in Fig. 3.8, plotted as a function the aspect ratio, along with the product $\beta\gamma$ (bottom-right).

cap shows a weak shear-thinning because, at a length to width to height ratio of about 2:2:1, this colloid is fairly close to spherical.

3.3.2.2. Helix

Helices were modeled as a rigid collection of primary particles distributed along a spiral of diameter $\varnothing = 63.3\sigma$, see Fig. 3.1. A short helix of two revolutions comprised 201 particles, amounting to a length of $L = 41.8\sigma$, a long helix of 7.5 revolutions and 751 particles reached a length of $L = 158.3$. For both helices, left and right-handed versions were created. The simulation results are presented in Fig. 3.11. The Péclet number is again defined as $\mathrm{Pe} = \dot{\gamma}/D_r$ where the rotational diffusion coefficient D_r is now obtained as k_BT times the eigenvalue of $\boldsymbol{\mu}_\tau^\omega$ along the helix's long axis, and the volume as $v_c = \frac{1}{4}\pi\varnothing^2 L$. Since all four helices share aspect ratios $p = L/\varnothing$ fairly close to unity, they show modest shear thinning. The low values of the Einstein coefficients, relative to spheroids of similar aspect ratios, indicates that the impact of the helix on the surrounding and enclosed fluid is less than that of similarly-sized spheroids. The handedness of the helix appears to play no role, as evidenced from the near coalescence of the markers in Fig. 3.11.

The handedness does affect the motion of the helices, however, thereby providing a means of separation of chircal objects [65–67]. The motion of the mobility center of our long helix was studied in a simple shear flow without thermal noise,

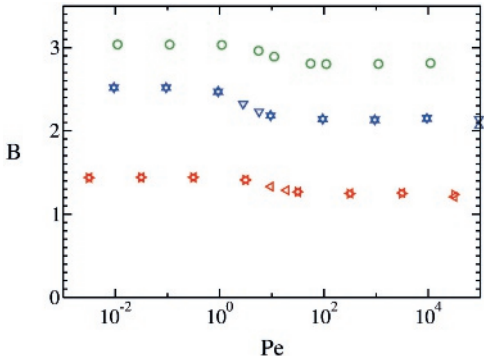

Figure 3.11: The Einstein coefficients of a hemi-spherical cap (circles), of two short helices (triangles pointing left and right for left and right-handedness, respectively) and of two long helices (triangles pointing up and down for left and right-handedness, respectively) as functions of the Péclet number.

for helices with their axis initially oriented parallel to the velocity, velocity-gradient and vorticity directions. After a transient time a periodic motion set in, with the axis typically performing a slight wobble around its original orientation; the curves in Fig. 3.12 are corrected to $\langle y \rangle = 0$, to suppress the motion along the flow direction. For helices initially oriented with their axes along the vorticity direction, we observe – as expected – drifts in the positive and negative vorticity direction (*i.e.* negative and positive z direction) for the right and left-handed helix, respectively. The drift velocity, however, is about two orders of magnitude smaller than the drift velocity for helices oriented in the flow plane and is therefore not discernible in Fig. 3.12 (bottom). The drift velocities are not constant; the variation is caused by the wobble of the axis for helices aligned along the vorticity direction and the tumbling motion of the axis for the helices aligned to the flow plane. Curiously, the orientations parallel and perpendicular to the vorticity direction result in opposite signs of the drift velocity, with the right-handed helix moving in the positive vorticity direction when oriented parallel to the vorticity, but in in the negative vorticity direction when oriented perpendicular to the vorticity. Simultaneously to this drift, the helix is periodically moving up and down along the velocity gradient, see Fig. 3.12 (top-right), and back and forth along the velocity direction, see Fig. 3.12 (top-left).

Whereas the axis of the long helix remains oriented approximately parallel to its initial orientation in a shear flow without thermal noise, the axis of the short helix fluctuates considerably more. Consequently, the long-term drift velocity along the vorticity direction gradually evolves, and may even change sign, as illustrated by two trajectories in Fig. 3.13. The motion periodically oscillates on the short time scale, as it also did for the long helix.

The dependence of the helix's drift on its initial orientation vanishes in the presence of Brownian noise. The averaged motion of the long helix along the vorticity direction is shown in Fig. 3.14, for a Péclet number near the start of the high Pe plateau; this value was selected as a computational feasible intermediate between a

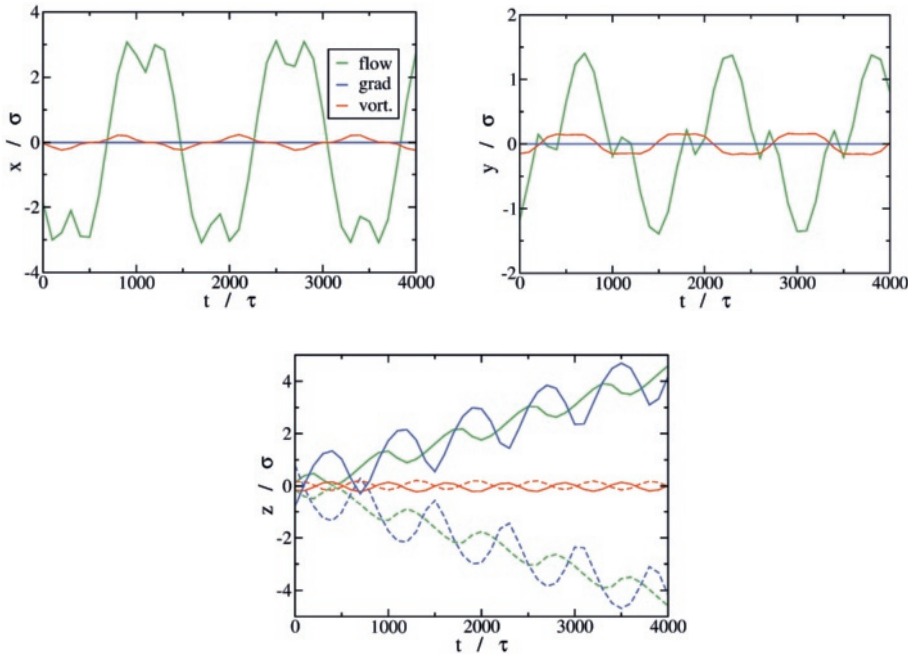

Figure 3.12: Motion of the hydrodynamic mobility center of the long helix under shear flow, in the absence of Brownian noise, along the flow velocity (x, top-left), velocity gradient (y top-right) and vorticity direction ($w = -z$, bottom), for right-handed (solid lines) and left-handed (dashed lines, only drawn when different from right-handed) helices with their axis initially aligned along the flow (green), gradient (red) or vorticity direction (blue).

shear-dominated motion along the vorticity direction and a diffusion-dominated motion along the gradient direction. The mean square displacement along y is linear, as is characteristic for diffusion. The diffusion coefficient closely matches (within 5%) the body-based translational mobilities $\boldsymbol{\mu}_f^v$ of the helix for motion perpendicular to the axis, as is to be expected for a helix that is predominantly flow-aligned. The mean square displacement along z approaches a quadratic curve, suggesting a systematic drift along that direction. The mean linear displacement along z indicates a systematic drift of the right-handed helix in the positive z direction, *i.e.* opposite to the vorticity direction, in agreement with the observations in Fig. 3.12 that a helix moving in the positive vorticity direction drifts far slower than a helix moving in the negative vorticity direction.

3.4. Summary and conclusions

A recently proposed efficient Brownian Dynamics scheme, utilizing quaternions for the rotational dynamics and taking advantage of the fixed body-based mobility matrix, has been used to simulate the dynamics of arbitrarily shaped colloids subjected

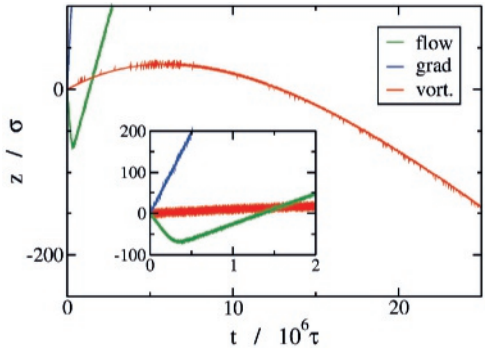

Figure 3.13: Motion of the hydrodynamic mobility center of the short helix under shear flow, in the absence of Brownian noise, along the vorticity direction ($w = -z$), for left-handed helices with their axis initially aligned along the flow velocity (green), velocity gradient (blue) or vorticity direction (red). The inset shows an enlargement of the initial dynamics.

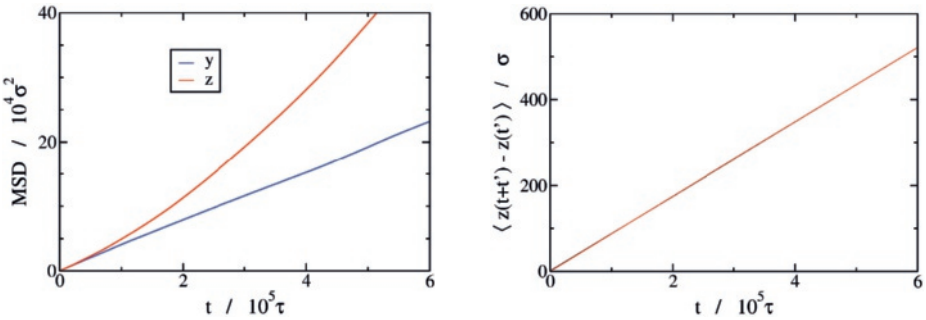

Figure 3.14: The mean square displacement (MSD, left) along the velocity-gradient y and vorticity z direction and the mean linear displacement along z (right), for the mobility center of the long right-handed helix in a simple shear flow, subject to relatively weak Brownian noise ($\mathrm{Pe} \approx 100$).

simultaneously to simple shear and Brownian motion. The calculated intrinsic viscosities for spheroids are in excellent agreement with theoretical predictions in the limits of high and low Péclet values, providing support for the validity of both theory and the employed simulation methodology. Intrinsic viscosities at intermediate Péclet values are well fitted with a modified Carreau model, providing a benchmark for future theories and experiments.

The motion of helices under shear flow was briefly explored. Counter intuitively, the drift along the vorticity direction is found to be dominated by a sideways motion of the helix, with the axis in the plane of the flow field, rather then by the screw-like motion with the axis directed along the vorticity direction. This may help explain the contradictory results reported in the experimental and simulation literature[68–70].

Acknowledgments

We thank Prof. Stefan Luding for stimulating discussions. This work is part of the 'Computational Sciences for Energy Research' program of the Netherlands Organisation for Scientific Research (NWO) under Project Nr. 13CSER060. This research programme is co-financed by Shell Global Solutions International B.V..

References

[1] A. Einstein, *Eine neue Bestimmung der Moleküldimensionen,* Ann. Phys. **19**, 289 (1906).

[2] A. Einstein, *Berichtigung zu meiner Abeit: "Eine neue Bestimmung der Moleküldimensionen",* Ann. Phys. **34**, 591 (1911).

[3] G. B. Jeffery, *The motion of ellipsoidal particles immersed in a viscous fluid,* Proc. Royal. Soc. London A **102**, 161 (1922).

[4] F. P. Bretherton, *The motion of rigid particles in a shear flow at low reynolds number,* J. Fluid Mech. **14**, 284 (1962).

[5] H. Brenner, *Rheology of a dilute suspension of axisymmetric brownian particles,* Int. J. Multiphase Flow **1**, 195 (1974).

[6] V. Dabade, N. K. Marath, and G. Subramanian, *The effect of inertia on the orientation dynamics of anisotropic particles in simple shear flow,* J. Fluid Mech. **791**, 631 (2016).

[7] J. M. Burgers, *On the motion of small particles of elongated form suspended in a viscous liquid,* in *Second Report on Viscosity and Plasticity* (Noord-Hollandsche Uitgeversmaatschappij, Amsterdam, The Netherlands, 1938) Chap. III, reprinted in [nieuwstadt2012selected].

[8] L. Onsager, *Viscosity and particle shape in colloid solutions,* Phys. Rev. **32**, 1028 (1940).

[9] R. Simha, *The influence of Brownian movement on the viscosity of solutions,* J. Phys. Chem. **44**, 25 (1940).

[10] W. Kuhn and H. Kuhn, *Die Abhängigkeit der Viskosität vom Strömungsgefälle bei hochverdünnten Suspensionen un Lösungen,* Helv. Chim. Acta **28**, 97 (1945).

[11] H. Giesekus, *Elasto-viskose Flüssigkeiten, für die in stationären schichtströmungen sämtliche Normalspannungskomponenten verschieden großsind,* Rheol. Acta. **2**, 50 (1962).

[12] E. J. Hinch and L. G. Leal, *The effect of brownian motion on the rheological properties of a suspension of non-spherical particles,* J. Fluid Mech. **52**, 683 (1972).

[13] L. G. Leal and E. J. Hinch, *The effect of weak brownian rotations on particles in shear flow,* J. Fluid Mech. **46**, 685 (1971).

[14] R. Rutgers, *Relative viscosity of suspensions of rigid spheres in Newtonian liquids,* Rheol. Acta. **2**, 202 (1962).

[15] R. Rutgers, *Relative viscosity and concentration,* Rheol. Acta. **2**, 305 (1962).

[16] A. M. Wierenga and A. P. Philipse, *Low-shear viscosity of isotropic dispersions of (Brownian) rods and fibres; a review of theory and experiments,* Coll. Surf. A **137**, 355 (1998).

[17] S. Mueller, E. W. Llewellin, and H. M. Mader, *The rheology of suspensions of solid particles,* Proc. Royal. Soc. A **466**, 1201 (2010).

[18] B. J. Konijn, O. B. J. Sanderink, and N. P. Kruyt, *Experimental study of the viscosity of suspensions: effect of solid fraction, particle size and suspending liquid,* Prowder Tech. **266**, 61 (2014).

[19] F. Lundell and A. Carlsson, *Heavy ellipsoids in creeping shear flow: transition of the particle rotation rate and orbit shape,* Phys. Rev. E **81**, 016323 (2010).

[20] J. Einarsson, J. R. Angilella, and B. Mehlig, *Orientational dynamics of weakly inertial axisymmetric particles in steady viscous flows,* Physica D **278-279**, 79 (2014).

[21] Z. Yu, N. Phan-Thien, and R. I. Tanner, *Rotation of a spheroid in a Couette flow at moderate Reynolds numbers,* Phys. Rev. E **76**, 026310 (2007).

[22] H. Huang, X. Yang, M. Krafczyk, and X.-Y. Lu, *Rotation of spheroidal particles in Couette flows,* J. Fluid Mech. **692**, 369 (2012).

[23] W. Mao and A. Alexeev, *Motion of spheroid particles in shear flow with inertia,* J. Fluid Mech. **749**, 145 (2014).

[24] T. Rosén, F. Lundell, and C. Aidun, *Effect of fluid inertia on the dynamics and scaling of neutrally buoyant particles in shear flow,* J. Fluid Mech. **738**, 563 (2014).

[25] T. Rosén, *Chaotic rotation of a spheroidal particle in simple shear flow,* Chaos **27**, 063112 (2017).

[26] G. Almondo, J. Einarsson, J. R. Angilella, and B. Mehlig, *Intrinsic viscosity of a suspension of weakly brownian ellipsoids in shear,* Phys. Rev. Fluids **3**, 064307 (2018).

[27] M. Makino and M. Doi, *Brownian motion of a particle of general shape in Newtonian fluids,* J. Phys. Soc. Japan **73**, 2739 (2004).

[28] Y. M. Harshe, L. Ehrl, and M. Lattuada, *Hydrodynamic properties of rigid fractal aggregates of arbitrary morphology,* J. Coll. Interf. Sci. **352**, 87 (2010).

[29] J. Wang, E. J. Tozzi, M. D. Graham, and D. J. Klingenberg, *Flipping, scooping, and spinning: drift of rigid curved nonchiral fibers in simple shear flow,* Phys. Fluids **24**, 123304 (2012).

[30] M. Daghooghi and I. Borazjani, *The effects of irregular shape on the particle stress of dilute suspensions,* J. Fluid Mech. **839**, 663 (2018).

[31] M. Makino and M. Doi, *Viscoelasticity of dilute solutions of particle of general shape,* J. Phys. Soc. Japan **73**, 3020 (2004).

[32] Y. M. Harshe and M. Lattuada, *Viscosity contribution of an arbitrary shape rigid aggregate to a dilute suspension,* J. Coll. Interf. Sci. **367**, 83 (2012).

[33] M. Daghooghi and I. Borazjani, *The influence of inertia on the rheology of a periodic suspension of neutrally bouyant rigid ellipsoids,* J. Fluid Mech. **781**, 506 (2015).

[34] D. Palanisamy and W. K. den Otter, *Efficient brownian dynamics of rigid colloids in linear flow fields based on the grand mobility matrix,* J. Chem. Phys. **148**, 194112 (2018).

[35] H. Goldstein, *Classical mechanics*, 2nd ed. (Addison-Wesley, Reading, MA, U.S.A., 1980).

[36] I. M. Ilie, W. J. Briels, and W. K. den Otter, *An elementary singularity-free Rotational Brownian dynamics algorithm for anisotropic particles,* J. Chem. Phys. **142**, 114103 (2015).

[37] S. Kim and S. Karrila, *Microhydrodynamics: Principles and Selected Applications*, Butterworth-Heinemann Series in Chemical Engineering (Butterworth-Heinemann, Stoneham, MA, U.S.A., 1991).

[38] S. Aragon, *A precise boundary element method for macromolecular transport properties,* J. Comput. Chem. **25**, 1191 (2004).

[39] S. Aragon, *Recent advances in macromolecular hydrodynamic modeling,* Methods **54**, 101 (2011).

[40] J. García de la Torre, G. del Rio Echenique, and A. Ortega, *Improved calculation of rotational diffusion and intrinsic viscosity of bead models for macromolecules and nanoparticles,* J. Phys. Chem. B **111**, 955 (2007).

[41] R. Kutteh, *Rigid body dynamics approach to stokesian dynamics simulations of nonspherical particles,* J. Chem. Phys. **132**, 174107 (2010).

[42] `https://www2.msm.ctw.utwente.nl/Oseen11/`.

[43] N. G. van Kampen, *Stochastic Processes in Physics and Chemistry* (revised and enlarged edition, Elsevier, Amsterdam, The Netherlands, 1992).

[44] H. C. Öttinger, *Stochastic Processes in Polymeric Fluids* (Springer-Verlag, Berlin, Germany, 1996).

[45] C. Gardiner, *Stochastic Methods. A handbook for the Natural and Social Sciences*, 4th ed., Springer Series in Synergetics (Springer-Verlag, Berlin, Germany, 2009).

[46] S. N. Naess and A. Elgsaeter, *Use of Cartesian rotation vectors in Brownian Dynamics algorithms: theory and simulation results,* Macromol. Theory Simul. **13**, 419 (2004).

[47] T. R. Evensen, A. Elgsaeter, and S. N. Naess, *Transient molecular electro-optics: Cartesian rotation vector versus eulerian angles,* Colloids Surf., B **56**, 80 (2007).

[48] T. R. Evensen, S. N. Naess, and A. Elgsaeter, *Free rotational diffusion of rigid particles with arbitrary surface topology: a Brownian Dynamics study using Eulerian angles,* Macromol. Theory Simul. **17**, 121 (2008).

[49] T. R. Evensen, S. N. Naess, and A. Elgsaeter, *Brownian Dynamics simulations of rotational diffusion using the Cartesian components of the rotation vector as generalized coordinates,* Macromol. Theory Simul. **17**, 403 (2008).

[50] T. R. Evensen, S. N. Naess, and A. Elgsaeter, *Use of the rotation vector in Brownian Dynamics simulation of transient electro-optical properties,* Macromol. Theory Simul. **18**, 50 (2009).

[51] G. Bossis and J. F. Brady, *The rheology of Brownian suspensions,* J. Chem. Phys. **91**, 1866 (1989).

[52] M. Doi and S. F. Edwards, *The Theory of Polymer Dynamics*, International Series of Monographs in Physics, 73 (Oxford Science Publishers, Oxford, U.K., 2013).

[53] J. K. G. Dhont, *An Introduction to Dynamics of Colloids*, Studies in Interface Science (Elsevier, Amsterdam, The Netherlands, 1996).

[54] E. Guazzelli and J. F. Morris, *A Physical Introduction to Suspension Dynamics*, Cambridge Texts in Applied Mathematics (Cambridge University Press, Cambridge, U.K., 2012).

[55] H. A. Scheraga, *Non-Newtonian viscosity of solutions of ellipsoidal particles,* J. Chem. Phys. **23**, 1526 (1955).

[56] W. E. Stewart and J. P. Sorensen, *Hydrodynamic interaction effects in rigid dumbbell suspensions. ii computations fotr steady shear flow,* Trans. Soc. Rheol. **16**, 1 (1972).

[57] P. Oswald, *Rheophysicsi. The deformation of flow and matter* (Cambridge University Press, Cambridge, U.K., 2009).

[58] N. Saitô, *The effect of the Brownian motion on the viscosity of solutions of macromolecules, i. ellipsoid of revolution,* J. Phys. Soc. Japan **6**, 297 (1951).

[59] A. Peterlin, *Über die Viskosität von verdünnten Lösungen und Suspensionen in Abhängigkeit von derTteilchenform,* Z. Physik **111**, 232 (1938).

[60] J. Rotne and S. Prager, *Variational treatment of hydrodynamic interaction in polymers,* J. Chem. Phys. **50**, 4831 (1969).

[61] H. Yamakawa, *Transport properties of polymer chains in dilute solution: hydrodynamic interaction,* J. Chem. Phys. **53**, 436 (1970).

[62] J. M. Dorrepaal, *The Stokes resistance of a spherical cap to translational and rotational motions in a linear shear flow,* J. Fluid Mech. **84**, 265 (1978).

[63] P.-O. Persson and G. Strang, *A simple mesh generator in matlab,* SIAM Rev. **46**, 329 (2004).

[64] MATLAB R2014a, The MathWorks Inc., Natick, MA, U.S.A. (2014).

[65] M. Makino and M. Doi, *Migration of twisted ribbon-like particles in simple shear flow,* Phys. Fluids **17**, 103605 (2005).

[66] S. Meinhardt, J. Smiatek, R. Eichhorn, and F. Schmid, *Separation of chiral particles in micro-or nanofluidic channels,* Phys. Rev. Lett. **108**, 214504 (2012).

[67] S. Ro, J. Yi, and Y. W. Kim, *Chiral separation by flows: The role of flow symmetry and dimensionality,* Sci. Rep. **6**, 35144 (2016).

[68] P. Chen and C.-H. Chao, *Lift forces of screws in shear flows,* Phys. Fluids **19**, 017108 (2007).

[69] Marcos, H. C. Fu, T. R. Powers, and R. Stocker, *Separation of microscale chiral objects by shear flow,* Phys. Rev. Lett. **102**, 158103 (2009).

[70] Q.-Y. Zhang, *Chirality-specific lift forces of helix under shear flows: Helix perpendicular to shear plane,* Chirality **29**, 97 (2017).

3.A. Appendices:

3.A.1. Mobility matrix

This appendix summarizes the derivation of the generalized mobility matrix of a rigid cluster of N primary identically sized spherical particles, as described in more detail in our previous work [1]. In the mobility picture, the hydrodynamic interactions couple every particle i with every particle j,

$$\begin{pmatrix} \bar{\mathbf{v}}_i - \bar{\mathbf{v}}^\infty(\bar{\mathbf{x}}_i) \\ \bar{\boldsymbol{\omega}}_i - \bar{\boldsymbol{\omega}}_\infty \\ -\bar{\bar{\mathbf{E}}}_\infty \end{pmatrix} = \sum_{j=i}^{N} \begin{pmatrix} \bar{\bar{\boldsymbol{\mu}}}_{f,j}^{v,i} & \bar{\bar{\boldsymbol{\mu}}}_{\tau,j}^{v,i} & \bar{\bar{\boldsymbol{\mu}}}_{S,j}^{v,i} \\ \bar{\bar{\boldsymbol{\mu}}}_{f,j}^{\omega,i} & \bar{\bar{\boldsymbol{\mu}}}_{\tau,j}^{\omega,i} & \bar{\bar{\boldsymbol{\mu}}}_{S,j}^{\omega,i} \\ \bar{\bar{\boldsymbol{\mu}}}_{f,j}^{E,i} & \bar{\bar{\boldsymbol{\mu}}}_{\tau,j}^{E,i} & \bar{\bar{\boldsymbol{\mu}}}_{S,j}^{E,i} \end{pmatrix} \begin{pmatrix} \bar{\mathbf{f}}_j \\ \bar{\boldsymbol{\tau}}_j \\ \bar{\bar{\mathbf{S}}}_j \end{pmatrix}. \tag{3.25}$$

Expressions for the various pair mobility matrices can be found in the literature [2–5]. The combination of variously sized matrices excludes the use of conventional rank two matrix manipulations, hence it proves convenient to reduce the strain and stress matrices to vectors. In the current case both the strain and the stress are symmetric and traceless, and hence can be reducud to five elements. The conversion of the strain is realized by rewriting the matrix as linear combinations of five (3×3) 'basis matrices' $\bar{\bar{\mathbf{e}}}_\kappa^E$,

$$\bar{\bar{\mathbf{E}}}_\infty = \sum_\kappa \bar{\bar{\mathbf{e}}}_\kappa^E \mathcal{E}_\infty^\kappa, \tag{3.26a}$$

$$\mathcal{E}_\infty^\kappa = \bar{\bar{\mathbf{e}}}_E^\kappa : \bar{\bar{\mathbf{E}}}_\infty, \tag{3.26b}$$

where the five parameters $\mathcal{E}_\infty^\kappa$ combine into the vector $\bar{\mathcal{E}}_\infty$ and the second line, with $\bar{\bar{\mathbf{e}}}_E^\kappa : \bar{\bar{\mathbf{e}}}_\lambda^E = \delta_\lambda^\kappa$ and δ the Kronecker-delta, provides the inverse transformation. A likewise conversion is used for the stress matrices $\bar{\bar{\mathbf{S}}}_j$, yielding the vectors $\bar{\mathcal{S}}_j$. The basis matrices need not be orthogonal, but it is recommendable to select $\bar{\bar{\mathbf{e}}}_\kappa^E = \bar{\bar{\mathbf{e}}}_S^\kappa$ in order to retain a symmetric grand mobility matrix. After re-expressing the grand mobility in terms of the strain and stress vectors, it reduces to a regular rank-two matrix and can be inverted by standard algorithms to yield

$$\begin{pmatrix} \mathbf{f}_i \\ \boldsymbol{\tau}_i \\ \mathcal{S}_i \end{pmatrix} = \sum_{j=1}^{N} \begin{pmatrix} \boldsymbol{\xi}_{v,j}^{f,i} & \boldsymbol{\xi}_{\omega,j}^{f,i} & \boldsymbol{\xi}_{\mathcal{E},j}^{f,i} \\ \boldsymbol{\xi}_{v,j}^{\tau,i} & \boldsymbol{\xi}_{\omega,j}^{\tau,i} & \boldsymbol{\xi}_{\mathcal{E},j}^{\tau,i} \\ \boldsymbol{\xi}_{v,j}^{\mathcal{S},i} & \boldsymbol{\xi}_{\omega,j}^{\mathcal{S},i} & \boldsymbol{\xi}_{\mathcal{E},j}^{\mathcal{S},i} \end{pmatrix} \begin{pmatrix} \mathbf{v}_j - \mathbf{v}_\infty(\mathbf{x}_j) \\ \boldsymbol{\omega}_j - \boldsymbol{\omega}_\infty \\ -\mathcal{E}_\infty \end{pmatrix}. \tag{3.27}$$

where the bars have been omitted. In the vector on the r.h.s., the velocities of and at the particles are related to the velocities of and at the cluster's center via the rigidity of the cluster and the linearity of the flow,

$$\mathbf{v}_j = \mathbf{v} + \boldsymbol{\omega} \times \mathbf{r}_j, \tag{3.28a}$$

$$\boldsymbol{\omega}_j = \boldsymbol{\omega}, \tag{3.28b}$$

$$\mathbf{v}_\infty(\mathbf{x}_j) = \mathbf{v}_\infty(\mathbf{x}) + \mathbf{E}^\infty \mathbf{r}_j + \boldsymbol{\omega}_\infty \times \mathbf{r}_j, \tag{3.28c}$$

where $\mathbf{r}_j = \mathbf{x}_j - \mathbf{x}$. In the vector on the l.h.s., the forces, torques and stresses on the particles can be summed into the total force, torque and stress on the cluster,

$$\mathbf{f} = \sum_{i=1}^{N} \mathbf{f}_i, \tag{3.29a}$$

$$\boldsymbol{\tau} = \sum_{i=1}^{N} \left(\boldsymbol{\tau}_i + \mathbf{r}_i \times \mathbf{f}_i\right), \tag{3.29b}$$

$$\mathbf{S} = \sum_{i=1}^{N} \left(\mathbf{S}_i + \mathbf{r}_i \otimes \mathbf{f}_i\right). \tag{3.29c}$$

By combining the above steps [1] one arrives at the grand resistance matrix of the cluster,

$$\begin{pmatrix} \mathbf{f} \\ \boldsymbol{\tau} \\ \mathcal{S} \end{pmatrix} = \begin{pmatrix} \xi_v^f & \xi_\omega^f & \xi_\mathcal{E}^f \\ \xi_v^\tau & \xi_\omega^\tau & \xi_\mathcal{E}^\tau \\ \xi_v^\mathcal{S} & \xi_\omega^\mathcal{S} & \xi_\mathcal{E}^\mathcal{S} \end{pmatrix} \begin{pmatrix} \mathbf{v} - \mathbf{v}_\infty(\mathbf{x}) \\ \boldsymbol{\omega} - \boldsymbol{\omega}_\infty \\ -\mathcal{E}_\infty \end{pmatrix}. \tag{3.30}$$

A partial inversion of the above expression, bringing the velocities to the left and the forces to the right, followed by a conversion back to stress and strain matrices, yields Eq. (3.2). Note that this partial inversion implies

$$\boldsymbol{\mu}_F^\mathcal{S} = \xi_\dot{Q}^\mathcal{S} \left(\xi_\dot{Q}^F\right)^{-1}, \tag{3.31}$$

as used in Eq. (3.10).

3.A.2. Quaternions

Unit quaternions, *i.e.* a four-vector $\mathbf{q} = (q_0, q_1, q_2, q_3)$ of unit length $q = |\mathbf{q}| = 1$, provide a convenient way to parameterize a rotation matrix in three dimensional space. The rotation matrix for the conversion from body-based to space-based coordinates reads as

$$\mathbf{A}_{(\mathrm{b})}^{(\mathrm{s})} = \begin{pmatrix} q_0^2 + q_1^2 - q_2^2 - q_3^2 & 2q_1q_2 - 2q_0q_3 & 2q_1q_3 + 2q_0q_2 \\ 2q_1q_2 + 2q_0q_3 & q_0^2 - q_1^2 + q_2^2 - q_3^2 & 2q_2q_3 - 2q_0q_1 \\ 2q_1q_3 - 2q_0q_2 & 2q_2q_3 + 2q_0q_1 & q_0^2 - q_1^2 - q_2^2 + q_3^2 \end{pmatrix}, \tag{3.32}$$

while the inverse conversion $\mathbf{A}_{(\mathrm{s})}^{(\mathrm{b})}$ is realized by the transposed of $\mathbf{A}_{(\mathrm{b})}^{(\mathrm{s})}$. A conversion matrix between angular velocities in the space frame and quaternion velocities is obtained by evaluating $\boldsymbol{\omega}^{(\mathrm{s})} \times \mathbf{x}^{(\mathrm{s})} = \dot{\mathbf{A}}_{(\mathrm{b})}^{(\mathrm{s})} \mathbf{A}_{(\mathrm{s})}^{(\mathrm{b})} \mathbf{x}^{(\mathrm{s})}$, which yields

$$\mathbf{B}_{(\mathrm{s})}^{\dot{q}} = \frac{\partial \dot{\mathbf{q}}}{\partial \boldsymbol{\omega}^{(\mathrm{s})}} = \frac{1}{2q^4} \begin{pmatrix} -q_1 & -q_2 & -q_3 \\ q_0 & q_3 & -q_2 \\ -q_3 & q_0 & q_1 \\ q_2 & -q_1 & q_0 \end{pmatrix}, \tag{3.33}$$

The conversion from an angular velocity in the body frame to a quaternion velocity can be derived likewise, yielding

$$\mathbf{B}^{\dot{q}}_{(\mathrm{b})} = \frac{\partial \dot{\mathbf{q}}}{\partial \boldsymbol{\omega}^{(\mathrm{b})}} = \frac{1}{2q^4}\begin{pmatrix} -q_1 & -q_2 & -q_3 \\ q_0 & -q_3 & q_2 \\ q_3 & q_0 & -q_1 \\ -q_2 & q_1 & q_0 \end{pmatrix}, \tag{3.34}$$

and can also be obtained from $\mathbf{B}^{\dot{q}}_{(\mathrm{b})} = \mathbf{B}^{\dot{q}}_{(\mathrm{s})}\mathbf{A}^{(\mathrm{s})}_{(\mathrm{b})}$.

References

[1] D. Palanisamy and W. K. den Otter, *Efficient brownian dynamics of rigid colloids in linear flow fields based on the grand mobility matrix,* J. Chem. Phys. **148**, 194112 (2018).

[2] D. J. Jeffrey and Y. Onishi, *Calculation of the resistance and mobility functions for two unequal rigid spheres in low-Reynolds-number flow,* J. Fluid Mech. **139**, 261 (1984).

[3] S. Kim and R. T. Mifflin, *The resistance and mobility functions of two equal spheres in low-Reynolds-number flow,* Phys. Fluids **28**, 2033 (1985).

[4] S. Kim and S. Karrila, *Microhydrodynamics: Principles and Selected Applications*, Butterworth-Heinemann Series in Chemical Engineering (Butterworth-Heinemann, Stoneham, MA, U.S.A., 1991).

[5] L. Durlofsky, J. F. Brady, and G. Bossis, *Dynamic simulations of hydrodynamically interacting particles,* J. Fluid Mech. **180**, 21 (1987).

4

Fluctuating stresslets and the viscosity of colloidal suspensions

Theory and simulation of Brownian colloids suspended in an implicit solvent, with the hydrodynamics of the fluid accounted for by effective interactions between the colloids, are shown to yield a marked and hitherto unobserved discrepancy between the viscosity calculated from the average shear stress under an imposed shear rate in the Stokesian regime and the viscosity extracted by the Green-Kubo formalism from the auto-correlations of thermal stress fluctuations in quiescent equilibrium. We show that agreement between both methods is recovered by accounting for the fluctuating Brownian stresses on the colloids, complementing and related to the traditional fluctuating Brownian forces and torques through an extended fluctuation-dissipation theorem based on the hydrodynamic grand resistance matrix. Time-averaging of the fluctuating terms gives rise to novel non-fluctuating stresslets. Brownian Dynamics simulations of spheroidal particles illustrate the necessity of these fluctuating and non-fluctuating contributions to obtaining consistent viscosities.

4.1. Introduction

Einstein derived in his thesis that adding rigid spherical colloids to a Newtonian fluid of viscosity η_0 creates a suspension of effective viscosity

$$\eta_s = \eta_0 (1 + B\phi), \tag{4.1}$$

with Einstein coefficient $B = 5/2$, for low colloidal volume fractions ϕ [1, 2]. This celebrated result, based on the analytic solution of Stokesian straining flow around

a spherical particle [3, 4], is readily reproduced by Brownian Dynamics (BD) simulations of an isolated spherical colloid suspended in a fluid subject to a linear shear flow. Viscosities can also be determined from quiescent fluids, using the Green-Kubo formalism of integrating the auto-correlations of the spontaneous stress fluctuations [5]. Rather surprisingly, both the aforementioned theory and BD simulations of an isolated spherical particle then yield $B = 0$, as will be demonstrated below. One might argue that this difference is an artefact of studying a one-particle system, which could be the reason that it appears not to have been discussed before in the literature, but we are of the opinion that it reveals a deficiency in the current understanding of stress calculations of suspensions of Brownian particles. We propose a solution, the inclusion of fluctuating Brownian stresses, that recovers agreement between equilibrium and non-equilibrium evaluations of the Einstein coefficient of a spherical particle, at $B = 5/2$. By expressing the stochastic equations for the motion and stress in the Itô form, two novel non-vanishing stress contributions emerge from correlations between the various fluctuations. These terms affect the Einstein coefficients of isolated non-spherical particles, both in quiescent fluids and in flowing fluids. The novel terms also contribute to the viscosities of non-dilute solutions, including suspensions of spherical particles [6, 7].

4.2. Brownian motion

Consider a non-Brownian particle with generalized velocity $\mathbf{U} = (\mathbf{v}, \boldsymbol{\omega})$, where $\mathbf{v}$ and $\boldsymbol{\omega}$ denote linear and angular velocity, respectively, in an incompressible fluid subject to a linear flow field characterized by the local generalized velocity $\mathbf{u}_\infty$ and the strain rate tensor $\mathbf{E}_\infty$, *i.e.* the traceless symmetric (3×3) velocity gradient matrix. In the limit of Stokesian flow, the generalized hydrodynamic force $\mathbf{F}_\mathrm{H}$, a vector comprizing three force components and three torque components, and the deviatoric hydrodynamic stress $\mathbf{S}_\mathrm{H}$, a traceless symmetric (3×3) matrix, acting on the particle are given by [3, 4, 8]

$$\begin{pmatrix} \mathbf{F}_\mathrm{H} \\ \mathbf{S}_\mathrm{H} \end{pmatrix} = -\begin{pmatrix} \boldsymbol{\xi}_U^F & \boldsymbol{\xi}_E^F \\ \boldsymbol{\xi}_U^S & \boldsymbol{\xi}_E^S \end{pmatrix} \begin{pmatrix} \mathbf{U} - \mathbf{u}_\infty \\ -\mathbf{E}_\infty \end{pmatrix}, \tag{4.2}$$

where $\boldsymbol{\xi}$ is the grand resistance matrix [3, 4], whose four parts are labeled with a lower index specifying the multiplication partner and an upper index highlighting the ensuing result. Upon neglecting inertial effects, the equation of motion for a colloid experiencing also a generalized potential-derived force $\mathbf{F}_\Phi$ and a fluctuating Brownian force $\delta\mathbf{F}$ is solved from a balance of forces, $\mathbf{F}_\Phi + \mathbf{F}_\mathrm{H} + \delta\mathbf{F} = \mathbf{0}$. A partial inversion of the above equation then gives [3, 4, 8]

$$\begin{pmatrix} \mathbf{U} \\ \mathbf{S} \end{pmatrix} = \begin{pmatrix} \boldsymbol{\mu}_F^U & \boldsymbol{\mu}_E^U \\ \boldsymbol{\mu}_F^S & \boldsymbol{\mu}_E^S \end{pmatrix} \begin{pmatrix} \mathbf{F}_\Phi + \delta\mathbf{F} \\ -\mathbf{E}_\infty \end{pmatrix} + \begin{pmatrix} \mathbf{u}_\infty \\ \mathbf{0} \end{pmatrix}, \tag{4.3}$$

where $\boldsymbol{\mu}$ is the generalized mobility matrix, again expressed as a combination of four labeled parts, and $\mathbf{S} = -\mathbf{S}_\mathrm{H}$ denotes the stress exerted on the fluid by the moving colloid. It is important to realize that the stress $\mathbf{S}$ is *not* the result of a balance of stresses, but a direct consequence of the velocity difference between colloid

and fluid. Should one desire so, for instance when studying easily deformable particles, a balance must be constructed between the total stress acting on the colloid – due to the hydrodynamic stress $\mathbf{S}_{\mathrm{H}}$, a potential-derived $\mathbf{S}_{\Phi}$ and Brownian contributions (as discussed below) – and the internal elastic stress of the particle $\mathbf{S}_{\mathrm{I}}$; after solving this balance for the unknown $\mathbf{S}_{\mathrm{I}}$, the combination thereof with the elasticity tensor of the colloid yields its deformation. We will here consider rigid particles instead, and note for completeness that their stress balances are closed by unspecified Lagrange multipliers for $\mathbf{S}_{\mathrm{I}}$ at vanishing deformation. The random force perturbations $\delta\mathbf{F}$ have zero mean, are uncorrelated in time (Markovian) and obey the classical fluctuation-dissipation theorem derived from the symmetric positive-definite (6×6) force-velocity segment of the resistance matrix [9, 10],

$$\langle \delta\mathbf{F}(t) \otimes \delta\mathbf{F}(t') \rangle = 2k_B T \boldsymbol{\xi}_U^F \delta(t - t'), \tag{4.4}$$

where t and t' denote times, k_B Boltzmann's constant, T the temperature and δ the Dirac delta function. The textbook proof of the fluctuation-dissipation theorem is its ability, in combination with a second-order Langevin equation of motion, to reproduce the Maxwell-Boltzmann equilibrium velocity distribution [5, 11]. Following the introduction of fluctuating hydrodynamics by Landau and Lifshitz [12, 13], several authors have shown that the above theorem for a colloid also follows from the fluctuation-dissipation theorem of the fluid [14–19]. Note that the force perturbations affect the velocity difference between colloid and fluid and thereby give rise to an indirect Brownian contribution to the stress [20], $\delta\mathbf{S}_{\delta\mathbf{F}} = \boldsymbol{\mu}_F^S \delta\mathbf{F}(t)$, as follows from Eq. (4.3).

For a free spherical particle of volume v in a linear shear flow, the above expressions give rise to the average stress $\langle \mathbf{S} \rangle = -\boldsymbol{\mu}_E^S \mathbf{E}_\infty$, where the minus sign indicates resistance to the flow. Inserting the theoretical expression for $\boldsymbol{\mu}_E^S$ [3, 4] then yields $B = 5/2$, as expected. But applying the Green-Kubo formalism to the spontaneous stress fluctuations $\Delta\mathbf{S}(t) = \mathbf{S}(t) - \langle \mathbf{S} \rangle$ in a quiescent fluid [5, 21],

$$B = \frac{1}{10 k_B T \eta_0 v} \int_0^\infty \langle \Delta\mathbf{S}(t) : \Delta\mathbf{S}(0) \rangle \, dt, \tag{4.5}$$

yields $B = 0$ for a spherical particle, as follows from observing that under these conditions $\Delta\mathbf{S}(t) = \delta\mathbf{S}_{\delta\mathbf{F}}(t) = \mathbf{0}$ since $\boldsymbol{\mu}_F^S = \mathbf{0}$ for a spherical particle. It is this disconcerting discrepancy between the B-s that motivates the current research.

4.3. Fluctuating Brownian stress

A suspended colloidal particle experiences a myriad of collisions due to the thermal motions of the surrounding solvent molecules. The sum over all collisions over a short time interval – sufficiently short to ignore the motion of the colloid, yet encompassing a large number of molecular collisions – gives rise to the fluctuating Brownian force $\delta\mathbf{F}(t)$ discussed above. Note that this generalized force comprises a force $\delta\mathbf{f}(t)$ and a torque $\delta\boldsymbol{\tau}(t)$, which represent distinct 'projections' of the same molecular noise integrated over the surface of the colloid [4, 8, 22]. Their common origin implies that the force and torque are correlated, as reflected by the

fluctuation-dissipation theorem in Eq. (4.4). It is only natural to assume that the collisions also give rise to a fluctuating Brownian stress on the particle, $\delta\mathbf{S}$, *i.e.* a stress distribution over the surface that would cause a soft particle to deform, which constitutes a third projection of the same molecular noise. This direct fluctuating Brownian stress $\delta\mathbf{S}$ is not to be confused with $\delta\mathbf{S}_{\delta\mathbf{F}}$, the latter being an indirect fluctuating stress resulting from a velocity difference between colloid and fluid caused by the first and second projections of the thermal noise. We next need to determine the strength of the fluctuating Brownian stress $\delta\mathbf{S}$, which in view of the preceding discussion does not follow from a stress balance on the particle. To conform with common practice in the field [3, 4], our interest here will be on the deviatoric parts of the stresses.

For any (non-Brownian) colloid experiencing a flow field, the hydrodynamic force acting on the particle is obtained as the zeroth moment of the traction vector integral over the surface while the torque and the stress or 'stresslet' on the particle are given by (a permutation of) the anti-symmetric and the symmetric first moments of the traction vector integral over the surface, respectively [4, 8, 22]. If this flow field is replaced by the fluctuating hydrodynamics of the fluid, the strengths of the resulting fluctuating Brownian force $\delta\mathbf{f}$ and torque $\delta\boldsymbol{\tau}$, as well as their cross-correlations, are given by the fluctuation dissipation theorem of Eq. (4.4). We now hypothesize that the fluctuations of $\delta\mathbf{F}$ and $\delta\mathbf{S}$, given their common origin as projections of fluctuating hydrodynamics, are related by a generalized fluctuation-dissipation theorem based on the grand resistance matrix,

$$\left\langle \begin{pmatrix} \delta\mathbf{F}(t) \\ \delta\mathbf{S}(t) \end{pmatrix} \otimes \begin{pmatrix} \delta\mathbf{F}(t') \\ \delta\mathbf{S}(t') \end{pmatrix} \right\rangle = 2k_BT \begin{pmatrix} \boldsymbol{\xi}_U^F & \boldsymbol{\xi}_E^F \\ \boldsymbol{\xi}_U^S & \boldsymbol{\xi}_E^S \end{pmatrix} \delta(t-t'). \tag{4.6}$$

Whereas the force correlations in this expression are well established [14–19], the stress correlations and the force-stress cross-correlations have attracted little attention. A recent study supports the validity of our assumption for spherical particles, however without providing an explicit expression [19]. Introducing the fluctuating stresslet into Eq. (4.3) gives the extended expression for the motion and the stress,

$$\begin{pmatrix} \mathbf{U} \\ \mathbf{S} \end{pmatrix} = \begin{pmatrix} \boldsymbol{\mu}_F^U & \boldsymbol{\mu}_E^U \\ \boldsymbol{\mu}_F^S & \boldsymbol{\mu}_E^S \end{pmatrix} \begin{pmatrix} \mathbf{F}_\Phi + \delta\mathbf{F} \\ -\mathbf{E}_\infty \end{pmatrix} + \begin{pmatrix} \mathbf{u}_\infty \\ \delta\mathbf{S} \end{pmatrix}. \tag{4.7}$$

It is evident that this expression produces identical translational and rotational Brownian motion to the classical expression, even though the fluctuating force is now correlated to the fluctuating stresslet. With the inclusion of the fluctuating stresslet, the analytic calculations of the viscosity for an isolated force-free rigid spherical particle under equilibrium and non-equilibrium conditions are now in agreement, both yielding $B = 5/2$ (and this result is unaffected by the full derivation below).

The interpretation of the stochastic differential equation of motion, Eq. (4.7), requires further attention to resolve an ambiguity: the impact of the Brownian force, as determined by the resistance matrix in the fluctuation-dissipation theorem and the mobility matrix in the equation of motion, varies with the coordinates $\mathbf{Q}$ of the particle, while the coordinates change due to this Brownian force. In the Itô

interpretation, *i.e.* using only parameter values at time t just before the impact of the Brownian force, the integration of the equation of motion over a time step Δt results in coordinate increments [23]

$$\begin{aligned}\Delta\mathbf{Q}(t) &= \mathbf{Q}(t+\Delta t) - \mathbf{Q}(t)\\ &= -\boldsymbol{\mu}_F^U \boldsymbol{\nabla}_Q\left(\Phi - \ln g_Q^{1/2}\right)\Delta t - \boldsymbol{\mu}_E^U \mathbf{E}_\infty \Delta t\\ &\quad + \mathbf{u}_\infty \Delta t + k_B T \boldsymbol{\nabla}_Q \cdot \boldsymbol{\mu}_F^U \Delta t\\ &\quad + \boldsymbol{\mu}_F^U \left[\boldsymbol{\rho}_U^F \boldsymbol{\Theta}^U(t) + \boldsymbol{\rho}_E^F \boldsymbol{\Theta}^E(t)\right]\sqrt{\Delta t},\end{aligned} \tag{4.8}$$

where g_Q denotes the metric of the coordinate space, $\boldsymbol{\rho}$ is the symmetric tensor solving $\boldsymbol{\rho}^2 = 2\pi k_B T \boldsymbol{\xi}$, and $\boldsymbol{\Theta}^U(t)$ and $\boldsymbol{\Theta}^E(t)$ are random vectors with zero mean, unit variance and devoid of correlations, containing six and five unique elements, respectively. The divergence term brings into account the coordinate-dependence of the hydrodynamic matrices [9, 11, 24, 25]; these additional displacements are not evident from Eq. (4.7) but are crucial to obtaining the equilibrium Boltzmann distribution and, as will be shown below, also contribute to the stress. An alternative interpretation, due to Einstein, gave rise to the name 'thermodynamic force' [4, 26, 27].

On a technical note, since in the current context the stress and strain rate tensors are symmetric and traceless (3×3) matrices, it proves convenient to replace both by five-vectors so the usual mathematical and numerical techniques can be applied to the resulting symmetric (11×11) hydrodynamic matrices [3, 28]. Because the hydrodynamic matrices and the conservative potential are typically expressed in terms of Cartesian velocities and Cartesian forces, and in angular velocities and torques around Cartesian axes, we furthermore take the freedom of evaluating the r.h.s. of Eqs. (4.7) and (4.8) in Cartesian coordinates, henceforth collectively denoted as $\mathbf{X}$. Since the Cartesian angular velocities are not time derivatives of angular coordinates, the rotation angle increments still require transformation to proper generalized coordinates $\mathbf{Q}$ describing the orientation of the colloid in terms of *e.g.* Euler angles or quaternions, or one may directly update the rotation matrix between the colloid-based axes frame and the space-based axes frame. The latter two options have the advantage that they do not require corrections resulting from the metric. [28–30].

Continuing in the Itô representation, we find by some mathematical manipulations of Eqs. (4.6) through Eq. (4.8) that the average stress exerted by the colloid

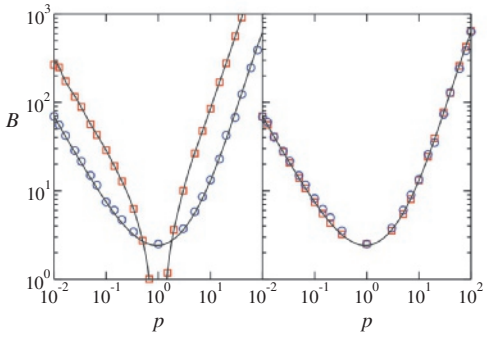

Figure 4.1: Einstein viscosity coefficients B for isolated rigid spheroidal particles of various aspect ratio p, as deduced from the average stress in simulations at low shear rate (blue circles) and the stress fluctuations at zero shear (red squares). Simulations based on the classical stress calculation of Eq. (4.3) show a marked difference between the two approaches (left), while the revisions proposed in Eq. (4.7) recover agreement (right). The smooth lines are guides to the eye.

on the fluid during a time step Δt reads as [23]

$$\begin{aligned}\bar{\mathbf{S}}(t) &= \frac{1}{\Delta t}\int_{t}^{t+\Delta t}\mathbf{S}(t')dt' \\ &= \boldsymbol{\mu}_F^S\mathbf{F}_\Phi - \boldsymbol{\mu}_E^S\mathbf{E}_\infty + \boldsymbol{\nabla}_X\cdot\boldsymbol{\mu}_F^S \\ &\quad + \left[\left(\boldsymbol{\nabla}_X\boldsymbol{\rho}_U^S\right)\boldsymbol{\rho}_U^F + \left(\boldsymbol{\nabla}_X\boldsymbol{\rho}_E^S\right)\boldsymbol{\rho}_E^F\right] : \boldsymbol{\mu}_F^U \\ &\quad + \frac{1}{\sqrt{\Delta t}}\Big\{\boldsymbol{\mu}_F^S\left[\boldsymbol{\rho}_U^F\boldsymbol{\Theta}^U(t) + \boldsymbol{\rho}_E^F\boldsymbol{\Theta}^E(t)\right] \\ &\qquad + \boldsymbol{\rho}_U^S\boldsymbol{\Theta}^U(t) + \boldsymbol{\rho}_E^S\boldsymbol{\Theta}^E(t)\Big\}.\end{aligned} \tag{4.9}$$

The first and second term on the r.h.s. are the two deterministic contributions to Eq. (4.7). The third term, usually derived along another route, results here by combining a term related to the divergence in Eq. (4.8) with a term resulting from correlations between $\delta\mathbf{F}$ and $\delta\mathbf{S}_{\delta\mathbf{F}}$, and is referred to in the literature as 'Brownian stress' or 'diffusion stress' [7, 20, 31, 32]. The fluctuating terms, collected between curly brackets in the last term to Eq. (4.9), have zero average and may therefore be ignored when calculating the time-averaged stress of a system under shear flow, but their correlations are crucial when applying the Green-Kubo formalism to a quiescent system. In both non-equilibrium and equilibrium cases, the time-averaged correlations of the fluctuating forces and the fluctuating stresslets give rise to two additional non-fluctuating stress contributions, the two $\boldsymbol{\nabla}_X\boldsymbol{\rho}_\circ^S$ terms in Eq. (4.9), which, to the best of our knowledge, are derived and reported here for the first time.

4.4. Numerical example

As an illustration of the revised stress calculation, we present numerical simulations of isolated spheroidal particles. For a rigid particle, the hydrodynamic matrices are

constant in the body frame and rotate with the body in the space frame, which permits efficient calculations of the motion and the stress without demanding re-evaluation of the hydrodynamics [28–30]. With $\mathbf{A}$ denoting the body-to-space rotation matrix, the three derivative-containing terms in Eq. (4.9) turn out to be of the form $\mathbf{AGA}^{\mathrm{T}}$, where $\mathbf{G}$ is a body-dependent constant (3×3) matrix and the superscript T indicates transposition. Simulations of a spherical particle confirm the theoretical results mentioned above, with the classical approach of Eq. (4.3) yielding Einstein coefficients of 5/2 under shear and zero by the Green-Kubo method, while the amendments proposed here yield $B = 5/2$ for both non-equilibrium and equilibrium simulations. Numerical results for the Einstein coefficients of spheroidal particles are presented in Fig. 4.1 as function of the aspect ratio $p = L/D$ between the length L along the symmetry axis and the diameter D in the perpendicular direction, ranging from disk-like oblate to needle-like prolate. For simulations based on Eq. (4.3), applying the Green-Kubo formalism to quiescent systems yields Einstein coefficients between four ($p \ll 1$) and eight ($p \gg 1$) times higher than the values obtained from the average stress in sheared systems, with an intermediate dip of B approaching zero for near-spherical particles. Simulations based on Eq. (4.7), however, show consistency between equilibrium and non-equilibrium viscosity evaluations, see Fig. 4.1. The biggest difference between the classical and the proposed methods is in the Einstein coefficients deduced from the thermal stress fluctuations in quiescent fluids, and mainly results from the inclusion of the Brownian fluctuating stress in Eq. (4.9). The two novel $\boldsymbol{\nabla}_X \boldsymbol{\rho}^S_\circ$ terms in said expression introduce a relatively modest increase of the Einstein coefficient obtained under shear, by about 1% at $p = 20$ and 5% at $p = 100$. The impact of these terms is larger for less symmetric bodies, amounting to about $+10\%$ for a semi-disk with diameter-to-thickness ratio of 40 and about -8% for a helix inscribing 7.5 revolutions in a cylinder with a length-to-diameter ratio of five.

4.5. Conclusions

The perpetual thermal motion of fluids contributes to the viscosity of colloidal suspensions, both by causing the Brownian motion of the colloids and by inducing flucuating stresses on the colloids. Inclusions of these Brownian stresses, absent in current theoretical and numerical implicit solvent methods for suspensions, is therefore necessary to obtain the correct viscosity. Our theoretical analysis of dilute suspensions of spherical particles and numerical simulations of spheroids illustrate the validity of the amendments proposed in the Brownian motion and stress calculation of Eq. (4.7) and the extended fluctuation-dissipation theorem of Eq. (4.6). Correlations between the various fluctuating terms then give rise to novel non-fluctuating contributions in the Itô representation of the stress, see Eq. (4.9). A more detailed exposition of the derivations outlined above, along with additional numerical results on colloids of various shapes, will be presented elsewhere [23]. The expression for the time-averaged stresslet on a colloid is readily extended to a collection of N particles, by enlarging the mobility and resistance matrices to $(11N \times 11N)$ matrices including hydrodynamic interactions between all colloids; the total deviatoric stress in the system is then obtained by adding up the stresslets of the individual particles,

the virial term due to generalized conservative forces on the colloids, and the shear resistance of the suspending fluid.

Acknowledgments

We thank Prof. Stefan Luding for stimulating discussions. This work is part of the Computational Sciences for Energy Research Industrial Partnership Programme co-financed by Shell Global Solutions B.V. and the Netherlands Organisation for Scientific Research (NWO).

References

[1] A. Einstein, *Eine neue Bestimmung der Moleküldimensionen,* Ann. Phys. **19**, 289 (1906).

[2] A. Einstein, *Berichtigung zu meiner Abeit: "Eine neue Bestimmung der Moleküldimensionen",* Ann. Phys. **34**, 591 (1911).

[3] S. Kim and S. J. Karrila, *Microhydrodynamics: Principles and Selected Applications*, Butterworth-Heinemann Series in Chemical Engineering (Butterworth-Heinemann, Stoneham, MA, U.S.A., 1991).

[4] E. Guazzelli and J. F. Morris, *A Physical Introduction to Suspension Dynamics*, Cambridge Texts in Applied Mathematics (Cambridge University Press, Cambridge, U.K., 2012).

[5] D. A. McQuarrie, *Statistical Mechanics* (Harper & Row Publishers, New York, NY, U.S.A., 1976).

[6] G. K. Batchelor and J. T. Green, *The determination of the bulk stress in a suspension of spherical particles to order* c^2*,* J. Fluid Mech. **56**, 401 (1972).

[7] G. K. Batchelor, *The effect of Brownian motion on the bulk stress in a suspension of spherical particles,* J. Fluid Mech. **83**, 97 (1977).

[8] L. Durlofsky, J. F. Brady, and G. Bossis, *Dynamic simulations of hydrodynamically interacting particles,* J. Fluid Mech. **180**, 21 (1987).

[9] D. L. Ermak and J. A. McCammon, *Brownian dynamics with hydrodynamic interactions,* J. Chem. Phys. **69**, 1352 (1978).

[10] J. F. Brady, *Brownian motion, hydrodynamics, and the osmotic pressure,* J. Chem. Phys. **98**, 3335 (1993).

[11] N. G. van Kampen, *Stochastic Processes in Physics and Chemistry* (revised and enlarged edition, Elsevier, Amsterdam, The Netherlands, 1992).

[12] L. D. Landau and E. M. Lifshitz, *Hydrodynamic fluctuations,* J. Exptl. Theoret. Phys. (Engl. Ed.) **5**, 512 (1957).

[13] E. M. Lifshitz and L. P. Pitaevskii, *Statistical Physics, Part 2*, in Landau and Lifshitz *Course of Theoretical Physics*, Vol. 9 (Butterworth and Heinemann, Oxford, U.K., 2004).

[14] R. Zwanzig, *Hydrodynamic fluctuations and Stokes' law friction,* J. Res. Natl. Bur. Stand. B **68**, 143 (1964).

[15] R. F. Fox and G. E. Uhlenbeck, *Contributions to non-equilibrium thermodynamics. I. Theory of hydrodynamical fluctuations,* Phys. Fluids **13**, 1893 (1970).

[16] E. H. Hauge and A. Martin-Löf, *Fluctuating hydrodynamics and Brownian motion,* J. Stat. Phys. **7**, 259 (1973).

[17] D. Bedeaux and P. Mazur, *Brownian motion and fluctuating hydrodynamics,* Physica **76**, 247 (1974).

[18] B. Noetinger, *Fluctuating hydrodynamics and Brownian motion,* Physica A **163**, 545 (1990).

[19] R. Singh and R. Adhikari, *Fluctuating hydrodynamics and the Brownian motion of an active colloid near a wall,* Euro. J. Comput. Mech. **26**, 78 (2017).

[20] G. Bossis and J. F. Brady, *The rheology of Brownian suspensions,* J. Chem. Phys. **91**, 1866 (1998).

[21] P. J. Daivis and D. J. Evans, *Comparison of constant pressure and constant volume nonequilibrium simulations of sheared model decane,* J. Chem. Phys. **100**, 541 (1994).

[22] G. K. Batchelor, *The stress system in a suspension of force-free particles,* J. Fluid Mech. **41**, 545 (1970).

[23] D. Palanisamy and W. K. den Otter, In preparation.

[24] H. C. Öttinger, *Stochastic Processes in Polymeric Fluids* (Springer-Verlag, Berlin, Germany, 1996).

[25] C. Gardiner, *Stochastic Methods. A handbook for the Natural and Social Sciences*, 4th ed., Springer Series in Synergetics (Springer-Verlag, Berlin, Germany, 2009).

[26] A. Einstein, *Über die von der molekularkinetischen Theorie der Wärme geforderte Bewegung von in ruhenden Flüssigkeiten suspendierten Teilchen,* Ann. Phys. **17**, 549 (1905).

[27] G. K. Batchelor, *Brownian diffusion of particles with hydrodynamic interactions,* J. Fluid Mech. **74**, 1 (1976).

[28] D. Palanisamy and W. K. den Otter, *Viscoelasticity of dilute solutions of particles of general shape,* J. Chem. Phys. **148**, 194112 (2018).

[29] M. Makino and M. Doi, *Brownian motion of a particle of general shape in Newtonian fluid,* J. Phys. Soc. Japan **73**, 2739 (2004).

[30] I. M. Ilie, W. J. Briels, and W. K. den Otter, *An elementary singularity-free Rotational Brownian Dynamics algorithm for anisotropic particles,* J. Chem. Phys. **142**, 114103 (2015).

[31] J. M. Rallison, *The effect of Brownian motion on the viscosity of solutions of macromolecules, 1. ellipsoids of revolution,* J. Fluid Mech. **84**, 237 (1978).

[32] M. Makino and M. Doi, *Viscoelasticity of dilute solutions of particles of general shape,* J. Phys. Soc. Japan **73**, 3020 (2004).

5

Fluctuating Brownian stress and the colloidal viscosities

The fluctuating Brownian stress – i.e. random Markovian contributions to the stress tensors of suspended colloidal particles, related to the random Markovian motions of these particles via a generalized fluctuation-dissipation theorem centering on the grand resistance matrix – is shown to affect the average stress, and hence the viscosity, of colloidal suspensions. Inclusion of the fluctuating Brownian stress is essential to determining the dynamic viscosity of a quiescent suspension by means of the Green-Kubo formalism, and cross-correlations between the Brownian terms are shown to give rise to a novel stress contribution in suspensions under shear. Brownian Dynamics simulations of spheroidal colloids are presented to show that the proposed revisions recover excellent agreement between equilibrium and non-equilibrium evaluations of the linear rheology.

5.1. Introduction

The effective viscosity η_s of a dilute suspension of rigid spherical colloidal particles, in a Newtonian fluid of viscosity η_0, rises linearly with the colloidal volume fraction ϕ,

$$\eta_s = \eta_0 (1 + B\phi), \tag{5.1}$$

as was famously shown by Einstein [1]. The proportionality constant, [2] $B = 5/2$, originates in the stress-strain coupling of Stokes flow around a spherical particle. In the century since, many researchers have explored the extension of viscosity calculations to higher volume fractions and non-spherical particles. In non-dilute suspensions of rigid spherical colloids, hydrodynamic interactions between the particles

start to play a role. More subtle, the natural tendency of Brownian motion to homogenize suspensions gives rise to a 'thermodynamic force' that results in a 'Brownian stress' in the suspension, as well as indirectly affecting the stress by its influence on the particle distribution [3–5]. Continuing the Taylor expansion in volume fraction started by Einstein, Batchelor and Green [6] derived the prefactor to the quadratic term as 7.6. Brownian Dynamics (BD) simulations of suspensions of rigid spherical particles, based on the first order Langevin equation of motion, have evolved into Stokesian Dynamics (SD), which combines far-field and near-field expressions for the hydrodynamic interactions between Brownian particles with coupling to an imposed flow field to evaluate the dynamics and viscosities of suspensions [7, 8].

For isolated rigid non-spherical particles, methods have been developed to determine their grand mobility and grand resistance matrices [9, 10]. Since these matrices are constant in the body frame, the motion of these particles in the presence of Brownian perturbations, flow and external force fields can be simulated efficiently when using quaternions or the rotation matrix as the rotational coordinates [10, 11]. An analytic expression has been obtained for the rotational mean square displacement of isolated arbitrarily shaped rigid particles [12], which permitted the determination of the storage and loss moduli of dilute solutions [13]. In the latter, the Brownian stress resurfaces as a self-interaction term which is more intuitively interpreted as a hydrodynamic effect originating in the orientation-dependence of the stress-torque relation (see below) [14]. For non-spherical colloids, the orientation-averaged Einstein coefficient B tends to exceed that of spherical colloids[15]. An ellipsoid with a rotational symmetry axis and relatively simple shape facilitated analytical evaluation of their motion under shear [16] and their intrinsic viscosities at low and high shear rates [15, 17–19]. Vast amount of reviews have been made on this topic with notable ones like Brenner[20], Guazzelli and Morris[21]. In particular the work on Intrinsic viscosity for arbitrary Brownian particles by Cichocki *et al.*[22] is relevant where they evaluate frequency dependent viscosities in Brownian limit. Besides the above theories and simulation techniques focusing on the colloids, with the fluid 'absorbed' in the equations motion of the colloids, the exponential rise in computational power over the last decades has made possible the simulation of colloids in an explicit solvent. By running LB simulations on a supercomputer, it is possible to study the flow of hundreds of deformable red blood cells through a vessel[23].

The theory of stresses in dilute suspensions of rigid colloidal particles subject to Brownian motion, and the Brownian Dynamics method to simulate colloidal motion, are well established. Yet they contain a peculiar asymmetry in that the multitude of random kicks against the colloid's surface, due to the thermal fluctuations of the solvent molecules, are assumed to induce random displacements of the colloids – the celebrated Brownian motion – but not to induce random stresses on these colloids. The tacit assumption appears to be that the latter average out, and therefore do not contribute to the stress, and hence the viscosity, of the suspension. Since theory and simulations already account for a 'Brownian stress,' which originates in the Brownian displacements of the particles, we will refer to the direct noise on the stress as the fluctuating Brownian stress. It will be shown that this fluctuating

Brownian stress does average out, while the correlations between this stress and the Brownian displacements give rise to a non-vanishing stress contribution. These correlations result from the fluctuation-dissipation theorem, which will be expressed here in terms of the (11×11) grand resistance matrix rather than the common formulation using the (6×6) mobility matrix. While both approaches yield comparable dynamics, reproducing identical translation and rotation diffusion, only the former recovers agreement between viscosities extracted under shear and those obtained from quiescent suspensions by means of the Green-Kubo formalism.

The structure of this paper is as follows: In Sections 5.2.1, 5.2.2 we will introduce the new extended fluctuation-dissipation theorem. Followed by a detailed derivation of the fluctuating Brownian stress in Sections 5.2.3, 5.2.4 and a new stress term due to rotational derivative of the mobility tensors in Section 5.2.5. We briefly outline the analysis methods to be employed for our simulation results in Section 5.2.6. In Section 5.3 we present numerical evaluated complex Einstein viscosities for a variety of particle shapes like ellipsoid, hemi-spherical cap, paddle and compare them against existing analytical expressions.

5.2. Theory

5.2.1. Conventional Brownian Dynamics

Consider a non-Brownian particle suspended in a homogeneous fluid subject to a linear flow field,

$$\bar{\mathbf{v}}_\infty(\bar{\mathbf{r}}) = \bar{\mathbf{v}}^0_\infty + \bar{\bar{\mathbf{E}}}_\infty \bar{\mathbf{r}} + \bar{\boldsymbol{\omega}}_\infty \times \bar{\mathbf{r}}, \tag{5.2}$$

where $\bar{\mathbf{r}}$ denotes position, $\bar{\mathbf{v}}^0_\infty$ the velocity at the origin of coordinate space, $\bar{\bar{\mathbf{E}}}_\infty$ the symmetric strain rate tensor, $\bar{\boldsymbol{\omega}}_\infty$ the angular velocity, and where the bars denote the ranks of the various tensors. Combining the position and orientation of the particle in the generalized coordinates $\bar{\mathbf{Q}}$, with velocities $\bar{\mathbf{U}}$, and likewise collecting the flow velocities $\bar{\mathbf{v}}_\infty$ and $\bar{\boldsymbol{\omega}}_\infty$ in $\bar{\mathbf{u}}_\infty$, the generalized hydrodynamic force $\bar{\mathbf{F}}_\mathrm{H}$ and stress $\bar{\bar{\mathbf{S}}}_\mathrm{H}$ exerted by the fluid on the slowly moving particle take the form

$$\begin{pmatrix} \bar{\mathbf{F}}_\mathrm{H} \\ \bar{\bar{\mathbf{S}}}_\mathrm{H} \end{pmatrix} = -\begin{pmatrix} \bar{\bar{\boldsymbol{\xi}}}^{F}_{U} & \bar{\bar{\boldsymbol{\xi}}}^{F}_{E} \\ \bar{\bar{\boldsymbol{\xi}}}^{S}_{U} & \bar{\bar{\boldsymbol{\xi}}}^{S}_{E} \end{pmatrix} \begin{pmatrix} \bar{\mathbf{U}} - \bar{\mathbf{u}}_\infty \\ -\bar{\bar{\mathbf{E}}}_\infty \end{pmatrix}, \tag{5.3}$$

where $\boldsymbol{\xi}$ is the grand resistance matrix. In the limit of negligible inertial effects, the velocity of a particle experiencing a conservative generalized force $\bar{\mathbf{F}}_\Phi$, derived from a potential Φ, is solved from the force balance

$$\bar{\mathbf{F}}_\mathrm{H} + \bar{\mathbf{F}}_\Phi = \mathbf{0}, \tag{5.4}$$

and its deformation $\bar{\bar{\mathbf{D}}}$ is obtained from the stress balance

$$\bar{\bar{\mathbf{S}}}_\mathrm{H} + \bar{\bar{\mathbf{S}}}_\Phi = \bar{\bar{\bar{\bar{\mathbf{C}}}}} \bar{\bar{\mathbf{D}}}, \tag{5.5}$$

where $\bar{\bar{\mathbf{S}}}_\Phi$ denotes the stress induced by the potential and $\bar{\bar{\bar{\bar{\mathbf{C}}}}}$ the particle's (orientation-dependend) elasticity tensor. For rigid particles, as considered here, the product on

the r.h.s. is finite at vanishing deformation and the deformation stress is solved by means of Lagrange multipliers. The velocity of the particle and the stress it induces on the solvent, *i.e.* $\bar{\bar{\mathbf{S}}} = -\bar{\bar{\mathbf{S}}}_{\mathrm{H}}$, follow by combining the three above equations into

$$\begin{pmatrix} \bar{\mathbf{U}} \\ \bar{\bar{\mathbf{S}}} \end{pmatrix} = \begin{pmatrix} \bar{\boldsymbol{\mu}}_F^U & \bar{\bar{\boldsymbol{\mu}}}_E^U \\ \bar{\bar{\boldsymbol{\mu}}}_F^S & \bar{\bar{\boldsymbol{\mu}}}_E^S \end{pmatrix} \begin{pmatrix} \bar{\mathbf{F}}_\Phi \\ -\bar{\bar{\mathbf{E}}}_\infty \end{pmatrix} + \begin{pmatrix} \bar{\mathbf{u}}_\infty \\ \mathbf{0} \end{pmatrix}, \tag{5.6}$$

where $\boldsymbol{\mu}$ is the generalized mobility matrix.

The resistance and mobility matrices combine tensors of different ranks, which prohibits the use of standard mathematical manipulations. It therefore proves convenient to rewrite the information contained in the stress and strain matrices into vector form, yielding $\bar{s}$ and $\bar{\mathcal{E}}_\infty$, respectively. Since in the current context both matrices are symmetric and traceless, the corresponding vectors reduce to five elements each. The transformation rules are detailed in Appendix 5.A.1. Rewriting the resistance and mobility matrices accordingly yields two (11×11) matrices, amenable to standard manipulations. Henceforth the bars will be omitted for notational convenience.

For a particle subject to Brownian motion, the force exerted by the fluid on the particle is supplemented by a stochastic Brownian force contribution $\delta\mathbf{F}$ to a total of $\mathbf{F}_{\mathrm{H}} + \delta\mathbf{F}$. The random forces have zero mean, are uncorrelated in time (Markovian) and obey a fluctuation-dissipation theorem derived from the symmetric positive-definite (6×6) force-velocity segment of the resistance matrix,

$$\langle \delta\mathbf{F}(t) \otimes \delta\mathbf{F}(t') \rangle = 2k_B T \boldsymbol{\xi}_U^F \delta(t - t'), \tag{5.7}$$

where the pointed brackets denote an average, t and t' are two times, k_B the Boltzmann constant, T the absolute temperature and δ the Dirac delta function. Using $\boldsymbol{\mu}_F^U = (\boldsymbol{\xi}_U^F)^{-1}$, see Eq. (5.50), one readily shows that including the Brownian force in the equation of motion is equivalent to adding Brownian velocities $\delta\mathbf{U}$ with zero mean and distributed following

$$\langle \delta\mathbf{U}(t) \otimes \delta\mathbf{U}(t') \rangle = 2k_B T \boldsymbol{\mu}_F^U \delta(t - t'), \tag{5.8}$$

with correlations derived from the symmetric positive-definite (6×6) velocity-force segment of the mobility matrix. Because these velocity fluctuations affect the velocity difference between colloid and fluid, they give rise to an additional stress on the particle,

$$\delta\mathbf{S}_{\delta\mathbf{F}}(t) = -\boldsymbol{\xi}_U^S \delta\mathbf{U}(t) = -\boldsymbol{\mu}_F^S \delta\mathbf{F}(t), \tag{5.9}$$

which evidently fluctuates around zero. For clarity of presentation, one displacement term and one stress term – both resulting from correlations between the fluctuating contributions – have been left out thus far, but they will be included below; at this point it suffices to note that both terms vanish identically for isolated spherical particles.

Upon applying the above expressions to a free spherical particle of radius a in a linear shear flow of shear rate $\dot{\gamma}$, $\mathbf{v}_\infty(\mathbf{r}) = \dot{\gamma} r_y \hat{\mathbf{e}}_x$, the average stress by the particle

on the liquid is given by [21]

$$\langle \mathbf{S} \rangle = -\boldsymbol{\mu}_E^S \mathbf{E}_\infty = -\frac{20}{3}\pi a^3 \eta_0 \mathbf{E}_\infty, \tag{5.10}$$

where use is made of the rotational symmetry of the particle. The minus sign indicates that the colloid resist the shear flow; it is this resistance that raises the viscosity of the suspension above that of the suspending fluid. The Einstein coefficient of a dilute suspension of spherical colloids, see Eq. (5.1), is obtained from the average stress induced by a single particle,

$$B = -\frac{1}{\eta_0 v}\frac{\langle S^{xy} \rangle}{\dot{\gamma}} = \frac{5}{2}, \tag{5.11}$$

where v is the volume of the colloid and $\dot{\gamma} = 2E_\infty^{xy}$. An alternative route to the Einstein coefficient is provided by the thermal fluctuations in an equilibrium system, following the Green-Kubo formalism [24–28]. The spontaneous stress fluctuations in a quiescent fluid, $\Delta\mathbf{S}(t) = \mathbf{S}(t) - \langle \mathbf{S} \rangle$, are auto-correlated to obtain the stress relaxation function,

$$G(t) = \frac{1}{10 k_B T}\langle \Delta\mathbf{S}(t+\tau) : \Delta\mathbf{S}(\tau) \rangle, \tag{5.12}$$

where the average is over the time τ. Due to the symmetries of the stress tensor, each of the six off-diagonal elements in this double contraction contributes the same average, namely $k_B T G(t)$, while each of the three diagonal elements contributes the average $\frac{4}{3} k_B T G(t)$, hence the prefactor $1/(10 k_B T)$ to the sum [29]. The intrinsic viscosity then follows from

$$B = \frac{1}{\eta_0 v}\int_0^\infty G(t)\, dt. \tag{5.13}$$

For a free spherical particle in a quiescent fluid $\Delta\mathbf{S} = -\delta\mathbf{S}_{\delta\mathbf{F}} = \mathbf{0}$, since $\boldsymbol{\mu}_F^S = \mathbf{0}$ for an isolated sphere, hence the Einstein coefficient vanishes identically. Evidently, the two approaches to the viscosity and Einstein coefficient yield conflicting results, suggesting a conceptual problem in the equation of motion and/or the stress expression.

5.2.2. Fluctuating Brownian stress

A colloidal particle in a suspensions is subjected to continuous collisions with the surrounding solvent molecules resulting from the perpetual thermal motion of the latter. The cumulative effect of these collisions over a short time interval – short compared to the time scale of colloidal motion, but long on the time scale of the collisions – is the origin of the generalized Brownian force $\mathbf{F}_\mathrm{B}(t) = \delta\mathbf{F}(t)$ acting on the particle, with zero mean and a temperature-relates variance. This generalized force comprises a force $\delta\mathbf{f}(t)$ and a torque $\delta\boldsymbol{\tau}(t)$, both representing distinct 'projections' of the same molecular noise. Hence the fluctuating force and torque

are related, and these correlations are faithfully reproduced by the conventional fluctuation-dissipation theorem, see Eq. (5.7). The collisions also give rise to a stress on the particle, which will be called the fluctuating Brownian stress $\mathbf{S}_{\mathrm{B}}(t)$. Note that this stress is a direct effect of the solvent collisions giving rise to a compressive stress on the colloid, while the above discussed stress contribution $\delta\mathbf{S}_{\delta\mathbf{F}}(t)$ is an indirect effect of the generalized Brownian force resulting in a generalized velocity that induces a hydrodynamic stress. Since the fluctuating Brownian stress and the generalized Brownian force are projections of the same molecular noise, they will be correlated. Expressing the stress as a vector to reduce the number of components, one finds that $\mathcal{S}_{\mathrm{B}}$ and $\mathbf{F}_{\mathrm{B}}$ collectively comprise 11 fluctuating terms. This suggests extending the fluctuation-dissipation theorem to combine force and stress fluctuations, thereby naturally leading to the hypothesis

$$\left\langle \begin{pmatrix} \mathbf{F}_{\mathrm{B}}(t) \\ \mathcal{S}_{\mathrm{B}}(t) \end{pmatrix} \otimes \begin{pmatrix} \mathbf{F}_{\mathrm{B}}(t') \\ \mathcal{S}_{\mathrm{B}}(t') \end{pmatrix} \right\rangle = 2k_B T \begin{pmatrix} \boldsymbol{\xi}_U^F & \boldsymbol{\xi}_{\mathcal{E}}^F \\ \boldsymbol{\xi}_U^{\mathcal{S}} & \boldsymbol{\xi}_{\mathcal{E}}^{\mathcal{S}} \end{pmatrix} \delta(t-t'), \tag{5.14}$$

where the matrix on the r.h.s. is the full (11×11) grand resistance matrix. The numerical examples below indicate that this hypothesis recovers agreement between Einstein coefficients calculated from sheared and non-sheared simulations, for a variety of colloidal shapes. Further work is required to relate this fluctuation-dissipation theorem for the colloid to the fluctuating hydrodynamics of the fluid surrounding the colloid [30–32]. Several authors have shown that fluctuating hydrodynamics gives rise to the usual fluctuation dissipation theorem [32–36]. To the best of our knowledge, only one publication addresses the stress fluctuations; although that study focusses on spherical particles and does not state explicit expressions for the stress, it appears to confirm the above hypothesis [37].

Inserting the fluctuating forces and stresses in Eq. (5.6), one arrives at

$$\begin{pmatrix} \mathbf{U} \\ \mathcal{S} \end{pmatrix} = \begin{pmatrix} \boldsymbol{\mu}_F^U & \boldsymbol{\mu}_{\mathcal{E}}^U \\ \boldsymbol{\mu}_F^{\mathcal{S}} & \boldsymbol{\mu}_{\mathcal{E}}^{\mathcal{S}} \end{pmatrix} \begin{pmatrix} \mathbf{F}_\Phi + \delta\mathbf{F} \\ -\mathcal{E}_\infty \end{pmatrix} + \begin{pmatrix} \mathbf{u}_\infty \\ \delta\mathcal{S} \end{pmatrix}, \tag{5.15}$$

where the total stress by the particle on the fluid reads as

$$\mathcal{S} = -(\mathcal{S}_{\mathrm{H}} + \delta\mathcal{S}_{\delta\mathbf{F}} + \mathcal{S}_{\mathrm{B}}), \tag{5.16}$$

and $\delta\mathcal{S} = -\mathcal{S}_{\mathrm{B}}$. Since the force fluctuations in Eq. (5.14) are identical to those in Eq. (5.7), while the stress fluctuations do not contribute to the velocities, the velocity fluctuations still conform to Eq. (5.8).

In the next two subsections, additional terms will emerge from the time integration of the above stochastic equation. For isolated spherical particles, which are not affected by these additional terms, the correlations for the spontaneous stress fluctuations are obtained as

$$\langle \Delta\mathbf{S}(t) \otimes \Delta\mathbf{S}(t') \rangle = \langle \delta\mathbf{S}(t) \otimes \delta\mathbf{S}(t') \rangle = 2k_B T \boldsymbol{\xi}_E^{\mathcal{S}} \delta(t-t'), \tag{5.17}$$

where the displacement contribution $\delta\mathbf{S}_{\delta\mathbf{F}}$ again cancels because for isolated spheres $\boldsymbol{\xi}_U^{\mathcal{S}} = \mathbf{0}$. One may now calculate the Einstein coefficient following the Green-

Kubo formalism, using the stress correlations provided by the extended fluctuation-dissipation theorem,

$$\langle \Delta \mathbf{S}(t) : \Delta \mathbf{S}(0) \rangle = 2k_B T \sum_{\alpha=1}^{3} \sum_{\beta=1}^{3} \xi_{E,\alpha\beta}^{S,\alpha\beta} \, \delta(t). \tag{5.18}$$

The summation is evaluated using the known $\boldsymbol{\xi}_E^S$ of a sphere [38] [despite appearances in Eq. (5.10), $\boldsymbol{\xi}_E^S$ is not a unit matrix], yielding $(100/3)\pi\eta_0 a^3$. Inserting this result in Eq. (5.13) and noting that the integral covers only half the delta peak, the Einstein coefficient is evaluated as $5/2$. Encouraged by this promising result, we now set forth to derive the general expression for particles of arbitrary shape.

5.2.3. Equation of motion

In the Itô representation of stochastic integrals, *i.e.* when calculating the coordinate updates during a timestep Δt based on information available at the start of the step, the discretized equation of motion of a colloid in a quiescent fluid reads as [39, 40]

$$\begin{aligned} \Delta \mathbf{Q}_t &= \mathbf{Q}_{t+\Delta t} - \mathbf{Q}_t \\ &= -\boldsymbol{\mu}_F^U \boldsymbol{\nabla}_Q \Big(\Phi - \frac{1}{2} \ln g \Big) \Delta t + k_B T \boldsymbol{\nabla}_Q \cdot \boldsymbol{\mu}_F^U \Delta t + \delta \mathbf{Q}_t \sqrt{\Delta t}, \end{aligned} \tag{5.19}$$

where g denotes the metric of the coordinate space. Since the simulations will be run in cartesian coordinates, *i.e.* the position of the hydrodynamic center and quaternions for the rotation around this center, we will henceforth dispense with metric contributions [10, 41]. The last term in the above expression represents the Brownian displacements, expressed in this particular form to highlight their square-root dependence on the time step. Normally these displacements are sampled using a fluctuation-dissipation theorem derived from Eq. (5.8), with the number of random terms equal to the dimension of $\boldsymbol{\mu}_F^U$. In the current context, the random contributions are sampled using

$$\delta \mathbf{Q}_t = \boldsymbol{\mu}_F^U \delta \mathbf{F}_t, \tag{5.20a}$$

$$\begin{pmatrix} \delta \mathbf{F}_t \\ -\delta \mathcal{S}_t \end{pmatrix} = \sqrt{2k_B T} \begin{pmatrix} \boldsymbol{\xi}_U^F & \boldsymbol{\xi}_{\mathcal{E}}^F \\ \boldsymbol{\xi}_U^S & \boldsymbol{\xi}_{\mathcal{E}}^S \end{pmatrix}^{1/2} \boldsymbol{\Theta}_t = \begin{pmatrix} \boldsymbol{\rho}_U^F & \boldsymbol{\rho}_{\mathcal{E}}^F \\ \boldsymbol{\rho}_U^S & \boldsymbol{\rho}_{\mathcal{E}}^S \end{pmatrix} \boldsymbol{\Theta}_t, \tag{5.20b}$$

where $\boldsymbol{\Theta}_t$ is a vector of 11 random components of zero mean, unit variance and devoid of correlations, and where $\boldsymbol{\rho}$ is the symmetric square root of $2k_B T \boldsymbol{\xi}$. The divergence term in Eq. (5.19) arises when the correlation matrix in the conventional fluctuation-dissipation theorem, *i.e.* $\boldsymbol{\mu}_F^U$, is a function of the coordinates. This term can be derived from the second order Langevin equation of motion of the colloid [42], and is required to recover the Boltzmann distribution as equilibrium. Because the correlation matrix for the displacements $\delta \mathbf{Q}_t$ is again provided by $\boldsymbol{\mu}_F^U$ in the revised fluctuation-dissipation term, it is this matrix that enters the discretized equation of motion.

We follow and extend the route taken by Bossis and Brady [14] to derive the stress from the continuous equation of motion. Equation (5.15) does not reproduce the divergence term in Eq. (5.19) and therefore requires amendment for this objective. Integration of Eq. (5.15) over a time interval Δt, in the absence of shear, gives

$$\Delta Q^a(t,\Delta t) = \int_t^{t+\Delta t} \mu_{F,b}^{U,a}(t')\left[F_\Phi^b(t') + \rho_{\circ,A}^{F,b}(t')\Theta^A(t')\right] dt', \tag{5.21}$$

where the Einstein summation convention is used, indices $\{a,b,c,...\}$ run over the six coordinates, indices $\{A,B,C,...\}$ over the six coordinates and five stress components, the superscript $\circ$ to $\boldsymbol{\rho}_\circ^F$ is to be read as U or $\mathcal{E}$ depending on the value of A, and the random components $\boldsymbol{\Theta}(t)$ are Markovian in continuous time. As a first approximation to the displacements, to first order in Δt,

$$\Delta Q_1^a(t,\Delta t) = \mu_{F,b}^{U,a}(t)F_\Phi^b(t)\Delta t + \int_t^{t+\Delta t} \mu_{F,b}^{U,a}(t')\rho_{\circ,A}^{F,b}(t')\Theta^A(t')\,dt'. \tag{5.22}$$

5

Taylor expansion of the non-fluctuating part of the integrand around t and retaining only terms up to first order in Δt,

$$\begin{aligned}\Delta Q_2^a(t,\Delta t) = {}& \mu_{F,b}^{U,a}(t)F_\Phi^b(t)\Delta t + \mu_{F,b}^{U,a}(t)\rho_{\circ,A}^{F,b}(t)\int_t^{t+\Delta t}\Theta^A(t')\,dt' \\ & + \frac{\partial \mu_{F,b}^{U,a}(t)\rho_{\circ,A}^{F,b}(t)}{\partial Q^c}\int_t^{t+\Delta t}\Delta Q_1^c(t,t'-t)\Theta^A(t')\,dt'.\end{aligned} \tag{5.23}$$

In the first integral on the r.h.s., the sum of many random contributions is again a random contribution,

$$\int_t^{t+\Delta t}\Theta^A(t')\,dt' = \Theta_t^A\sqrt{\Delta t}, \tag{5.24}$$

while the second integral, where only the fluctuating term in $\Delta Q_1^c(t,t'-t)$ contributes to first order in Δt, yields – after averaging – the leading term

$$\int_t^{t+\Delta t}\int_t^{t'} \mu_{F,d}^{U,c}(t'')\rho_{\circ,B}^{F,d}(t'')\langle\Theta^B(t'')\Theta^A(t')\rangle\,dt''\,dt' = \mu_{F,d}^{U,c}(t)\rho_{\circ,A}^{F,d}(t)\Delta t. \tag{5.25}$$

Combining these partial results gives

$$\Delta Q_2^a(t,\Delta t) = \mu_{F,b}^{U,a}F_\Phi^b\Delta t + \mu_{F,b}^{U,a}\rho_{\circ,A}^{F,b}\Theta_t^A\sqrt{\Delta t} + \frac{\partial \mu_{F,b}^{U,a}\rho_{\circ,A}^{F,b}}{\partial Q^c}\mu_{F,d}^{U,c}\rho_{\circ,A}^{F,d}\Delta t, \tag{5.26}$$

where, just as in Eq. (5.19), all terms on the r.h.s. are evaluated at t, *i.e.* at the start of the time interval. Using

$$\mu_{F,b}^{U,a}\rho_{\circ,A}^{F,b}\mu_{F,d}^{U,c}\rho_{\circ,A}^{F,d} = \mu_{F,b}^{U,a}\xi_{U,d}^{F,b}\mu_{F,c}^{U,d} = \mu_{F,c}^{U,a}, \tag{5.27a}$$

$$\frac{\partial \mu_{F,b}^{U,a}\rho_{\circ,A}^{F,b}}{\partial Q^c}\mu_{F,d}^{U,c}\rho_{\circ,A}^{F,d} + \mu_{F,b}^{U,a}\rho_{\circ,A}^{F,b}\frac{\partial \mu_{F,d}^{U,c}\rho_{\circ,A}^{F,d}}{\partial Q^c} = \frac{\partial \mu_{F,c}^{U,a}}{\partial Q^c}, \tag{5.27b}$$

and comparing $\Delta Q_2^a(t,\Delta t)$ against the desired result of Eq. (5.19), it follows that the integrated equation of motion differs by the second term on the l.h.s. of the last line. Hence, the continuous equation of motion must be corrected by adding this term,

$$U^a(t) = \mu_{F,b}^{U,a}\left[F_\Phi^b + \rho_{\circ,A}^{F,b}\frac{\partial \mu_{F,d}^{U,c}\rho_{\circ,A}^{F,d}}{\partial Q^c} + \rho_{\circ,A}^{F,b}\Theta^A(t)\right], \tag{5.28}$$

to recover to first order in Δt the same trajectory as the discretized equation of motion, Eq. (5.19). The displacements due to the flow are linear in time and hence are easily added,

$$U^a(t) = \mu_{F,b}^{U,a}\left[F_\Phi^b + \rho_{\circ,A}^{F,b}\frac{\partial \mu_{F,d}^{U,c}\rho_{\circ,A}^{F,d}}{\partial Q^c} + \rho_{\circ,A}^{F,b}\Theta^A(t)\right] + u_\infty^a - \mu_{E,\alpha\beta}^{U,a}E_\infty^{\alpha\beta}, \tag{5.29}$$

where the indices $\{\alpha,\beta,\gamma,\ldots\}$ run over the three coordinate directions.

5

5.2.4. Stress

Having established the continuous equation of motion, the resistance picture of Eq. (5.3) is used to determine the corresponding instantaneous stress – with the fluctuating Brownian stress still to be added. The stress over a time step Δt is obtained as a time average,

$$\tilde{S}^I(t) = \frac{1}{\Delta t}\int_t^{t+\Delta t}\xi_{U,a}^{S,I}(t')\left[U^a(t') - u_\infty^a\right] - \xi_{\mathcal{E},J}^{S,I}(t)\mathcal{E}_\infty^J - \rho_{\circ,A}^{S,I}(t')\Theta^A(t')\,dt', \tag{5.30}$$

where indices $\{I,J,K,\ldots\}$ run over the five components of the stress and strain. Substituting the velocity difference between square brackets by the continuous equation of motion gives

$$\begin{aligned}\tilde{S}^I(t) = \frac{1}{\Delta t}\Bigg\{&\int_t^{t+\Delta t}\xi_{U,a}^{S,I}(t')\mu_{F,b}^{U,a}\left[F_\Phi^b + \rho_{\circ,A}^{F,b}\frac{\partial \mu_{F,d}^{U,c}\rho_{\circ,A}^{F,d}}{\partial Q^c} + \rho_{\circ,A}^{F,b}\Theta^A(t)\right]dt' \\ &- \int_t^{t+\Delta t}\left[\xi_{U,a}^{S,I}(t')\mu_{\mathcal{E},J}^{U,a} + \xi_{\mathcal{E},J}^{S,I}(t)\right]\mathcal{E}_\infty^J + \rho_{\circ,A}^{S,I}(t')\Theta^A(t')\,dt'\Bigg\},\end{aligned} \tag{5.31}$$

which can be simplified by the matrix relations of Eq. (5.50) to arrive at a stress expression in the mobility picture. The integrals are again evaluated to first order in Δt,

$$\begin{aligned}\tilde{S}^I(t) = \frac{1}{\Delta t}\Bigg\{&\mu_{F,b}^{S,I}(t)\left[F_\Phi^b(t) + \rho_{\circ,A}^{F,b}(t)\frac{\partial \mu_{F,d}^{U,c}(t)\rho_{\circ,A}^{F,d}(t)}{\partial Q^c}\right]\Delta t - \mu_{\mathcal{E},J}^{S,I}(t)\mathcal{E}_\infty^J\Delta t \\ &+ \int_t^{t+\Delta t}\left[\mu_{F,b}^{S,I}(t')\rho_{\circ,A}^{F,b}(t') - \rho_{\circ,A}^{S,I}(t')\right]\Theta^A(t)\,dt'\Bigg\},\end{aligned} \tag{5.32}$$

where the fluctuating terms are collected in the remaining integral. Rewriting the integral by Taylor expanding the non-fluctuating part of the integrand around time t, inserting the continuous equation of motion, making use of Eqs. (5.24) and (5.25), and retaining only terms up to first order in Δt, the stress becomes

$$\begin{aligned}\tilde{S}^I(t) = \mu^{S,I}_{F,b}(t)\left[F^b_\Phi(t) + \rho^{F,b}_{\circ,A}(t)\frac{\partial \mu^{U,c}_{F,d}(t)\rho^{F,d}_{\circ,A}(t)}{\partial Q^c}\right] - \mu^{S,I}_{\mathcal{E},J}(t)\mathcal{E}^J_\infty \\ + \left[\mu^{S,I}_{F,b}(t)\rho^{F,b}_{\circ,A}(t) - \rho^{S,I}_{\circ,A}(t)\right]\frac{\Theta^A_t}{\sqrt{\Delta t}} \\ + \frac{\partial\left[\mu^{S,I}_{F,b}(t)\rho^{F,b}_{\circ,A}(t) - \rho^{S,I}_{\circ,A}(t)\right]}{\partial Q^c}\mu^{U,c}_{F,d}(t)\rho^{F,d}_{\circ,A}(t).\end{aligned} \tag{5.33}$$

The two partial derivatives of mobility matrix segments can be combined into

$$\mu^{S,I}_{F,b}(t)\rho^{F,b}_{\circ,A}(t)\frac{\partial \mu^{U,c}_{F,d}(t)\rho^{F,d}_{\circ,A}(t)}{\partial Q^c} + \frac{\partial \mu^{S,I}_{F,b}(t)\rho^{F,b}_{\circ,A}(t)}{\partial Q^c}\mu^{U,c}_{F,d}(t)\rho^{F,d}_{\circ,A}(t) = \frac{\partial \mu^{S,I}_{F,c}(t)}{\partial Q^c}. \tag{5.34}$$

5

Reverting to stress and strain in matrix form,

$$\begin{aligned}\tilde{S}^{\alpha\beta}(t) = \mu^{S,\alpha\beta}_{F,b}(t)F^b_\Phi(t) - \mu^{S,\alpha\beta}_{E,\gamma\delta}(t)E^{\gamma\delta}_\infty + \frac{\partial \mu^{S,\alpha\beta}_{F,c}(t)}{\partial Q^c} - \frac{\partial \rho^{S,\alpha\beta}_{\circ,A}(t)}{\partial Q^c}\mu^{U,c}_{F,d}(t)\rho^{F,d}_{\circ,A}(t) \\ + \left[\mu^{S,\alpha\beta}_{F,b}(t)\rho^{F,b}_{\circ,A}(t) - \rho^{S,\alpha\beta}_{\circ,A}(t)\right]\frac{\Theta^A_t}{\sqrt{\Delta t}},\end{aligned} \tag{5.35}$$

where the subscript A, for the combined sum over generalized coordinates and Cartesian directions, is retained for notational compactness. The first term on the r.h.s. denotes the stress induced by the potential acting on the colloids, the second term that due to the flow, the third term recovers the conventional Brownian stress and the last term represents the fluctuating contributions to the stress, resulting here from Brownian forces as well as from the fluctuating Brownian stress, with correlations between these fluctuating terms giving rise to the fourth term. While the fluctuating Brownian stress term averages to zero, and therefore is only relevant in studies focussing on stress fluctuations, the fourth term does not fluctuate and therefore makes a contribution to the stress – and hence the viscosity – in colloidal suspensions under shear. To the best of our knowledge, this contribution has not been derived before.

The above derivations can be extended to suspensions of N interacting colloids, by extending the mobility and resistance matrices to $(11N \times 11N)$ matrices describing the hydrodynamic interactions between all colloids. The total deviatoric stress then follows as the sum of the stresses on the colloids, supplemented by a virial contribution from the potential interactions between the colloids.

5.2.5. Stress in a dilute suspension

In a dilute suspension one may ignore the hydrodynamic interactions between the colloids. Our objective here is to deduce the stress induced by an isolated rigid

colloid, by deriving expressions for the derivatives in Eq. (5.35). Rigidity implies that any point i on the body will have a fixed position $\bar{\mathbf{r}}_i$ in the body frame (over bar), while its position in the space frame (under bar) reads as

$$\underline{\mathbf{r}}_i = \underline{\mathbf{x}} + \bar{\mathbf{A}}\bar{\mathbf{r}}_i, \qquad \underline{r}_i^{\alpha} = \underline{x}^{\alpha} + \bar{A}_{\beta}^{\alpha}\bar{r}_i^{\beta}, \tag{5.36}$$

where $\underline{\mathbf{x}}$ denotes the position in space of the origin of the body-based coordinate system, and $\bar{\mathbf{A}}$ is the rotation matrix from body to space frame. Rigidity also implies that the grand mobility and resistance matrices in the body frame are constant, and rotate along with the body to give the grand mobility and resistance matrices in the space frame. Introducing the rotation matrix from space to body frame $\underline{\mathbf{A}}$, with $\underline{A}_{\beta}^{\alpha} = \bar{A}_{\alpha}^{\beta}$, the mobility matrix in the body frame, henceforth subdivided into nine components by splitting the generalized velocity into translation and rotation and the generalized force into force and torque,

$$\bar{\boldsymbol{\mu}} = \begin{pmatrix} \bar{\boldsymbol{\mu}}_f^v & \bar{\boldsymbol{\mu}}_\tau^v & \bar{\boldsymbol{\mu}}_E^v \\ \bar{\boldsymbol{\mu}}_f^\omega & \bar{\boldsymbol{\mu}}_\tau^\omega & \bar{\boldsymbol{\mu}}_E^\omega \\ \bar{\boldsymbol{\mu}}_f^S & \bar{\boldsymbol{\mu}}_\tau^S & \bar{\boldsymbol{\mu}}_E^S \end{pmatrix}, \tag{5.37}$$

is converted into a mobility matrix in the space frame following

$$\underline{\mu}_{f,\gamma}^{v,\alpha} = \bar{A}_{\kappa}^{\alpha}\bar{\mu}_{f,\mu}^{v,\kappa}\underline{A}_{\gamma}^{\mu}, \tag{5.38a}$$

$$\underline{\mu}_{E,\gamma\delta}^{v,\alpha} = \bar{A}_{\kappa}^{\alpha}\bar{\mu}_{E,\mu\nu}^{v,\kappa}\underline{A}_{\gamma}^{\mu}\underline{A}_{\delta}^{\nu}, \tag{5.38b}$$

$$\underline{\mu}_{\tau,\gamma}^{S,\alpha\beta} = \bar{A}_{\kappa}^{\alpha}\bar{A}_{\lambda}^{\beta}\bar{\mu}_{\tau,\mu}^{S,\kappa\lambda}\underline{A}_{\gamma}^{\mu}, \tag{5.38c}$$

and so on, with identical relations applying for $\boldsymbol{\xi}$ and $\boldsymbol{\rho}$. Since the mobilities are invariant under translations, the divergence term in Eq. (5.35) reduces to the rotation derivative [43] $\mathcal{R}$ of the stress-torque coupling,

$$\underline{\mathcal{G}}^{\alpha\beta} = \frac{\partial \underline{\mu}_{F,c}^{S,\alpha\beta}}{\partial Q^c} = \mathcal{R}_{\gamma}\underline{\mu}_{\tau,\gamma}^{S,\alpha\beta} = \bar{A}_{\kappa}^{\alpha}\bar{A}_{\lambda}^{\beta}\bar{\mathcal{G}}^{\kappa\lambda}, \tag{5.39a}$$

$$\bar{\mathcal{G}}^{\kappa\lambda} = \epsilon_{\nu}^{\kappa\mu}\bar{\mu}_{\tau,\mu}^{S,\nu\lambda} + \epsilon_{\nu}^{\lambda\mu}\bar{\mu}_{\tau,\mu}^{S,\kappa\nu}, \tag{5.39b}$$

where the rules for differentiating rotation matrices are summarized in Appendix 5.A.2, and the Levi-Civita symbol $\epsilon_{\gamma}^{\alpha\beta}$ returns $+1$ if $\{\alpha,\beta,\gamma\}$ is a cyclic combination of $\{x,y,z\}$, -1 for an anti-cyclic combination, and zero otherwise.

Under the aforementioned conditions, the second derivative in Eq. (5.35) also reduces to the rotation derivative only. Due to the A index to $\boldsymbol{\xi}$ running over trans-

lation, rotation and strain, the result is a sum of three terms,

$$\underline{\mathcal{H}}^{\alpha\beta} = \frac{\partial \underline{\rho}^{S,\alpha\beta}_{\circ,A}}{\partial Q^c} \underline{\mu}^{U,c}_{F,d} \underline{\rho}^{F,d}_{\circ,A} = \left(\mathcal{R}_\gamma \underline{\rho}^{S,\alpha\beta}_{\circ,A}\right) \underline{\mu}^{\omega,\gamma}_{F,d} \underline{\rho}^{F,d}_{\circ,A} \tag{5.40a}$$

$$= \bar{A}^\alpha_\kappa \bar{A}^\beta_\lambda \left(\bar{\mathcal{H}}^{\kappa\lambda}_v + \bar{\mathcal{H}}^{\kappa\lambda}_\omega + \bar{\mathcal{H}}^{\kappa\lambda}_E\right), \tag{5.40b}$$

$$\bar{\mathcal{H}}^{\kappa\lambda}_v = \left(\epsilon^\kappa_{\mu\pi} \bar{\rho}^{S,\pi\lambda}_{v,\nu} + \epsilon^\lambda_{\mu\pi} \bar{\rho}^{S,\kappa\pi}_{v,\nu} + \epsilon^{\mu\pi}_\nu \bar{\rho}^{S,\kappa\lambda}_{v,\pi}\right) \bar{\mu}^{\omega,\mu}_{F,d} \bar{\rho}^{F,d}_{v,\nu}, \tag{5.40c}$$

$$\bar{\mathcal{H}}^{\kappa\lambda}_\omega = \left(\epsilon^\kappa_{\mu\pi} \bar{\rho}^{S,\pi\lambda}_{\omega,\nu} + \epsilon^\lambda_{\mu\pi} \bar{\rho}^{S,\kappa\pi}_{\omega,\nu} + \epsilon^{\mu\pi}_\nu \bar{\rho}^{S,\kappa\lambda}_{\omega,\pi}\right) \bar{\mu}^{\omega,\mu}_{F,d} \bar{\rho}^{F,d}_{\omega,\nu}, \tag{5.40d}$$

$$\bar{\mathcal{H}}^{\kappa\lambda}_E = \left(\epsilon^\kappa_{\mu\pi} \bar{\rho}^{S,\pi\lambda}_{E,\nu\xi} + \epsilon^\lambda_{\mu\pi} \bar{\rho}^{S,\kappa\pi}_{E,\nu\xi} + \epsilon^{\mu\pi}_\nu \bar{\rho}^{S,\kappa\lambda}_{E,\pi\xi} + \epsilon^{\mu\pi}_\xi \bar{\rho}^{S,\kappa\lambda}_{E,\nu\pi}\right) \bar{\mu}^{\omega,\mu}_{F,d} \bar{\rho}^{F,d}_{E,\nu\xi}, \tag{5.40e}$$

where $\epsilon^\alpha_{\beta\gamma} = \epsilon^{\alpha\beta}_\gamma$. The pattern in these expressions is in the three or four indices to $\bar{\rho}^S_v$, $\bar{\rho}^S_\omega$ and $\bar{\rho}^S_E$ consecutively being subjected to a Levi-Civita permutation; in the notation used, the permuted index appears as the single sub- or superscript to the Levi-Civita symbol.

5

5.2.6. Simulation methods

Numerical simulations were performed on non-spherical rigid colloids to ascertain whether the revised stress expression recovers agreement between viscosities derived from equilibrium and non-equilibrium conditions. In the simulations, the position of the colloid is conveniently identified as the location of its hydrodynamic center, *i.e.* the particular point for which $\boldsymbol{\mu}^\omega_f = \boldsymbol{\mu}^v_\tau$. The rotation of the colloid around this center will be described using unit quaternions, *i.e.* a four-vector $\mathbf{q} = (q_0, q_1, q_2, q_3)^{\mathrm{T}}$ of unit length $q = |\mathbf{q}| = 1$, which are well-known in classical mechanics to avoid the singularities associated with rotational dynamics in three coordinates [44]. In Brownian Dynamics, the additional features are the cancelation of the metric term in Eq. (5.19) and – provided $\underline{\mathbf{x}}$ coincides with the hydrodynamic center – the cancelation of the divergence term in said equation [10, 41]. The equation of motion then takes the form

$$\begin{pmatrix} \Delta\underline{\mathbf{x}} \\ \Delta\underline{\mathbf{q}} \end{pmatrix} = \begin{pmatrix} \bar{\mathbf{A}} & \mathbf{0} \\ \mathbf{0} & \bar{\mathbf{B}} \end{pmatrix} \begin{pmatrix} \bar{\boldsymbol{\mu}}^v_f & \bar{\boldsymbol{\mu}}^v_\tau & \bar{\boldsymbol{\mu}}^v_E \\ \bar{\boldsymbol{\mu}}^\omega_f & \bar{\boldsymbol{\mu}}^\omega_\tau & \bar{\boldsymbol{\mu}}^\omega_E \end{pmatrix} \left[\begin{pmatrix} \underline{\mathbf{A}}\mathbf{f} \\ \underline{\mathbf{A}}\boldsymbol{\tau} \\ -\underline{\mathbf{AE}}_\infty \bar{\mathbf{A}} \end{pmatrix} \Delta t + \begin{pmatrix} \delta\bar{\mathbf{f}}_t \\ \delta\bar{\boldsymbol{\tau}}_t \\ \mathbf{0} \end{pmatrix} \sqrt{\Delta t} \right] + \begin{pmatrix} \underline{\mathbf{v}}_\infty \\ \underline{\mathbf{B}}\boldsymbol{\omega}_\infty \end{pmatrix} \Delta t + \begin{pmatrix} \mathbf{0} \\ \lambda\mathbf{q} \end{pmatrix}. \tag{5.41}$$

Here the potential forces and strain in the space frame are converted to the body frame, the force balances are solved for velocities in the body frame, followed by conversions to increments of the position in the space frame and of the quaternions, where the (4×3) matrices $\bar{\mathbf{B}} = \partial\dot{\mathbf{q}}/\partial\bar{\boldsymbol{\omega}}$ and $\underline{\mathbf{B}} = \partial\dot{\mathbf{q}}/\partial\underline{\boldsymbol{\omega}}$ are derived in Appendix 5.A.3. The fluctuating contributions are conveniently sampled in the body

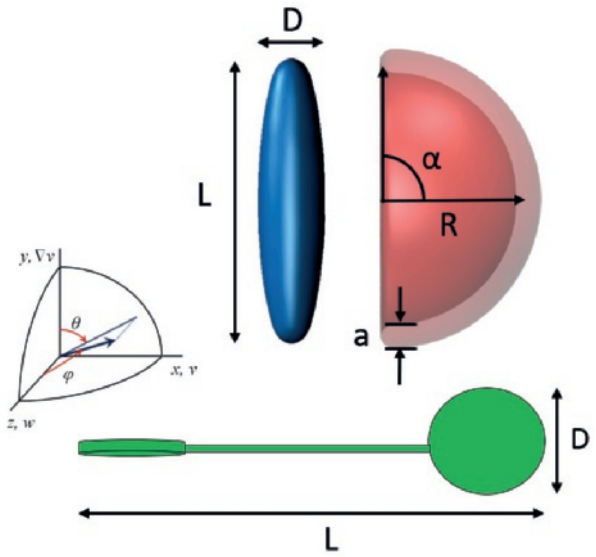

Figure 5.1: The simulated bodies: a prolate spheroid (blue) of length L and diameter D, a hemi-spherical cap (red) of radius R, thickness a and top angle α, and a paddle with blades of diameter D and a top-to-tip length $L = 4D$.

frame,

$$\begin{pmatrix} \delta\tilde{\mathbf{f}}_t \\ \delta\tilde{\boldsymbol{\tau}}_t \\ -\delta\tilde{S}_t \end{pmatrix} = \sqrt{2k_BT} \begin{pmatrix} \tilde{\xi}_v^f & \tilde{\xi}_\omega^f & \tilde{\xi}_\mathcal{E}^f \\ \tilde{\xi}_v^\tau & \tilde{\xi}_\omega^\tau & \tilde{\xi}_\mathcal{E}^\tau \\ \tilde{\xi}_v^S & \tilde{\xi}_\omega^S & \tilde{\xi}_\mathcal{E}^S \end{pmatrix}^{1/2} \boldsymbol{\Theta}_t \tag{5.42}$$

where $\boldsymbol{\Theta}_t$ is a vector of 11 random numbers devoid of correlations. The quaternion displacements $\Delta\mathbf{q}$ are perpendicular to $\mathbf{q}$, and hence conserve the unit length of $\mathbf{q}$, in the limit of infinitesimal time steps. For finite Δt, a constraint force is introduced to impose unit length; its strenght is determined from the condition

$$\left|\mathbf{q}(t+\Delta t)\right| = \left|\mathbf{q}^{\mathrm{u}}(t+\Delta t) + \lambda\mathbf{q}(t)\right| = 1, \tag{5.43}$$

where $\mathbf{q}^{\mathrm{u}}(t+\Delta t)$ denotes the quaternion vector after an unconstrained step ($\lambda = 0$), which is readily shown to yield a quadratic expression for the Lagrange multiplier λ.

The simulation results are presented using ϵ as the unit of energy, σ as the unit of length and τ as the unit of time. The suspending fluid had a viscosity $\eta_0 = 1\epsilon\tau/\sigma^3$ and a thermal energy $k_BT = 1\epsilon$. The time step was 0.1τ. Particles of several differing shapes were simulated, spheroids ranging from oblate to prolate, a hemi-spherical cap and a paddle, see Fig. 5.1. The mobility and resistance matrices of the former were obtained from the literature [38], while those of the latter two were determined by approximating the bodies as rigid collections of ~ 2000

non-overlapping identical primary spherical particles of radius σ [10]. For a single particle in a linear shear flow, the intrinsic viscosity was derived from the ratio of the average stress induced by the particle and the shear rate $\dot{\gamma}$, see Eq. (5.11). For a single particle in a quiescent fluid, the stress relaxation function G was determined from the auto-correlation of the fluctuating stresses, see Eq. (5.12), employing an efficient on-the-fly multiple-tau correlator [45, 46] (with 64 elements at every level, raw data for every step entering at the lowest level, averaging over two elements when filling the next level, and using up to 50 levels to correlate over the entire simulation). For a suspension exposed to an oscillatory small amplitude shear of angular frequency ω, the stress is related to the strain rate by the complex viscosity, $\eta_s^*(\omega)$. The corresponding complex intrinsic viscosity was calculated as

$$B^*(\omega) = B'(\omega) - iB''(\omega) = \frac{1}{\eta_0 v}\int_0^\infty G(t)e^{-i\omega t}dt. \tag{5.44}$$

Makino and Doi [13] obtained an analytic expression for particles of arbitrary shape by evaluating to first order the flow-induced perturbation of the isotropic equilibrium orientation distribution and the resulting stress. After a long calculation, they arrived at

$$B(\omega) = \frac{1}{10\eta_0 v}\left[k_B T\sum_{j=1}^{5}\frac{\alpha_j}{2k_B T\lambda_j + i\omega} - \sum_{\alpha,\beta}\left(\mu_{E,\alpha\beta}^{S,\alpha\beta} - \frac{1}{3}\mu_{E,\beta\beta}^{S,\alpha\alpha}\right)\right]. \tag{5.45}$$

We refer the interested reader to the original work [13] for the explicit expressions relating the ten coefficients α_j and λ_j to the elements of the generalized mobility matrix. Makino and Doi noted that the skewness of the particle, *i.e.* the matrix elements $\bar{\boldsymbol{\mu}}_\tau^v$ and $\bar{\boldsymbol{\mu}}_f^\omega$ coupling translation and rotation, were conspicuous by its absence in the above expression. Further work is required to expand their theory with the novel stress terms obtained here.

5.3. Numerical results

To validate the theory proposed in the previous section, we here present numerical results obtained by Brownian dynamics simulations of isolated particles, using the methodology outlined in Sections 5.2.5 and 5.2.6.

5.3.1. Spheroids

The first non-spherical particle under consideration is a spheroid. The stress relaxation function obtained from equilibrium simulations of a prolate spheroid, with an aspect ratio $p = L/D = 10$, is presented in Fig. 5.2. A delta peak at $t = 0$, see inset, is followed by a shoulder that continues for about 10τ before collapsing to zero. Under the prevalent conditions, the total stress of Eq. (5.35) reduces to three non-vanishing terms: the mobility-gradient term $\underline{\mathcal{G}}$ evaluated following Eq. (5.39), the cross-correlation term term $\underline{\mathcal{H}}$ evaluated following Eq. (5.40), and the Brownian term $\underline{\mathcal{B}}$ combining the direct and indirect random contributions to the stress.

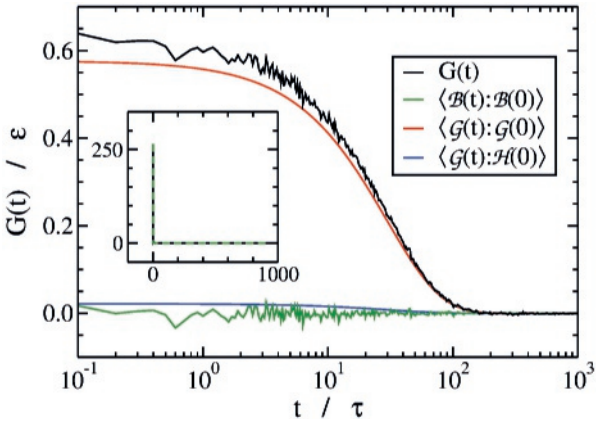

Figure 5.2: Stress relaxation function $G(t)$ of a prolate spheroid with aspect ratio $p = 10$ (black lines). The inset shows the response function on a linear time scale, the main figure shows an enlargement of the shoulder on a logarithmic time scale. The coloured lines represent the three major contributions to $G(t)$.

5

Together these generate nine distinct contributions to the stress relaxation function. As shown in Fig. 5.2, only three combinations make a significant impact: the delta peak at $t = 0$ is dominated by $\langle \underline{\mathcal{B}}(t) : \underline{\mathcal{B}}(0) \rangle$; the shoulder mainly results from $\langle \underline{\mathcal{G}}(t) : \underline{\mathcal{G}}(0) \rangle$, with a small but systematic contribution from $\langle \underline{\mathcal{G}}(t) : \underline{\mathcal{H}}(0) \rangle$. The plot also shows residual noise from $\langle \underline{\mathcal{B}}(t) : \underline{\mathcal{B}}(0) \rangle$ for $t > 0$, which will diminish with increasing run length, while the six other contributions to $G(t)$ are at least an order of magnitude smaller than this noise.

Fourier transformation of the stress relaxation function yields the complex intrinsic viscosity of Fig. 5.3. The real part, also known as the dynamic intrinsic viscosity, is constant at both low and high angular velocities, with a transition around $4 \cdot 10^{-2} \tau^{-1}$. At around the same frequency, the imaginary part transits from $B'' \propto \omega$ for smaller ω to from $B'' \propto \omega^{-1}$ for larger ω. These properties are characteristic of a Jeffrey fluid with one dominant mode [47] Also shown is the theoretical stress relaxation curve in the limit of $\dot{\gamma} \to 0$, as derived by Makino and Doi [13], see Eq. (5.45), which agrees well with the simulation results. The small but systematic difference between theory and simulation is larger than the contributions to B^* from $\underline{\mathcal{H}}$, suggesting that it originates instead in the first order approximation of the theory. Complex intrinsic viscosities calculated using the traditional expressions for the stress, *i.e.* in the absence of $\delta \underline{\mathbf{S}}_t$ and $\underline{\mathcal{H}}$, do not recover agreement with the theoretical curve see Fig. 5.3.

A comparison between the dynamic intrinsic viscosity and the intrinsic viscosity in simulations under linear shear is presented in Fig. 5.4. Good agreement between both perspectives on the intrinsic viscosity is obtained for low angular frequencies and low shear rates, where the intrinsic viscosities are essentially independent of ω and $\dot{\gamma}$, as illustrated for spheroids of two differing aspect ratios. The plateaus

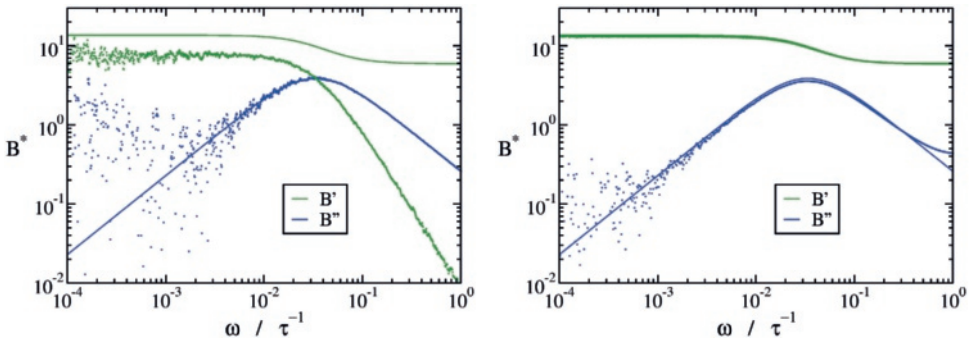

Figure 5.3: The real (B', blue) and imaginary (B'', green) parts of the intrinsic viscosity due to a spheroid with aspect ratio $p = 10$, using the conventional (left) and proposed (right) stress calculation. Markers represent simulation results by Fourier transforming the $G(t)$ of Fig. 5.2, solid lines the theory by Makino and Doi [13], see Eq. (5.45).

in $B'(\omega)$ and $B(\dot{\gamma})$ give way to decreasing curves at about the same values of ω and $\dot{\gamma}$, as predicted by the Cox-Merz rule [47]. But whereas the dynamic intrinsic viscosity levels off at a second plateau within one to two orders of magnitude in ω, the shear viscosity continues to decay over many orders of magnitude in $\dot{\gamma}$, before reaching a far lower plateau value. This shear-thinning phenomenon – the shear flow substantially distorts the particle orientation distribution from the isotropic orientation at low and vanishing shear rates – clearly lies outside the domain of the dynamic intrinsic viscosity, nor is it captured by the first-order perturbation theory of Makino and Doi.

Direct integration of the stress relaxation function provides access to the intrinsic viscosity at low shear rates, $B'(\omega \to 0) = B(\dot{\gamma} \to 0)$. Both approaches have been used to determine the intrinsic viscosities of dilute solutions of spheroid particles ranging from disc-like ($p = 10^{-2}$) to needle-like ($p = 10^{2}$), see Fig. 5.5. By comparing simulation results based on the traditional and proposed stress expressions, depicted on the left and right respectively, it is evident that the former does not recover agreement between the two perspectives on the intrinsic viscosity while the later yields excellent agreement. This result once more confirms that the direct Brownian contribution to the stress makes an essential contribution to the stress in quiescent colloidal suspension, which hitherto has been overlooked. In the limits of large and small aspect ratio the intrinsic viscosities approach the theoretical limits derived by Leal and Hinch [19]. The numerical results indicated that the $\underline{\mathcal{H}}$ term, absent in said theory, makes only a minor contribution to the total stress under shear.

5.3.2. Cap and paddle

The mobility matrix of a spheroid os still relatively sparse, containing only the three diagonal blocks and rotation-strain coupling, $\bar{\boldsymbol{\mu}}_E^{\omega}$ and $\bar{\boldsymbol{\mu}}_{\tau}^{S}$. As additional tests

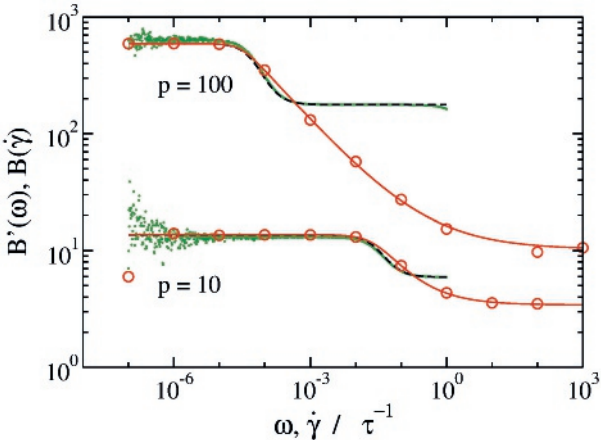

Figure 5.4: The intrinsic dynamic viscosity (B', green) and the intrinsic viscosity under shear (B, red) for spheroids of aspect ratios $p = 10$ and 100. Markers represent simulation results, dashed black lines the theory by Makino and Doi, [13] and the solid red lines are fits with a Carreau-like model [10].

of our amendments, simulations are presented of a hemi-spherical cap, incurring translation-strain coupling $\bar{\boldsymbol{\mu}}_E^v$ and $\bar{\boldsymbol{\mu}}_f^S$, and of a paddle, adding translation-rotation coupling $\bar{\boldsymbol{\mu}}_\tau^v$ and $\bar{\boldsymbol{\mu}}_f^\omega$. The mobility and resistance matrices of these bodies, see Fig. 5.1, were determined by approximating them as rigid collections of N nearly-touching primary spheres, with radius 1σ. Evaluating the hydrodynamic interactions between these spheres at the Rotne-Prager-Yamakawa level [48, 49], the resulting $(11N \times 11N)$ hydrodynamic matrix can be condensed into (11×11) hydrodynamic matrices for a colloid of arbitrary shape [10]. The employed code, `Oseen11`, is freely available online [50]. Approaching the spheroids of the previous subsection as hollow shells of ~ 2000 particles yielded intrinsic viscosities in good agreement with the above results. The hemi-spherical cap, with a top angle $\alpha = \pi/2$, was modeled as 2051 primary particles placed on the corner points of a triangulated mesh generated using the `DistMesh` routine [51] in `MATLAB` [52], resulting in a shell with radius $R \approx 47.8\sigma$ and thickness $a = 2\sigma$. The two blades of the paddle are constructed as identical discs of 737 particles each, with a radius of $R \approx 37.8\sigma$, positioned at a relatively angle of $90°$ at the two ends of a connecting rod of length $4R$ and negligible thickness, akin to the paddle simulated by Makino and Doi [11, 13].

The stress relaxation functions of the bodies are presented in Fig. 5.6. As seen from figure, for more asymmetric particles many stress relaxations components appear (compared to an prolate spheroid in Fig. 5.2). We plot the dynamic intrinsic viscosity and the viscosity under shear for a cap and a paddle in 5.7. Even though we see qualitative agreement between the various methods it is not satisfactory to the level seen earlier for the case of prolate spheroids. Curves generated using Makino and Doi's analytical expression also show similar behavior. This is due to the difficulty in capturing higher order orientational distributions deviating from an isotropic case and will be a subject of on-going research work.

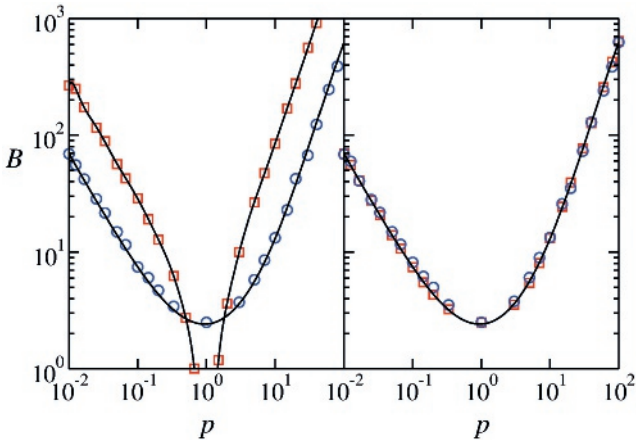

Figure 5.5: Einstein viscosity coefficients B for spheroids covering a wide range in aspect ratio p, as deduced from the average stress in simulations at low shear rate (blue circles) and the from the stress fluctuations at zero shear (red squares). Simulations based on the classical stress calculation show a marked difference between the two approaches (left), while the revisions proposed here recover agreement (right). The smooth lines are guides to the eye.

5.4. Summary and conclusions

The conventional stress calculation in Brownian Dynamics simulations is shown to yield a marked difference between equilibrium and non-equilibrium evaluations of the linear rheology of a colloidal suspension. The inclusion of fluctuating Brownian stresses, which are hypothesized to be related to the Brownian forces by a generalized fluctuation dissipation theorem, solves the discrepancy and recovers agreement. The fluctuating Brownian stress is essential to studies in equilibrium, but averages to zero – and can hence be neglected – in non-equilibrium studies. The derivation in Section 5.2 reveals a non-vanishing stress contribution that ought to be included in both equilibrium and non-equilibrium; this term turns out to be fairly small numerically for the systems simulated here. Further research is required to explore the relevance of this term for non-dilute colloidal suspensions.

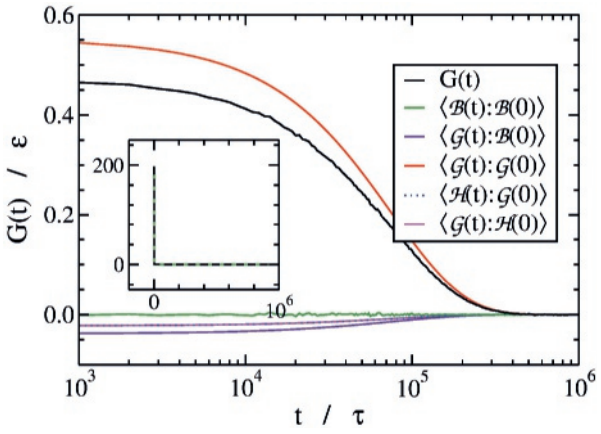

Figure 5.6: Stress relaxation functions $G(t)$ of a paddle. The inset shows the response function on a linear time scale, the main figure shows an enlargement of the shoulder on a logarithmic time scale. The coloured lines represent the five major contributions to $G(t)$.

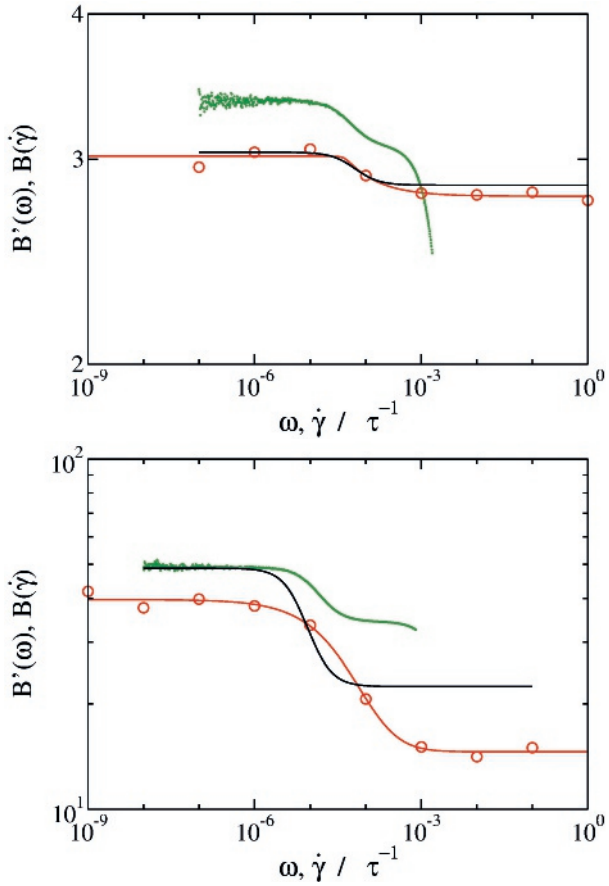

Figure 5.7: The intrinsic dynamic viscosity (B', green) and the intrinsic viscosity under shear (B, red) for a hemi-spherical cap (left) and a paddle (right). Markers represent simulation results, dashed black lines the theory by Makino and Doi, [13] and the solid red lines are fits with a Carreau-like model [10].

Acknowledgments

This work is part of the 'Computational Sciences for Energy Research' program of the Netherlands Organisation for Scientific Research (NWO) under Project Nr. 13CSER060. This research programme is co-financed by Shell Global Solutions International B.V..

References

[1] A. Einstein, *Eine neue Bestimmung der Moleküldimensionen,* Ann. Phys. **19**, 289 (1906).

[2] A. Einstein, *Berichtigung zu meiner Abeit: "Eine neue Bestimmung der Moleküldimensionen",* Ann. Phys. **34**, 591 (1911).

[3] J. G. Kirkwood and P. L. Auer, *The visco-elastic properties of solutions of rod-like macromolecules,* J. Chem. Phys. **19**, 281 (1951).

[4] N. Saitô, *The effect of Brownian motion on the viscosity of solutions of macromolecules, 1. ellipsoids of revolution,* J. Phys. Soc. Japan **6**, 297 (1951).

[5] G. K. Batchelor, *The effect of Brownian motion on the bulk stress in a suspension of spherical particles,* J. Fluid Mech. **83**, 97 (1977).

[6] G. K. Batchelor and J. T. Green, *The determination of the bulk stress in a suspension of spherical particles to order* c^2*,* J. Fluid Mech. **56**, 401 (1972).

[7] L. Durlofsky, J. F. Brady, and G. Bossis, *Dynamic simulations of hydrodynamically interacting particles,* J. Fluid Mech. **180**, 21 (1987).

[8] J. F. Brady and G. Bossis, *Stokesian Dynamics,* Ann. Rev. Fluid Mech. **20**, 111 (1988).

[9] S. Aragon, *A precise boundary element method for macromolecular transport properties,* J. Comput. Chem. **25**, 1191 (2004).

[10] D. Palanisamy and W. K. den Otter, *Viscoelasticity of dilute solutions of particles of general shape,* J. Chem. Phys. **148**, 194112 (2018).

[11] M. Makino and M. Doi, *Brownian motion of a particle of general shape in Newtonian fluid,* J. Phys. Soc. Japan **73**, 2739 (2004).

[12] L. D. Favro, *Theory of the rotational Brownian motion of a free rigid body,* Phys. Rev. **119**, 53 (1960).

[13] M. Makino and M. Doi, *Viscoelasticity of dilute solutions of particles of general shape,* J. Phys. Soc. Japan **73**, 3020 (2004).

[14] G. Bossis and J. F. Brady, *The rheology of Brownian suspensions,* J. Chem. Phys. **91**, 1866 (1998).

[15] E. J. Hinch and L. G. Leal, *The effect of brownian motion on the rheological properties of a suspension of non-spherical particles,* J. Fluid Mech. **52**, 683 (1972).

[16] G. B. Jeffery, *The motion of ellipsoidal particles immersed in a viscous fluid,* Proc. Royal. Soc. London A **102**, 161 (1922).

[17] J. M. Burgers, *On the motion of small particles of elongated form suspended in a viscous liquid,* in *Second Report on Viscosity and Plasticity* (Noord-Hollandsche Uitgeversmaatschappij, Amsterdam, The Netherlands, 1938) Chap. III, reprinted in [Nieuwstadt].

[18] H. Giesekus, *Elasto-viskose Flüssigkeiten, für die in stationären schicht-strömungen sämtliche Normalspannungskomponenten verschieden großsind,* Rheol. Acta. **2**, 50 (1962).

[19] L. G. Leal and E. J. Hinch, *The effect of weak brownian rotations on particles in shear flow,* J. Fluid Mech. **46**, 685 (1971).

[20] H. Brenner, *Rheology of a dilute suspension of axisymmetric brownian particles,* Int. J. Multiphase Flow **1**, 195 (1974).

[21] E. Guazzelli and J. F. Morris, *A Physical Introduction to Suspension Dynamics*, Cambridge Texts in Applied Mathematics (Cambridge University Press, Cambridge, U.K., 2012).

[22] B. Cichocki, M. L. Ekiel-Jeżewska, and E. Wajnryb, *Intrinsic viscosity for brownian particles of arbitrary shape,* in *J. Phys. Conf. Ser.*, Vol. 392 (IOP Publishing, 2012) p. 012004.

[23] B. Kaoui, J. Harting, and C. Misbah, *Two-dimensional vesicle dynamics under shear flow: Effect of confinement,* Phys. Rev. E **83**, 066319 (2011).

[24] M. S. Green, *Markoff random processes and the statistical mechanics of time-dependent phenomena. II. irreversible processes in fluids,* J. Chem. Phys. **22**, 398 (1954).

[25] R. Kubo, *Statistical-mechanical theory of irreversible processes. I. general theory and simple applications to magnetic and conduction problems,* J. Phys. Soc. Japan **12**, 570 (1957).

[26] D. A. McQuarrie, *Statistical Mechanics* (Harper & Row Publishers, New York, NY, U. S. A., 1976).

[27] B. J. Berne and R. Pecora, *Dynamic light scattering. With applications to chemstry, biology, and physics* (Dover Publications, Mineola York, NY, U. S. A., 2000).

[28] D. J. Evans and G. Morriss, *Statistical mechanics of nonequilibrium liquids*, 2nd ed. (Cambridge University Press, Cambridge, U.K., 2008).

[29] P. J. Daivis and D. J. Evans, *Comparison of constant pressure and constant volume nonequilibrium simulations of sheared model decane,* J. Chem. Phys. **100**, 541 (1994).

[30] L. D. Landau and E. M. Lifshitz, *Hydrodynamic fluctuations,* J. Exptl. Theoret. Phys. (Engl. Ed.) **5**, 512 (1957).

[31] E. M. Lifshitz and L. P. Pitaevskii, *Statistical Physics, Part 2*, in Landau and Lifshitz *Course of Theoretical Physics*, Vol. 9 (Butterworth and Heinemann, Oxford, U.K., 2004).

[32] R. F. Fox and G. E. Uhlenbeck, *Contributions to non-equilibrium thermodynamics. I. Theory of hydrodynamical fluctuations,* Phys. Fluids **13**, 1893 (1970).

[33] R. Zwanzig, *Hydrodynamic fluctuations and Stokes' law friction,* J. Res. Natl. Bur. Stand. B **68**, 143 (1964).

[34] E. H. Hauge and A. Martin-Löf, *Fluctuating hydrodynamics and Brownian motion,* J. Stat. Phys. **7**, 259 (1973).

[35] D. Bedeaux and P. Mazur, *Brownian motion and fluctuating hydrodynamics,* Physica **76**, 247 (1974).

[36] B. Noetinger, *Fluctuating hydrodynamics and Brownian motion,* Physica A **163**, 545 (1990).

[37] R. Singh and R. Adhikari, *Fluctuating hydrodynamics and the Brownian motion of an active colloid near a wall,* Euro. J. Comput. Mech. **26**, 78 (2017).

[38] S. Kim and S. J. Karrila, *Microhydrodynamics: Principles and Selected Applications*, Butterworth-Heinemann Series in Chemical Engineering (Butterworth-Heinemann, Stoneham, MA, U. S. A., 1991).

[39] H. C. Öttinger, *Stochastic Processes in Polymeric Fluids* (Springer-Verlag, Berlin, Germany, 1996).

[40] C. Gardiner, *Stochastic Methods. A handbook for the Natural and Social Sciences*, 4th ed., Springer Series in Synergetics (Springer-Verlag, Berlin, Germany, 2009).

[41] I. M. Ilie, W. J. Briels, and W. K. den Otter, *An elementary singularity-free Rotational Brownian Dynamics algorithm for anisotropic particles,* J. Chem. Phys. **142**, 114103 (2015).

[42] D. L. Ermak and J. A. McCammon, *Brownian dynamics with hydrodynamic interactions,* J. Chem. Phys. **69**, 1352 (1978).

[43] M. Doi and S. F. Edwards, *The Theory of Polymer Dynamics*, International Series of Monographs on Physics, Vol. 73 (Oxford University Press, Oxford, U.K., 2013).

[44] H. Goldstein, *Classical Mechanics*, 2nd ed. (Addison-Wesley, Reading, MA, U. S. A., 1980).

[45] D. Magatti and F. Ferri, *Fast multi-tau real-time software correlator for dynamic light scattering,* Appl. Opt. **40**, 4011 (2001).

[46] J. Ramírez, S. K. Sukumaran, B. Vorselaars, and A. E. Likhtman, *Efficient on the fly calculation of time correlation functions in computer simulations,* J. Chem. Phys. **133**, 154103 (2010).

[47] P. Oswald, *Rheophysics. The deformation and flow of matter* (Cambridge University Press, Cambridge, U. K., 2009).

[48] J. Rotne and S. Prager, *Variational treatment of hydrodynamic interaction in polymers,* J. Chem. Phys. **50**, 4831 (1969).

[49] H. Yamakawa, *Transport properties of polymer chains in dilute solution: hydrodynamic interaction,* J. Chem. Phys. **53**, 436 (1970).

[50] `https://www2.msm.ctw.utwente.nl/Oseen11/`.

[51] P.-O. Persson and G. Strang, *A simple mesh generator in matlab,* SIAM Rev. **46**, 329 (2004).

[52] MATLAB R2014a, The MathWorks Inc., Natick, MA, U.S.A. (2014).

5.A. Appendices:

5.A.1. Stress and strain vectors

By analogy to a vector being expressed as a weighted sum of non-orthogonal basis vectors, the stress tensor $\mathbf{S}$ can be expressed as a weighted sum of basis matrices $\mathbf{e}_\kappa^S$,

$$\mathcal{S}^{\alpha\beta} = \mathcal{S}^\kappa (\mathbf{e}_\kappa^S)^{\alpha\beta}, \tag{5.46a}$$

$$\mathcal{S}^\kappa = (\mathbf{e}_S^\kappa)^{\alpha\beta} S^{\alpha\beta}, \tag{5.46b}$$

where the Einstein summation convention is used. The components $\mathcal{S}^\kappa$, extracted from the matrix by the dual basis $\mathbf{e}_S^\kappa$, constitute the stress vector, $\mathcal{S}$. The strain $\mathbf{E}_\infty$ is likewise converted to a vector, $\mathcal{E}_\infty$, on the basis $\mathbf{e}_\kappa^E$. As both stress and strain are symmetric and traceless in the current context, the vectors can be reduced to five components by an appropriate choice of the basis matrices [1].

$$\begin{pmatrix} \mu_{F,b}^{U,a} & \mu_{\mathcal{E},\lambda}^{U,a} \\ \mu_{F,b}^{\mathcal{S},\kappa} & \mu_{\mathcal{E},\lambda}^{\mathcal{S},\kappa} \end{pmatrix} = \begin{pmatrix} \mu_{F,b}^{U,a} & \mu_{E,\alpha\beta}^{U,a} (\mathbf{e}_\lambda^E)^{\alpha\beta} \\ (\mathbf{e}_S^\kappa)^{\alpha\beta} \mu_{F,b}^{S,\alpha\beta} & (\mathbf{e}_S^\kappa)^{\alpha\beta} \mu_{E,\gamma\delta}^{S,\alpha\beta} (\mathbf{e}_\lambda^E)^{\gamma\delta} \end{pmatrix} \tag{5.47}$$

Because the grand mobility and resistance matrices introduced in Section 5.2.1 satisfy a number of symmetry rules, it proves convenient to choose

$$\mathbf{e}_\kappa^S = \mathbf{e}_E^\kappa \quad \text{and} \quad \mathbf{e}_\kappa^E = \mathbf{e}_S^\kappa, \tag{5.48}$$

as this creates symmetric (11×11) matrices. The two ways of expressing stress and strain are entirely equivalent – the main purpose to introduce the vector form is to allow recourse to standard numerical techniques.

The generalized mobility and resistance matrices introduced in Section 5.2.1 are not each-other's inverses. One readily shows that

$$\begin{pmatrix} \boldsymbol{\mu}_F^U & \boldsymbol{\mu}_\mathcal{E}^U \\ \boldsymbol{\mu}_F^\mathcal{S} & \boldsymbol{\mu}_\mathcal{E}^\mathcal{S} \end{pmatrix} = \begin{pmatrix} (\boldsymbol{\xi}_U^F)^{-1} & -(\boldsymbol{\xi}_U^F)^{-1} \boldsymbol{\xi}_\mathcal{E}^F \\ \boldsymbol{\xi}_U^\mathcal{S} (\boldsymbol{\xi}_U^F)^{-1} & \boldsymbol{\xi}_\mathcal{E}^\mathcal{S} - \boldsymbol{\xi}_U^\mathcal{S} (\boldsymbol{\xi}_U^F)^{-1} \boldsymbol{\xi}_\mathcal{E}^F \end{pmatrix}, \tag{5.49}$$

and consequently

$$\boldsymbol{\mu}_F^U = (\boldsymbol{\xi}_U^F)^{-1}, \tag{5.50a}$$

$$\boldsymbol{\mu}_F^\mathcal{S} = \boldsymbol{\xi}_U^\mathcal{S} \boldsymbol{\mu}_F^U, \tag{5.50b}$$

$$\boldsymbol{\mu}_\mathcal{E}^\mathcal{S} = \boldsymbol{\xi}_\mathcal{E}^\mathcal{S} + \boldsymbol{\xi}_U^\mathcal{S} \boldsymbol{\mu}_\mathcal{E}^U. \tag{5.50c}$$

5.A.2. Rotational derivative of a rotation matrix

The derivative of a function $f(\mathbf{r})$ under a rotation of the point $\mathbf{r}$ around an axis $\hat{\mathbf{e}}_\alpha$ of the coordinate system reads as

$$\mathcal{R}_\alpha f(\mathbf{r}) = (\hat{\mathbf{e}}_\alpha \times \mathbf{r}) \cdot \frac{\partial f(\mathbf{r})}{\partial \mathbf{r}} = \left[\mathbf{r} \times \frac{\partial f(\mathbf{r})}{\partial \mathbf{r}} \right]_\alpha. \tag{5.51}$$

A right-handed rotation matrix $\bar{\mathbf{A}}$ can be regarded as a collection of three perpendicular unit columns, $\bar{\mathbf{A}} = (\bar{\mathbf{a}}_1\ \bar{\mathbf{a}}_2\ \bar{\mathbf{a}}_3)$, related by $\epsilon^{\mu}_{\kappa\lambda}\bar{\mathbf{a}}_\mu = \bar{\mathbf{a}}_\kappa \times \bar{\mathbf{a}}_\lambda$, where the Levi-Civita symbol $\epsilon^{\mu}_{\kappa\lambda}$ returns $+1$ if $\{\kappa,\lambda,\mu\}$ is a cyclic combination of $\{1,2,3\}$, -1 for an anti-cyclic combination, and zero otherwise. Defining a function $f(\mathbf{r}) = \mathbf{r}\cdot\hat{\mathbf{e}}_\lambda$, one readily shows that

$$\mathcal{R}_\alpha \bar{A}^\lambda_\kappa = \mathcal{R}_\alpha f(\bar{\mathbf{a}}_\kappa) = \epsilon^\gamma_{\alpha\beta}(\bar{\mathbf{a}}_\kappa)^\beta \frac{\partial(\bar{\mathbf{a}}_\kappa)^\lambda}{\partial(\bar{\mathbf{a}}_\kappa)^\gamma} = \epsilon^\lambda_{\alpha\beta}(\bar{\mathbf{a}}_\kappa)^\beta = \epsilon^\lambda_{\alpha\beta}\bar{A}^\beta_\kappa, \tag{5.52}$$

which is used repeatedly in Section 5.2.5. Another expression used in that section follows by taking the cross product of two columns of a rotation matrix,

$$\epsilon^\alpha_{\beta\gamma}\bar{A}^\beta_\kappa\bar{A}^\gamma_\lambda = \epsilon^\alpha_{\beta\gamma}(\bar{\mathbf{a}}_\kappa)^\beta(\bar{\mathbf{a}}_\lambda)^\gamma = (\bar{\mathbf{a}}_\kappa \times \bar{\mathbf{a}}_\lambda)_\alpha = \left(\epsilon^\mu_{\kappa\lambda}\bar{\mathbf{a}}_\mu\right)_\alpha = \epsilon^\mu_{\kappa\lambda}\bar{A}^\alpha_\mu, \tag{5.53}$$

where use was made of the right-handedness of $\bar{\mathbf{A}}$.

5

5.A.3. Quaternions

Unit quaternions are four-vectors, $\mathbf{q} = (q_0, q_1, q_2, q_3)$, of unit length, $q = |\mathbf{q}| = 1$, providing a convenient parameterization of rotation matrices. The rotation from the body-frame to the space-frame is realized by

$$\bar{\mathbf{A}} = \begin{pmatrix} q_0^2+q_1^2-q_2^2-q_3^2 & 2q_1q_2-2q_0q_3 & 2q_1q_3+2q_0q_2 \\ 2q_1q_2+2q_0q_3 & q_0^2-q_1^2+q_2^2-q_3^2 & 2q_2q_3-2q_0q_1 \\ 2q_1q_3-2q_0q_2 & 2q_2q_3+2q_0q_1 & q_0^2-q_1^2-q_2^2+q_3^2 \end{pmatrix}, \tag{5.54}$$

and the inverse rotation by $\underline{\mathbf{A}} = \bar{\mathbf{A}}^{-1} = \bar{\mathbf{A}}^{\mathrm{T}}$. For a colloid rotating around its stationary center, it follows from Eq. (5.36) that $\underline{\boldsymbol{\omega}} \times \underline{\mathbf{r}}_i = \dot{\bar{\mathbf{A}}}\bar{\mathbf{r}}_i = \dot{\bar{\mathbf{A}}}\underline{\bar{\mathbf{A}}\mathbf{r}}_i$ and therefore

$$\underline{\mathbf{B}} = \frac{\partial\dot{\mathbf{q}}}{\partial\underline{\boldsymbol{\omega}}} = \frac{1}{2q^4}\begin{pmatrix} -q_1 & -q_2 & -q_3 \\ q_0 & q_3 & -q_2 \\ -q_3 & q_0 & q_1 \\ q_2 & -q_1 & q_0 \end{pmatrix}. \tag{5.55}$$

Futhermore, $\underline{\mathbf{A}}\dot{\bar{\mathbf{A}}}\bar{\mathbf{r}}_i = \underline{\mathbf{A}}\left(\underline{\boldsymbol{\omega}} \times \underline{\mathbf{r}}_i\right) = \bar{\boldsymbol{\omega}} \times \bar{\mathbf{r}}_i$ and therefore

$$\bar{\mathbf{B}} = \frac{\partial\dot{\mathbf{q}}}{\partial\bar{\boldsymbol{\omega}}} = \frac{1}{2q^4}\begin{pmatrix} -q_1 & -q_2 & -q_3 \\ q_0 & -q_3 & q_2 \\ q_3 & q_0 & -q_1 \\ -q_2 & q_1 & q_0 \end{pmatrix}, \tag{5.56}$$

as follows also from $\bar{\mathbf{B}}\bar{\boldsymbol{\omega}} = \underline{\mathbf{B}}\bar{\mathbf{A}}\bar{\boldsymbol{\omega}}$.

References

[1] D. Palanisamy and W. K. den Otter, *Viscoelasticity of dilute solutions of particles of general shape,* J. Chem. Phys. **148**, 194112 (2018).

6

Aggregation dynamics of sticky colloids

In traditional simulations of diffusion limited cluster aggregation (DLCA), it is assumed that the translational diffusional mobilities of aggregates are related to those of the primary particles by a simple power law and that the effect of rotations can be ignored. We present Brownian Dynamics (BD) simulations of DLCA employing mobilities based on intra-aggregate hydrodynamic interactions and including rotational motion. Whereas traditional simulations with spherical primary particles yield aggregates with fractal dimensions around 1.75, we find that rotations result in a reduction to 1.65. The aggregation process also proceeds faster, which is particular noticeable for rod-like primary particles. The distributions of aggregate sizes still conforms with accepted scaling laws, where the relevant powers are no longer a consequence of the selected scaling law.

6.1. Introduction:

Aggregation of colloidal particles suspended in a fluid is a topic of long standing interest [1]. In diffusion limited cluster aggregation (DLCA), *i.e.* for low particle concentrations and weak long range inter-particle interactions, the aggregation process is dominated by the diffusive motions of the primary particles and their aggregates [2]. The simplest form of aggregation is the hit-and-stick collision mechanism where identical primary particles stick upon contact and remain in a fixed relative orientation for the remainder of the experiment [3]. One of the characteristics of the aggregates formed in this manner is their fractal nature, see Fig. 6.1, with the number of primary particles in an aggregate, s, scaling with the spatial size of the cluster, R, as $s \propto R^{d_f}$, where d_f is known as the fractal dimension [2]. In a three-dimensional world, the value of d_f ranges from unity for a linear aggregate to three

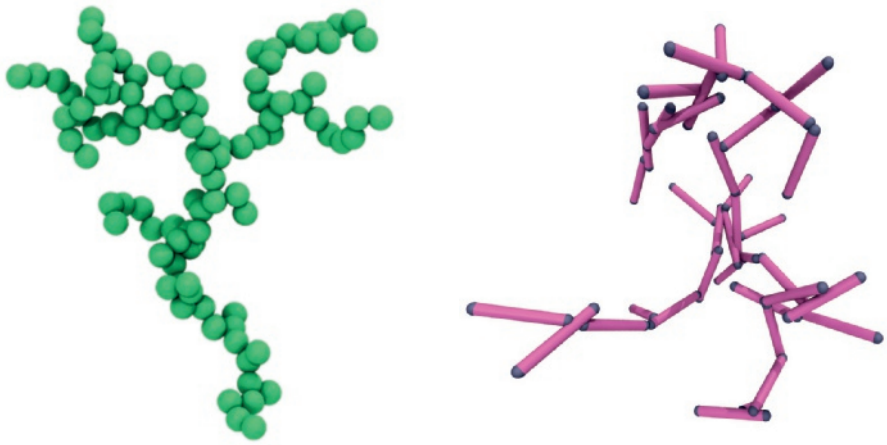

Figure 6.1: Snapshot of a cluster consisting of 130 spherical primary particles, formed at $t = 600\tau$ in a $\phi = 10^{-3}$ suspension (left) and a cluster consisting of 34 rod shaped particles, $p = 13$ (right), formed at $t = 30\tau$ in a $\phi = 2 \cdot 10^{-3}$ suspension simulated with rotational Brownian Dynamics and intra-cluster hydrodynamics.

for a densely packed aggregate.

Simulations have been instrumental in studying the scaling behaviour of DLCA, as well as in establishing master curves describing the time evolution of the aggregation process. Early simulations employed particles moving on two-dimensional lattices [2, 4], which were subsequently extended to three dimensions [5]. In these studies diffusion is simulated by randomly selecting a particle or an aggregate, moving it to an adjacent lattice cell where it may click to a neighbouring particle or aggregate, and incrementing the simulation time by an amount scaling with the size of the moved object. A universality was observed in the fractal dimension of the aggregates, with $d_f \approx 1.45$ in 2D and $d_f \approx 1.8$ in 3D. Similar values were reported for experiments on gold, silica and polystyrene sticky spherical colloidal particles, among others, suspended in a 3D bulk fluid or at a 2D interface [3, 6–8]. Later simulations also include off-lattice methods, with the scalar mobilities of the particles and aggregates typically assumed to follow a simple scaling law, $\mu_s = \mu_1 s^\gamma$, which gives best agreement with experimental DLCA when selecting $\gamma = 1/d_f$. The rotational diffusion of the aggregates is typically ignored in these simulations, probably motivated by the absence of rotation in the pioneering lattice-based simulations and an early study indicating that rotations are of minor importance to the aggregation process [9]. While earlier models employed simple scaling laws some recent simulations started exploring the cluster shape anisotropy and its effects on aggregation.[10–13] This renewed interest is also due to some recent experimental results which showed some interesting features like occurrence of low fractal dimension clusters than predicted by earlier DLCA models[14, 15] We present simulation results of DLCA addressing the two approximations discussed above, by including rotational dynamics and by endowing every aggregate with

a shape-specific tensorial mobility. The simulation method employed is Brownian Dynamics (BD), using a recently introduced algorithm for the combined translation and rotation dynamics of rigid colloidal bodies [16]. The diffusive motion of an aggregate is based on the translation and rotation mobility tensors of that aggregate, which are determined – accounting for hydrodynamic interactions within the aggregate at the Rotne-Prager-Yamakawa [17, 18] level – using the freely available hydro++ package of García de la Torre and coworkers [19, 20]. Since the aggregates are rigid, this hydrodynamic problem is solved only once for every new aggregate being formed. Our simulations indicate that rotational dynamics does impact the aggregation process of spherical primary particles, resulting in a reduction of the fractal dimension. A paper that recently appeared confirms this observation, though the mobilities employed in that study are not based on the hydrodynamic interactions within the aggregates [13]. The structure of this paper is as follows. The simulation and analysis methods are described in Section 6.2, simulation results on spherical and rod-like primary particles are presented in Section 6.3, and the paper ends with a discussion of the main findings in Section 6.4.

6.2. Methods

6.2.1. Simulation methods

The translational Brownian motion of a rigid colloidal cluster of arbitrary shape is simulated using the equation of motion

$$\mathbf{R}(t+\Delta t) = \mathbf{R}(t) + \boldsymbol{\mu}^{\mathrm{t(s)}}\mathbf{F}^{\mathrm{(s)}}\Delta t + \sqrt{2k_{\mathrm{B}}T\Delta t}\left(\boldsymbol{\mu}^{\mathrm{t(s)}}\right)^{1/2}\boldsymbol{\Theta}^{\mathrm{t}}, \tag{6.1}$$

where $\mathbf{R}$ denotes the position of a reference point on the cluster and Δt is the integration time step. All terms on the r.h.s. are evaluated at time t, before the time step, following the Itô interpretation of stochastic equations. In the second term, $\mathbf{F}^{\mathrm{(s)}}$ represents the total potential-based force acting on the cluster and $\boldsymbol{\mu}^{\mathrm{t(s)}}$ denotes the mobility matrix for translational motion (t), both expressed in the space-fixed coordinate system (s). The balance between this force and the Stokesian drag by the fluid gives rise to a drift velocity linear in $\mathbf{F}^{\mathrm{(s)}}$, and multiplication by the time step yields a displacement. The last term on the r.h.s. accounts for the stochastic Brownian contribution to the cluster's motion, with k_{B} Boltzmann's constant and T the absolute temperature, and where $\boldsymbol{\Theta}^{\mathrm{t}}$ denotes a vector of three random numbers with zero average, unit standard deviation, no correlations between the Cartesian directions and no correlations in time (Markovian). The standard deviations of the random displacements are related to the mobility matrix by the fluctuation-dissipation theorem, as incorporated in the last term of the equation of motion, where $\left(\boldsymbol{\mu}^{\mathrm{t(s)}}\right)^{1/2}$ denotes the symmetric square root of the symmetric mobility matrix.

For a rotating non-isotropic rigid cluster of primary particles, the position of the i^{th} particle can be expressed as

$$\mathbf{r}_i^{\mathrm{(s)}} = \mathbf{A}\mathbf{r}_i^{\mathrm{(b)}} + \mathbf{R}, \tag{6.2}$$

where the superscript (b) refers to the body-fixed frame and $\mathbf{A}$ is a rotation matrix. The reference point on the cluster coincides with the origin of the body-fixed frame.

The mobility tensor is constant in this frame, hence the space-based mobility tensor and its square root rotate with the cluster following

$$\boldsymbol{\mu}^{\mathrm{t(s)}} = \mathbf{A}\boldsymbol{\mu}^{\mathrm{t(b)}}\mathbf{A}^{\mathrm{T}}, \tag{6.3}$$

$$\left(\boldsymbol{\mu}^{\mathrm{t(s)}}\right)^{1/2} = \mathbf{A}\left(\boldsymbol{\mu}^{\mathrm{t(b)}}\right)^{1/2}\mathbf{A}^{\mathrm{T}}. \tag{6.4}$$

The number of time-consuming evaluations of mobility matrices thereby reduces to once for every newly formed cluster. The equation of motion effectively being used reads as

$$\mathbf{R}(t+\Delta t) = \mathbf{R}(t) + \mathbf{A}\boldsymbol{\mu}^{\mathrm{t(b)}}\mathbf{A}^{\mathrm{T}}\mathbf{F}^{\mathrm{(s)}}\Delta t + \sqrt{2k_{\mathrm{B}}T\Delta t}\mathbf{A}\left(\boldsymbol{\mu}^{\mathrm{t(b)}}\right)^{1/2}\boldsymbol{\Theta}^{\mathrm{t}}, \tag{6.5}$$

where the force balance is solved in the body frame and the random displacements are assigned in the body frame, with both followed up by rotations to the space frame.

The orientation of the cluster also follows a Brownian equation of motion. As one of us has shown recently [16], this motion is readily solved by employing unit quaternions $\mathbf{q}$ as the orientation coordinates [21, 22]. The redundancy of using four coordinates and a length constraint, $|\mathbf{q}| = 1$, outweigh the complexities encountered in BD simulations based on three orientation coordinates: the singularities for certain coordinate values as well as subtle terms accounting for the metric of the non-Cartesian coordinate space and the coordinate-dependence of the mobility matrix [16, 23–27]. By virtue of a fortunate cancellation of the latter two terms, the equation of motion in quaternions takes the deceptively simple form [16]

$$\mathbf{q}(t+\Delta t) = \mathbf{q}(t) + \mathbf{B}\boldsymbol{\mu}^{\mathrm{r(b)}}\mathbf{A}^{\mathrm{T}}\boldsymbol{\tau}^{\mathrm{(s)}}\Delta t + \sqrt{2k_{\mathrm{B}}T\Delta t}\mathbf{B}\left(\boldsymbol{\mu}^{\mathrm{r(b)}}\right)^{1/2}\boldsymbol{\Theta}^{\mathrm{r}} + \lambda\mathbf{q}, \tag{6.6}$$

which closely copies the structure of Eq. (6.5). Here $\boldsymbol{\tau}^{\mathrm{(s)}}$ represents the total potential-based torque acting on the cluster in the space frame and $\boldsymbol{\mu}^{\mathrm{r(b)}}$ denotes the rotational mobility tensor in the body-fixed frame. The balance between this torque and the Stokesian torque by the fluid gives rise to an angular drift velocity linear in $\boldsymbol{\tau}^{\mathrm{(s)}}$, solved from the body's perspective in the second term on the r.h.s.. Conversion to a quaternion velocity and multiplication by the time step yields a displacement. Explicit expressions for the (3×3) rotation matrix $\mathbf{A}(\mathbf{q})$ and the (4×3) conversion matrix $\mathbf{B}(\mathbf{q})$ are provided in the Appendix. The elements of the random vector $\boldsymbol{\Theta}^{\mathrm{r}}$ have zero average, unit variance, are uncorrelated, have no memory (Markovian) and are independent of $\boldsymbol{\Theta}^{\mathrm{t}}$. The last term on the r.h.s. of Eq. (6.6) imposes the unit length constraint on the quaternion vector, using a Lagrange multiplier λ that can be solved analytically from a quadratic equation [16].

The simulated clusters, ranging in size from one to hundreds of primary particles, diffuse freely in the absence of potential forces and torques in a quiescent fluid. Any two clusters merge as soon as a particle of the first cluster overlaps with a particle of the second cluster. The hydro++ program [19, 20] is then used to determine the hydrodynamic center and the corresponding mobility matrix of the newly created cluster. This center defines the reference position $\mathbf{R}$, and all space-based particle positions $\mathbf{r}_i^{(\mathrm{s})}$ can now be converted in their body-based counterparts $\mathbf{r}_i^{(\mathrm{b})}$ by defining the body-based coordinate axes as momentarily aligned with the space-based

coordinate axes, *i.e.* $\mathbf{A} = \mathbf{1}$ for a newly created cluster. The mobility matrices $\boldsymbol{\mu}^{\mathrm{t(b)}}$ and $\boldsymbol{\mu}^{\mathrm{r(b)}}$ are extracted as the two (3×3) block-diagonal elements of the (6×6) mobility matrix calculated by hydro++. We verified that, for the clusters grown in the simulations, the elements of the off-diagonal blocks are considerably smaller than those of the diagonal blocks, and hence that coupling between translational and rotational Brownian displacements may safely be ignored. During the course of this work an extended simulation algorithm was developed that can handle cross-terms in the mobility matrix, *i.e.* forces giving rise to rotations and torques giving rise to translations, along with the corresponding coupling between the rotational and translational random displacements [28]. Several simulations were rerun using this algorithm, thereby establishing that these contributions indeed are of a minor importance for the aggregation dynamics in quiescent fluids. For clarity, we stress that all bonds are permanent: the clusters do not restructure (which tends to result in compactation), nor do clusters break up.

All simulations were performed using cubic boxes of constant size L_{b}, with periodic boundary conditions in all three Cartesian directions. The number of primary particles was fixed at $N_{\mathrm{p}} = 16,384$ (2^{14}), except for a few runs to explore system size dependencies. Typical particle volume fractions ϕ were in the range 10^{-3} and 10^{-2}. The diameter σ of the spherical mono-disperse primary particles was taken as the unit of length, the units of energy and time were ϵ and τ, respectively. In these units, the thermal energy was set at $k_{\mathrm{B}}T = 1\epsilon$, the solvent viscosity at $\eta = 1\epsilon\tau/\sigma^3$, and the time step at $\Delta t = 10^{-3}\tau$. To facilitate the conversion to experimental units, for colloidal particles of 100 nm diameter in water at room temperature the time unit corresponds to $\tau \approx 0.25$ ms. Initial configurations were prepared by sequentially placing primary particles at random positions in the simulation boxes, excluding those insertions that produced overlap with previously introduced particles. The system was further equilibrated by a short simulation with a purely repulsive Weeks-Chandler-Anderson potential interacting between the particles. Production runs, using the scheme outlined above, were discontinued when the largest inter-particle distance within a newly formed cluster exceeded half the box size. Most numerical results presented in the next section are averages over five independent runs corresponding the same macroscopic parameters but differing in their initial microscopic configurations; the variation between these runs was used to estimate error bars on selected data points. In several cases the averaging was extended to 25 runs to enhance sampling.

6.2.2. Analysis methods

Previous studies have shown that the number of clusters $n_s(t)$ containing s particles at time t evolves as

$$n_s(t) \approx s^{-2} f\left(\frac{s}{t^z}\right), \tag{6.7}$$

where f is a master function that depends on the dynamical properties of the clusters, their reaction kinetics and the overall particle density, and likewise for the power z. The prefactor is dictated by conservation of the number of primary parti-

cles,

$$N_{\mathrm{p}} = \sum_s s n_s(t) \approx \int s^{-1} f\left(\frac{s}{t^z}\right) ds = \int x^{-1} f\,(x)\, dx, \tag{6.8}$$

where the last integral, with $x = s/t^z$, clearly is independent of time. The average number of clusters at time t then reads as

$$N_{\mathrm{c}}(t) = \sum_s n_s(t) \approx \int s^{-2} f\left(\frac{s}{t^z}\right) ds = t^{-z} \int x^{-2} f\,(x)\, dx, \tag{6.9}$$

and therefore, with the last integral being constant, $N_{\mathrm{c}} \propto t^{-z}$. The evolving average cluster size $S(t)$ can be calculated from the cluster perspective, $i = 0$, by running over all clusters and averaging their sizes, and from the particle perspective, $i = 1$, by running over all particles and averaging the sizes of the clusters they belong to,

$$S_i(t) = \frac{\sum_s s^{i+1} n_s(t)}{\sum_s s^i n_s(t)} \propto t^z. \tag{6.10}$$

Since $S_0(t) = N_{\mathrm{p}}/N_{\mathrm{c}}(t)$, we will henceforth follow the common practice of defining $S = S_1$. For noise reduction purposes, it proves convenient to introduce the cumulative size distribution,

$$N_s(t) = \sum_{i=1}^{s} n_i(t) \approx s^{-1} g\left(\frac{s}{t^z}\right), \tag{6.11}$$

where the master function g is related to its counterpart by $f(x) \approx x g'(x) - g(x)$. One readily confirms that $N_{\mathrm{c}}(t) = N_\infty(t)$ and $N_{\mathrm{p}} = N_1(0)$.

The stickiness of the primary particles results in the formation of disordered structures with fractal properties. The radius of gyration R_{g} measures the average distance between all particles in a cluster and the center of mass of that cluster, $\mathbf{R}_{\mathrm{com}}$, which is equivalent to the average distance between any two particles in a cluster,

$$R_{\mathrm{g}}^2 = \frac{1}{s} \sum_{i=1}^{s} \left|\mathbf{r}_i^{(\mathrm{s})} - \mathbf{R}_{\mathrm{com}}\right|^2 = \frac{1}{s^2} \sum_{i=1}^{s-1} \sum_{j=i+1}^{s} \left|\mathbf{r}_i^{(\mathrm{b})} - \mathbf{r}_j^{(\mathrm{b})}\right|^2. \tag{6.12}$$

The expected power-law scaling of the radius of gyration with cluster size yields the exponent $1/d_{\mathrm{f}}$.

6.3. Results

6.3.1. Spherical particles

In the simulations, aggregation of the spherical primary particles starts rapidly after the stickiness of the particles is turned on. Following a transient period, a power-law growth sets in of the average cluster size, see Fig. 6.2 (left), while simultaneously

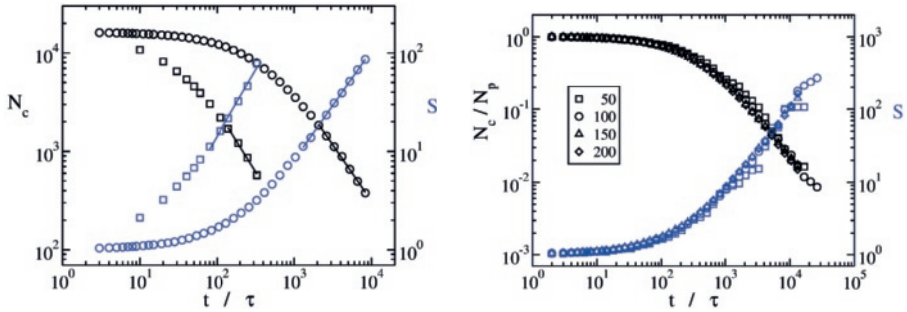

Figure 6.2: Total number of clusters N_c (black) and the mean cluster size S (blue) as functions of time for aggregating suspensions in the standard box of $N_\mathrm{p} = 16,384$ primary particles (left) at colloidal volume fractions of 10^{-3} (○) and 10^{-2} (□). The straight lines for $S \geq 10$ and $N_\mathrm{c} \leq N_\mathrm{p}/10$ are power-law fits, yielding the exponents z plotted in Fig. 6.3. Near coalescence (left) of the normalized number of clusters (black) and the average cluster size (blue) for four box sizes (see L_b in legend, in units of σ; the largest of these systems contains 15278 particles) at the same volume fraction, $\phi = 10^{-3}$.

the number of clusters decays following a power law. In a comparison of equally dense system of various sizes, see Fig. 6.2 (right), the data for $S(t)$ nearly coalesce while the data for $N_\mathrm{c}(t)$ coalesce after scaling by N_p; this suggests that the system size used in the production runs is sufficiently large to eliminate system size dependencies. The transient period is shorter, and the growth of the average cluster size proceeds faster, at higher particle volume fractions. The powers z extracted by fitting $S \propto t^z$ and $N_\mathrm{c} \propto t^{-z}$ are plotted as functions of the particle volume fraction in Fig. 6.3. For the lowest concentrations the power z is slightly above unity, corresponding to an average cluster size growing almost linearly in time, followed by a steady rise of the power with volume fraction until a plateau of nearly 1.4 (based on N_c) or nearly 1.5 (based on S) is reached for volume fractions exceeding $\phi \approx 5 \cdot 10^{-3}$.

The simulations were discontinued when the largest span of an aggregate exceeded half the box length. This termination time scales with the volume fraction as $t \propto \phi^{-1.94}$. But since the number of primary particles was kept fixed, the corresponding final cluster sizes also vary with the volume fraction. The elapsed time to grow aggregates of identical sizes was therefore also determined, for which the radius of gyration was used. The time elapsed to reach a fixed value, selected as just below the maximum attained R_g in the densest system, is shown in Fig. 6.4 to scale as $t \propto \phi^{-1.37}$.

The size distribution $n_s(t)$ extracted from the simulations at $\phi = 2 \cdot 10^{-3}$ is presented in Fig. 6.5, as a function of time after binning by cluster size (left) and as a function of cluster size after binning by time (right). Dashed lines indicate common tangents, and the dotted line the power law scaling of n_s at larger times. It is notable that the common tangent in the right plot does not yield the universal tangent slope of -2 proposed by Meakin *et al.* [5], which was argued to 'provide[s] a strong support for the scaling form' of Eq. (6.7). Even though deviating from this universal tangent, the simulation results still faithfully follow the scaling form,

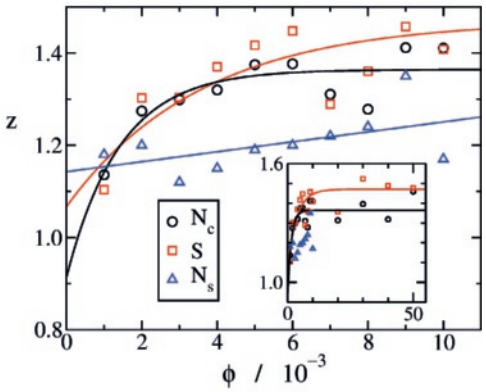

Figure 6.3: Scaling exponents for the time, z, extracted from the power law behaviours of the number of clusters (circles) and the average cluster size (squares), see Fig. 6.2, as well as from the coalescence of cumulative cluster size distributions onto a master curve (triangles), see Fig. 6.8. The smooth lines are guides to the eye.

as can be seen in Fig. 6.6 where the master function $f(s/t)$ is pieced together by overlaying the distributions at various times and sizes. If the size distribution follows the master function of Eq. (6.7), the two plots in Fig. 6.6 ought to be mirror images. Superficially they are, but closer inspection reveals that the shallow slopes (at low s/t) and the steep slopes (at s/t) do not fully agree. These deviations are attributed to the limited amount of data to analyse, the resulting use of bins to compensate, and the inaccuracies in visually overlaying the various curves. The resulting aggregate size distribution, shown in Eq. (6.7), agrees with theoretical predictions [29], experimental observations [3] and simulations with scaling-law diffusion dynamics [30]: the number of clusters varies relatively weakly with s up to a time-dependent maximum, close to the mean cluster size $S_0(t)$, and subsequently decays rapidly.

Cumulative size distributions were extracted at regular intervals during the simulations. Size-weighted cumulative distributions, see Eq. (6.11), are presented in Fig. 6.8 for two volume fractions. Plotted as functions of t/s, the scatter plot looks like a wide line. But upon rescaling time to t^z, using a distinct z for every volume fraction, the data coalesce to an appreciably thinner line, confirming the existence of a master curve $g(s/t^z)$ (which could, though, still depend on ϕ). The powers z obtained at ten volume fractions are included in Fig. 6.3; the are distributed around $z \approx 1.2$ and show a weak tendency to rise with ϕ. The master curve $g(s/t^z)$ provides an alternative route to the cluster size distribution $g(s/t^z)$, as discussed in Section 6.2.2. As this route requires differentiation, the coalesced data points were fitted [31], see Fig. 6.8, to allow numerical differentiation. The resulting curve, shown in Fig. 6.6, has the same global shape as the master curves that were pieced together. The slope of 2.17 at low s/t^z nearly matches with the pieced-together curve in the left panel, but is slightly lower than that of the pieced-together curve on the right. A steep decay sets in for $s/t^z > 10^{-2}\tau^{-z}$, with a slope that is sensitive

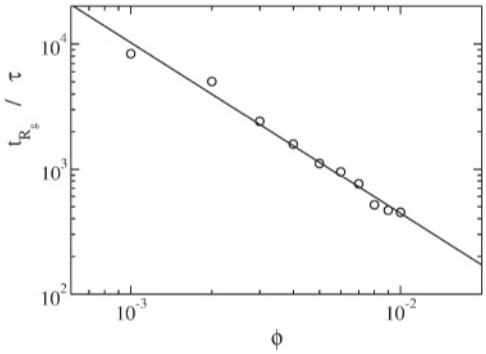

Figure 6.4: The time taken till the largest radius of gyration of the growing aggregates reaches a fixed value, close to the maximum R_g attained by the densest system, across a range of volume fractions. The solid line is a power-law fit with an exponent of -1.37.

to the details of the fit of $g(s/t^z)$. The deviations between the various approaches to f are attributed to the binning procedures, the limited amount of data to analyse, and the inaccuracy in overlaying the various curves by the eye.

As can be seen in Fig. 6.8, the master curves $g_\phi(s/t^z)$ of the size-weighted cumulative size distributions vary with volume fraction but have a similar shape. They can be made to coalesce into a single master function by introducing a scaling parameter $\alpha(\phi)$ that varies with the volume fraction. Defining the f_ϕ at the lowest volume fraction as the reference, $\alpha(10^{-3}) = 1$, the values for other volume fractions are obtained by overlapping the various data sets (by visual inspection). For low volume fractions α is inversely proportional with the volume fraction, and hence with the number density, indicating the existence of a master function

$$N_s(t) \propto s^{-1} h\left(\frac{s}{\phi\, t^{z(\phi)}}\right) \tag{6.13}$$

in this regime the existence of a master function. It is tempting to speculate that the deviation from ϕ^{-1} scaling at higher volume fractions originates in the non-negligibility of the volume of the particles.

The fractal dimension of the collection of aggregates is deduced from the power-law relation between cluster size and radius of gyration, as shown in Fig. 6.10, excluding monomers since their R_g is undefined. Evaluation of the power as a function of elapsed time yields the curves in Fig. 6.11. The fractal dimension is seen to steadily rise with time, indicating that the aggregates gradually become compacter. It appears that the fractal dimension has not converged at the termination of the simulations. Extrapolation of the data, however, is not likely to reach the accepted limit for DLCA of $d_f \approx 1.75$. Since this value was established for aggregates performing translational motion only, additional simulations were performed with disabled rotational dynamics leaving all other properties unchanged. As shown in Fig. 6.11, the absence of rotations results in a substantial increase of the fractal dimension of the aggregates, which now approaches the accepted limiting value.

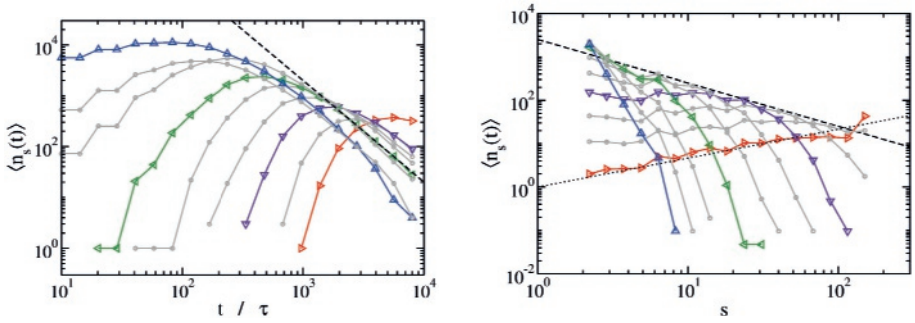

Figure 6.5: The cluster size distribution $n_s(t)$ as function of time at several sizes (left) and as function of size at several times (right), averaged over 20 simulations at $\phi = 2 \cdot 10^{-3}$. In the left (right) plot, with increasing size (time) the distribution is represented by triangles pointing up (blue), left (green), down (purple) and right (red), with intermediate lines in grey. The intervals between the curves grow exponentially, *i.e.* are equally distributed on a logarithmic scale, with sizes ranging from 1 to 150 (left) and times ranging from 30τ to 6500τ (right). For statistical purposes, averages are taken over all sizes within the exponentially growing bins, thus including every cluster in the plotted curves. In the left plot the slope of the dashed line is -2, in the right plot the slopes of the dashed and dotted lines are -1 and $2/3$, respectively.

It is also notable that eliminating the rotations more than doubles the average time required to reach the termination condition of the simulations, *i.e.* an intra-cluster span exceeding half the box length.

The impact of the aggregates's mobilities on the aggregation process is further explored by comparing the hydrodynamics-based mobilities employed thusfar against the commonly used scaling law of the translation mobility $\mu_s = \mu_1 s^{-\gamma}$ in the absence of a rotation mobility. Figure 6.12 indicates, as expected, that a reduction of the diffusive motion of aggregates – by increasing γ from unity, as in the Rouse model for polymers, to 1.8, *i.e.* equating γ to the expected d_f – results in a slowing down of the aggregation process and hence in a lower power z. It is notable that the system with hydrodynamics and rotation aggregates faster than either of these purely translational systems.

6.3.2. Rods

The shape of the primary particles affects the aggregation process, as elongated particles are known to form percolating networks at lower volume fractions than spherical particles[32, 33]. The shape selected here is a cylinder of diameter $D = 1\sigma$ capped by two hemispheres of the same diameter, resulting in a tip-to-tip length L and an aspect ratio $p = L/D$. Detection of overlap of two of these particles is fairly straightforward. Mobility matrices are obtained by approximating the rods as linear chains of touching spherical particles of diameters equal to those of the rods; with this substitution in mind, only integer aspect ratios are selected. The same substitution is also used when determining fractal dimensions, where the monomers are now included in the scaling law. Since the phase diagram of a suspension of rods is not determined by the volume fraction but by $(L/D)\phi$, the latter product will

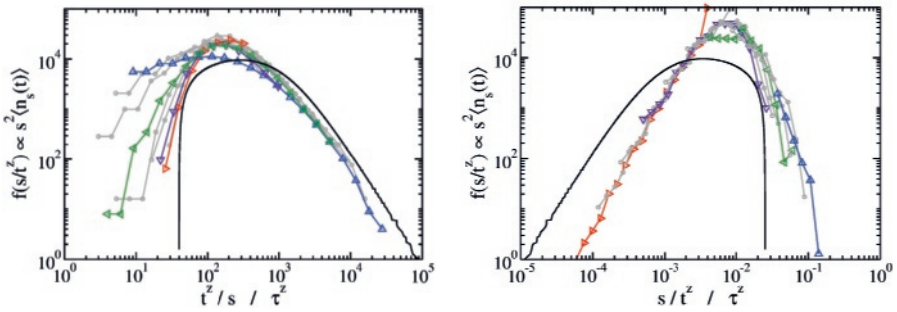

Figure 6.6: Reconstruction of the master function $f(s/t)$. The coloured and grey curves on the left and right are obtained by shifting the data on the left and right in Fig. 6.5 along the horizontal axis through division by s and t^z, respectively, assuming $z = 1.2$, followed by shifting each curve vertically to attain approximate coalescence (by visual inspection). The two plots resemble mirror images, as they should be if they follow the same master function; note that the two horizontal axes are mirror images, $\ln(t/s) = -\ln(s/t)$. Also shown, as solid black lines, is the master function extracted from the cumulative size distribution of Fig. 6.8.

appear frequently in the analysis.

The evolution of the number of cluster and their average size for spheres and rods of two aspect ratios, for the three systems sharing $(L/D)\phi = 10^{-2}$ and $L_b = 275\sigma$, is depicted in Fig. 6.13. With increasing aspect ratio the mobilities of the rods decrease and consequently the aggregation slows down. But the size of the aggregate still benefits from the aspect ratio, hence the largest intra-aggregate span reaches half the box size for a considerably lower average aggregate size – it even appears that $p = 5$ and 17 reach this size at about the same time. The termination times of simulations at constant $(L/D)\phi$ show less variation for nominal aspect ratios ($p <= 30$) with a sharp drop for ($p = 45$), see Fig. 6.14. Simulations at constant volume fraction show a much stronger dependence, $t = 0.75 - 0.21 \ln p$. A dependence on the logarithm of the aspect ratio was predicted on theoretical grounds [34], with the logarithm originating in the diffusion constant of the rods. The negative termination times upon extrapolation of the current data to higher aspect ratios suggest that the random depositions of rods produces a percolating network under those conditions.

The fractal dimension of aggregates of rods increases with time, see Fig. 6.15, reminiscent of the aggregates of spheres. The values at the end of the run are again below the classical DLCA limit, the more so as the rods are more elongated; these final values are collected in Fig. 6.16. By switching to larger box sizes, this time using a constant number of particles and a constant volume fraction, it is found that the aggregates at the end of the simulation exceed the DLCA limit for spheres, for aspect ratios around ten and higher. The fractal dimension at first increases approximately linear with p, while leveling off at higher p, as was also observed in experiments [33].

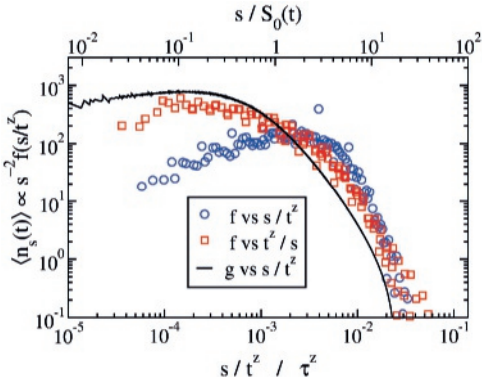

Figure 6.7: Reconstructed aggregate size distributions as function of size, with the size s rescaled relative to the elapsed time (bottom axis) and the mean cluster size (top axis), with $S_0(t) = N_p/N_c(t)$. The distributions are normalized to unit area on a linear scale.

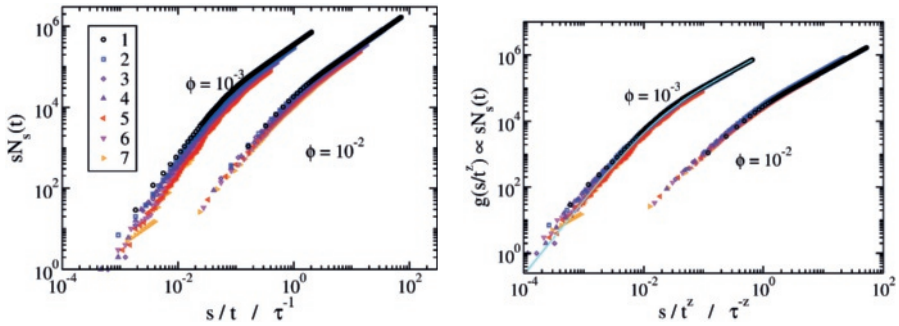

Figure 6.8: Size-weighted cumulative size distributions for volume fractions $\phi = 10^{-3}$ and 10^{-2}. The horizontal axis on the left denotes s/t, the axis on the left is rescaled to s/t^z with the employed values of z – one for each volume fraction – selected to maximize the overlap of the data (by visual inspection). The legend indicates elapsed time intervals since the start of the aggregation process, with an interval $5.4 \cdot 10^3\tau$ for $\phi = 10^{-3}$ and 60τ for $\phi = 10^{-3}$. The cyan line in the right panel is a fit.

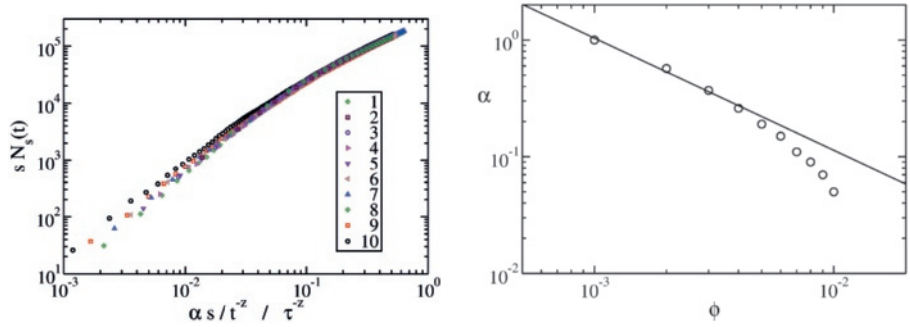

Figure 6.9: The master curves of Eq. (6.8) coalesce to a master curve that is independent of the volume fraction, by shifting along the horizontal axis (left). The volume fractions are indicated in the legend, as multiples of 10^{-3}. The scaling parameter α, which maps the individual master functions onto that of the lowest volume fraction, scales as a power law in the volume fraction (right).

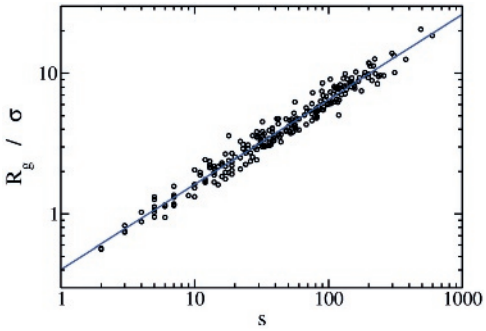

Figure 6.10: Scatter plot of the radius of gyration, R_g, versus the number of primary particles, s, for all clusters present at $t = 5 \cdot 10^3 \tau$ into the aggregation process at $\phi = 2 \cdot 10^{-3}$. Monomers are excluded from the graph. The fractal dimension d_f extracted from the power-law fit evolves in time, see Fig. 6.11.

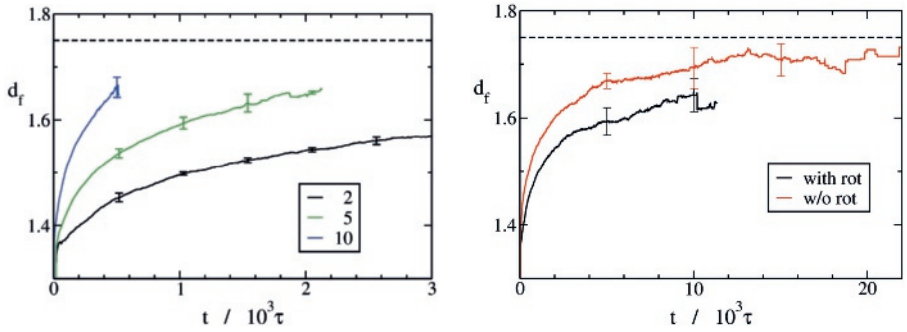

Figure 6.11: The fractal dimensions d_f, as extracted from power-law fits to the radius of gyration, see Fig. 6.10, as a function of time. Simulations at three volume fractions (left, with values of $10^3\phi$ indicated in the legend) struggle to reach the accepted limiting value of $d_f \approx 1.75$ in DLCA (dashed bar). The error bars indicate standard deviations over 5 to 25 uncorrelated simulations. Disabling the rotational dynamics of the aggregates (right, $\phi = 2 \cdot 10^{-3}$) results in a marked increase of the fractal dimension.

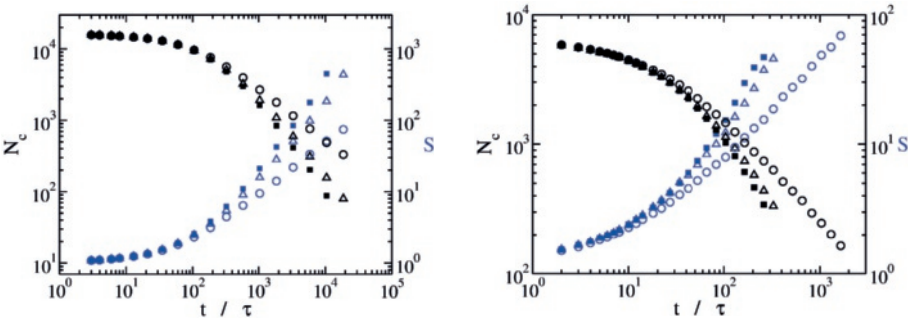

Figure 6.12: Total number of clusters N_c (black) and the mean cluster size S (blue) as functions of time for simulations including internal hydrodynamic interactions and rotational dynamics (filled markers), and simulations with non-rotating clusters (empty markers) assuming diffusion coefficients scaling as $\mu_s = \mu_1 s^{-1}$ (triangles) and as $\mu_s = \mu_1 s^{-1/1.8}$ (circles), for volume fractions of $2 \cdot 10^{-3}$ (left) and 10^{-2} (right).

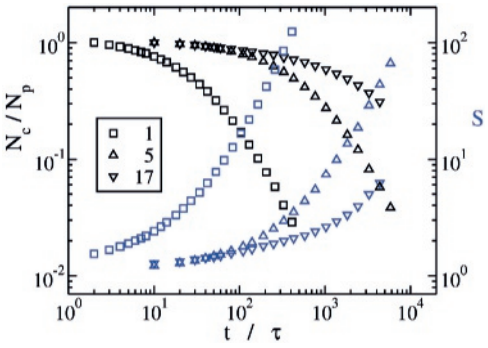

Figure 6.13: Total number of clusters N_c (black) and the mean cluster size S (blue) as functions of time for aggregating suspensions of spheres and rods at $(L/D)\phi = 10^{-2}$ and $L_b = 275\sigma$. Aspect ratios $p = L/D$ are indicated in the legend.

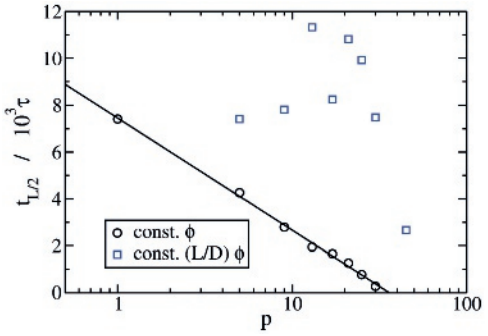

Figure 6.14: The time taken till the largest span within an aggregate of rods reaches half the box size, versus the aspect ratio p of the rods, at constant volume fraction $\phi = 2 \cdot 10^{-3}$ and at constant $(L/D)\phi = 10^{-2}$, in boxes of the same size. The solid line is a fit.

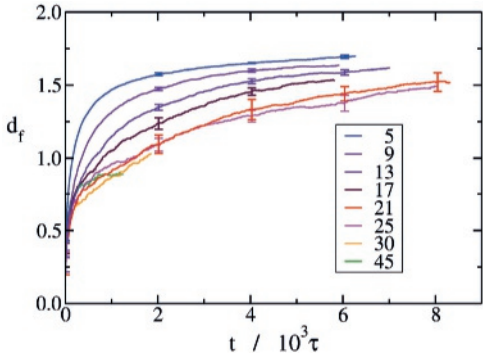

Figure 6.15: Fractal dimensions as functions of time during the aggregation of rods of various aspect ratios (see legend), at $(L/D)\phi = 10^{-2}$ and $L_b = 275\sigma$. The error bars indicate standard deviations over 5 runs. The dashed line represents the classical DLCA limit.

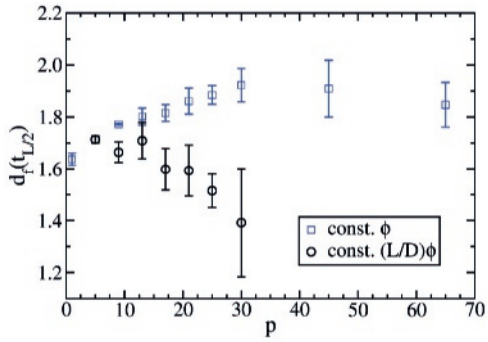

Figure 6.16: Fractal dimensions at the termination of the simulation, in simulations of rods, plotted against the aspect ratio of the rods. One set of simulations was performed at at $(L/D)\phi = 10^{-2}$ and $L_b = 275\sigma$ (black circles, see also Fig. 6.15), the other set uses 16,384 rods at $\phi = 2 \cdot 10^{-3}$ (blue squares).

6.4. Discussion and conclusions

Rotational diffusion dynamics reduces the fractal dimension of aggregates formed by diffusion limited aggregation, and increases the rate of the aggregation process. Adding rotational diffusion to translational diffusion increases the displacements of the primary particles in an aggregate, and thereby increases the probability of an aggregate coming into contact with another aggregate, resulting in their permanent fusion. We speculate that rotational diffusion enables these contacts to occur at larger distances between the centers of the aggregates, and thereby results in aggregates that are more elongated and posses a lower fractal dimension. It should be noted that the fractal dimension steadily increases with the elapsed time since the onset of aggregation. Hence, it can not be ruled out that aggregates subject to rotational motion may eventually recover the traditional fractal dimension on time scales far longer than considered here.

6.5. Acknowledgments

This work is part of the 'Computational Sciences for Energy Research' program of the Netherlands Organisation for Scientific Research (NWO) under Project Nr. 13CSER060. This research programme is co-financed by Shell Global Solutions International B.V..

References

[1] D. W. Schaefer, J. E. Martin, P. Wiltzius, and D. S. Cannell, *Fractal geometry of colloidal aggregates,* Phys. Rev. Lett. **52**, 2371 (1984).

[2] T. A. Witten Jr and L. M. Sander, *Diffusion-limited aggregation, a kinetic critical phenomenon,* Phys. Rev. Lett. **47**, 1400 (1981).

[3] M. Y. Lin, H. M. Lindsay, D. A. Weitz, R. C. B. R. Klein, R. C. Ball, and P. Meakin, *Universal diffusion-limited colloid aggregation,* J. Phys. Condens. Matt. **2**, 3093 (1990).

[4] T. Vicsek and F. Family, *Dynamic scaling for aggregation of clusters,* Phys. Rev. Lett. **52**, 1669 (1984).

[5] P. Meakin, T. Vicsek, and F. Family, *Dynamic cluster-size distribution in cluster-cluster aggregation: Effects of cluster diffusivity,* Phys. Rev. B **31**, 564 (1985).

[6] D. A. Weitz and M. Oliveria, *Fractal structures formed by kinetic aggregation of aqueous gold colloids,* Phys. Rev. Lett. **52**, 1433 (1984).

[7] A. J. Hurd and D. W. Schaefer, *Diffusion-limited aggregation in two dimensions,* Phys. Rev. Lett. **54**, 1043 (1985).

[8] J. Stankiewicz, M. A. C. Vílchez, and R. H. Alvarez, *Two-dimensional aggregation of polystyrene latex particles,* Phys. Rev. E **47**, 2663 (1993).

[9] P. Meakin and F. Family, *Structure and kinetics of reaction-limited aggregation,* Phys. Rev. A **38**, 2110 (1988).

[10] W. Heinson, C. Sorensen, and A. Chakrabarti, *Does shape anisotropy control the fractal dimension in diffusion-limited cluster-cluster aggregation?* Aerosol Sci. Technol. **44**, i (2010).

[11] M. Lattuada, H. Wu, and M. Morbidelli, *A simple model for the structure of fractal aggregates,* J. Colloid Interface Sci. **268**, 106 (2003).

[12] S. Babu, J.-C. Gimel, and T. Nicolai, *Diffusion limited cluster aggregation with irreversible slippery bonds,* Eur. Phys. J. E **27**, 297 (2008).

[13] S. Jungblut, J.-O. Joswig, and Eychmüller, *Diffusion-limited cluster aggregation: impact of rotational diffusion,* J. Phys. Chem. C **123**, 950 (2019).

[14] R. K. Chakrabarty, H. Moosmüller, W. P. Arnott, M. A. Garro, G. Tian, J. G. Slowik, E. S. Cross, J.-H. Han, P. Davidovits, T. B. Onasch, *et al.*, *Low fractal dimension cluster-dilute soot aggregates from a premixed flame,* Phys. Rev. Lett. **102**, 235504 (2009).

[15] M. Sander, R. I. Patterson, A. Raj, and M. Kraft, *Comment on "low fractal dimension cluster-dilute soot aggregates from a premixed flame",* Phys. Rev. Lett. **104**, 119601 (2010).

[16] I. M. Ilie, W. J. Briels, and W. K. den Otter, *An elementary singularity-free rotational brownian dynamics algorithm for anisotropic particles,* J. Chem. Phys. **142**, 114103 (2015).

[17] J. Rotne and S. Prager, *Variational treatment of hydrodynamic interaction in polymers,* J. Chem. Phys. **50**, 4831 (1969).

[18] H. Yamakawa, *Transport properties of polymer chains in dilute solution: hydrodynamic interaction,* J. Chem. Phys. **53**, 436 (1970).

[19] B. Carrasco and J. García de la Torre, *Improved hydrodynamic interactions in macromolecular bead models,* J. Chem. Phys. **111**, 4817 (1999).

[20] J. García de la Torre, G. del Rio Echenique, and A. Ortega, *Improved calculation of rotational diffusion and intrinsic viscosity of bead models for macromolecules and nanoparticles,* J. Phys. Chem. B **111**, 955 (2007).

[21] M. P. Allen and D. J. Tildesley, *Computer Simulations of Liquids* (Clarendon, Oxford, 1987).

[22] H. Goldstein, *Classical mechanics*, 2nd ed. (Addison-Wesley, Reading, MA, U.S.A., 1980).

[23] S. N. Naess and A. Elgsaeter, *Use of Cartesian rotation vectors in Brownian Dynamics algorithms: theory and simulation results,* Macromol. Theory Simul. **13**, 419 (2004).

[24] T. R. Evensen, A. Elgsaeter, and S. N. Naess, *Transient molecular electro-optics: Cartesian rotation vector versus eulerian angles,* Colloids Surf., B **56**, 80 (2007).

[25] T. R. Evensen, S. N. Naess, and A. Elgsaeter, *Free rotational diffusion of rigid particles with arbitrary surface topology: a Brownian Dynamics study using Eulerian angles,* Macromol. Theory Simul. **17**, 121 (2008).

[26] T. R. Evensen, S. N. Naess, and A. Elgsaeter, *Brownian Dynamics simulations of rotational diffusion using the Cartesian components of the rotation vector as generalized coordinates,* Macromol. Theory Simul. **17**, 403 (2008).

[27] T. R. Evensen, S. N. Naess, and A. Elgsaeter, *Use of the rotation vector in Brownian Dynamics simulation of transient electro-optical properties,* Macromol. Theory Simul. **18**, 50 (2009).

[28] D. Palanisamy and W. K. den Otter, *Efficient brownian dynamics of rigid colloids in linear flow fields based on the grand mobility matrix,* J. Chem. Phys. **148**, 194112 (2018).

[29] R. J. Cohen and G. B. Benedek, *Equilibrium and kinetic theory of polymerization and the sol-gel transition,* J. Phys. Chem. **86**, 3696 (1982).

[30] M. Lach-Hab, A. E. González, and E. Blaisten-Barojas, *Concentration dependence of structural and dynamical quantities in colloidal aggregation: computer simulations,* Phys. Rev. E **54**, 5456 (1996).

[31] The function being used is $g(x) = \alpha x^{\beta}/(1+\gamma x^{\delta})$, where the greek letters are fit parameters.

[32] A. P. Philipse, *The random contact equation and its implications for (colloidal) rods in packings, suspensions, and anisotropic powders,* Langmuir **12**, 1127 (1996).

[33] A. Mohraz, D. B. Moler, R. M. Ziff, and M. J. Solomon, *Effect of monomer geometry on the fractal structure of colloidal rod aggregates,* Phys. Rev. Lett. **92**, 155503 (2004).

[34] A. P. Philipse and A. M. Wierenga, *On the density and structure formation in gels and clusters of colloidal rods and fibers,* Langmuir **14**, 49 (1998).

6.A. Appendix

A rotation matrix $\mathbf{A}$ can be parameterized with a unit length quaternion vector $\mathbf{q}$ following

$$\mathbf{A} = \begin{pmatrix} q_0^2 + q_1^2 - q_2^2 - q_3^2 & 2q_1q_2 - 2q_0q_3 & 2q_1q_3 + 2q_0q_2 \\ 2q_1q_2 + 2q_0q_3 & q_0^2 - q_1^2 + q_2^2 - q_3^2 & 2q_2q_3 - 2q_0q_1 \\ 2q_1q_3 - 2q_0q_2 & 2q_2q_3 + 2q_0q_1 & q_0^2 - q_1^2 - q_2^2 + q_3^2 \end{pmatrix}, \tag{6.14}$$

where the four elements of the quaternion have been labelled with ordinal numbers zero to three. In Eq. (6.6), the matrix

$$\mathbf{B} = \frac{1}{2}\begin{pmatrix} -q_1 & -q_2 & -q_3 \\ q_0 & -q_3 & q_2 \\ q_3 & q_0 & -q_1 \\ -q_2 & q_1 & q_0 \end{pmatrix} \tag{6.15}$$

is used to convert angular velocities in the body-fixed frame to quaternion velocities.

7

Conclusion and Outlook

The aim of thesis was development of computer model to better understand the shear rheology of colloidal aggregates for flow batteries. We started by focusing on the aggregation kinetics of carbon black colloidal particles. A simple aggregation model was created by employing Brownian dynamics and rigid multi-bead hydrodynamic model. We performed equilibrium simulations and observed the effects of rotational diffusion on aggregation, detailed in Chapter 6. However we were unable to study cluster aggregation under shear due to lack of shear-to-translation mobilities in literature. This led to the development of an quaternion-based Brownian algorithm in Chapter 2. We had extended the mobility calculations to include shear-to-translation coupling terms thereby enabling simulation of arbitrary shaped particles in flow-fields. As a by-product we obtained the stress experienced by the Brownian particles enabling estimation of suspension viscosities. We created an open-source version of our mobility calculation method, `Oseen11` available here: `www2.msm.ctw.utwente.nl/Oseen11`. In Chapter 3 we showcased the versatility of our algorithm by performing shear rheology on various shaped particles and comparing them against existing analytical results and shear-thinning models. The probing of shear-viscosities led to the curiosity of evaluating viscosities from equilibrium simulations via Green-Kubo relations. We identified the shortcomings of existing stress evaluation schemes and improved them by incorporating fluctuating stresslets, in Chapter 4. In particular the extended fluctuation-dissipation theorem presented in Chapters 4, 5 is a first of its kind and would go a long in improving the stress calculation from Brownian simulations. Since equilibrium viscosity analyse are orders of magnitude faster compared to non-equilibrium shear computations. A combination of our new Brownian dynamics algorithm in Chapter 2 with stress evaluation schemes in Chapters 4, 5 and analyze methods in Chapters 3, 6 will form the necessary toolkit for simulation and analysis of any arbitrary shaped particles under external force fields, linear flow fields and Brownian motion.

Outlook

There are several possible avenues of research that could be established by building upon the conclusions from the thesis. We enumerate a couple of them below

1. The extended hydrodynamic mobilities derived by us are currently limited to a single arbitrary shaped particle. Even though this could be easily extended for particle-particle interactions by constructing bigger grand mobility matrices for multiple particles, it will be extremely memory intensive, limiting the system size to a few hundred particles. A coarse-grained way of incorporating leading order particle interactions will be an interesting and essential aspect of research.

2. The theories on fluctuating stresslets and BD / aggregation algorithms developed in thesis can be seamlessly combined to model complex phenomena. For e.g. simulating aggregation process under flow and computing the system viscosities which can serve as an universal modelling platform in areas like colloidal suspensions, flow batteries, bio-macromolecular flows, etc.

3. The colloidal clusters in our simulations were rigidified for the sake of computational efficiency. However real-life systems are not bound by such restraints, thus trying to incorporate cluster flexibility like restructuring, breakup can be a challenging line of study in future.

8

Acknowledgements

First and foremost, I would like to thank Prof. Stefan Luding for offering me the PhD position and the opportunity to work at Multi-Scale Mechanics Group. You were always a source of motivation throughout the PhD. And the level of scientific freedom you gave me and the others in group was unparalleled. This led us to explore the uncharted territories of science boldly and come up with new and interesting research findings at the end. Thanks to your wife Gerlinde, always a warm and gentle soul. Your constant support and guidance helped me in finishing mt PhD with ease.

Next I would like thank my supervisor Dr. Wouter den Otter, for guiding me throughout the PhD. You are probably the smart person I have ever come across with expertise in wide ranging fields of science and mathematics. All the day-to-day discussions we had and hands-on training were an invaluable asset to me. Thank you for teaching me how to do research in the right and rigorous way, I am happy to see the things we were able accomplish from writing new codes to new algorithms and finally even new equations. It was exciting to dive deep into the fundamentals and your simple explanations were always a guiding light for me to navigate. It's been a privilege working with you. And I would like to thank all my committee members for evaluating my thesis and being part of my graduation.

Now it's time to thank the colleagues and members of MSM. First Sylvia, you are the kindest and happiest person I ever met, always being cheerful and cheering all the gloomy science nerds surrounding you 😄!. From the first day onwards you took care of all the logistical things which made my stay at Enschede a pleasant and memorable one. Thank you for assisting me in busier times and helping us stay positive. Next is Thejas and Jagruti (Joki), It's difficult even to thank you guys separately as you both were there for me together always like a brother-sister duo. I can't imagine how I would have finished my PhD without your friendly support. You both were an integral part of social life from all the home visits to weekend trips. All the scientific discussions I had with Thejas were invigorating and helped me to sharpen my viewpoint. And it was nice to visit your parents in Bangalore

and be in touch with them. Joki you are the most take-it-easy type person I met, always helping me to stay less stressed and be more lively. Thank you for being there for me always 😊. And Jagurti's husband, Amit you are such a charismatic person always thinking how you can improve yourself. I admire your energy and you kindness to stuff me with so so much food whenever I visit your place 😂. Thanks Hao for your heart-warming friendship from the beginning of PhD till the end. It was great socializing with you and get to know so much about the Chinese culture. You always welcomed me to your home with open heart and it was nice to meet your wife, Yidan. And always fun to hangout with your daughter Iris, and now the little one. Thanks to Hong and your wife, Xinyan for the friendship. Thanks Hamid for being such a great buddy, I always admired your optimism. We were the best duo in Volleyball !!. Thanks Ranisha, Roeland for the friendship and joining us in our Volleyball sessions. I would like to thank Deepak, Sampann and Youssef for the fun times we had hanging out and going to Ali Baba restaurant with Anthony literally like every other day!!. Thanks to Vanessa, Thomas, Anthony for your support and friendship. Thanks Wouter den Breeijen for all the technical support and always helping me in hour of need.

I would like to take this opportunity to thank my former and current labmates - Bert, Marnix, Sudeshna, Rohit, Kia, Ahmed, Irana, Kay, Saeed and Kuni. Thanks Nishant, you were the first office mate I had. Thanks for the friendship, it was nice visiting your home for your marriage. Thanks Keerthi, Vishal Metri, Sridevi, Vijay for the occasional outings and dinners. Thanks Keerthi for being always thoughtful, I really loved your go away present, a documentary channel subscription. Thanks Bharath, as I moved to Netherlands, our friendship from bachelors time made me feel comfortable in a new country. You and your wife, Nirupa were kind enough to visit me and invite me home. Our friendship is one to cherish for lifetime. Thanks Thiyagamani, hanging out with you in Germany some years after school days, brought back memories of home. Thanks Sridhar for being there for me always in Bangalore. I couldn't have asked for a better friend. It is so nice to be near you now and bug you even more 😈 !!. Thanks Babu, Shyam, Dhana and Deva, my bunch for outings in Bangalore. And it's so nice to reconnect with old friends like Shan, Anirudh, Ram, Prabha, Mc, bala and Joseph. Thanks to the new colleagues Somil, Shantanu, Valli, Vishal who were old friends in Shell PhD program. It's nice to see familiar faces in the new environment. Thanks to Ram, Suchi for helping me settle into my new job in Bangalore.

I want to thank my teachers from schooldays who motivated me and encouraged to strive for higher goals. Thanks to Aurnachalam sir for putting together a great team of teachers. Thanks to my two favorite teachers Babu john and Vijayalashmi, who made learning Chemistry and Physics so much exciting. Your belief in me gave the strength to pursue a career in Science.

Now it's time for the family, who went the extra mile of taking care of me while I moved abroad for my master studies and welcoming me back now with open-arms as I move to India. Without you I wouldn't be able to pursue my dreams, for that I thank you all from the bottom of my heart. Thanks Mohana, Arul, Karthi, Ritish, Mohit, Perima, Periappa for being there and taking care of Patti, Thatha, mom and dad,

I am forever in debt to you. With you guys around I didn't have to worry about anything at home. And thanks to the fluffy dough Bairavi (doggo) , you were always an instant stress buster. Thanks to Thangayya even though I don't remember the days from childhood, I heard nothing but warmth and affection you provided to everyone in the family. Nadumani mama for making my childhood summers joyful, teaching me how to ride, to swim and more importantly how to be courageous. Thanks Patti (Grandma), for being the bed rock of family and showing your unfathomable affection for us. Thanks Thatha (Grandpa) for sharing your wisdom and showcasing your strong character, you will be dearly missed. Thanks Chitappa, Chithi, Satya, Ponnusamy mama, Natarasu mama, Kutti mama, Thendral for looking after mom and dad, and helping me whenever needed. I would like to take this opportunity to thank people who helped me in so many ways - Maruthamba akka (for taking care of dad), Kannan, Kaushik (for driving us around everywhere), Ramya akka and her husband (for finding me a house in Bangalore). Neighbhors/friends - Teacher family, Padmini aunty, Trs uncle, priya aunty and uncle, Valli akka family (valli amma, sankar, kumar, thambidurai mamas) for helping us at any instant without second thoughts. Your help means a lot to me and my parents.

Appa (dad), thanks for being there always and letting me pursue my career goals with no questions asked, aiding me in my studies and just asking to take care of my health. Your sense of sincerity and punctuality is a constant source of motivation. Amma (mom), thanks for being everything, even knowing my emotions and thoughts as if reading my mind 😱. And helping me to stay cool, calm and enjoy life. Without you nothing would have been possible.

Thanks to the new members of the family, Yavana's dad, mom and Karthi. I am so happy to be part of the family and hope for more cheerful memories to be made. Karthi thanks for your friendliness and companionship.

Finally, my fiancee Yavana. Thanks for being there during the final hectic days of my PhD and helping me keep my composure. Your determination and hard-working nature is source of awesomeness. And I am privileged to have such a strong and caring woman to be part of my life. Love you loads Peppa 😍

Duraivelan Palanisamy

University of Twente
May, 2019

Summary

Brownian simulations are used to study colloidal dynamics in the Stokes or low Reynolds number regime. The solvent is modeled implicitly with stochastic noise in terms of random forces and torques obeying fluctuation-dissipation theorem. Typically rigid multi-bead models are used to calculate the mobility matrix of arbitrarily shaped bodies with hydrodynamic self-interaction (like the HYDRO++ package by de la Torre *et al.*). However this approach is limited to translational, rotational and translational-rotational coupling terms, and therefore can not be applied to bodies in a shear flow. We have extended the formalism to include coupling between the rate-of-strain and the translational and rotational motions, yielding a single square 11x11 matrix describing the full hydrodynamic mobility tensor of the rigid body. This extended mobility calculation provides access to dynamic stresses acting on the body and thereby the intrinsic viscosity of a dilute suspension of these objects. In combination with a recently developed rotational Brownian dynamics scheme by Ilie *et al.*, this enables direct simulation of arbitrarily shaped rigid bodies in the presence of flow fields. The new algorithm was used to study the shear-thinning rheology of ellipsoids of various aspect ratios. And shear rheology of more asymmetric objects like hemi-spherical caps, helices were considered. In Chapters 4, 5 we focus on the fluctuation-dissipation theorem. Even though this theorem has been used extensively in simulating dynamics of a colloid, little attention is made to stress fluctuations. We have derived an accurate evaluation of colloidal Brownian stresses by including rotational derivatives of the mobility matrix and extended the fluctuation-dissipation theorem to include stress fluctuations. The inclusion of fluctuating stresses which has neglected in all the previous Brownian dynamics formulaisms enables auto-correlation of stress at the pure Brownian limit (Pe=0). Combined with the Green-Kubo relations the auto-correlation functions yield viscosity of the colloidal suspensions. We see agreement between the Einstein viscosity coefficients evaluated from our auto-correlation estimates and low Peclet shearing simulations. Storage and loss moduli were also obtained by performing Fourier transforms of the auto-correlation function. In the last Chapter we performed cluster aggregation simulations to see the effect of our improved simulation and mobility calculation algorithms on aggregation kinetics. This will facilitate us in the simulation of colloidal aggregation under shear flow, with the aim of improving the understanding and efficiency of flow batteries.

Samenvatting

Brownse simulaties zijn gebruikt om colloïdale dynamica te bestuderen in het Stokes of lage Reynoldsgetallen regime. De vloeistof is impliciet gemodeleerd met stochastisch ruis in termen van aselecte krachten en koppels die voldoen aan het fluctuatie-dissipatie theorema. Typisch zijn starre veel-deeltjes modellen gebruikt om de mobiliteitsmatrices te berekenen van willekeurig vormgegeven objecten met hydrodynamische zelf-interactie (zoals in het hydro++ pakket van de la Torre *et al.*). Maar deze methode is beperkt tot translatie, rotatie en translatie-rotatie koppeling termen, en kan daarom niet gebruikt worden voor objecten in een afschuifstroming. We hebben het formalisme uitgebreid door koppeling tussen de deformatiesnelheid en de translatie en rotatie bewegingen op te nemen, leidend tot een enkele 11x11 matrix die de volledige hydrodynamische mobiliteitstensor van het starre object beschrijft. Deze uitgebreide mobiliteitsberekening geeft toegang tot de dynamische spanningen die op het object werken en daarmee tot de intrinsieke viscositeit van een ijle suspensie van deze objecten. In combinatie met een recent ontwikkeld rotationele Brownse Dynamica schema by Ilie *et al.* maakt dit directe simulaties mogelijk van willekeurig vormgegeven objecten in de aanwezigheid van stromingsvelden. Het nieuwe algoritme werd gebruikt om de 'shear-thinning' rheologie te bestuderen van ellipsoïdes met gevarieerde aspect ratios. En de afschuifrheologie van asymmetrischere objecten, zoals een halve bolkap en helixen, zijn beschouwd. In hoofdstukken 4 en 5 richten we de aandacht op het fluctuatie-dissipatie theorema. Alhoewel dit theorema al uitgebreid gebruikt wordt in simulaties van colloïdale dynamica, is er weinig aandacht besteed aan spanningsfluctuaties. We hebben een nauwkeurige evaluatie van colloidale Brownse spanningen afgeleid door de rotationele afgeleides van de mobiliteitsmatrix mee te nemen en het fluctuatie-dissipatie theorema uit te breiden met spannings fluctuaties. De inclusie van fluctuerende spanningen, die genegeerd werden in alle voorgaande Brownse dynamica formalismes, maakt zelf-correlaties van de spanningen in de puur Brownse limiet (Pe = 0) mogelijk. Gecombineerd met de Green-Kubo relaties leveren de zelf-correlatiefuncties de viscositeit van de colloidale suspensies. We zien overeenstemming tussen de Einstein viscositeitscoëfficiënten geëvalueerd met onze zelf-correlaties en laag Pécletgetal afschuifsimulaties. Opslag- en verliesmoduli zijn ook verkregen door het uitvoeren van Fouriertransformaties van de zelf-correlatiefunctie. In het laatste hoofdstuk voerden we cluster-aggregatie simulaties uit om het effect te zien van onze verbeterde simulatie- en mobiliteitsberekeningsalgoritmes op de aggregatiekinetiek. Dit maakt het ons makkelijker in de simulatie van colloïdale aggregatie in afschuifstromingen, met als doel het verbeteren van het begrip en de efficiëntie van stromingsbatterijen.

Curriculum Vitæ

Duraivelan Palanisamy

27-08-1990 Born in Neyveli, India.

Education

2008–2012 B. E. in Electronics and Communication Engineering
National Institute of Technology, Tiruchirappalli

2012–2014 M. S. in Nanotechnology
University of Pennsylvania, Philadelphia

2014–2019 PhD candidate Multi Scale Mechanics
University of Twente, Netherlands

Thesis:	Micro-hydrodynamics of non-spherical colloids
Promotor:	Prof.dr. S. Luding
Co-Promotor:	Dr. ir. W. K. den Otter

Industrial Experience

2019– Researcher, Computational Chemistry and Materials Science
Shell, Bangalore

List of Publications

1. **D. Palanisamy**, and W. K. den Otter, *Efficient Brownian Dynamics of rigid colloids in linear flow fields based on the grand mobility matrix*, Journal of Chemical Physics **148**, 194112 (2018).

2. **D. Palanisamy**, and W. K . den Otter, *Fluctuating stresslets and the viscosity of colloidal suspensions*, submitted.

3. **D. Palanisamy**, and W. K. den Otter, *Einstein viscosities of non-spherical colloids by Brownian Dynamics simulations*, in preparation.

4. **D. Palanisamy**, and W. K. den Otter, *Fluctuating Brownian stress and the viscosity of colloidal suspensions*, in preparation.

5. **D. Palanisamy**, and W. K. den Otter, *Aggregation dynamics of sticky colloids: effect of rotational Brownian dynamics and intra-cluster hydrodynamics on diffusion limited cluster aggregation*, in preparation.